A characterization of the physical environment at eelgrass (Zostera marina) sites along the Atlantic coast of Nova Scotia

Kira A. Krumhansl, Michael Dowd, Melisa C. Wong

Science Branch, Coastal Ecosystem Sciences Division
Maritimes Region, Fisheries and Oceans Canada
Bedford Institute of Oceanography
1 Challenger Drive
Dartmouth, NS B2Y 4A2

2020

Canadian Technical Report of Fisheries and Aquatic Sciences 3361

Fisheries and Oceans Canada

Pêches et Océans Canada

Canada

Canadian Technical Report of Fisheries and Aquatic Sciences

Technical reports contain scientific and technical information that contributes to existing knowledge but which is not normally appropriate for primary literature. Technical reports are directed primarily toward a worldwide audience and have an international distribution. No restriction is placed on subject matter and the series reflects the broad interests and policies of Fisheries and Oceans Canada, namely, fisheries and aquatic sciences.

Technical reports may be cited as full publications. The correct citation appears above the abstract of each report. Each report is abstracted in the data base *Aquatic Sciences and Fisheries Abstracts*.

Technical reports are produced regionally but are numbered nationally. Requests for individual reports will be filled by the issuing establishment listed on the front cover and title page.

Numbers 1-456 in this series were issued as Technical Reports of the Fisheries Research Board of Canada. Numbers 457-714 were issued as Department of the Environment, Fisheries and Marine Service, Research and Development Directorate Technical Reports. Numbers 715-924 were issued as Department of Fisheries and Environment, Fisheries and Marine Service Technical Reports. The current series name was changed with report number 925.

Rapport technique canadien des sciences halieutiques et aquatiques

Les rapports techniques contiennent des renseignements scientifiques et techniques qui constituent une contribution aux connaissances actuelles, mais qui ne sont pas normalement appropriés pour la publication dans un journal scientifique. Les rapports techniques sont destinés essentiellement à un public international et ils sont distribués à cet échelon. II n'y a aucune restriction quant au sujet; de fait, la série reflète la vaste gamme des intérêts et des politiques de Pêches et Océans Canada, c'est-à-dire les sciences halieutiques et aquatiques.

Les rapports techniques peuvent être cités comme des publications à part entière. Le titre exact figure au-dessus du résumé de chaque rapport. Les rapports techniques sont résumés dans la base de données *Résumés des sciences aquatiques et halieutiques.*

Les rapports techniques sont produits à l'échelon régional, mais numérotés à l'échelon national. Les demandes de rapports seront satisfaites par l'établissement auteur dont le nom figure sur la couverture et la page du titre.

Les numéros 1 à 456 de cette série ont été publiés à titre de Rapports techniques de l'Office des recherches sur les pêcheries du Canada. Les numéros 457 à 714 sont parus à titre de Rapports techniques de la Direction générale de la recherche et du développement, Service des pêches et de la mer, ministère de l'Environnement. Les numéros 715 à 924 ont été publiés à titre de Rapports techniques du Service des pêches et de la mer, ministère des Pêches et de l'Environnement. Le nom actuel de la série a été établi lors de la parution du numéro 925.

Canadian Technical Report of
Fisheries and Aquatic Sciences 3361

2020

A characterization of the physical environment at eelgrass (*Zostera marina*)
sites along the Atlantic coast of Nova Scotia

By

Kira A. Krumhansl, Michael Dowd[1], and Melisa C. Wong

Science Branch
Maritimes Region
Coastal Ecosystem Sciences Division
Fisheries and Oceans Canada
1 Challenger Drive
Dartmouth, NS B2Y 4A2

[1] Department of Mathematics and Statistics, Dalhousie University, Halifax, NS B3H 4R2

Correct citation for this publication:

Krumhansl, K., Dowd, M., Wong, M.C. 2020. A characterization of the physical environment at eelgrass (*Zostera marina*) sites along the Atlantic coast of Nova Scotia. Can. Tech. Rep. Fish. Aquat. Sci. 3361: v + 213 p.

iii

TABLE OF CONTENTS

Abstract

Krumhansl, K., Dowd, M., Wong, M.C. 2020. A characterization of the physical environment at eelgrass (*Zostera marina*) sites along the Atlantic coast of Nova Scotia. Can. Tech. Rep. Fish. Aquat. Sci. 3361: v + 213 p.

Eelgrass (*Zostera marina*) supports diverse and productive ecosystems in the coastal zone, and is at threat from a variety of human activities. Warming seawater temperatures, changing storm patterns, and altered dynamics of freshwater and nutrient run-off associated with climate change have already impacted eelgrass communities worldwide, and are expected to continue to do so into the future. In this report we characterize the physical environment at 10 eelgrass sites along the Atlantic Coast of Nova Scotia to provide a documentation of the range of environmental conditions under which eelgrass occurs in this region, and set the stage for the development of empirical relationships between physical conditions and eelgrass ecosystem status. We present metrics of temperature, currents, light, wave exposure, and site characteristics (e.g. depth, slope, tidal range) generated from data collected April 2017 to September 2018, and relate temporal changes in these parameters to coastal processes, including winds, tides, and upwelling. We describe heat accumulation at each site using the Growing Degree Day metric, and define and characterize warm water events where temperatures exceeded physiologically-relevant thresholds (23°C and 27°C). Our analysis identified sites where temperatures tended to remain warmer, current speeds were low, and waters were relatively turbid. Tidal and daily heating and cooling during summer months were more extreme at these sites, and they experienced warm water events that lasted on the order of hours to days. These sites tended to be shallow and occur in areas protected from wave exposure, and in general were less strongly influenced by coastal upwelling. These metrics are consistent with more stressful conditions for eelgrass. We also identified sites that were deeper, more consistently cooler, and had lower turbidity and higher current speeds. These sites tended to be more wave exposed and more strongly influenced by coastal upwelling, suggesting environments more conducive to eelgrass health. These results can contribute to conservation planning by supporting decision making around identifying target beds for protection, and will enable predictions regarding how eelgrass ecosystems will respond to future changes in environmental conditions associated with climate change.

Résumé

Krumhansl, K., Dowd, M., Wong, M.C. 2020. A characterization of the physical environment at eelgrass (*Zostera marina*) sites along the Atlantic coast of Nova Scotia. Can. Tech. Rep. Fish. Aquat. Sci. 3361: v + 213 p.

Les herbiers de zostère marine (*Zostera marina*) constituent des écosystèmes diversifiés et productifs dans la zone côtière et sont menacés par diverses activités humaines. Le réchauffement de la température de l'eau de mer, l'évolution des tempêtes et la modification de la dynamique des eaux douces et du ruissellement des nutriments, associés au changement climatique, ont déjà affecté les communautés de zostères du monde entier et devraient continuer de le faire à l'avenir. Dans ce rapport, nous caractérisons l'environnement physique de 10 sites de zostères le long de la côte atlantique de la Nouvelle-Écosse pour fournir une documentation de l'éventail des conditions environnementales dans lesquelles la zostère se maintient dans cette région, et préparons le terrain pour le développement de relations empiriques entre les conditions physiques et l'état de l'écosystème de la zostère. Nous présentons des mesures de la température, de courants, de la lumière, de l'exposition aux vagues et des caractéristiques du site (e.g. profondeur, pente, amplitude des marées) générées à partir des données recueillies d'avril 2017 à septembre 2018, et relions les changements temporels de ces paramètres aux processus côtiers, y compris les vents, les marées et les remontées des eaux côtières. Nous décrivons l'accumulation de chaleur pour chaque site à l'aide de la métrique du degré jour de croissance et définissons et caractérisons les événements thermiques extrêmes où les températures dépassent les seuils physiologiquement pertinents (23 °C et 27 °C). Notre analyse a identifié des sites où les températures avaient tendance à rester plus chaudes, les vitesses de courants étaient faibles et les eaux étaient relativement troubles. Les réchauffements et refroidissements journaliers dus à la marée pendant les mois d'été étaient plus extrêmes sur ces sites, et ils ont connu des événements thermiques extrêmes qui ont duré de l'ordre de quelques heures à quelques jours. Ces sites avaient tendance à être peu profonds et se trouvent dans des zones protégées de l'exposition aux vagues et, en général, étaient moins fortement influencés par la remontée des eaux côtières. Ces caractéristiques sont associées avec des conditions plus stressantes pour la zostère. Nous avons également identifié des sites plus profonds, régulièrement plus frais, avec une turbidité plus faible et des vitesses de courant plus élevées. Ces sites avaient tendance à être davantage exposés aux vagues et plus fortement influencés par l'upwelling côtier, ce qui suggère des environnements plus propices à la santé des zostères. Ces résultats peuvent contribuer à la planification de la protection des zones côtières en soutenant la prise de décision concernant l'identification des herbiers à protéger, et permettront des prédictions concernant la façon dont les écosystèmes de zostères répondront aux changements futurs des conditions environnementales associés au changement climatique.

__Introduction__

Declines in seagrass ecosystems have been documented worldwide (Waycott et al. 2009), and environmental factors are considered key drivers of change (Unsworth et al. 2015). Seagrass loss is associated with human activities that cause eutrophication, decreased light availability, increased sedimentation, increased incidence of physical disturbance (e.g. storms), and warming temperatures associated with climate change (Orth et al. 2006, Waycott et al. 2009). Seagrass ecosystems provide habitat for a high diversity of species in the coastal zone, and provide ecosystem services that include carbon sequestration, coastal protection, the maintenance of commercial fisheries, and the filtration and cycling of nutrients (Hemminga and Duarte 2000, Orth et al. 2006, Barbier et al. 2011). Documenting the environmental conditions experienced by seagrass beds throughout their range is critical towards understanding how these valuable habitats are likely to respond to climate change, and for management and conservation actions aimed at seagrass ecosystem protection.

Characteristics of seagrass beds, including their spatial distribution, biomass, patchiness, and productivity are tightly regulated by environmental factors, including sediment characteristics, hydrodynamics (e.g. waves and currents), light availability, water quality (e.g. nutrients, total suspended solids), and temperature (Fonseca & Bell 1998, Koch 2001, Lee et al. 2007, Krause-Jensen et al. 2011). The occurrence of epiphytes on seagrass blades, increases in dissolved nutrients, high levels of organic and non-organic particulates, and sedimentation are all factors that can increase light attenuation, thereby reducing light levels and causing seagrass declines (Short & Wyllie-Echeveria 1996, Lee et al. 2007). Waves and currents regulate sediment dynamics, and cause physical disturbances that can dislodge seagrasses and introduce patchiness at different scales (Fonseca & Bell 1998). High water velocities also increase suspended particulates that reduce light availability (Kemp et al. 1984), and can increase the incidence of self-shading as blades are pushed flat towards the substrate in high flow (Fonseca et al. 1982). Low water velocities, however, are associated with the accumulation of organic material and consequently high sulfide concentrations in sediments, a thickening of the diffusive boundary layer around seagrass blades that can cause a reduction in nutrient uptake, and increased solar heating leading to high water temperatures, all of which can be detrimental to seagrasses (Koch 2001). Therefore, intermediate water velocities are generally considered best for seagrass health and productivity.

Water temperature is also known to regulate seagrass growth and productivity, with seasonal changes in temperature leading to high growth rates in spring and summer and declines through fall and winter (Lee et al. 2007). Seagrass growth and productivity increase with temperature until a certain point, after which high water temperatures can cause growth inhibition and mortality (Barber & Behrens 1985, Lee et al. 2007). The impacts of warm water events are gaining increased attention in marine environments, as their occurrence has been linked to large-scale losses of marine habitat-forming macroalgae and seagrass (Ruthrof et al. 2018). Previous work has identified optimal and lethal temperatures for growth and productivity of seagrasses in temperate ecosystems (Lee et al. 2007), but relatively little attention has been paid to the impacts of spatial variation in temperature in driving patterns of seagrass health. Moreover, analyses tend to focus on mean, maximum, and standard deviation of temperature as the main metrics driving biological responses, though it may be the case that simple characterizations of physical conditions such as these may not adequately capture species responses to environmental conditions. Alternative methods of characterizing temperature, including calculations of growing degree day (i.e. the thermal integral), descriptions of warm water events (e.g. their frequency of occurrence and intensity), and analyses linking temperature change to coastal oceanographic dynamics (e.g. upwelling, winds) have been used in other natural systems and may more effectively describe spatial and temporal patterns of ecosystem change.

Zostera marina is the dominant seagrass species occupying soft-sediment areas protected from wave action in Atlantic Canada. Anecdotal evidence suggests that some areas in the region may be experiencing losses of eelgrass habitat through the combined effects of coastal development, increased nutrient run-off, climate change, and invasive species (Schmidt et al. 2012). The purpose of this research

is to document the physical conditions experienced by eelgrass beds at a range of sites along the Atlantic Coast of Nova Scotia, including temperature, current speeds, light levels, depth, slope and wave exposure at each site. These metrics can be used to evaluate the ecosystem status and resilience of these eelgrass beds. We look for relationships among environmental variables to begin to identify the mechanisms by which current speeds, wind speeds, and upwelling impact temperature and light conditions at each site. The results can be used to develop a predictive empirical model to evaluate how changing environmental conditions impact the status of eelgrass beds in the region. This is useful in the context of identifying target beds for conservation measures.

Materials and Methods

Study Sites

Environmental variables were recorded at 10 sites along the Atlantic coast of Nova Scotia from May/June 2017-April/May 2018 (Figure 1). These 10 sites were chosen to represent the range of conditions over which eelgrass beds occur in the region, spanning different dominant substrate types (e.g. sandy, muddy), proximities to human impacts, and degrees of current and wave exposure. At 6 of the sites, subsites or "locations" were chosen to examine within-site variation due to depth (e.g. "deep" or "shallow") or dominant substrate (e.g. "sandy" or "muddy") (see Table 1 for site descriptions). The average depth at high tide at all sites ranged 0.8-6.2m (Table 1).

Data Collection, Processing, and Analysis

Temperature

At each site, temperatures were recorded in each location using a HOBO tidbit temperature logger (Onset Corp) anchored to the substrate with cinder blocks, patio stones, and/or chain. All instruments were placed away from the edges of each bed, and in the direct vicinity of where biological measures were taken (not reported here), and thus are intended to record conditions that are representative of what the eelgrass experiences at each site. Loggers were deployed in May-early June 2017 at all sites and remained in the water until April-May 2018. Loggers recorded temperatures continuously every 10 minutes for the duration of deployment. Raw temperature data were used to generate summary metrics of temperature conditions, including the mean, standard deviation, maximum, minimum, and 95th percentile temperature at each site and location within site. Summary metrics were calculated for the summer and early fall period only (June-September 2017) and for the entire year. Eelgrasses at some of the sites monitored are exposed to the air at low tide. Temperatures recorded during these periods were left in the temperature records while calculating summary temperature metrics as aerial temperatures are known to significantly impact seagrass physiology and survival through desiccation, heat stress, and exposure to photo inhibitory irradiances (Erftemeiher and Herman 1994, Kim et al. 2016, Leuschner et al. 1998).

Temperature data were then filtered to separate variation into three components: 1) high-frequencies, defined as temperature changes that occur over a period of 36 hours or less, 2) mid-frequencies, defined as temperature changes that occur over a period of 37 hours to 60 days, and 3) low-frequencies, defined as changes occurring over a period of time greater than 60 days. High-frequency temperature changes are those that would be expected to occur in association with tidal exchanges and diel fluctuations in air temperature associated with solar heating. Mid-frequency temperatures are those that would be expected in association with storm and upwelling events, or other processes occurring at time scales of days to weeks. Low-frequency temperature changes are those occurring in relation to seasonal and annual cycles, on the order of months to a year. Low-frequency signals were modeled by fitting a third order polynomial function to raw temperature data, and a prediction was generated using this model for comparison among sites. High-frequency signals were isolated by applying a 6th order

Butterworth low-pass filter, and then subtracting this smoothed data from the raw data values. Subtracting the high and low-frequency bands from the raw data isolated mid-frequency temperature changes.

Temperature data isolated into frequency bands were then used to characterize processes occurring over those time scales. Temperature variation in the middle and high frequency bands were calculated as the standard deviation of filtered temperatures in each band, and the ratio of high to mid frequency variation was calculated as an indication of the influence of the tides and solar radiation (high frequency) in causing changes in temperature relative to those caused by winds and storms (mid frequency). A spectral analysis was used to identify the dominant signal frequencies in the high-frequency band. High frequency temperature time series were then aligned with the start of a low tide at the beginning of June at each site and location, and clipped at the end of October. Each truncated time series was then split into 12.42 hour sections and averaged across all sections to generate an estimate of the average change in temperature over the daily tidal cycle. Mean temperature changes over the daily cycle were calculated in a similar manner by aligning the beginning of each time series at 18:00 in early June and then splitting the remaining time series into 24 hour sections. Data averaged across these 24 hour sections was then used to identify the mean range of temperatures experienced at each site over the daily heating and cooling cycle.

Warm water events were also characterized from temperature records, as warm temperatures are considered harmful for seagrasses through inhibition of photosynthetic and respiratory processes. A literature review of studies examining optimal temperatures for photosynthesis for *Z. marina* in temperate locations identified two possible thresholds. The mean optimal temperature as recorded from field and laboratory studies is listed as 23°C by Lee et al. (2007). When only controlled laboratory studies are considered, the optimal temperature threshold is considerably higher: 27°C. Summary metrics of warm water events were calculated using both thresholds (23°C and 27°C). There was also a discrepancy in the literature as to the duration of exposure to above-optimal temperatures needed to cause a physiological response. In some cases, responses were observed after as little as 15 minutes (Beibel & McRoy 1971, Marsh et al. 1986), whereas in others responses weren't observed for hours to weeks (Evans et al. 1986, Gao et al. 2017). As a result of this discrepancy, we have set variable durations according to the temperature threshold used. With the lower 23°C threshold, a minimum duration of 2 hours at this temperature is needed to be considered a warm-water event. For the higher temperature threshold of 27°C, a minimum duration of 10 minutes at this temperature is needed to be considered a warm-water event. For events to be considered distinct, they must be separated by at least 3 days (Oliver et al. 2018). For each site, the total number of hours above each threshold value, the total number of events, and the mean duration of events was summarised. Note duration is calculated as the total time within the date range that temperatures were above the set threshold. In some cases this results in a shorter event duration than the time encompassed by the date range. The thermal integral was calculated as the area under the temperature curve for each warm water event as an indicator of the amount of additional heat entering the system above these physiologically-relevant temperature thresholds.

Growing degree days (GDD) is a metric commonly used in horticulture to quantify heat accumulation in a system. Here, it is calculated by subtracting a set base temperature ($Tbase$) from the average of the daily maximum ($Tmax$) and minimum temperatures ($Tmin$) at time t, and sequentially adding these across the temperature record (Eqn 1) (Neuheimer and Taggert 2007).

$$GDD_t = \frac{Tmax+Tmin}{2} - Tbase \hspace{3cm} \text{Eqn. 1}$$

The GDD calculation will be strongly influenced by the chosen base temperature, usually selected to represent the threshold for the biological process of interest. *Z. marina* is capable of photosynthesizing at temperatures as low as 0°C, but photosynthesis increases rapidly between 0-5°C, with a peak in the ratio of photosynthesis to respiration at 5°C (Beibel & McRoy 1971, Marsh et al. 1986). Thus, we elected to use a baseline temperature of 5°C. In many cases, threshold temperatures for the physiological process of interest are not known. Thus, statistical methods have been developed to estimate an appropriate base

temperature for GDD calculations (Yang et al. 1995). One such method is to calculate the standard deviation of GDD across multiple plantings (in this case sites) using a range of baseline temperatures. The baseline temperature for which the standard deviation of GDD calculations is lowest is said to represent the best baseline temperature for the final GDD calculation. For this study, GDD was calculated using temperatures ranging from 0-13°C at all sites. The standard deviation of GDD values were at their lowest at 11°C, so this temperature was also used for GDD calculations at each site. If the average daily temperature was lower than the baseline temperature, the GDD for that day was set to zero (i.e. no heat accumulation for that day). Since the GDD calculation relies on selecting maximum and minimum temperatures for each day, temperature data were filtered to remove spikes and dips in the record corresponding to the sensor being out of the water, specifically removing any values that fell outside the range of ±2 standard deviations from the mean. GDD calculations for land plants often cap temperatures at 30°C, with the rationale that growth generally does not occur above this temperature. However, for *Z. marina*, P:R remain above 1 to 35°C. Given that temperatures did not exceed this level in the present study, no maximum temperature cap was used.

Winds and upwelling

Wind speeds at the Shearwater naval base (44° 37' 47.000" N, 63° 30' 48.000" W, data recorded at 10 m above ground) were acquired from Environment Canada (http://climate.weather.gc.ca/). Wind stress was calculated from wind speed using Eqn 1.

$$\tau = C_D \times \rho_a \times U^2$$
Eqn. 2

Where C_D is a dimensionless drag coefficient (0.0014), ρ_a is the density of air (1.22 kg m^{-3}), and U is hourly wind speed. Wind stress values were back averaged using a rolling mean function with a backward window length of 2 days to generate a value of wind conditions that represents persistent wind events, and are therefore more likely to cause changes to surface seawater temperatures. The window length of 2 days was chosen by selecting a series of window lengths (0-10), and selecting the window length where wind had the highest correlation with temperature in the middle frequency band. The moving average was calculated using the movavg function in the pracma package (Borchers 2018) in R (R Core Team 2017).

Across u and along-shelf v wind speeds were calculated from wind data, and used to calculate meridonal wind stress (τ), using the density of air ρ_a (1.22 kg m^{-3}) and a dimensionless drag coefficient C_d (0.0014) (Eqn 2).

$$\tau = \rho_a \times C_d \times \sqrt{u^2 + v^2} \times v$$
Eqn. 3

Wind direction was offset by 60 degrees prior to this calculation to align with the dominant along-shore wind direction in Nova Scotia that causes coastal upwelling (Petrie et al. 1987). Ekman transport Q (used as an index of upwelling, Pond & Pickard 1983) was then calculated using this wind stress value, along with seawater density ρ_w (1025 kg m^{-3}), and the Coriolis parameter f (1 x 10^{-4}) (Eqn 3).

$$Q = \frac{\tau}{f \times \rho_w} \times 10^3$$
Eqn. 4

The units of the index are cubic meters of water per second per km of coastline. This index value was then back-averaged using a rolling mean function with a backward window length of 17 days. This window length was chosen by selecting a series of window lengths from 1-30 days and correlating these data with temperatures in the middle frequency band. Correlations were highest at 17 days.

Depth

Pressure sensors (HOBO Water Level Logger) were deployed along with current meters to generate a record of water depth. Water depth (h) was calculated from the pressure record (P_{total}) using standard atmospheric pressure (P_{atmos}= 1.01 x 10^5 N/m^2), the density of seawater (ρ = 1.03 x 10^3), and the acceleration of gravity (g = 9.8 m/s) (Eqn 5).

$$h = \frac{P_{total} - P_{atmos}}{\rho \times g}$$
Eqn. 5

Depth data recorded every 10 minutes were used to calculate the mean depth at high tide at each site. This was done by isolating local maxima within 12.4 hour intervals in the depth record, and averaging these depths across all high tides in the data set. The tidal signal associated with the principal lunar tide (M2) was then extracted from the depth record using harmonic regression, and the tidal range at each site was determined by multiplying the amplitude of the resulting function by two.

Currents
Electromagnetic current meters (Infinity-EM AEM, JFE Advantech) were deployed on cinder block or patio stone moorings at each site for a 2-4 week period. Instrument deployments were staggered in time across sites, with deployments occurring from June-September 2018. Where sites contained deep and shallow locations, current meters were deployed at deep locations only. Current meters recorded current speed and direction in burst samples (20 samples per burst, 2 second intervals between bursts) every 10 minutes for the duration of deployment.
Current data were used to generate summary metrics of current conditions at each site, including the mean, maximum, minimum, and standard deviation of currents. Prior to calculating these summary metrics, data were quality controlled by applying a filter to remove values that were more than 2 standard deviations above and below the mean for each burst sample. Following this, current speeds were averaged across the burst to generate an estimate of current speed for each 10-minute period in the record. Mid (>24 hours) and high-frequency (<24 hours) changes in current speed were then isolated from each record of current speed by applying a 6th order Butterworth low-pass filter, and then subtracting this smoothed data from the raw data values.

Light
Light conditions were characterized at each site and location within site using sensors that record Photosynthetically Active Radiation (PAR, 400-700 nm) (DEFI2-L, JFE Advantech). PAR sensors measured downwards irradiance at 2 depths that were fixed relative to each other and the bottom, and separated by 0.5-1.0 m. PAR sensors were deployed for 1-2 weeks at each site and location within site, and recorded irradiance every 10 minutes.
Light data were used to calculate the light attenuation coefficient (K_d), using the equation shown in Eqn 6.

$$K_d = \frac{1}{z_2 - z_1} \ln \frac{E_d(z_1)}{E_d(z_2)}$$
Eqn. 6

Where z represents the two depths (1 = shallower depth [*top*], 2 = deeper depth [*bottom*]) at which the PAR sensors were deployed, and E_d represents the downwards irradiance at depth z. Light data with values less than 50 umol m^{-2} s^{-1} were filtered prior to these calculations, as these values generally occurred during the night and were low relative to the accuracy limit of the instrument (200 umol m^{-2} s^{-1}). Further, light values were removed if they were outside of the range of ±2SD from the hourly mean, or if the light sensor was exposed at low tide. Following this filtering, hourly averages were generated and used to calculate light attenuation. Light attenuation values below 0 were then removed, as they represent instances where the top light sensor was reading lower light measurements than the bottom light sensor,

either due to measurement error or fouling on the top sensor. Summary metrics of light were then calculated for each site and location, including the mean, maximum, and standard deviation of the absolute value of light as read by the bottom sensor (after filtering), and the mean, maximum, and median light attenuation.

Wave Exposure

A relative index of wave exposure was calculated for all sites and locations, modified from Keddy (1982) (Eqn. 7):

$$REI = \sum_{i=1}^{36}(V_i \times W_i \times F_i)$$
<div align="right">Eqn. 7</div>

Where V_i is monthly average wind speed, W_i is wind frequency, and F_i is fetch (m) from the ith direction. Fetch, wind speed, and wind frequency were measured in 36 increments of 10°. Exposure was calculated using wind data from January 2016-December 2017, obtained from Environment Canada, as described above. Fetch was calculated using the fetch function in R (package fetchR, Seers 2018).

Seafloor Slope

The slope angle of each site was estimated by measuring depth at 2m increments along 2-3, 50m transects at each location. Transects were positioned perpendicular to shore at each location within site, except where deep and shallow locations were located less than 50m apart in an inshore-offshore direction (Sambro and Croucher Island). From these depth data, the slope angle was calculated for each 2m interval as the arctangent of the depth difference between sequential points divided by the along bottom distance (2m). The slope along the transect was calculated by averaging the resulting slope angles across sequential points. A site average was generated by averaging values across transects within a site/location.

Relationships between environmental parameters

All metrics were synthesized across sites to enable comparisons of environmental conditions (Figures 2-12). Site-specific results are provided in more detail in the supplementary material (Figures S1-S120). Temperature metrics were related to metrics of wind and upwelling to identify the influence of these processes on temperature conditions. Specifically, temperatures in the middle frequency bands were related to wind stress and the upwelling index using cross-correlation analyses. For analyses with wind stress, temperatures were averaged hourly, and for analyses with upwelling, wind stress was averaged daily. These analyses identified the lag time at which the strongest correlation occurred between temperatures, winds, and upwelling. In addition, lags of -10 to 0 were isolated in the correlation between mid-frequency temperatures and upwelling, and the maximum correlation recorded within this range was determined. This time range is assumed to be the period over which upwelling is most likely to influence temperatures within this frequency range at eelgrass sites. Lag times and the strength of the correlations between winds, upwelling, and mid-frequency temperatures were then compared across sites and locations.

Current speeds were related to winds and tidally-driven changes in depth to investigate the relative importance of storms and tides in influencing water motion at each site. Spectral analyses were conducted on low-pass filtered current data to identify dominant signal frequencies in current and depth records at each site, and a cross-spectral analysis was done to identify the frequencies at which the highest coherence between the two time series records exist. Coherence values were then isolated for the frequencies corresponding to the semi-diurnal tidal constituents (M_2, S_2, N_2, v_2, MU_2, $2"N_2$, Λ_2, T_2, R_2, $2SM_2$, L_2, K_2, frequency = 0.0126-0.0150, period = 11.1-12.9 hours) to evaluate the strength of the relationship between tidally-driven changes in water depth and current speeds. Hourly current speeds

were also correlated with total wind stress at each site using cross-correlation function analysis. Correlations at lags of 0-24 hours were isolated to identify the strength of the relationship between wind stress and current speeds at the time frame over which wind speeds are likely to influence currents (within 24 hours of a wind event). Time series analyses (cross-spectral and cross correlation function analyses) were not performed at the muddy location at Port Joli because there were significant gaps in the time series that occurred because of exposure of the current meter at low tide.

Light attenuation was correlated with measures of wind stress and current speed using linear regression analysis. Current data were not collected concurrently with light at Lower Three Fathom, Sambro, and Port L'Hebert, so these correlations were not performed. Linear regression was used to analyze these relationships because large gaps in time series prevented the use of time series analyses.

All time series analyses were done in R using functions in the signal (Signal developers 2013), TSA (Chan & Ripley 2012), astsa (Stoffer 2017), and tseries (Trapletti & Hornik 2018) packages in R (R Core Team 2017).

Results

Temperature

Temperatures varied across eelgrass sites, with the coldest annual mean temperatures recorded at Sambro Island, Sacrifice Island, Cable Island, and Taylor's Head (Table 2, Figure 2). The warmest annual mean temperatures were recorded at Port L'Hebert, Port Joli, and Lower Three Fathom (Table 2, Figure 2). Annual mean temperatures at all sites ranged from 8.31°C at Sambro deep to 10.84°C at Port Joli muddy, a difference of 2.53°C. Summer temperatures ranged more broadly across sites, with the warmest mean temperature recorded at Lower Three Fathom (19.53°C) and the coldest mean temperature at the deep location at Sambro Island (11.34°C), a difference of 8.19°C (Table 3). Differences in summer temperatures across sites largely mirrored annual differences in mean temperatures. The warmest maximum temperatures overall were observed at Port Joli (34.57°C) and Port L'Hebert (34.37 °C) during the summer months, recorded while loggers were out of the water. Thus, these temperatures represent solar heating of the bed while exposed at low tide. The coldest minimum temperatures were observed at the shallow location at Cable Island (-9.44°C), Mason's Island (-11.51°C), and Port L'Hebert (-8.00°C) in the winter (Tables 2, 3). These cold winter temperatures represent what is experienced when the beds are exposed to the air at low tide in winter, as they are well below the freezing temperature of seawater.

Warm water events where temperatures exceeded the 23°C threshold were observed at four of the ten sites (Port Joli, Port L'Hebert, Lower Three Fathom, and Cable Island) (Table 4, Figure 4). The muddy location at Port Joli had the greatest number of events (n = 9), while Port L'Hebert and the sandy site at Port Joli had the second and third highest number of events (n = 8, 7 respectively) (Figure 4). Lower Three Fathom had the highest average event duration (77.67 hours) as compared with the other sites, where warm water events lasted 24.35 to 33.50 hours on average (Table 4, Figure 4). Warm water events at the 27°C threshold were observed at Port Joli, Port L'Hebert, and Lower Three Fathom, but not at Cable Island. There were fewer events at this threshold (n = 1-6 across sites), and they tended to be less than 5 hours in duration (Table 4, Figure 4).

Plots of growing degree days, or the thermal integral at the 5°C and 11°C thresholds show varying heat accumulation across sites (Figure 5). Consistent with other methods of visualizing overall temperature differences, these plots show higher heat accumulation at Port L'Hebert, Port Joli, and Lower Three Fathom as compared to the other sites. The lowest accumulation of heat occurred at Sambro and Taylor's Head. For both thresholds, there was an accumulation of heat in the spring, summer, and fall, with no accumulation in winter when temperatures dropped below set thresholds (December for 5°C, November for 11°C) (Figure 5).

Seasonal changes in temperature showed similar trends across sites, with a warming from March to September, followed by cooling from October to February (Figure 6). Plots of low-frequency temperature changes showed the largest seasonal ranges at Port Joli, Port L'Hebert, and Lower Three Fathom, with smaller seasonal changes at Sambro, Cable, Croucher, and La Have (Table 5, Figure 6). Mid-frequency temperature changes showed similar trends through time across sites, suggesting a dominant influence of coast-wide processes at all sites in this frequency range, though some sites experienced higher amplitude changes (e.g. Croucher Island, Port Joli, La Have) relative to others (Table 5, Figure 6). Changes in temperature in the mid-frequency range were higher overall than those in the high frequency range, with the ratio of variation in the high to mid frequency ranges being below zero at all sites. This ratio was highest of all sites at the shallow location at Cable Island, Mason's Island, and Port L'Hebert, indicating a stronger influence of tidal and daily heating and cooling processes at these sites relative to others.

High-frequency changes in temperature were greatest at Port L'Hebert, Port Joli, the shallow location at Cable Island, and Mason's Island (Table 5, Figure 6), with these sites having the highest spectral densities at tidal and daily frequencies (Figures 7, 8). For most sites, changes in temperature due to solar heating and cooling were higher than those caused by the tides, except for Mason's Island where the tidal signal was greater. Changes in temperature over the tidal cycle generally followed a trend of cooling during the incoming tide, followed by heating during the outgoing tide. Temperature ranges during the tidal cycle in summer (June-September) ranged from 0.08°C at the deep location at Cable Island to 0.69°C at Mason's Island (Figure 9). Diel changes in temperature generally followed the trend of cooling during the night period and a gradual warming during the day, with variation in the amplitude of this cycle across sites (Figure 9). Day-night changes in temperature ranged from 0.36°C at the shallow location at Croucher Island to 3.33°C at Port L'Hebert (Figure 9).

Drops in temperature in the mid-frequency range generally corresponded to increases in the coastal upwelling index during the spring and summer (Figures 10, 11). Temperatures at all sites were influenced by upwelling to some degree, with the strongest influence occurring at Cable Island (both locations), Sambro (both locations), Sacrifice (both locations), and Mason's Island (cross-correlation < -0.6, Figure 11). At these sites, the highest correlation between changes in upwelling and changes in mid-frequency temperature occurred at a lag time of 0 days (Figure 11). Temperatures at Port L'Hebert, Port Joli (both locations), Lower Three Fathom, and Croucher (both locations) were not strongly influenced by upwelling (Figure 11). Drops in temperature at the mid-frequency range were also influenced by total wind stress at all sites, with temperatures cooling at higher wind stress values, however the direct influence of winds on local mixing was relatively low as compared with wind-induced upwelling at all sites (cross-correlation = -0.20-0 at all sites, Figure 12). The wind had the strongest direct effect at La Have, Port Joli, Lower Three Fathom, and Port L'Hebert. Correlations between mid-frequency temperature changes and wind stress from the direction over which the largest fetch values occur at each site were also examined, but these correlations were much weaker overall than those between total wind stress and temperature, suggesting a dominant influence of coast-wide processes driven by wind than a local wind effect on temperatures (Figures S12, S14, S26, S28, S37, S46, S54, S63, S76, S78, S90, S92, S104, S106, S118, S120).

Shallow locations at each site were generally warmer than deep locations (Tables 2, 3, Figures S1, S15, S65, S93, S107), and experienced wider amplitude changes in temperature over tidal, daily, and seasonal cycles relative to deep locations (Table 5, Figures 6-9, S2-S6, S16-20, S66-70, S80-84, S94-98, S108-112). Temperature variation in the mid-frequency range was generally greater at the deep locations at all sites relative to shallow (Table 5), and were more strongly correlated with the upwelling index at the deep as compared to the shallow locations at the sites most strongly influenced by upwelling (Sacrifice, Sambro) (Figures 11, S7-14, S21-28, S71-78, S99-106, S113-120). The muddy location at Port Joli was generally warmer than the sandy location (Tables 2-3, Figures 3, S79), experiencing more warm water events (Table 4, Figure 4) and higher daily fluctuations in temperature (Figures 7-9). Fluctuations in temperature over the tidal cycle, however, were greater at the sandy location relative to the muddy

location at this site (Figures 7-9, S82-84). Correlations between winds, upwelling, and mid-frequency temperatures were similar between the sandy and muddy locations at Port Joli (Figure 10-12, S85- S92).

Currents and Depth

Current speeds were highest on average at La Have Island (mean = 6.81 cm/s) and lowest at Lower Three Fathom (0.66 cm/s) (Figures 13, 14, Table 6). La Have Island also had the highest maximum current speed (26.04 cm/s), and the highest standard deviation of current speed (4.01 cm/s) (Table 5), while Lower Three Fathom had the lowest minimum (0.15 cm/s) and standard deviation of current speed (0.48 cm/s) (Table 6). Sambro and Croucher Islands also had relatively high current speeds overall, while Mason's Island and Port L'Hebert had relatively low current speeds (Figures 13, 14, Table 6). The deepest site overall was Sambro Deep (6.2 m), while the shallowest site was Lower Three Fathom (0.9 m). The tidal range varied across sites from 0.03 m at Lower Three Fathom to 1.32 m at Mason's Island and Port Joli Sandy (Table 1).

Time series of current speeds at all sites were characterized by fluctuations in the high (< 24 hours) and middle frequency (> 24 hours) bands, with the relative importance of variation in each band differing across sites (Figure 13, Table 7, Figures S121, S124, S127, S130, S133, S136, S139, S142, S143, S146, S149). High-frequency variation in current speeds was greater than mid-frequency variation at Cable Island, La Have Island, Mason's Island, Port L'Hebert, Port Joli (muddy and sandy), Sacrifice Island and Sambro Island. This indicates a dominant influence of short-periodicity (tidally-driven) current fluctuations at these sites relative to changes driven by longer-period processes (e.g. storms) (Table 7). Changes in current speed through time were well explained by changes in water depth at Mason's Island, Taylor's Head, Sambro, Sacrifice, and Port L'Hebert (coherence from cross-spectral analysis > 0.75, Figures 15, S122, S125, S128, S131, S134, S137, S140, S144, S147, and S150). In contrast, variation in current speeds in the middle frequency band was dominant over variation in the high frequency band at Croucher Island, Lower Three Fathom, and Taylor's Head (Table 7), indicating a dominance influence of wind and storm events on current speeds at these sites. Correlations between wind stress and current speeds were highest of all sites at Taylor's Head and Lower Three Fathom (cross correlation > 0.75, Figure 16). In contrast, correlations between wind stress and current speeds were lowest at Sacrifice Island, Port Joli, and Sambro, with longer lag times between changes in wind stress and changes in current speed at Port Joli Sandy and Sambro (7-8 hours) relative to other sites. Most other sites had relatively short lag times (0-1 hour), except for Cable Island and Taylor's Head (3-6 hours) (Figures 16, S123, S126, S129, S132, S135, S138, S141, S145, S148, and S151).

Light

Light levels varied across sites, with the highest values at the shallow locations at Sambro, Cable, and Croucher Islands, and La Have, and the lowest values at the deep sites at Taylor's Head, Sambro Island, Sacrifice Island, and the sandy site at Port Joli (Figures 17, 18, Table 8). Light levels were higher at the shallow locations at each site as compared to the deep locations (Figures 17, 18). Mean light attenuation (K_d) ranged from 0.27 m^{-1} at the shallow location at Sambro Island to 1.62 m^{-1} at the sandy location at Port Joli. The highest overall light attenuation value was observed at Mason's Island (4.22 m^{-1}). Correlations between light attenuation and wind stress and current speed were weak or not present at all sites and locations (Figures S152-178). Though there were significant correlations between light attenuation and current speed at the shallow location at Cable Island (Figure S154), the deep location at Sacrifice Island (Figure S173), and the sandy location Port Joli (Figure S167) , the R^2 values were low (<0.05) . Similarly, significant correlations were observed between light attenuation and wind stress at Lower Three Fathom (Figure S162) and La Have (Figure S160), though the R^2 values were low (<0.07).

Wave Exposure and Slope

Wave exposure varied by two orders of magnitude across sites (Table 9). The lowest exposure values were observed at Lower Three Fathom and Mason's Island, while the highest were observed at

Taylor's Head, Cable Island, and Sambro Island (Table 9). Slope angle also varied widely across sites, with the lowest slopes observed at Port Joli (muddy = 0.14°, sandy=1.11°), Lower Three Fathom (0.18°), and Cable Island shallow (0.78°), and the highest values observed at Sambro (8.03°), Croucher (6.96°), and Taylor's Head (shallow = 4.56°, deep = 4.80°) (Figure 19).

Discussion

These data demonstrate that *Z. marina* occurs across a wide range of physical conditions in Atlantic Canada, tolerating water temperatures that range from -1.76 to 34.6 °C, current speed ranging from 0.17 to 26.04 cm/sec, and light attenuation as high as 4.22 m^{-1}. Overall mean and seasonal changes in temperature varied across sites, with the lowest annual mean temperatures observed at Sambro Island, Sacrifice Island, and Taylor's Head, and the warmest annual mean temperatures observed at Port L'Hebert, Port Joli, and Lower Three Fathom. Eelgrass beds at deeper depths tended to remain cooler throughout the summer months, accumulating less heat and experiencing smaller ranges in temperature throughout the year as compared to shallower sites. Deeper beds also had lower amplitude heating and cooling over tidal and daily cycles as compared to shallow beds. At all sites, mean annual and summer temperatures remained below what is considered optimal for photosynthesis in *Z. marina* occurring in temperate zones (23°C, Lee et al. 2007).

On occasion, however, temperatures at some shallow sites exceeded the 23°C and 27°C thresholds used to define warm water events, with the duration of exposure to these temperatures ranging from 2.00-77.67 hours at the 23°C threshold and 1.27-4.33 hours at the 27°C threshold. Previous work shows a high degree of variation in the exposure time needed to elicit a physiological response to warm temperatures, but studies indicate that impacts can be observed when temperatures rise above 30°C in as little as 15 minutes (Beibel & McRoy 1971, Marsh et al. 1986), or as long as 1-7 days at temperatures above 19-28°C (Evans et al. 1986, Gao et al. 2017). Temperatures at our sites rose above the 23°C and 27°C thresholds for hours to days, and in some cases, above 30°C. Given this, it is likely that eelgrasses at sites experiencing warm water events are displaying negative physiological responses to these temperatures. The sites with the most warm water events and highest maximum temperatures were also the sites with higher mean temperatures (Port Joli, Port L'Hebert, Lower Three Fathom). In some cases, macrophytes display stronger negative responses to disturbances at sites with warmer mean temperatures (Wernberg et al. 2010), but thermal adaptation may render these populations less vulnerable to warm water events through acclamation. Marin-Guirao et al. (2016) found that populations of the tropical seagrass species *Posidonia oceanica* at shallow sites were more tolerant to an experimental heat wave relative to plants at deeper sites, likely because they were adapted to the consistently higher temperatures experienced while occupying depths shallower than the thermocline. More research is needed to determine if the shallow, warmer eelgrass sites monitored in this study are more or less susceptible to the impacts of climate change because of relatively high mean, maximum, and variation in water temperatures than eelgrasses at the cooler, deeper sites we monitored.

All sites and locations experienced similar patterns of temperature change through time in the middle-frequency band, indicating a dominant influence of coast-wide processes (e.g. storms, upwelling) over local events (e.g. site-specific wind effects). The degree to which middle-frequency changes in temperature were associated with winds directly and wind-induced upwelling varied across sites. When isolating the effects of wind stress, temperature fluctuations at shallow sites were more heavily influenced by winds than at deeper sites. Deeper locations were more strongly influenced by upwelling than shallow locations where the relationship between mid-frequency temperatures and upwelling was strongest (Sambro, Sacrifice), but for all other sites upwelling had a stronger influence on temperatures at the shallow locations as compared to the deep. In general, temperatures were much more strongly influenced by wind-induced upwelling than direct measures of wind stress. Upwelling can bring nutrient-rich water into the coastal zone, which can promote high rates of growth and photosynthesis. The effect of upwelling-driven nutrient input on seagrass bed health is mediated by the degree to which human-derived

nutrients are being added on top of nutrients delivered by natural processes (Hessing-Lewis et al. 2015). High nutrient input is linked to declining health of eelgrass beds through decreases in light availability occurring from overgrowth of epiphytic algae, and the occurrence of phytoplankton blooms in the water column.

Average current speeds at all sites (0.66-6.81 cm s^{-1}) were generally on the low end or below the range known to be tolerated by marine angiosperms (5-180 cm s^{-1}, Koch 2001). Current speed has been shown previously to have a strong effect on seagrass bed characteristics (Fonseca & Bell 1998, Valle et al. 2013). Fonseca & Bell (1998) found declines in seagrass cover and increases in total edge area at higher current speeds when measured over the range of 5-37 cm s^{-1}, indicating that seagrass habitats were more fragmented at sites with higher flow. Fonseca & Bell (1998) also found that higher current speeds decreased the percent of the silt/clay fraction and organic content in sediment, which may promote seagrass health through increases in sediment Redox potential and reductions in sulfide concentrations (van der Heide et al. 2009, Valle et al. 2011). Given this, it is generally thought that seagrass beds thrive at intermediate current speeds. Lower Three Fathom, Mason's Island, Port L'Hebert, Port Joli Sandy, and Cable Island had the lowest mean and maximum current speeds of all sites sampled, and as a result may be stressed relative to sites that experienced higher water flow. The maximum current speed measured at La Have and Sambro were in the middle of the range of maximum current speeds shown elsewhere to cause increases in habitat fragmentation (Fonseca & Bell 1998). Therefore, it is possible that the moderate current speeds observed at these sites promote eelgrass health through a reduction in sediment organic matter, while not being sufficiently high to cause bed damage.

We investigated relationships between current speed, depth, and wind speed to characterize the dominant processes driving water flow dynamics at each site. Temporal variation in current speed at Cable Island, La Have, Mason's Island, Port Joli, Port L'Hebert, Sambro Island and Sacrifice Island was higher in the high-frequency band relative to the mid-frequency band and was more strongly correlated with water depth, indicating that currents at these sites are mainly influenced by short-term processes (e.g. tides) relative to processes occurring on the order of several days or more (e.g. storms). Current speeds were generally less variable in the mid-frequency band than the high-frequency band, except at Lower Three Fathom, Croucher Island, and Taylor's Head. This suggests a stronger influence of coast-wide processes (e.g. storms, large-scale circulation patterns) on currents at these sites than the diurnal tidal cycle. Current speed showed the highest correlation with wind stress at Lower Three Fathom, which is in a shallow lagoon that is not fully open to tidal flows. Wind stress was also highly correlated with current speed at Taylor's Head, which is one of the sites with the highest relative wave exposure values. Taylor's Head occurs in a fairly open bay that is exposed to the winds and storms originating from the southwest, which from our data appear to most strongly influence current speed at this site. Sambro Island also had a relatively high wave exposure, but winds stress was not strongly correlated with current speed. This may be due to the time of year current measurements were taken (July 2018), and the fact that current measurements were taken over a relatively short period of time (2-4 weeks). Wave exposure was calculated using wind data from all seasons, so it may be the case that there is a stronger associated between current speed and winds at this site and others during other times of the year.

Light has consistently been considered one of the most important environmental parameters determining seagrass health, as seagrasses are known to have higher light requirements than other marine and terrestrial autotrophs (Duarte 1991, Dennison et al. 1993). The result is that seagrasses are particularly sensitive to decreasing light levels as a consequence of natural and human-induced processes (e.g. nutrient and sediment run-off, storms). Ambient light levels and light attenuation varied across our sites, with mean K_d values ranging from 0.27-1.62 m^{-1}. Sites with lower light attenuation included Sambro, Sacrifice, Croucher, and La Have Islands, while Port Joli sandy and muddy, Port L'Hebert, Lower Three Fathom, and Mason's Island had the highest light attenuation. Maximum light attenuation values tolerated by *Z. marina* elsewhere in the species' distribution ranges from 0.16-1.5 m^{-1} (Dennison et al. 1993). Mean K_d values at all sites monitored in the present study were within this range, but values exceeded 1.5 m^{-1} on some occasions at Cable Island (deep and shallow), Mason's Island, Lower Three Fathom, Port Joli (muddy and sandy), and Port L'Hebert. This may indicate that these beds are

experiencing stress as a result of low light. However, seagrasses are able to acclimate to low light conditions by increasing blade tissue pigment concentrations and per unit leaf biomass (Lee et al. 2007). Seagrasses occupying sites with consistently lower light levels can have higher photosynthetic efficiencies than those at sites with higher light levels (Masini and Manning 1997, Ruiz & Romero 2003, Lee et al. 2007). Nevertheless, acute light stress events can cause mortality, among other negative impacts, if turbidity events are out of the range of what is typically experienced (Moore et al. 1997).

Light attenuation was not strongly correlated with wind stress or current speed at our sites, indicating that there are other mechanisms at play in driving temporal and spatial variation in light attenuation. From our results, it may be more likely that freshwater run-off from land is contributing to higher concentrations of dissolved and particulate organic and inorganic materials at some of the sites monitored, or that there are other human activities in the area increasing turbidity (e.g. dredging, fishing, aquaculture) (Ralph et al. 2007). Seagrass photosynthesis is known to follow seasonal cycles and vary from year to year with changes in light levels and temperature, with the highest rates occurring in spring and summer relative to fall and winter (Herzka and Dunton 1997, Lee et al. 2007, Moore et al. 2014). Our light measurements targeted the time of year when light levels and seasonal growth are at their optimum. We may have seen a different level of variation across sites had they been sampled at the time of year when the most freshwater run-off is being delivered into the coastal zone or when storm intensities are highest (spring and fall). It is also important to note that light was measured over a relatively short period of time in the summer (2 weeks); different results likely would have been obtained if sensors recorded data for a longer period. Spatial variation across sites may also have been influenced by differences in the timing of when light was measured at all sites (June-September 2018). Nevertheless, given that our sampling was largely constrained to the summer months, comparisons across sites provide useful indication of the differences in light conditions experienced by eelgrass beds in these areas.

Summary

When combining results from temperature, current speed, and light measurements, Port Joli, Port L'Hebert, Lower Three Fathom, and Mason's Island appear to be experiencing environmental conditions that are consistent with higher levels of eelgrass ecosystem stress. These sites had the highest temperatures, lowest current speeds, and highest light attenuation values of all sites monitored. In contrast, Sambro, La Have, and Sacrifice Islands tended to be cooler, have higher current speeds, and experience light attenuation values below levels considered to induce stress responses in eelgrasses. Further analyses will aim to correlate environmental conditions with metrics of eelgrass ecosystem health, and further define the role of adaptation in mediating the response of these different beds to environmental disturbances. Ultimately these results are useful for generating predictive maps of eelgrass distribution in the region, understanding how eelgrass beds in Atlantic Canada may respond to climate change and other physical disturbances, and determining which beds are likely to be the best targets for conservation protection.

References

Barber, B. J., Behrens, P. J. 1985. Effects of elevated temperature on seasonal in situ leaf productivity of *Thalassia testudinum*. Aquat Bot 22: 61–69.

Barbier, E. B., Hacker, S. D., Kennedy, C., Koch, E. W., Stier, A. C., Silliman, BR. 2011. The value of estuarine and coastal ecosystem services. Ecol Monogr 81: 169-193.

Biebl, R., McRoy, C. P. 1971. Plasmatic resistance and rate of respiration and photosynthesis of *Zostera marina* at different salinities and temperatures. Marine Biology 8: 48-56.

Borchers, H. W. 2018. pracma: Practical Numerical Math Functions. R package version 2.1.5.https://CRAN.R-project.org/package=pracma

Chan, K. S., Ripley, B. 2012. TSA: Time Series Analysis. R package version 1.01. https://CRAN.R-project.org/package=TSA

Dennison, W. C., Orth, R. J., Moore, K. A., Stevenson, J. C., Carter, V., Kollar, S., Bergstrom, P. W., Batiuk, R. A. 1993. Assessing water quality with submersed aquatic vegetation. BioScience 43: 86-94.

Duarte, C.M. 1991. Seagrass depth limits. Aquatic Botany 40: 363–377.

Erftemeijer, P. L. A., Herman, P. M. J. 1994. Seasonal changes in environmental variables, biomass, production and nutrient contents in two contrasting tropical intertidal seagrass beds in South Sulawesi, Indonesia. Oecologia 99: 45:59.

Evans, A. S., Webb, K. L., Penhale, P. A. 1986. Photosynthetic temperature acclimation in two coexisting seagrasses, *Zostera marina* L. and *Ruppia maritima*. Aquatic Botany 24:.185-197.

Fonseca, M. S., Bell, S. S. 1998. Influence of physical setting on seagrass landscapes near Beaufort, North Carolina, USA. Mar Ecol Prog Ser 171:.109-121.

Fonseca, M. S., Fisher, J. S., Zieman, K. C., Thayer, G. W. 1982. Influence of the seagrass *Zostera marina* on current flow. Estuarine Coastal and Shelf Science 15: 351-364.

Gao, Y., Fang, J., Du, M., Fang, J., Jiang, W., Jiang, Z. 2017. Response of the eelgrass (*Zostera marina*) to the combined effects of high temperatures and the herbicide, atrazine. Aquatic Botany 142:.41-47.

Hemminga, M. A., Duarte, C. M. 2000. Seagrass Ecology. Cambridge University Press, First ed.

Herzka, S. Z., Dunton, K. H. 1997. Seasonal photosynthetic patterns of the seagrass Thalassia testudinum in the western Gulf of Mexico. Mar Ecol Prog Ser 152: 103–117.

Hessing-Lewis, M. L., Hacker, S. D., Menge, B. A., McConville, S-O., Henderson, J. 2015. Are large macroalgal blooms necessarily bad? Nutrient impacts on seagrass in upwelling-influenced estuaries. Eco App 25:.1330-1347.

Keddy, P. A. 1982. Quantifying within-lake gradients of wave energy: interrelationships of wave energy, substrate particle size and shoreline plants in Axe Lake, Ontario. Aquat Bot 14:.41-58.

Kemp, W. M., Boynton, W. R., Twilley, R. R., Stevenson, J. C., Ward, L. G. 1984. Influences of submersed vascular plants on ecological processes in the upper Chesapeake Bay, p 367-394. In VS Kennedy (ed.), The estuary as a filter. Academy Press, New York

Kim, J-H., Kim, S. H., Kim Y. K., Park J-I, Lee K-S. 2016. Growth dynamics of the seagrass Zostera japonica at its upper and lower distributional limits in the intertidal zone. Estuar, Coast, Shelf Sci 175:.1-9.

Koch, E. W. 2001. Beyond Light: Physical, Geological, and Geochemical Parameters as Possible Submerged Aquatic Vegetation Habitat Requirements. Estuaries 24:.1-17.

Krause-Jensen, D., Carstensen, J., Nielsen, S. L., Dalsgaard, T., Christensen, P. B., Fossing, H., Rasmussen, M. B. 2011. Sea bottom characteristics affect depth limits of eelgrass *Zostera marina*. Mar Ecol Prog Ser 425:.91-102.

Lee, K. S., Park, S. R., Kim, Y. K. 2007. Effects of irradiance, temperature, and nutrients on growth dynamics of seagrasses: A review. J Exp Mar Biol Ecol 350: 144-175.

Leuschner, C., Landwehr, S., Mehlig, U. 1998. Limitation of carbon assimilation of intertidal *Zostera noltii* and *Z. marina* by desiccation at low tide. Aqua Bot 62: 171-176.

Marin-Guirao, L., Ruiz, J. M., Dattolo, E., Garcia-Munoz, E., Procaccini, G. 2016. Physiological and molecular evidence of differential short-term heat tolerance in Mediterranean seagrasses. Nature Scientific Reports 6: 28615

Marsh, J. A., Dennison, W. C., Alberte, R. S. 1986. Effects of temperature on photosynthesis and respiration in eelgrass (*Zostera marina*). J Exp Mar Biol Ecol 101: 257-267.

Masini, R. J., Manning, C. R. 1997. The photosynthetic responses to irradiance and temperature of four meadow-forming seagrasses. Aqua Bot 58: 21–36.

Moore, K. A., Shields, E. C., Parrish, D. B. 2014. Impacts of varying estuarine temperature and light conditions on *Zostera marina* (Eelgrass) and its interactions with *Ruppia maritima* (Widgeongrass). Estuaries and Coasts 2014: S20-S30.

Moore, K. A., Wetzel, R. L., Orth, R. J. 1997. Seasonal pulses of turbidity and their relations to eelgrass (*Zostera marina*) survival in an estuary. J Exp Mar Biol Ecol 215: 115-134.

Neuheimer, A.B., Taggart, C.T. 2007. The growing degree-day and fish size-at-age: the overlooked metric. Can J Fish and Aquat Sci 64: 375-385.

Oliver, E. C., Donat, M. G., Burrows, M. T., Moore, P. J., Smale, D. A., Alexander, L. V., Benthuysen, J. A., Feng, M., Gupta, A. S., Hobday, A. J., Holbrook, N. J., Perkins-Kirkpatrick, S. E., Scannell, H. A., Straub, S. C., Wernberg, T. 2018. Longer and more frequent marine heatwaves over the past century. Nature Communications 9: 1324.

Orth, R. J., Carruthers, T. J. B., Dennison, W. C., Duarte, C. M., Fourqueran, J. W., Heck, K. L., Hughes, A.R., Kendrick, G. A., Kenworthy, W. J., Olyarnik, S., Short, F. T., Waycott, M., Williams, S. L. 2006. A global crisis for seagrass ecosystems. BioScience 56: 987-996.

Ralph P. J., Durako, M. J., Enriquez, S., Collier, C. J., Doblin, M. A. 2007. Impact of light limitation on seagrasses. J Exp Mar Biol Ecol 350: 176-193.

Ruiz, J. M., Romero, J. 2003. Effects of disturbances caused by coastal constructions on spatial structure, growth dynamics and photosynthesis of the seagrass Posidonia oceanica. Mar Pollut Bull 46: 1523–1533.

Ruthrof, K. X., Breshears, D. D., Fontaine, J. B., Froend, R. H., Matusick, G., Kala, J., Miller, B., Mitchell, P. J., Wilson, S. K., van Keulen M., Enright, N. J., Law, D. J., Wernberg, T., Hardy, G. E. S. J. 2018. Subcontinental heat wave triggers terrestrial and marine, multi-taxa responses. Scientific Reports: 13094.

Schmidt, A. L., Wysmyk, J. K. C., Craig, S. E., Lotze, H. K. 2012. Regional-scale effects of eutrophication on ecosystem structure and services of seagrass beds. Limnology and Oceanography 57: 1389-1402.

Seers, B. 2018. fetchR: Calculate Wind Fetch. R package version 2.1-1. https://CRAN.R-project.org/package=fetchR

Short, F. T., Wyllie-Echeverria, S. 1996. Natural and human-induced disturbance of seagrasses. Environ Conserv 23: 17–27.

Signal developers. 2013. signal: Signal processing. URL: http://r-forge.r-project.org/projects/signal/

Stoffer, D. 2017. astsa: Applied Statistical Time Series Analysis. R package version 1.8. https://CRAN.R-project.org/package=astsa

Trapletti, A., Hornik, K. 2018. tseries: Time Series Analysis and Computational Finance. R package version 0.10-44

Waycott, M., Duarte, C. M. , Carruthers, T. J. B., Orth, R. J., Dennison, W. C., Olyarnik, S., Calladine, A., Forqurean, J. W., Heck, K. L., Hughes, A. R., Kendrick, G. A., Kenworth, W. J., Short, F. T., Williams, S. L. 2009. Accelerating loss of seagrasses across the globe threatens coastal ecosystems. Proc Nat Acad Sci USA 106: 12377-12381.

Wernberg, T., Thomsen, M. S., Tuya, F., Kendrick, G. A., Staehr, P. A., Toohey, B. D. 2010. Decreasing resilience of kelp beds along a latitudinal temperature gradient: potential implications for a warmer future. Ecol Let 13: 685-694.

R Core Team. 2017. R: A language and environment for statistical computing. R Foundation for Statistical Computing, Vienna, Austria. URL https://www.R-project.org/

Unsworth, R. K. F., Collier, C. J., Waycott, M., Mckenzie, L. J., Cullen-Unsworth, L. C. 2015. A framework for the resilience of seagrass ecosystems. Marine Pollution Bulletin 100: 34-36.

van der Heide, T., Peeters, E. T. H. M., Hermus, D. C. R., van Katwijk, M. M., Roelofs, J. G. M., Smolders, A. J. P. 2009. Predicting habitat suitability in temperate seagrass ecosystems. Limnol Oceanogr 54: 2018-2024.

Valle, M., Borja, A., Chust, G., Galparsoro, I., Garmendia, J. M. 2011. Modelling suitable estuarine habitats for *Zostera noltii,* using Ecological Niche Factor Analysis and Bathymetric LiDAR. Estuar Coast Shelf Sci 94: 144-154.

Valle, M., van Katwijk, M. M., de Jong, D. J., Bouma, T. J., Schipper, A. M., Chust, G., Benito, B. M., Garmendia, J. M., Borja, A. 2013. Comparing the performance of species distribution models of *Zostera marina*: Implications for conservation. J Sea Res 83: 56-64.

Tables

Table 1. Geographic location, mean depth at high tide, and the mean slope at each seagrass site and location.

Site	Location	Latitude	Longitude	Depth (m)	Mean tidal range (m)	Mean slope angle (°)
Cable	Shallow	44.74507	-62.8010	1.9		0.78
Cable	Deep	44.74650	-62.7928	3.4	1.11	3.53
Croucher	Shallow	44.64138	-63.9564	3.5		7.63
Croucher	Deep	44.64148	-63.9563	6.0	1.28	6.48
Lower Three Fathom		44.63537	-63.2940	0.9	0.03	0.18
La Have		44.22278	-64.3808	1.6	0.97	3.05
Mason's Island		44.38990	-64.2788	1.9	1.32	3.24
Port L'Hebert		43.86807	-64.9633	1.7	1.16	1.82
Port Joli	Muddy	43.87538	-64.9009	1.3	1.3	0.14
Port Joli	Sandy	43.87190	-64.8952	1.4	1.32	1.11
Sacrifice	Shallow	44.39638	-64.2355	3.3		3.54
Sacrifice	Deep	44.39553	-64.2367	5.1	1.11	1.49
Sambro	Shallow	44.45533	-63.5881	1.8		10.77
Sambro	Deep	44.45590	-63.5877	6.2	0.82	6.01
Taylor's Head	Shallow	44.82017	-62.5726	3.2		4.55
Taylor's Head	Deep	44.82060	-62.5722	5.1	0.68	4.79

Table 2. Summary statistics for the full record of temperature at each site, running from May/June 2017 to April/May 2018, including mean, maximum, and minimum temperatures, temperature variability (StDev Temp), and the 95th percentile temperature.

Site	Location	Mean Temp (°C)	Max Temp (°C)	Min Temp (°C)	StDev Temp (°C)	95th percentile Temp (°C)
Cable	Shallow	9.27	23.69	-9.44	6.55	18.68
Cable	Deep	8.77	20.84	-0.45	6.04	17.82
Croucher	Shallow	10.03	20.70	0.19	6.18	18.90
Croucher	Deep	9.64	20.32	0.96	5.89	18.51
Lower Three Fathom		10.56	27.41	-1.61	8.28	22.20
La Have		9.38	22.75	-1.04	5.61	18.03
Mason's Island		9.53	23.69	-11.51	6.84	18.94
Port L'Hebert		10.10	34.37	-8.00	7.58	21.66
Port Joli	Muddy	10.84	34.57	-2.28	7.80	22.51
Port Joli	Sandy	10.58	33.65	-1.76	7.64	22.06

Sacrifice	Shallow	9.23	21.06	0.94	6.45	18.60
Sacrifice	Deep	8.89	19.48	-1.61	6.10	17.70
Sambro	Shallow	9.03	20.39	-0.17	5.88	17.94
Sambro	Deep	8.31	19.72	0.14	5.40	17.20
Taylor's Head	Shallow	8.88	21.18	0.55	6.72	18.48
Taylor's Head	Deep	8.50	20.77	0.31	6.35	17.96

Table 3. Summary statistics for the summer period (June-September 2017) at each site, including mean, maximum, and minimum temperatures, temperature variability (StDev Temp), and the 95th percentile temperature.

Site	Location	Mean Temp (°C)	Max Temp (°C)	Min Temp (°C)	StDev Temp (°C)	95th percentile Temp (°C)
Cable	Shallow	15.01	23.69	7.47	3.45	19.86
Cable	Deep	13.43	20.84	17.18	3.78	18.51
Croucher	Shallow	15.16	20.70	5.90	3.37	19.82
Croucher	Deep	13.95	20.32	4.51	3.80	19.58
Lower Three Fathom		19.53	27.41	13.06	2.47	23.57
La Have		14.96	22.75	7.01	2.82	19.53
Mason's Island		16.05	23.69	8.42	2.53	19.98
Port L'Hebert		18.64	34.37	7.48	2.86	23.97
Port Joli	Muddy	19.52	34.57	10.15	2.89	24.61
Port Joli	Sandy	19.01	33.65	11.27	2.83	23.95
Sacrifice	Shallow	15.02	21.06	8.02	2.98	19.27
Sacrifice	Deep	13.90	19.48	6.81	3.21	18.56
Sambro	Shallow	13.45	20.39	5.26	3.89	18.41
Sambro	Deep	11.34	19.72	4.51	4.38	18.06
Taylor's Head	Shallow	16.21	21.18	6.46	2.64	19.79
Taylor's Head	Deep	13.96	20.77	5.87	3.64	19.48

Table 4. Summary of warm water events at each site and location, including the total number of days above the threshold value, the number of distinct events, the mean duration of all events, and the mean thermal integral of warm water events.

Site	Location	Temperature Threshold (°C)	Total Days above Threshold	Number of Events	Mean Event Duration (hours)	Mean Thermal Integral of Events
Cable	Deep	23	0.0	0	0.00	0.00
Cable	Shallow	23	0.1	1	2.00	1.17
Croucher	Deep	23	0.0	0	0.00	0.00
Croucher	Shallow	23	0.0	0	0.00	0.00
Lower Three Fathom		23	9.9	3	77.67	5.19×10^3
La Have		23	0.0	0	0.00	0.00
Masons		23	0.3	0	0.00	0.00
Port L'Hebert		23	8.6	8	24.35	2.21×10^7
Port Joli	Muddy	23	12.8	9	33.02	2.20×10^7
Port Joli	Sandy	23	10.2	7	33.50	2.21×10^7
Sacrifice	Deep	23	0.0	0	0.00	0.00
Sacrifice	Shallow	23	0.0	0	0.00	0.00
Sambro	Deep	23	0.0	0	0.00	0.00
Sambro	Shallow	23	0.0	0	0.00	0.00
Taylor's Head	Deep	23	0.0	0	0.00	0.00
Taylor's Head	Shallow	23	0.0	0	0.00	0.00
Cable	Deep	27	0.0	0	0.00	0.00
Cable	Shallow	27	0.0	0	0.00	0.00
Croucher	Deep	27	0.0	0	0.00	0.00
Croucher	Shallow	27	0.0	0	0.00	0.00
Lower Three Fathom		27	0.2	1	4.33	1.85×10^3
La Have		27	0.0	0	0.00	0.00
Masons		27	0.0	0	0.00	0.00
Port L'Hebert		27	0.3	5	1.27	1.16×10^6
Port Joli	Muddy	27	1.1	6	4.03	1.77×10^6
Port Joli	Sandy	27	0.1	2	1.00	4.73×10^5
Sacrifice	Deep	27	0.0	0	0.00	0.00
Sacrifice	Shallow	27	0.0	0	0.00	0.00
Sambro	Deep	27	0.0	0	0.00	0.00
Sambro	Shallow	27	0.0	0	0.00	0.00
Taylor's Head	Deep	27	0.0	0	0.00	0.00
Taylor's Head	Shallow	27	0.0	0	0.00	0.00

Table 5. Variation in temperature (as standard deviation) in the middle and high frequency bands, and the ratio of the high frequency variation relative to the middle frequency variation.

Site	Location	Mid-Freq Var	High-Freq Var	Ratio HF:MF
Cable	Deep	1.44	0.48	0.33
Cable	Shallow	1.26	0.90	0.71
Croucher	Deep	2.04	0.56	0.28
Croucher	Shallow	1.60	0.44	0.27
Lower Three Fathom		1.94	0.67	0.34
La Have		1.50	0.55	0.37
Mason's Island		1.23	0.93	0.76
Port L'Hebert		2.01	1.29	0.64
Port Joli	Sandy	2.04	0.95	0.47
Port Joli	Muddy	2.02	1.11	0.55
Sacrifice	Deep	1.41	0.36	0.26
Sacrifice	Shallow	1.32	0.46	0.35
Sambro	Deep	1.85	0.45	0.24
Sambro	Shallow	1.40	0.44	0.32
Taylor's Head	Deep	1.39	0.52	0.38
Taylor's Head	Shallow	1.28	0.55	0.43

Table 6. Summary of current conditions at each site, including the mean, standard deviation, maximum, and minimum current speeds.

Site	Mean Speed (cm/s)	StDev Speed (cm/s)	Max Speed (cm/s)	Min Speed (cm/s)
Cable Deep	3.689293	1.3823512	15.077895	1.1236842
Croucher Deep	5.037925	2.3265363	19.656500	0.9466667
Lower Three Fathom	0.664172	0.4796225	3.859900	0.1473333
La Have	6.813340	4.0057080	26.035368	0.9115789
Mason's Island	2.149314	1.6098181	13.784737	0.1711111
Port L'Hebert	3.389319	1.8342301	9.863105	0.2396500
Port Joli Muddy	4.961640	3.0525548	16.844737	0.3611111
Port Joli Sandy	3.669667	2.1150404	15.109000	0.2440000
Sacrifice Deep	4.006695	2.9216330	18.796500	0.4950000

Sambro Deep	6.612133	3.5183502	21.993684	1.6121053
Taylor's Head Deep	3.809544	1.9158188	17.448000	0.9168421

Table 7. Variation in current speeds (as standard deviation) in the middle and high frequency bands, and the ratio of the two.

Site	Mid-Freq SD	High-Freq SD	Ratio HF:MF
Cable Deep	0.83	1.10	1.325
Croucher Deep	1.72	1.47	0.857
Lower Three Fathom	0.35	0.31	0.869
La Have	1.24	3.76	3.025
Mason's Island	0.55	1.50	2.733
Port L'Hebert	0.55	1.73	3.143
Port Joli Muddy	0.44	2.44	5.531
Port Joli Sandy	0.75	1.96	2.619
Sacrifice Deep	0.87	2.78	3.186
Sambro Deep	1.64	2.86	1.743
Taylor's Head Deep	1.64	0.94	0.577

Table 8. Light conditions at each site and location, including the mean, max, and standard deviation of light intensity as read by the bottom sensor (filtered), and the mean, median, and max light attenuation (KD).

Site	Location	Mean Light Intensity (umol m^{-2} s^{-1})	Max Light Intensity (umol m^{-2} s^{-1})	StDev Light Intensity (umol m^{-2} s^{-1})	Mean KD (m^{-1})	Median KD (m^{-1})	Max KD (m^{-1})
Cable Island	Deep	279.15	844.08	178.55	0.70	0.70	1.64
Cable Island	Shallow	325.32	758.40	204.36	0.65	0.60	2.83
Croucher Island	Deep	246.28	592.98	138.40	NA	NA	NA
Croucher Island	Shallow	322.65	795.55	188.35	0.39	0.37	1.32
Lower Three Fathom		294.50	704.23	174.20	0.80	0.80	1.78
La Have		320.69	769.12	210.39	0.47	0.46	1.21
Mason's Island		256.45	753.48	170.24	0.74	0.45	4.22
Port L'Hebert		276.69	802.90	185.76	0.89	0.92	2.11
Port Joli	Sandy	225.01	667.96	154.91	1.62	1.48	3.71
Port Joli	Muddy	301.05	748.23	187.10	0.89	0.82	2.08
Sacrifice	Deep	219.15	535.57	124.48	0.39	0.36	1.06
Sacrifice	Shallow	245.36	658.23	154.30	0.31	0.30	1.14
Sambro	Deep	197.01	428.38	104.66	0.45	0.44	0.71
Sambro	Shallow	331.55	764.85	208.34	0.27	0.22	1.03
Taylor's Head	Deep	189.74	524.23	114.77	0.47	0.46	1.43

Taylor's Head	Shallow	263.42	759.98	164.64	0.55	0.54	1.53

Table 9. Relative exposure index calculated for each site and location, using an index modified from Keddy 1982.

Site	Location	REI
Cable Island	Deep	19.52
Cable Island	Shallow	17.95
Croucher Island	Deep	92.42
Croucher Island	Shallow	21.89
Lower Three Fathom		3.00
La Have		47.11
Mason's Island		5.35
Port L'Hebert		16.39
Port Joli	Sandy	10.95
Port Joli	Muddy	11.83
Sacrifice	Deep	66.88
Sacrifice	Shallow	12.80
Sambro	Deep	179.68
Sambro	Shallow	127.49
Taylor's Head	Deep	285.82
Taylor's Head	Shallow	284.50

<u>Figures</u>
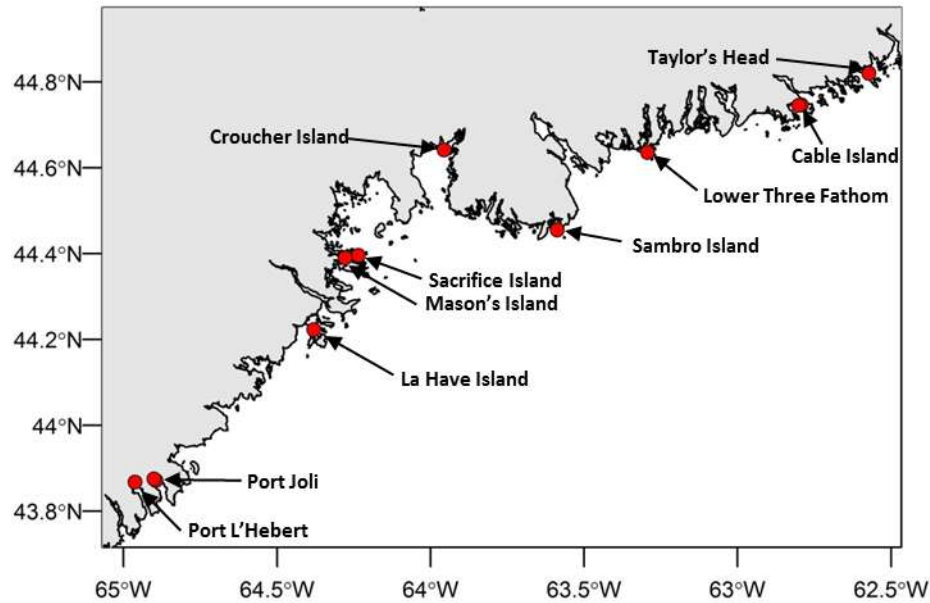
Figure 1. The location of the 10 seagrass sites along the Atlantic coast of Nova Scotia where physical conditions were characterized.
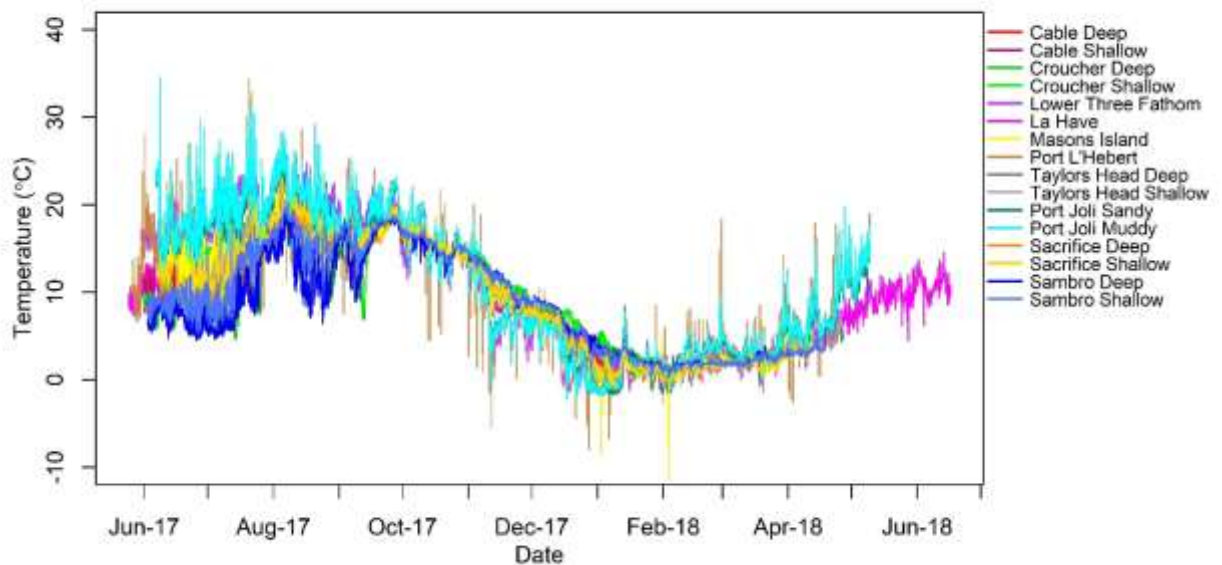
Figure 2. Temperature records at 10 seagrass sites monitored for ecosystem status in 2017-2018. Note some sites include multiple locations (e.g. deep/shallow, sandy/muddy).
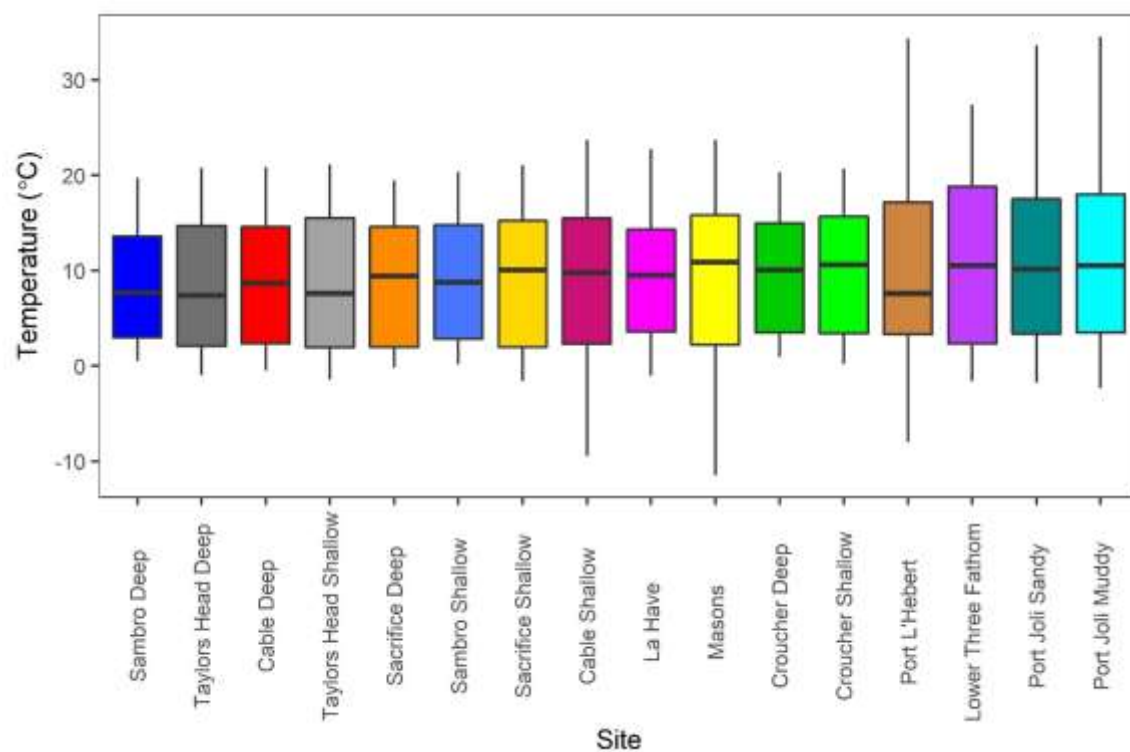
Figure 3. Boxplots of temperature conditions at each site, with boxes showing the median, first, and third quartiles. Upper and lower whiskers correspond to the largest and smallest values, meeting the condition that they are no further than 1.5*IQR from the first and third quartiles. Sites are ordered left to right according to the mean (smallest to largest).
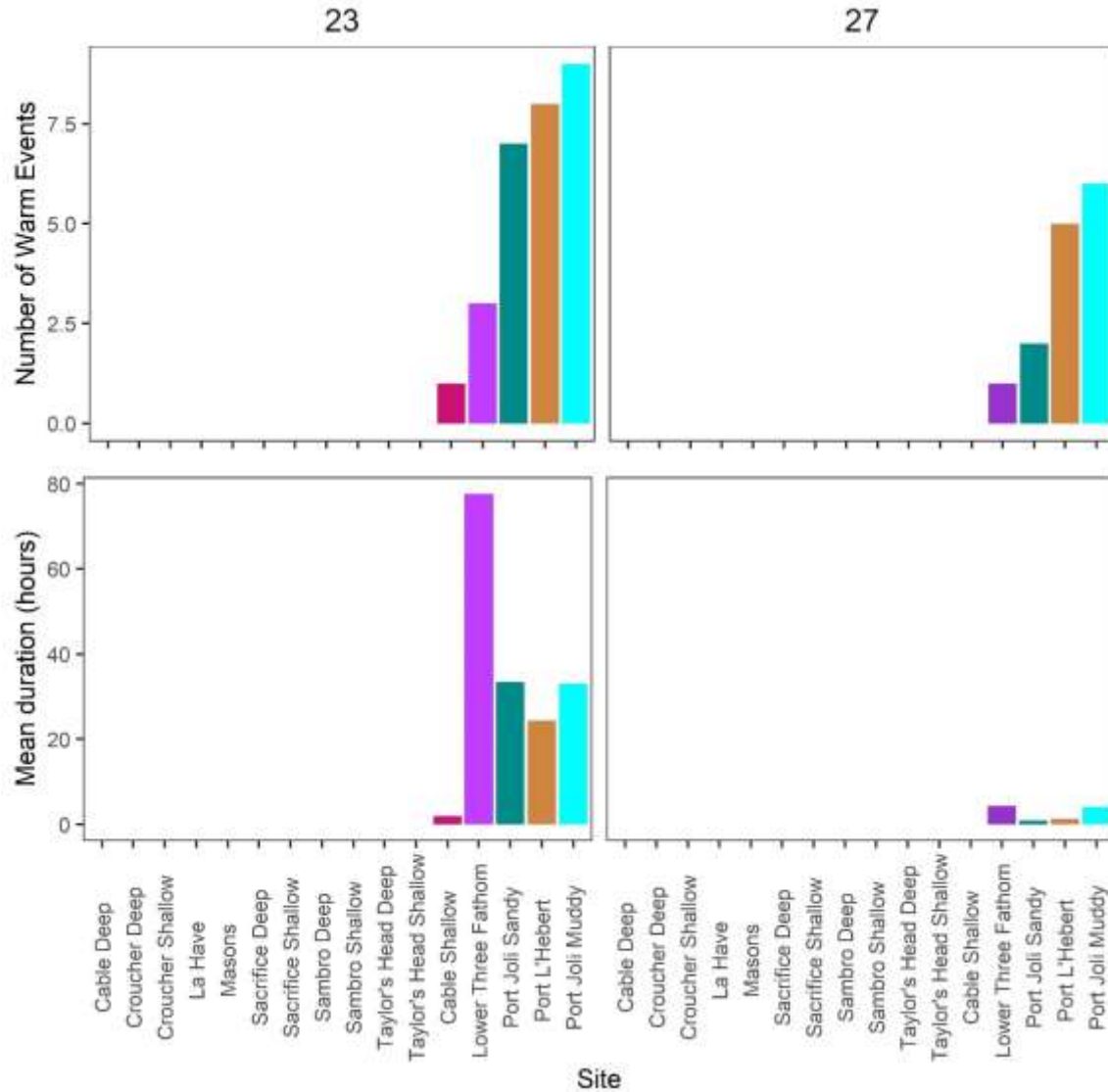
Figure 4. A characterization of warm water events at each site and location, including the total number of events at two threshold values (23°C and 27°C), and the mean duration of events in each threshold category. No bar appears where there were no warm water events.
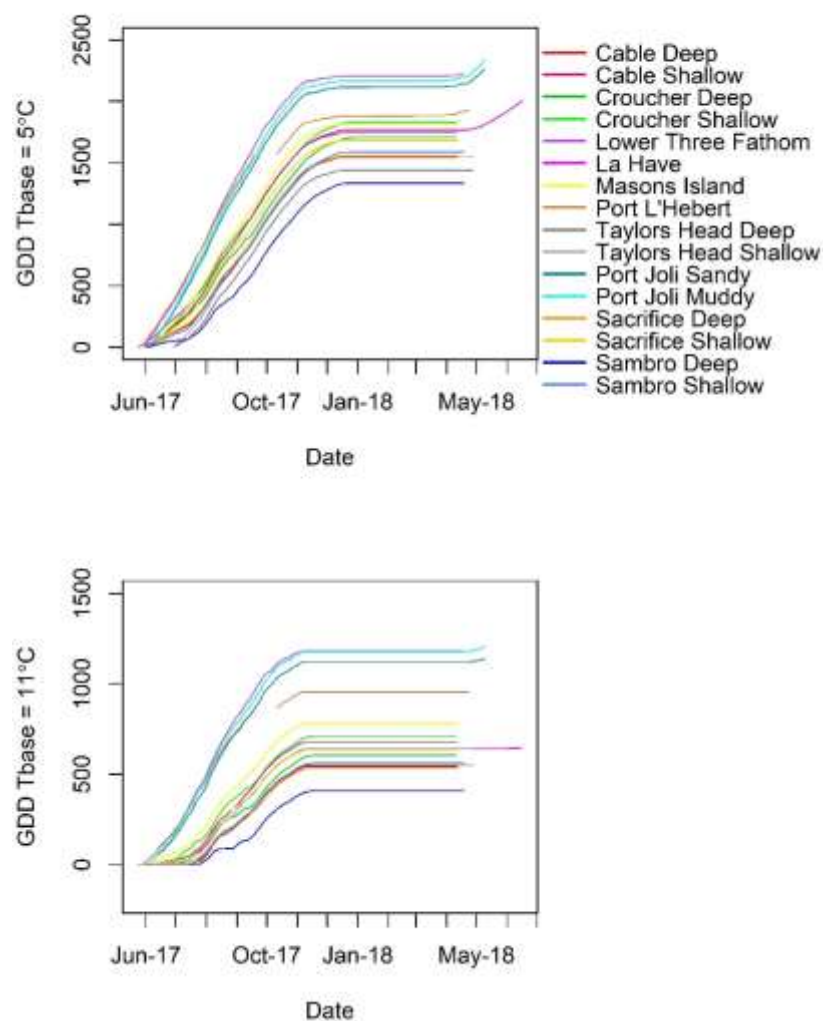
Figure 5. Growing degree days at each site and location calculated at two base temperature values: 5°C and 11°C. Figures show temperatures summed for the full period for which there is temperature data at each site (May/June 2017-April/May 2018).
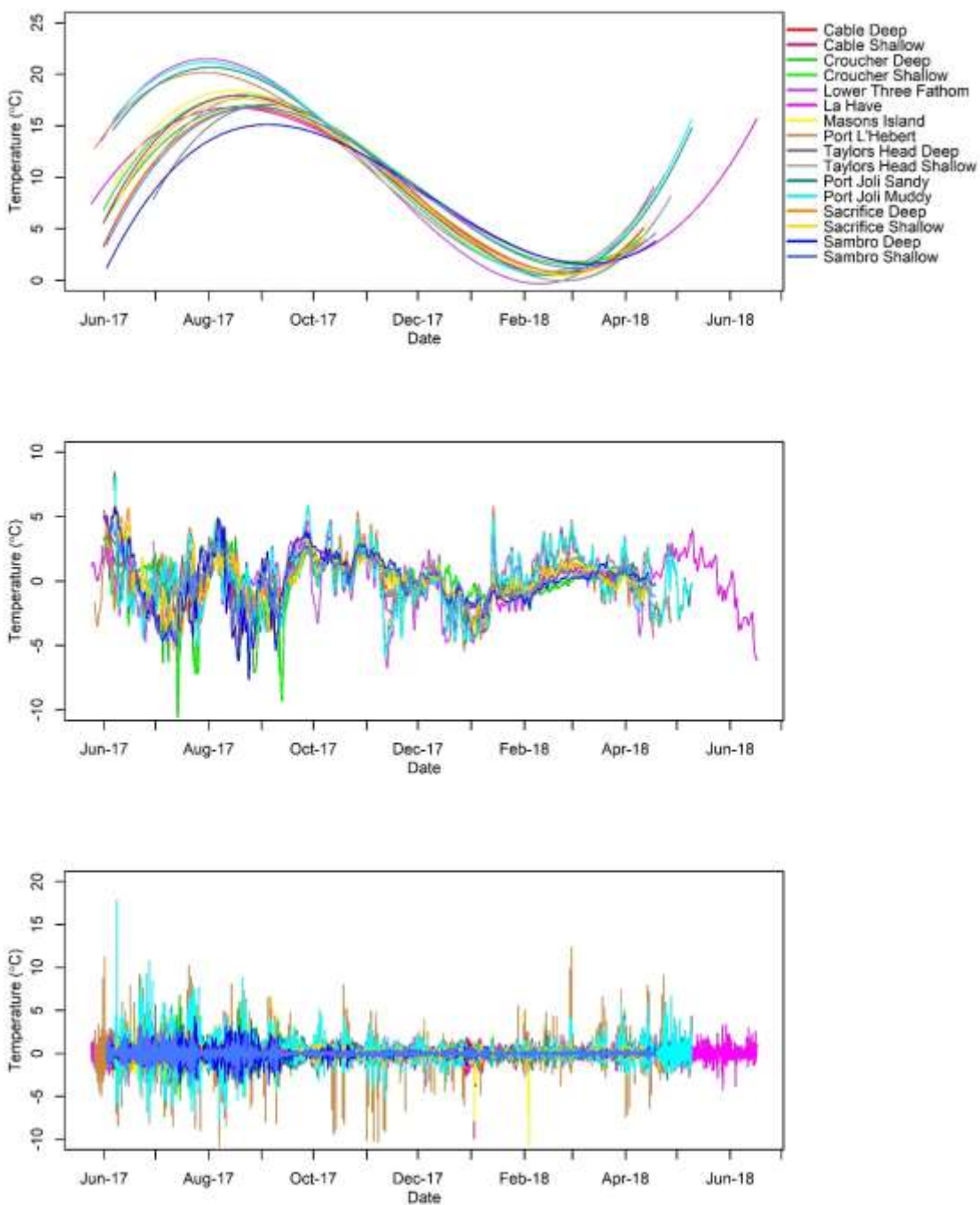
Figure 6. Low (> 60 days, top panel), middle (37 hours to 60 days, middle panel), and high frequency (<36 hours, bottom panel) temperature variability isolated at each site and location for the full temperature records.
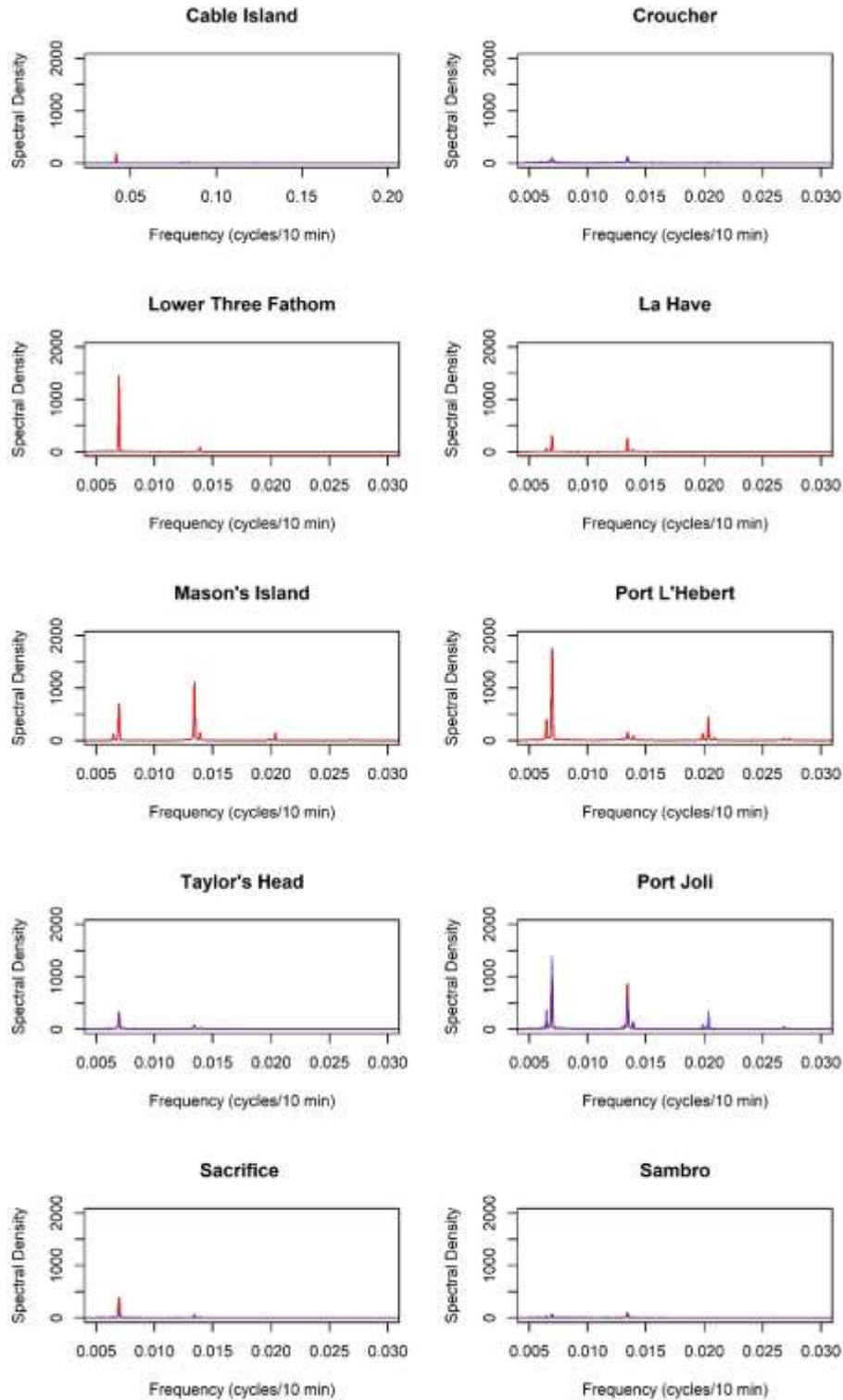
Figure 7. Spectral analysis of high frequency temperature signals at each site, representing fluctuations in temperatures due to tides (frequency = 0.0134 cycles/10 minutes), and the daily heating and cooling cycle (frequency = 0.0069 cycles/10 minutes). Deep sites are shown in blue in each location (where applicable), while shallow sites are shown in red. At Port Joli, the sandy location is shown in red while the muddy location is shown in blue.
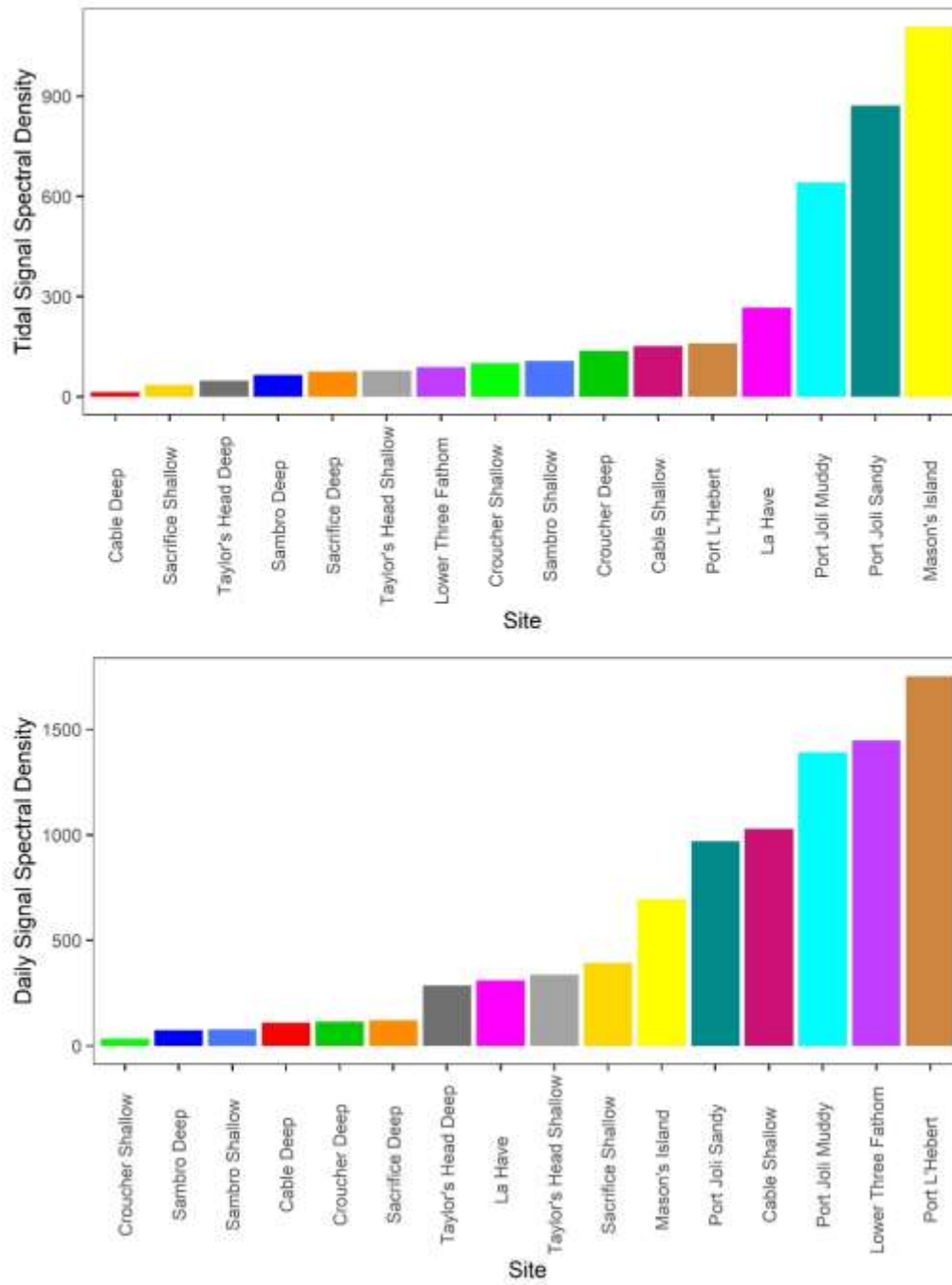
Figure 8. The spectral density of tidal (frequency = 0.0134 cycles/10 minutes, time = 12.42 hours) and daily (frequency = 0.0069 cycles/10 minutes, time = 24 hours) temperature fluctuations at each site and location, representing the strength of the signal at these two frequencies.
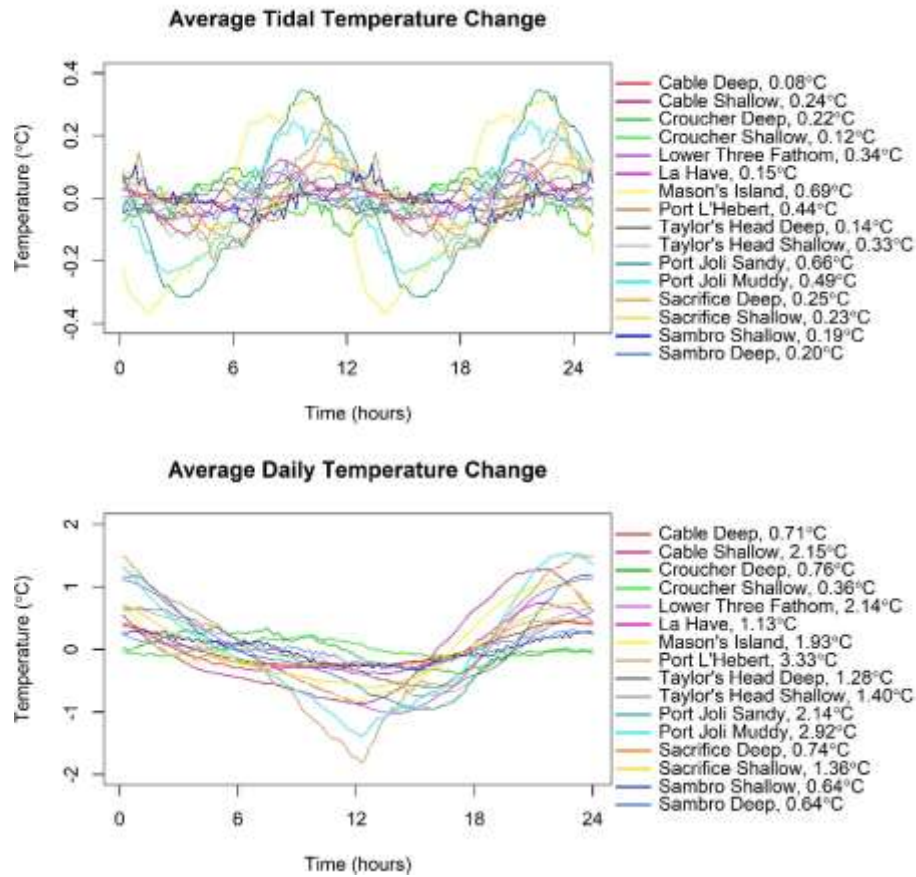
Figure 9. The average temperature change over the 12.42-hour tidal cycle (top panel) and daily heating and cooling cycle (bottom panel) for the summer period only (June-Sept 2017). The range of temperatures at each site is shown in the legend to the right of the panel. Note, time 0 for the average tidal temperature range is low tide, and time 0 for the average daily temperature change is dusk (18:00).
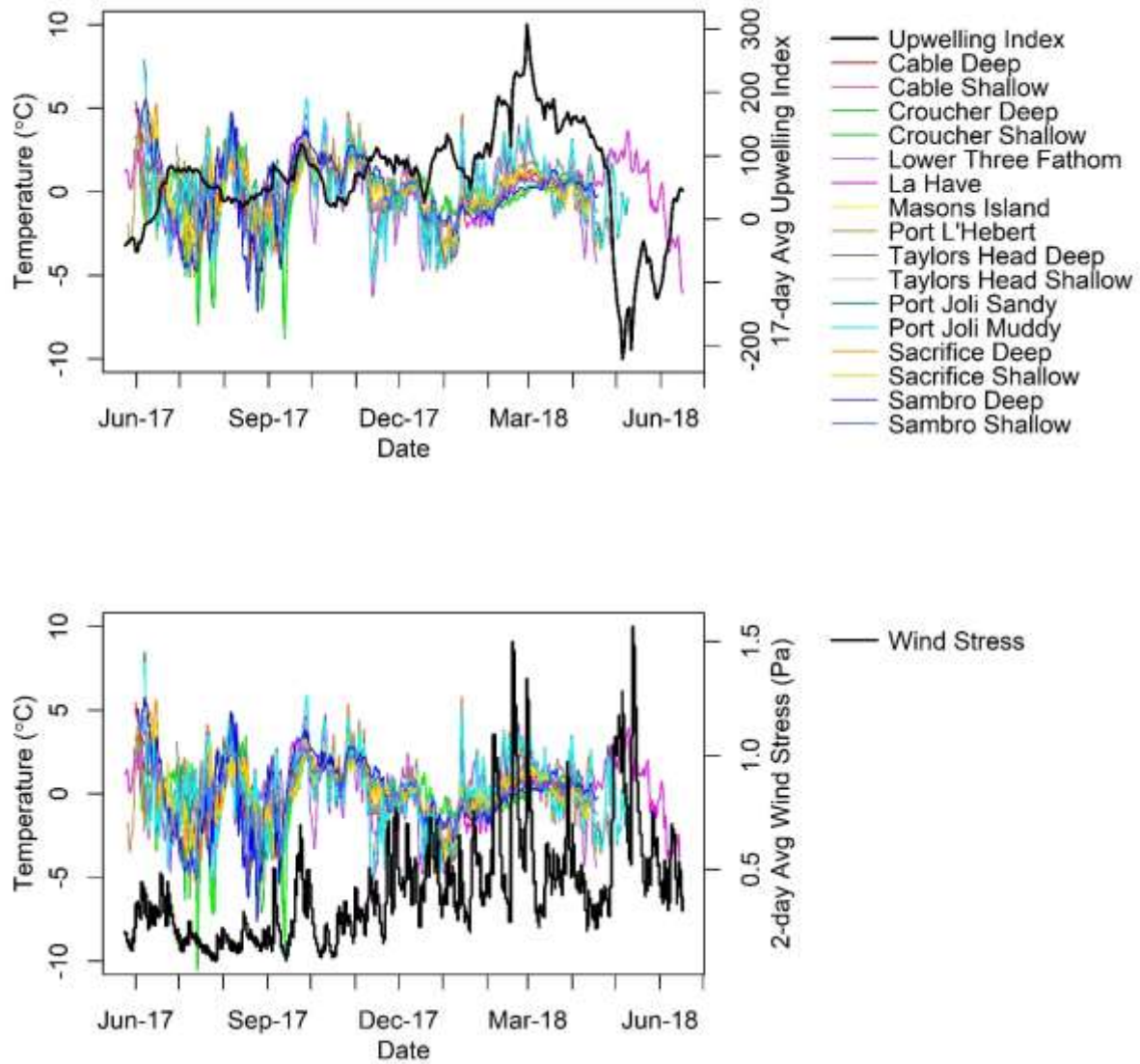
Figure 10. Mid-frequency temperature changes at all sites and locations plotted with a 17-day back-averaged upwelling index (top panel) and 2-day averaged wind stress (bottom-panel). Temperatures are averaged daily in the top panel and hourly in the bottom panel.
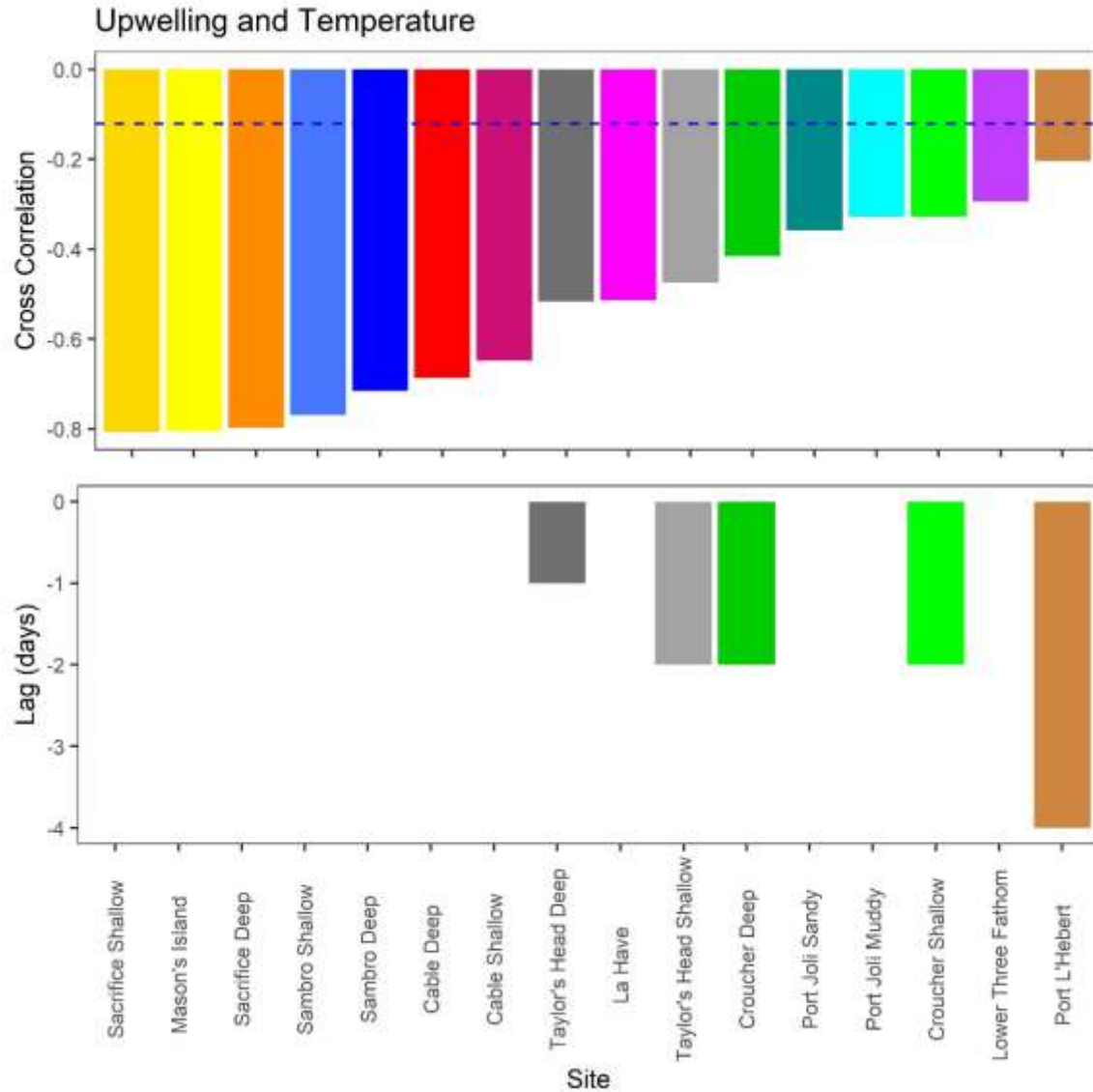
Figure 11. Lagged correlations between mid-frequency temperature changes (daily average) and a 17-day averaged upwelling index for all sites and locations (top panel). The dotted blue line indicates the 95% confidence interval for strict white noise. Bottom panel shows the time lag with the greatest correlation, considering only lags of 0 to -10 days. Where no bars are seen, lag times are 0.
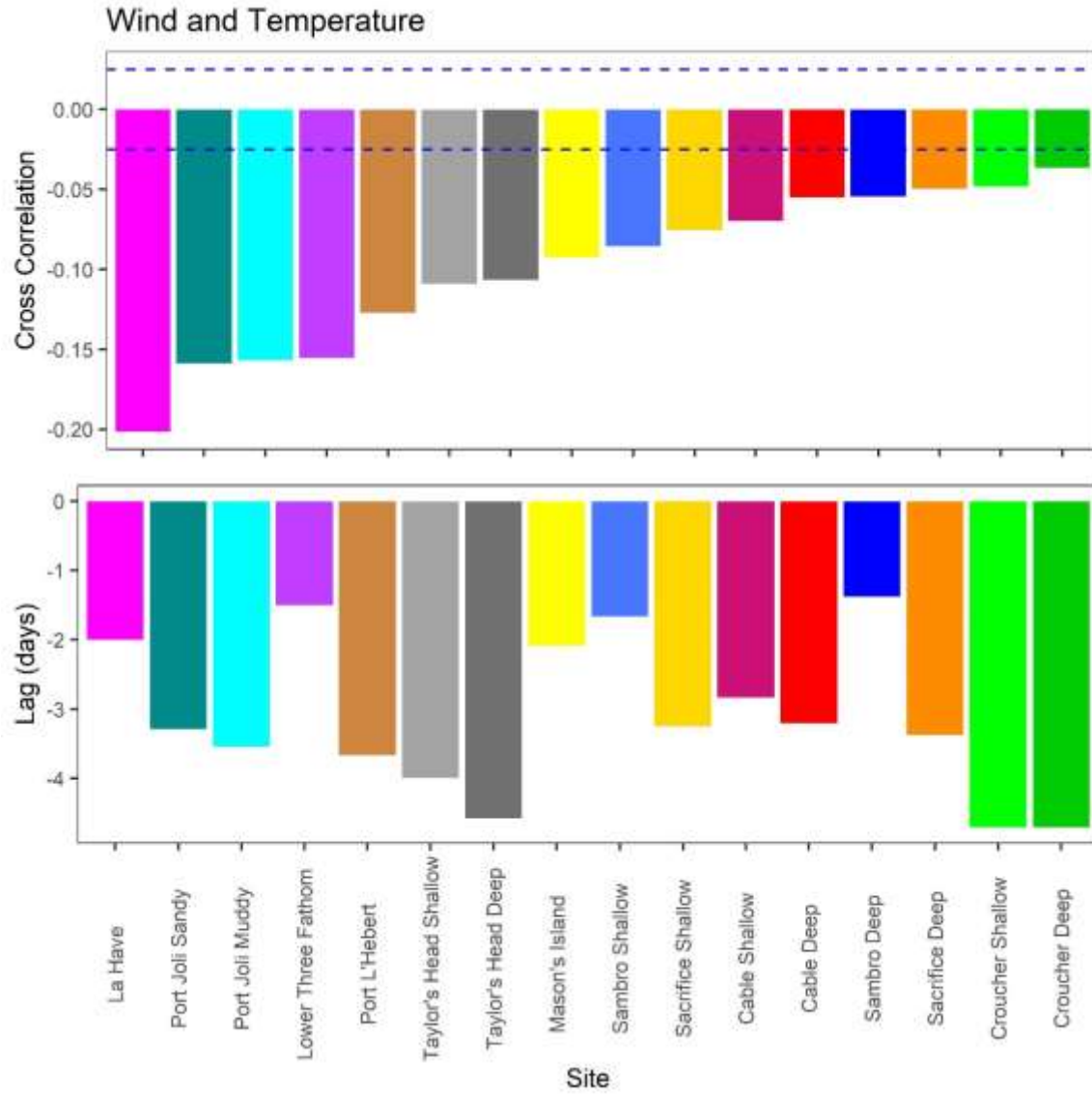
Figure 12. Lagged correlations between hourly temperature changes in the middle frequency band and hourly wind stress for all sites and locations (top panel). The dotted blue line indicates the 95% confidence interval for strict white noise. Bottom panel shows the time lag with the greatest correlation.
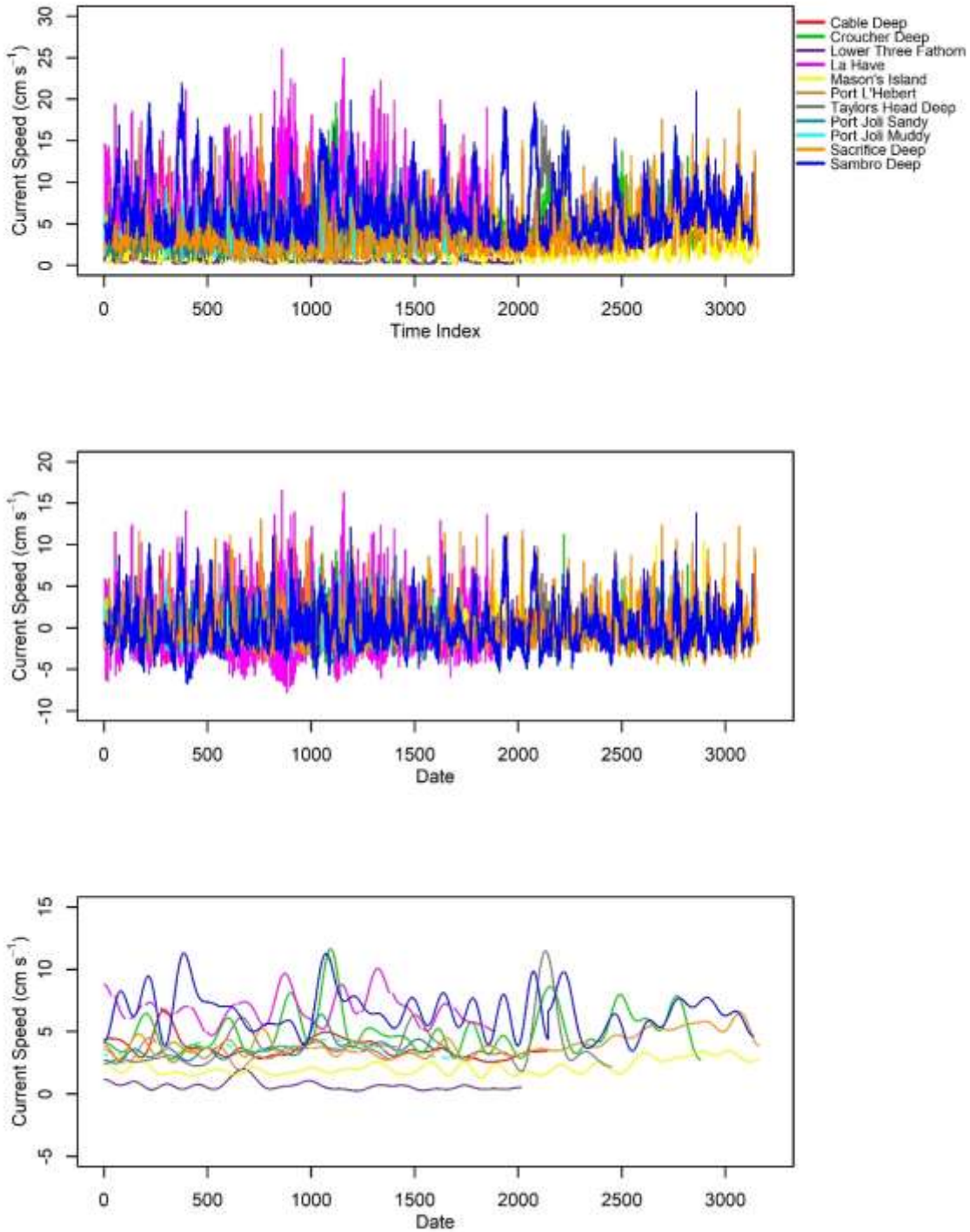
Figure 13. Current speed (cm/s) recorded every 10 minutes for 2-4 week periods at all 10 sites, including the sandy and muddy locations at Port Joli (top panel). Middle panel shows variation in currents in the high frequency range, while the bottom panel shows variation in currents in the middle frequency range.
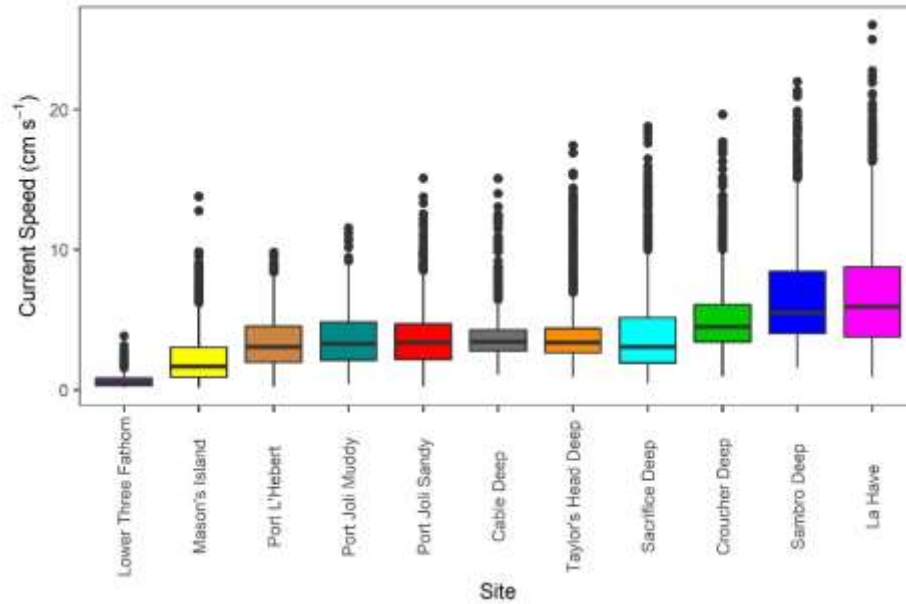
Figure 14. Boxplots of current speeds at each site, with boxes showing the median, first and third quartile current speeds. Upper and lower whiskers correspond to the largest and smallest values, meeting the condition that they are no further than 1.5*IQR from the first and third quartiles. Outliers are shown as black dots at the end of each whisker. Sites are ordered left to right according to the mean (smallest to largest).
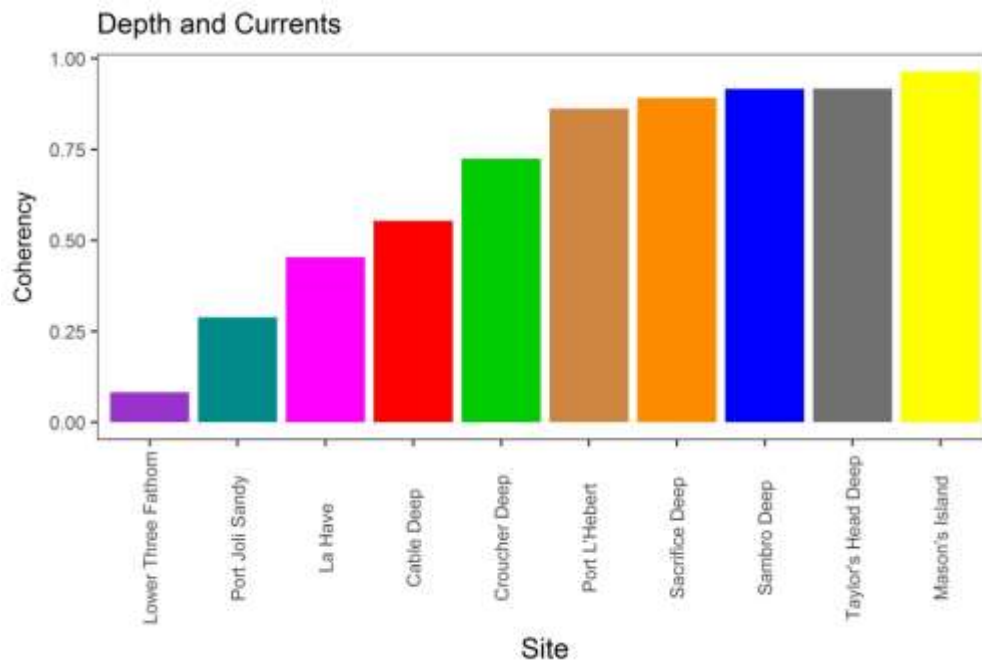
Figure 15. Coherence (spectral analysis) between time series of depth and current speed at each of the 10 sites within the frequency range associated with the diurnal tidal constituents (0.126-0.144, 11.6-12.9 hours).
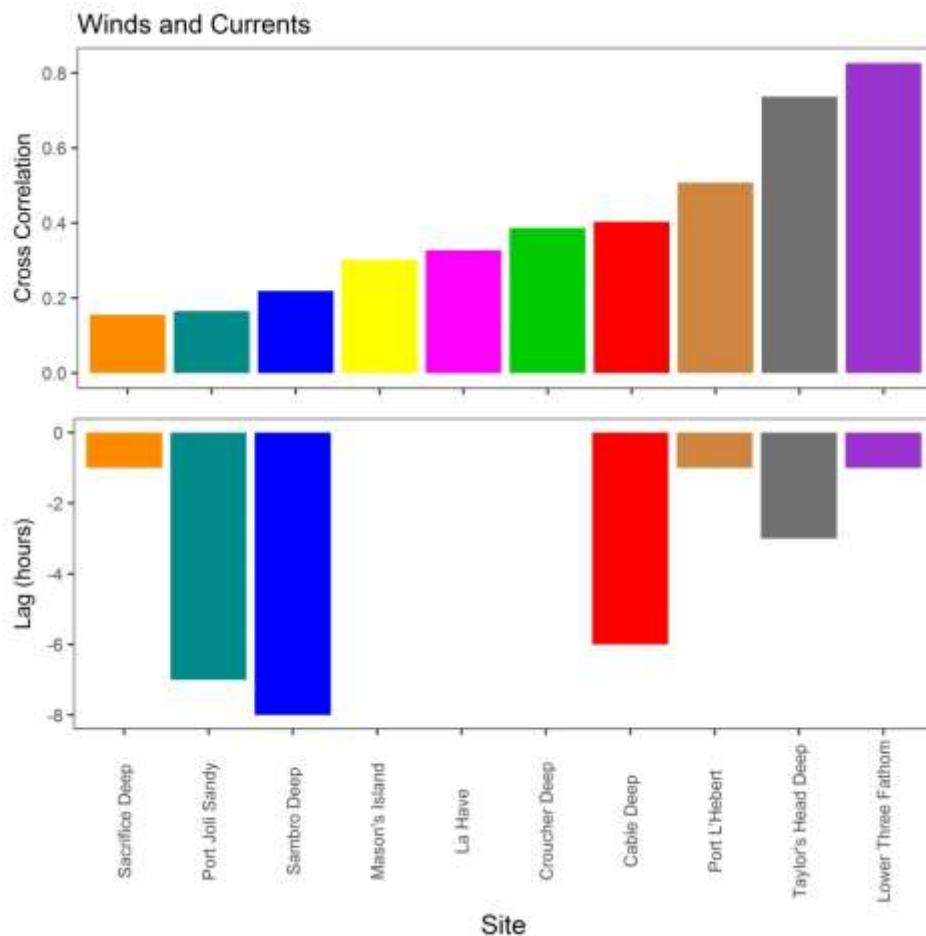
Figure 16. Top panel shows the correlation between current speed and wind stress at each of the 10 sites within time lags of -24-0. Bottom panel shows the time lag with the strongest correlation at each site. Note, no bar represents a t=0 lag value.
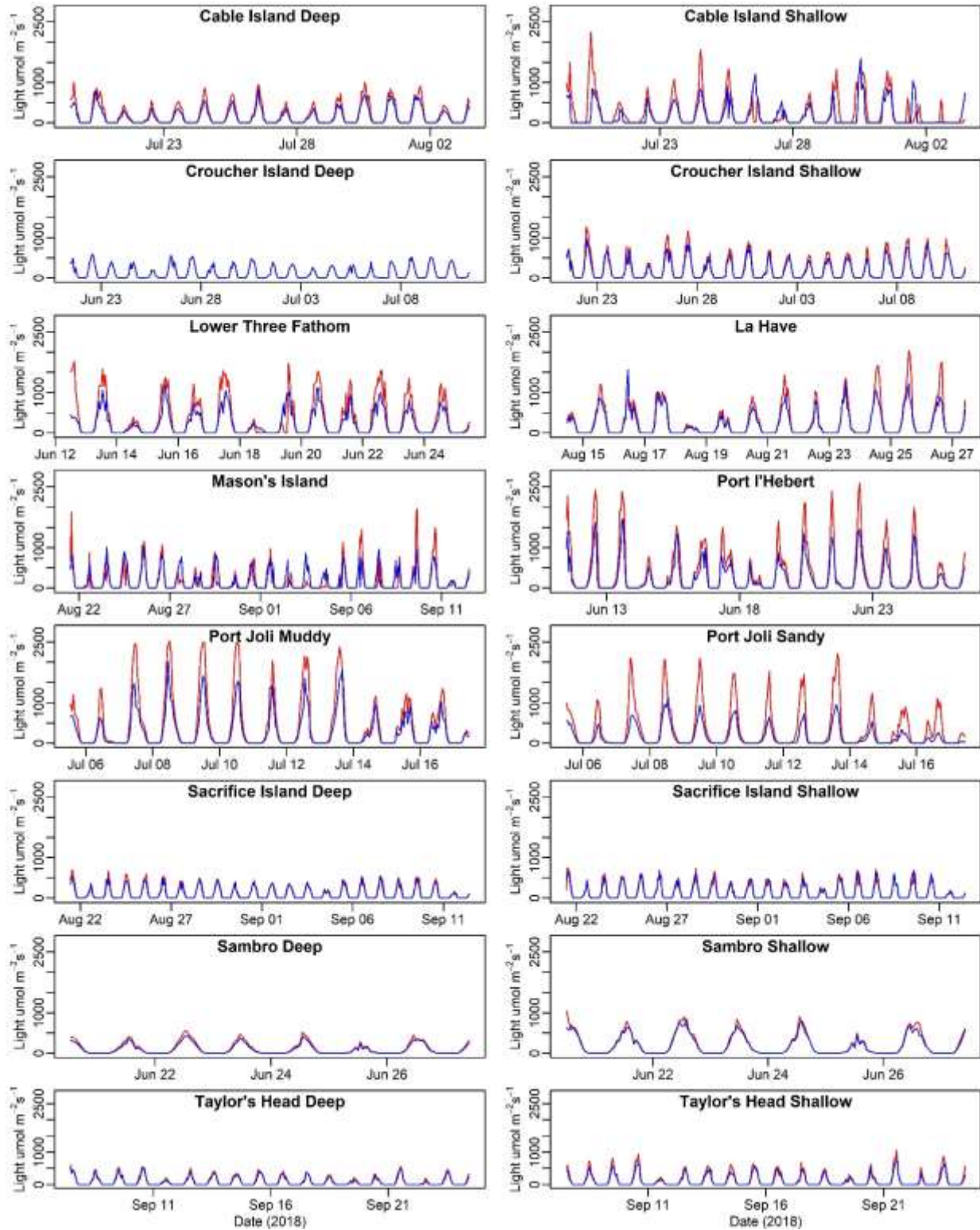
Figure 17. Raw (unfiltered) light levels recorded at all sites and locations. Blue lines show light data recorded from the bottom (deeper) sensor, while red lines show light data recorded from the top (shallower) sensor.
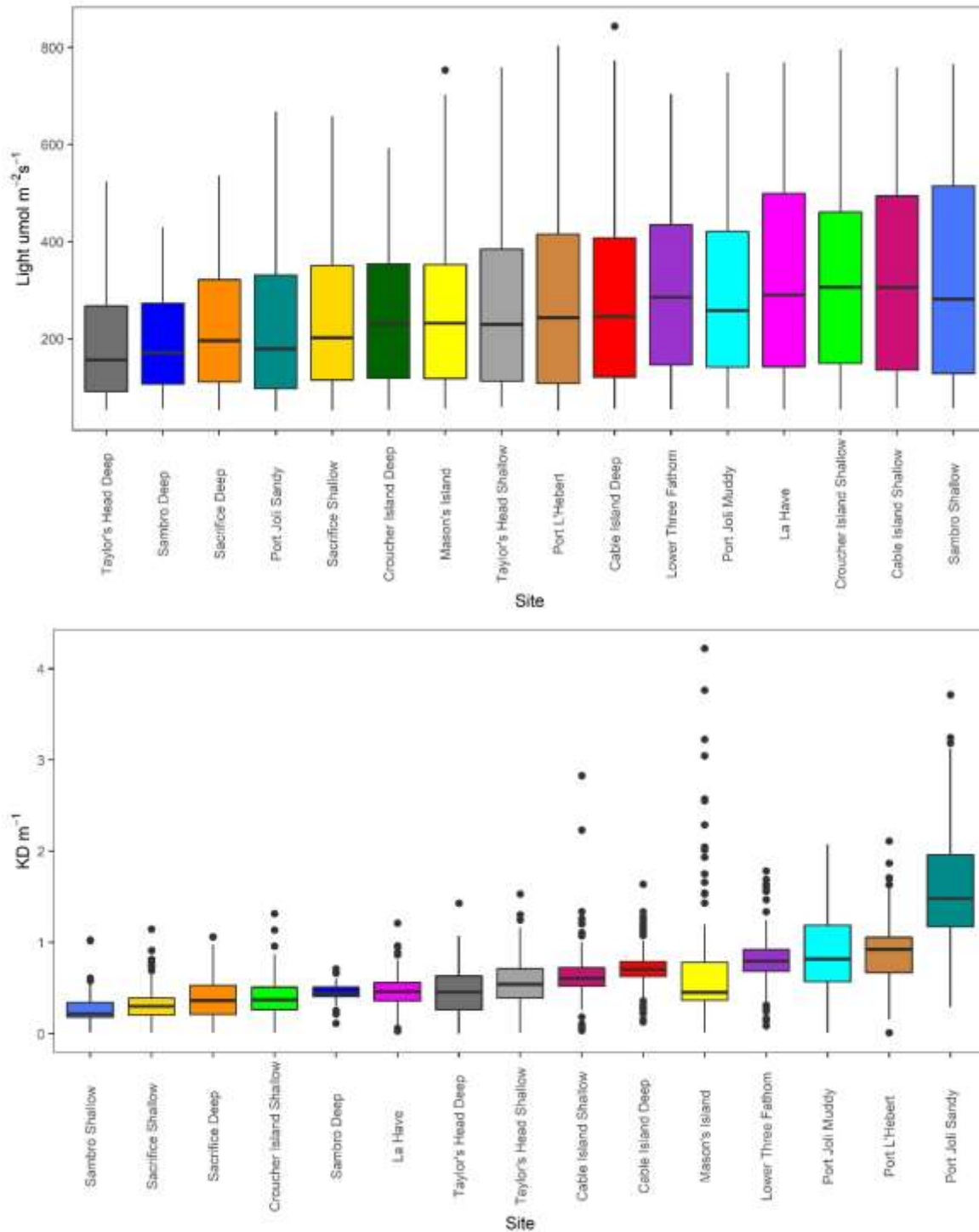
Figure 18. Boxplot of light levels as recorded by the bottom sensor at each site (top panel) and light attenuation. . Upper and lower whiskers correspond to the largest and smallest values, meeting the condition that they are no further than 1.5*IQR from the first and third quartiles. Outliers are shown as black dots at the end of each whisker. Sites are ordered left to right according to the mean of each parameter (smallest to largest).
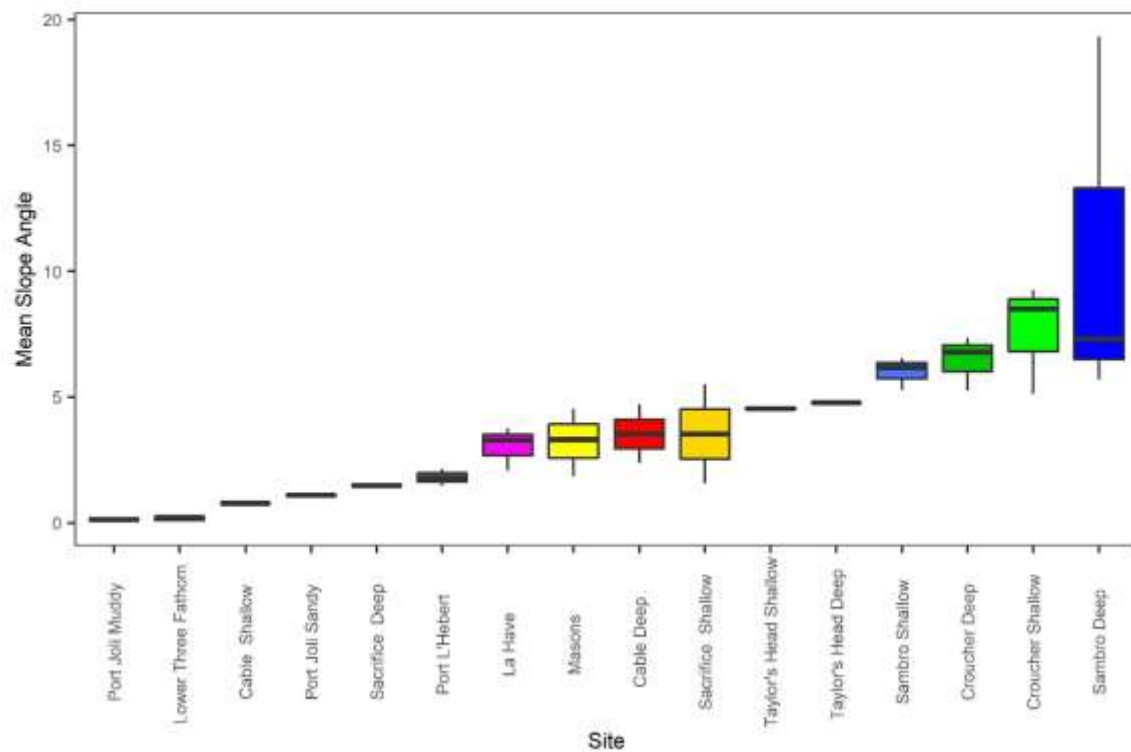
Figure 19. Boxplot of mean slope angle at each eelgrass site. For sites where there was less than 50m separating the deep and shallow locations, there is only one value per site.

Supplemental Figures

Temperature

Cable Island
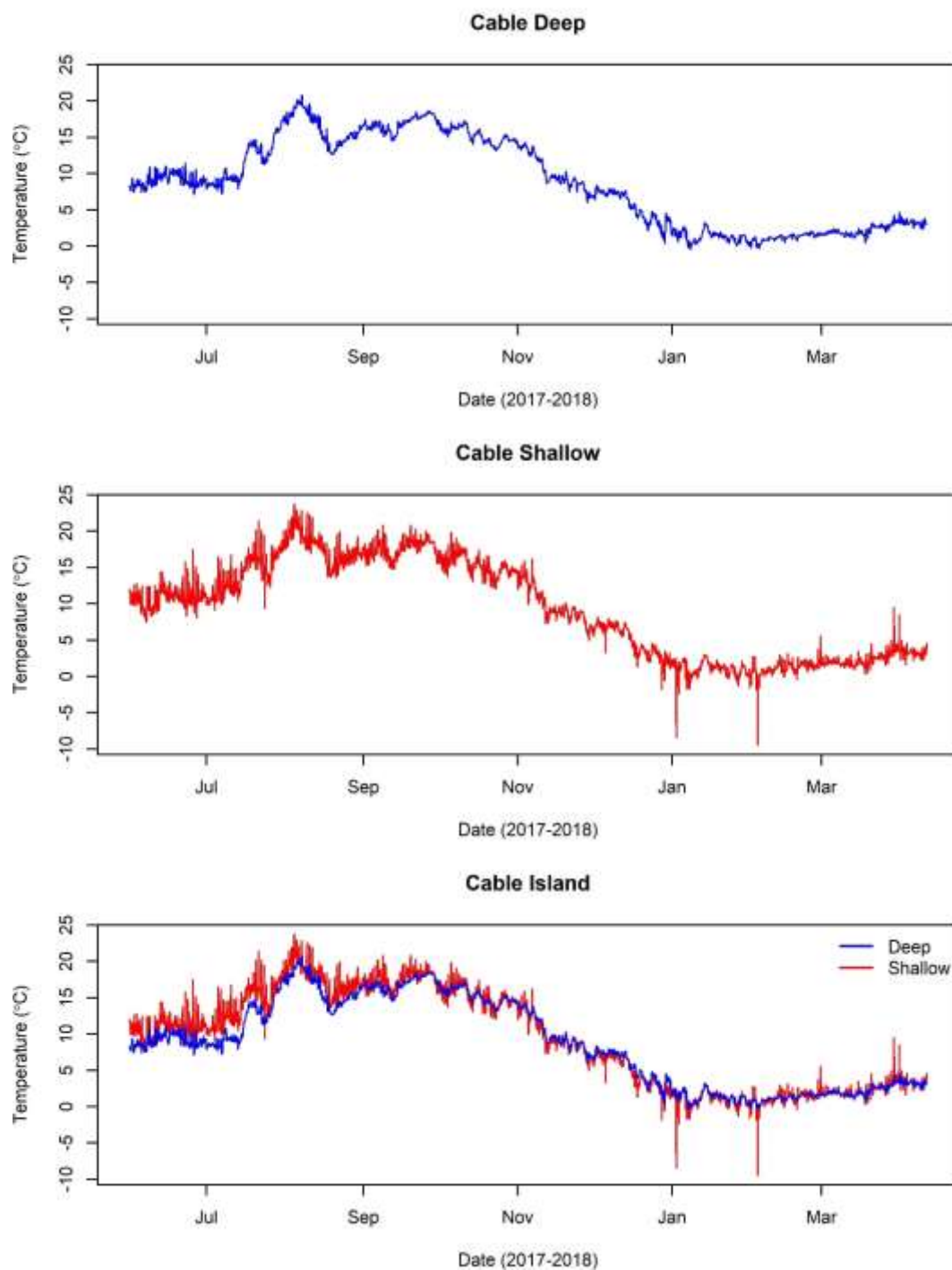
Figure S1. Temperature records at the deep and shallow locations at Cable Island, recorded from May 31, 2017 to April 11, 2018.
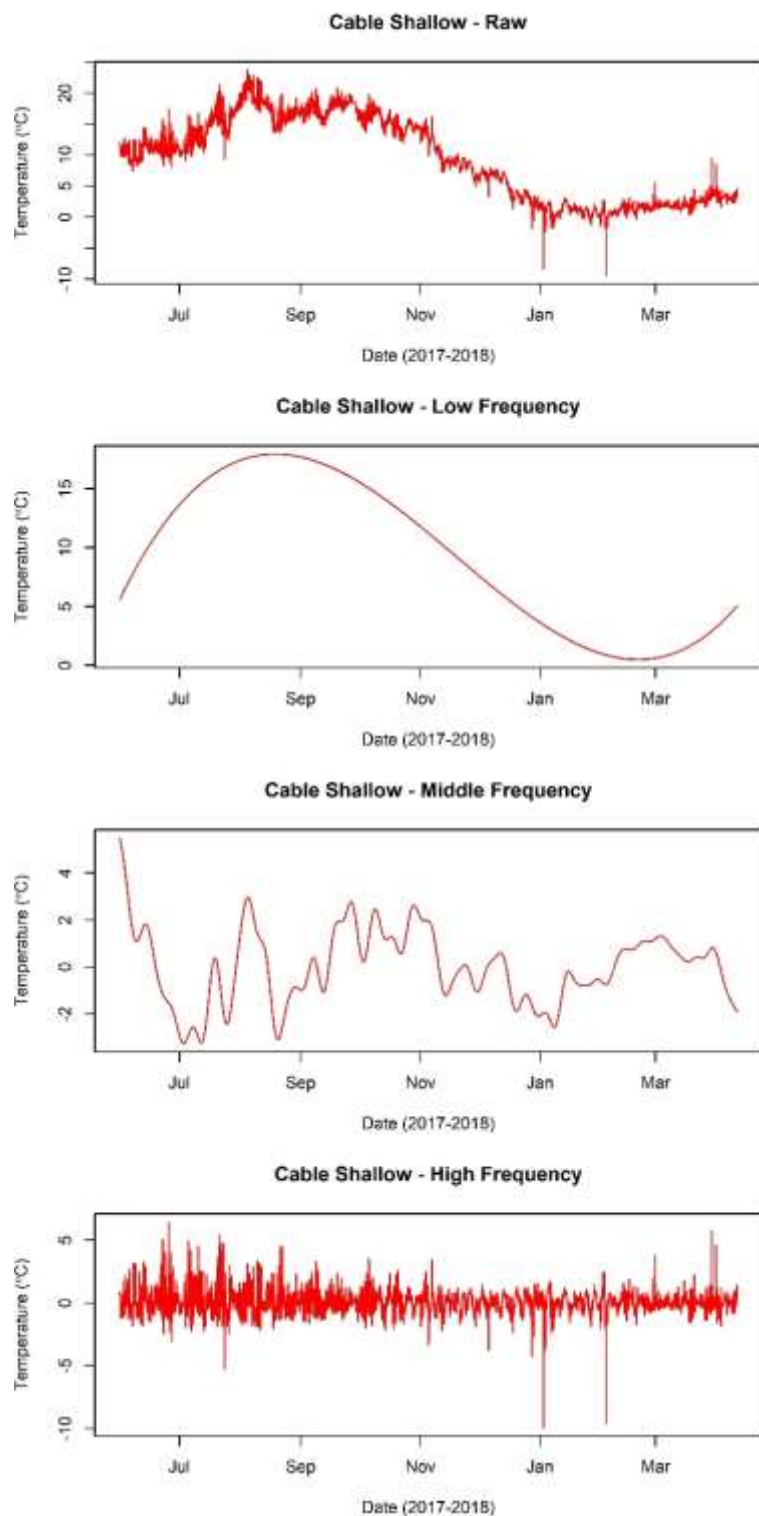
Figure S2. Raw temperatures (top panel), low (second panel), middle (third panel), and high frequency (bottom panel) temperature variability isolated at the shallow location at Cable Island.
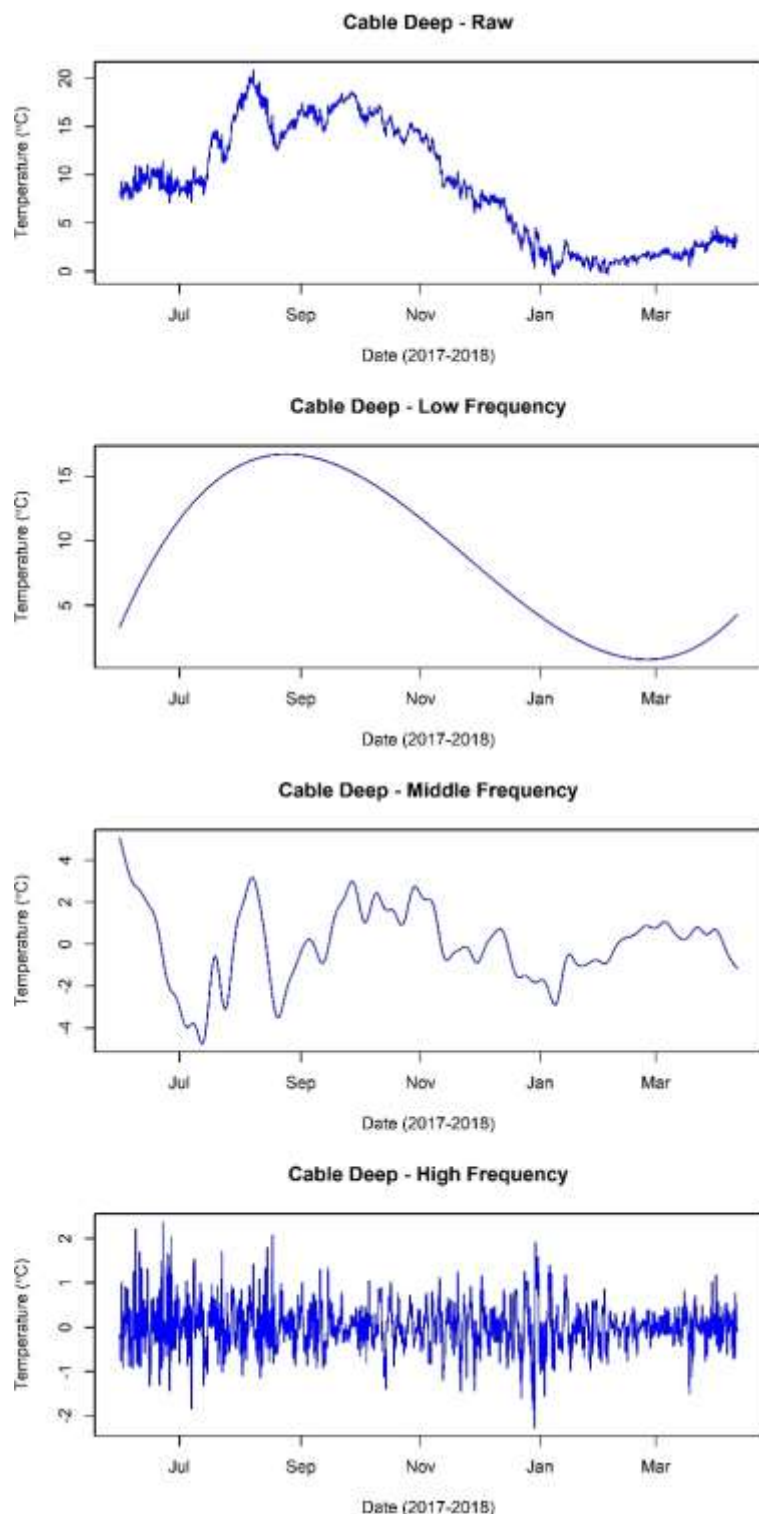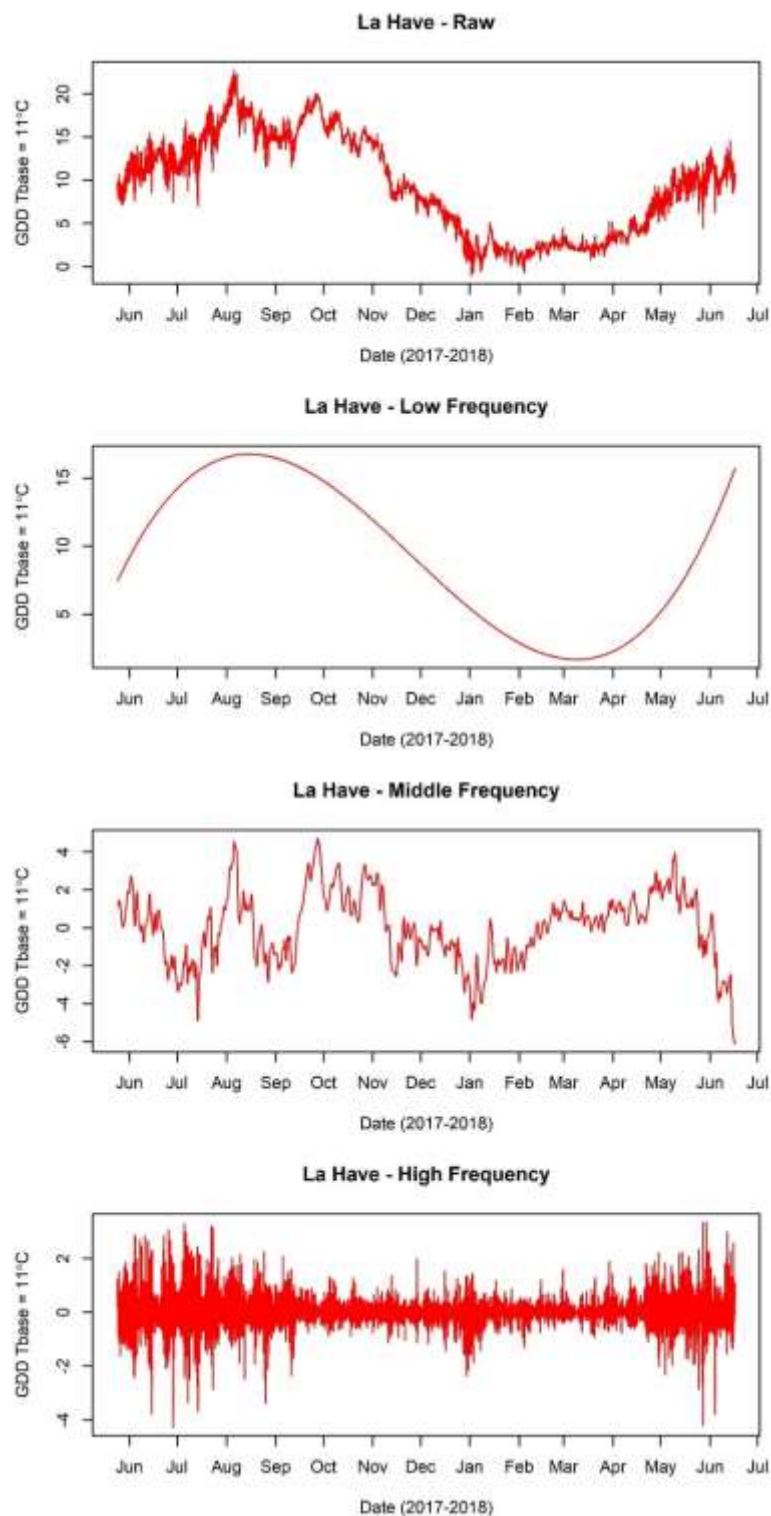
Figure S3. Raw temperatures (top panel), low (second panel), middle (third panel), and high frequency (bottom panel) temperature variability isolated at the deep location at Cable Island.
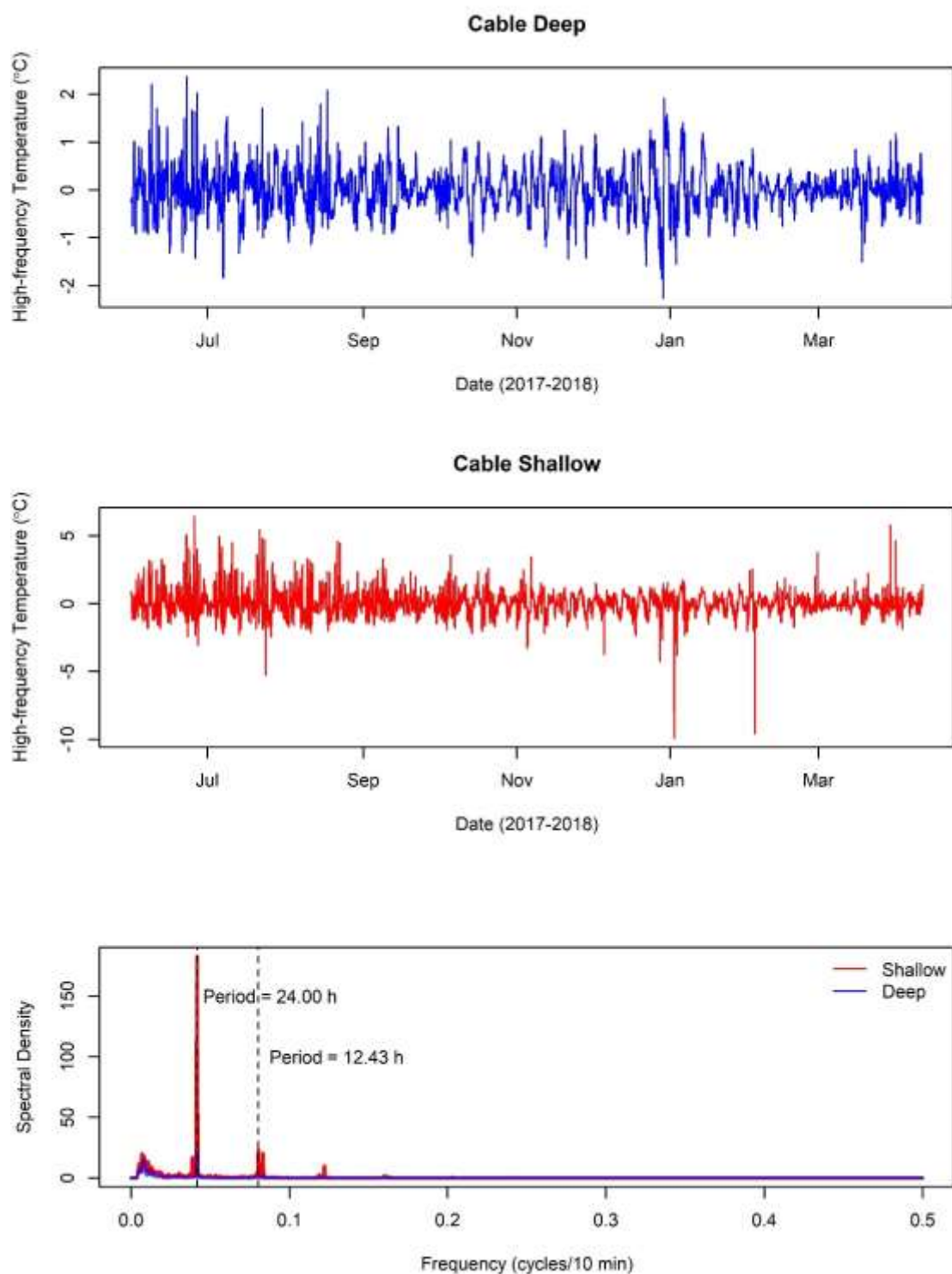
Figure S4. High frequency temperature changes at the shallow and deep locations at Cable Island (top two panels). The bottom panel shows the results of a spectral analysis, with the dominant frequencies shown in dotted lines and the period shown in text.
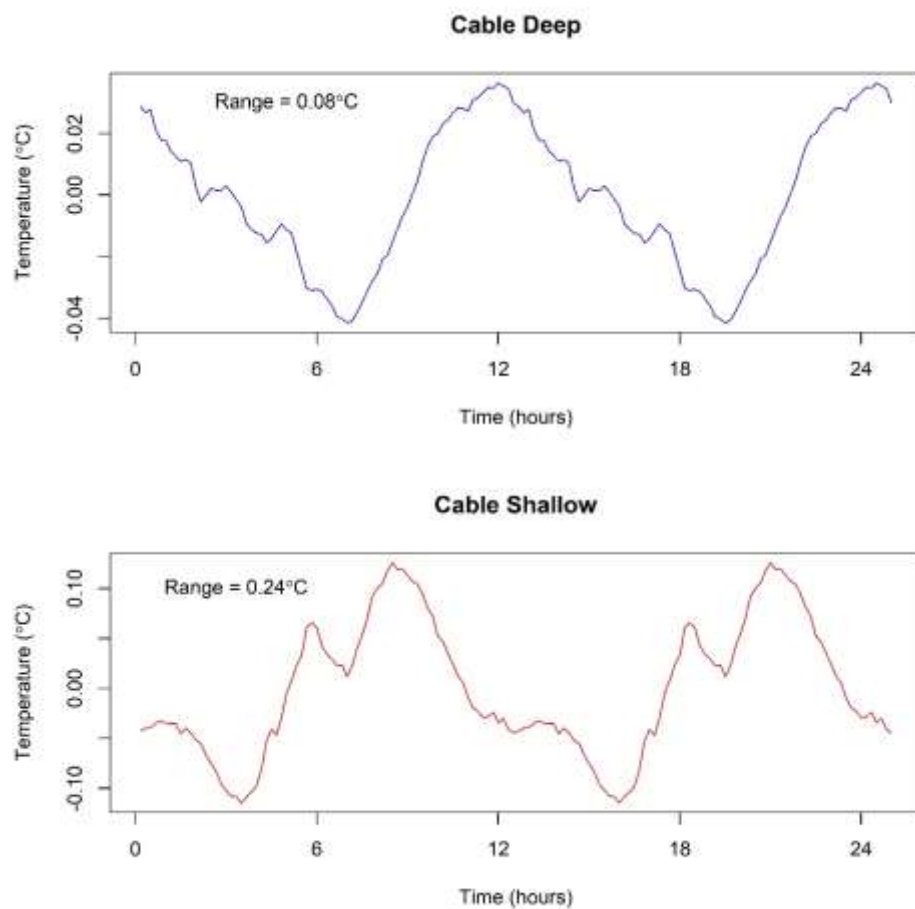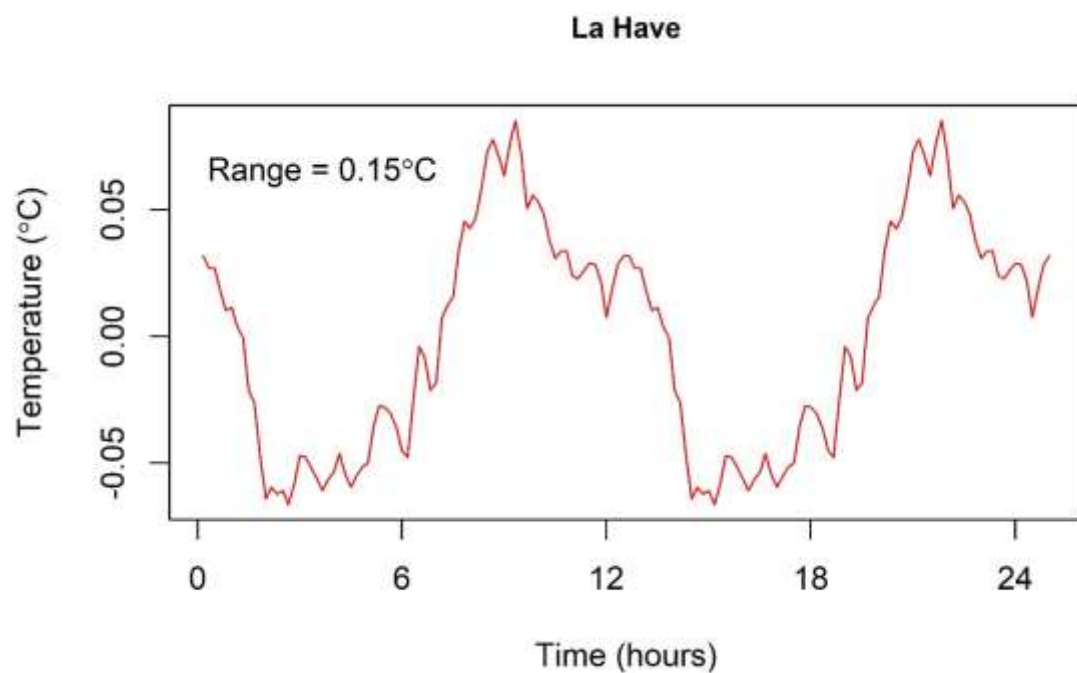
Figure S5. Average temperature changes over the 12.42-hour tidal cycle at Cable Island deep and shallow, calculated for the summer period (June-October 2017).

Cable Deep

Range = 0.71°C

Cable Shallow

Range = 2.15°C
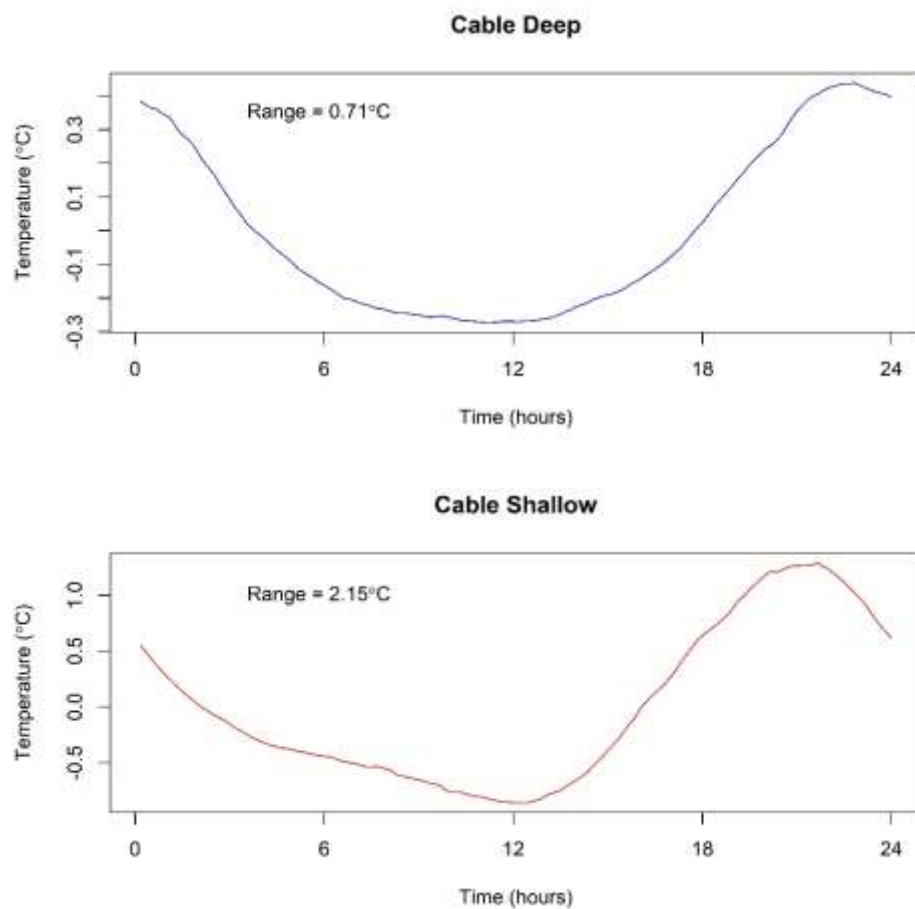
Figure S6. Average temperature changes over the 24-hour daily heating and cooling cycle at Cable Island deep and shallow, calculated for the summer period (June-October 2017).
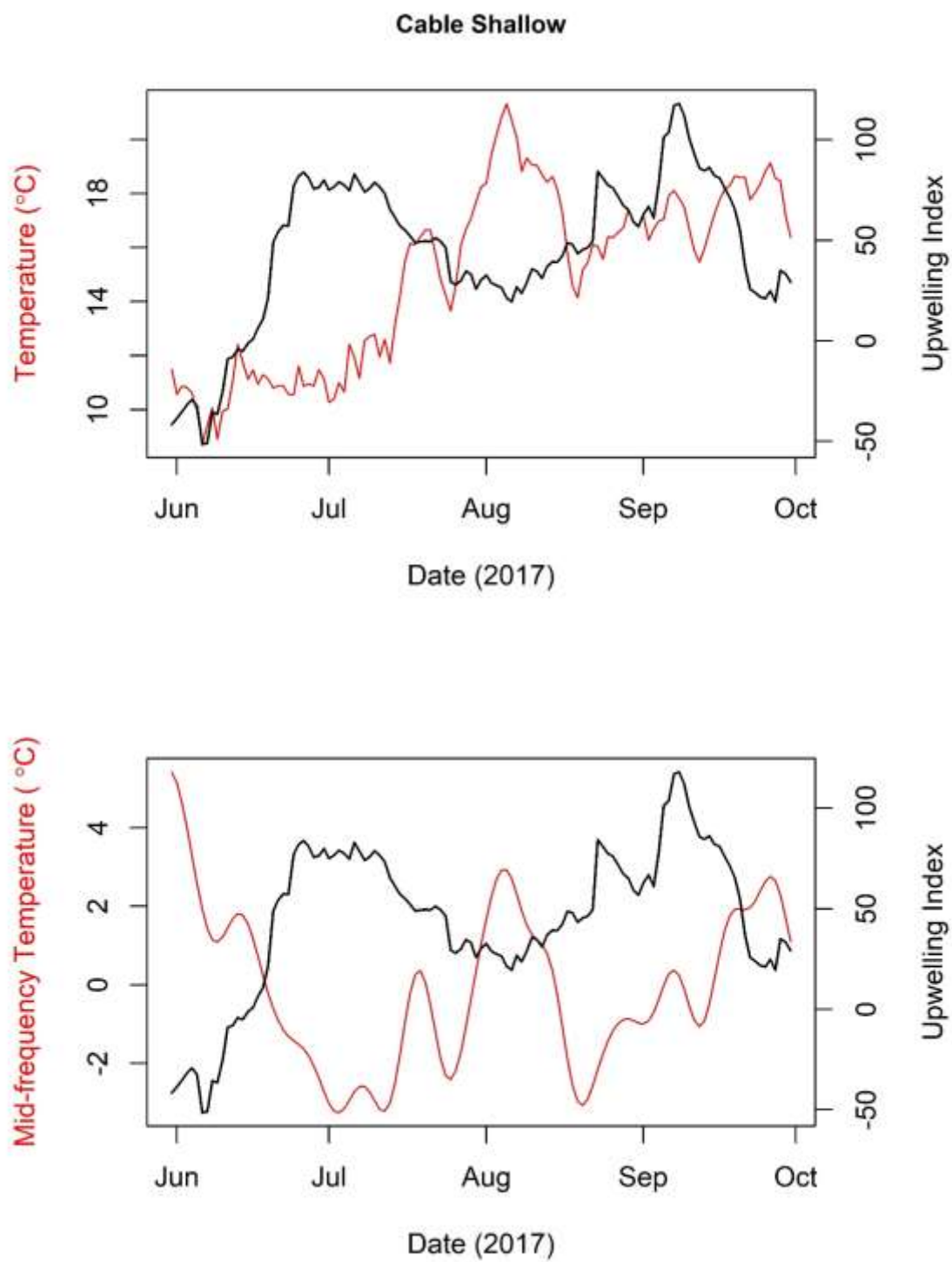
Cable Shallow

Figure S7. A 17-day back-averaged upwelling index plotted against average daily temperatures (top panel) and mid-frequency temperatures (bottom panel) at the shallow location at Cable Island.
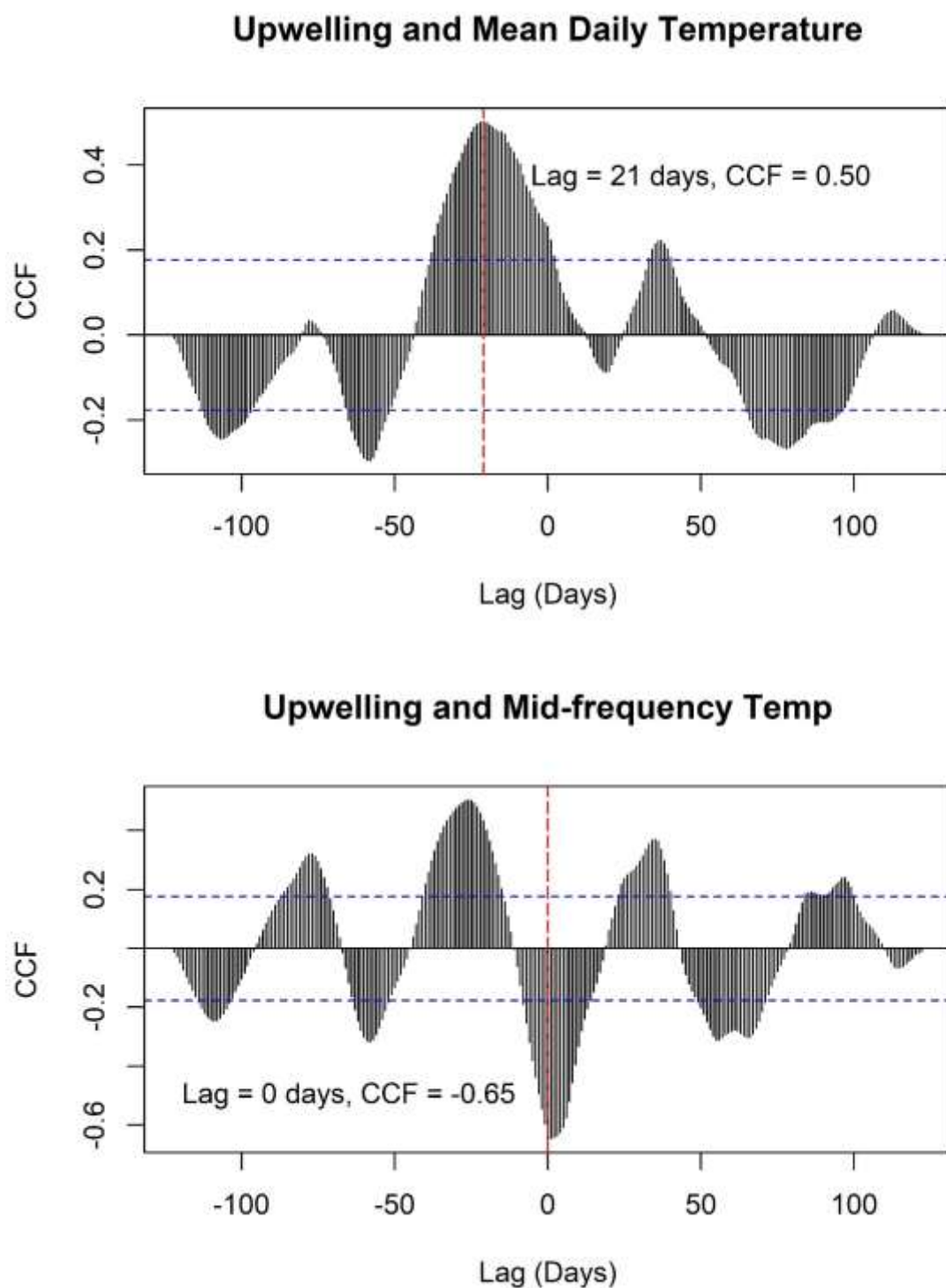
Figure S8. Correlations (CCFs) between a 17-day back-averaged upwelling index and average daily temperatures (top panel), and mid-frequency temperatures (bottom panel) at the shallow location at Cable Island. Shown on each pane are the dominant lags and corresponding CCF value for each measure of temperature.
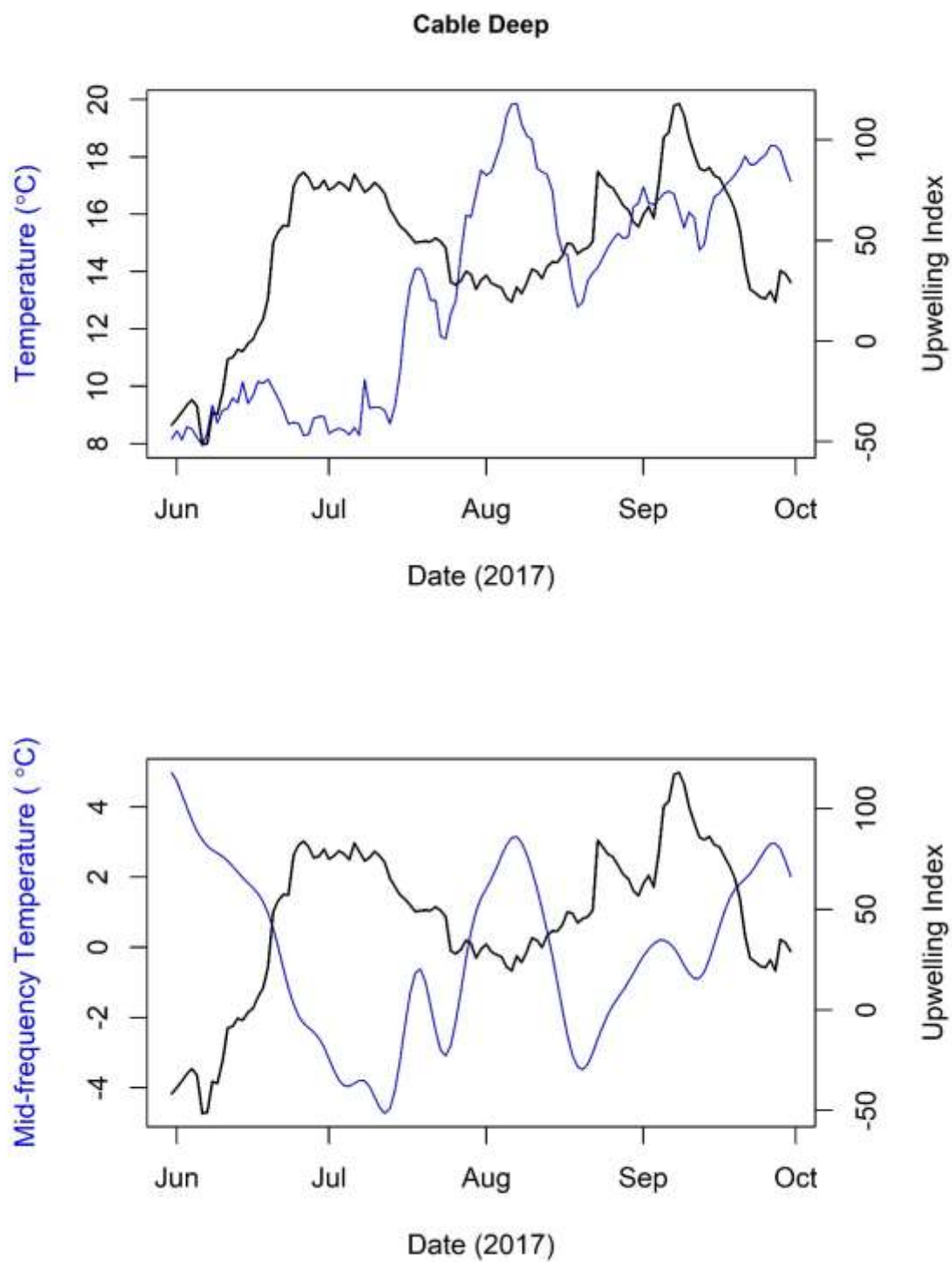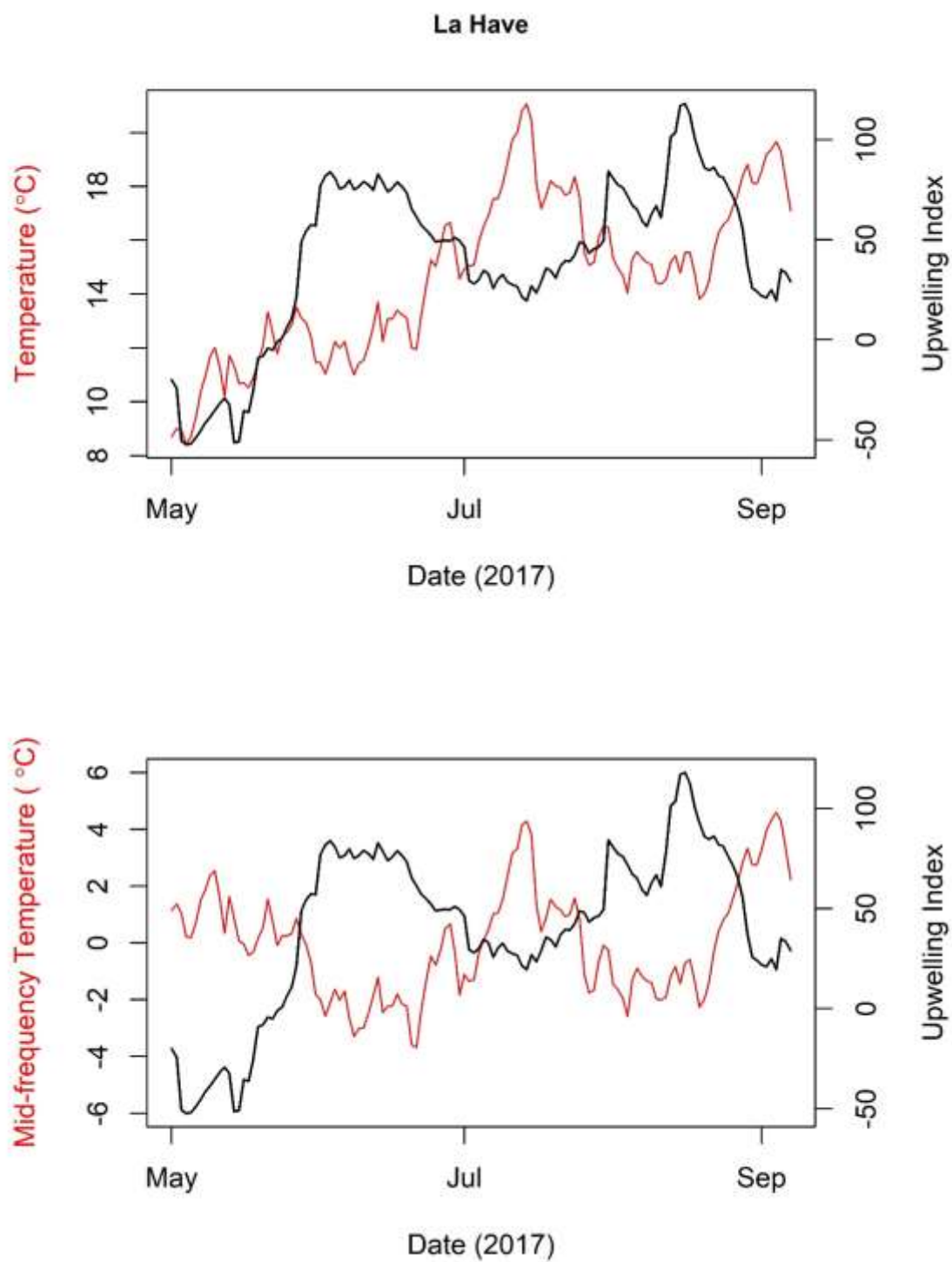
Cable Deep

Figure S9. A 17-day back-averaged upwelling index plotted against average daily temperatures (top panel) and mid-frequency temperatures (bottom panel) at the deep location at Cable Island.

Upwelling and Mean Daily Temperature

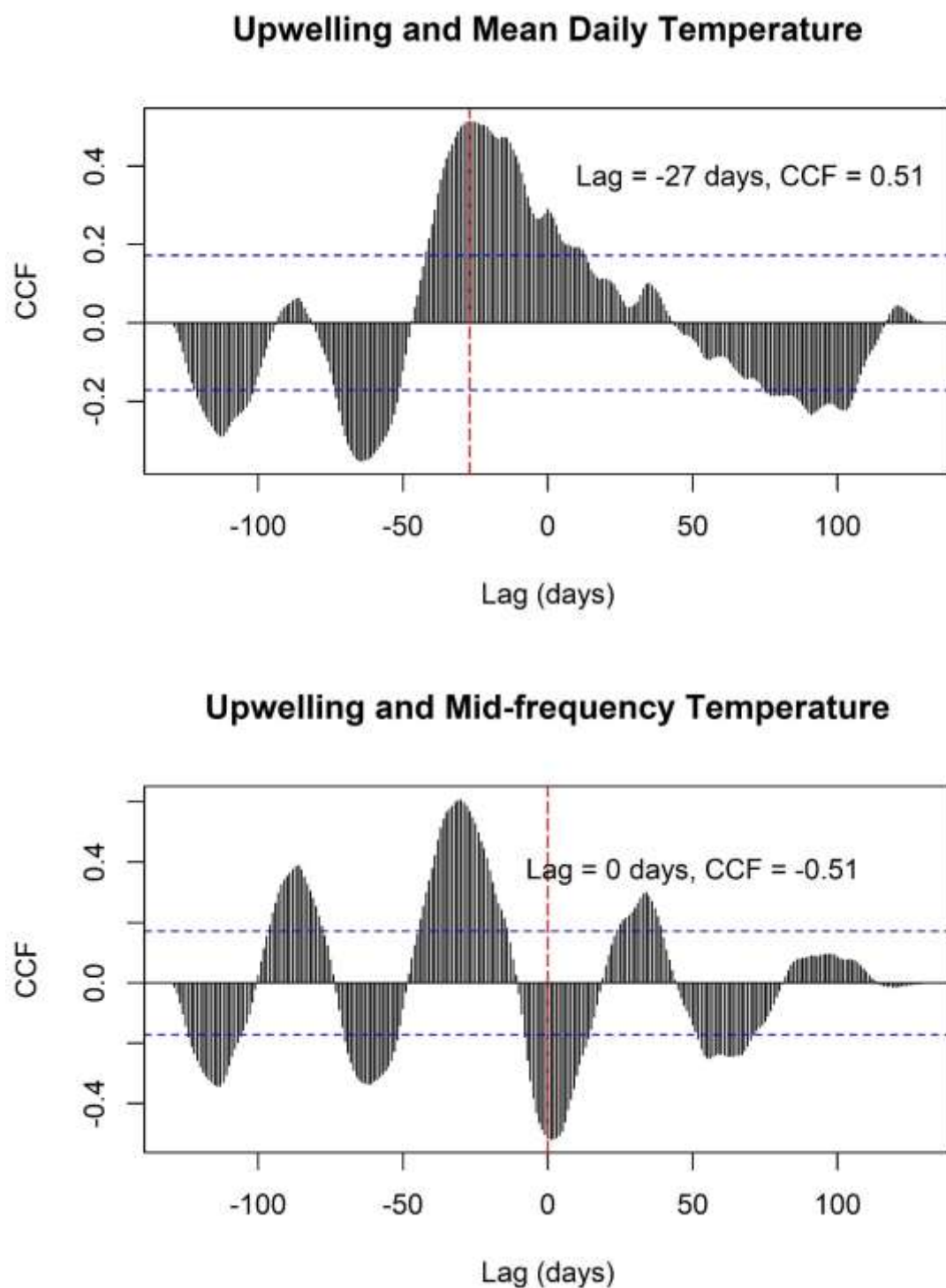## Upwelling and Mid-frequency Temperature
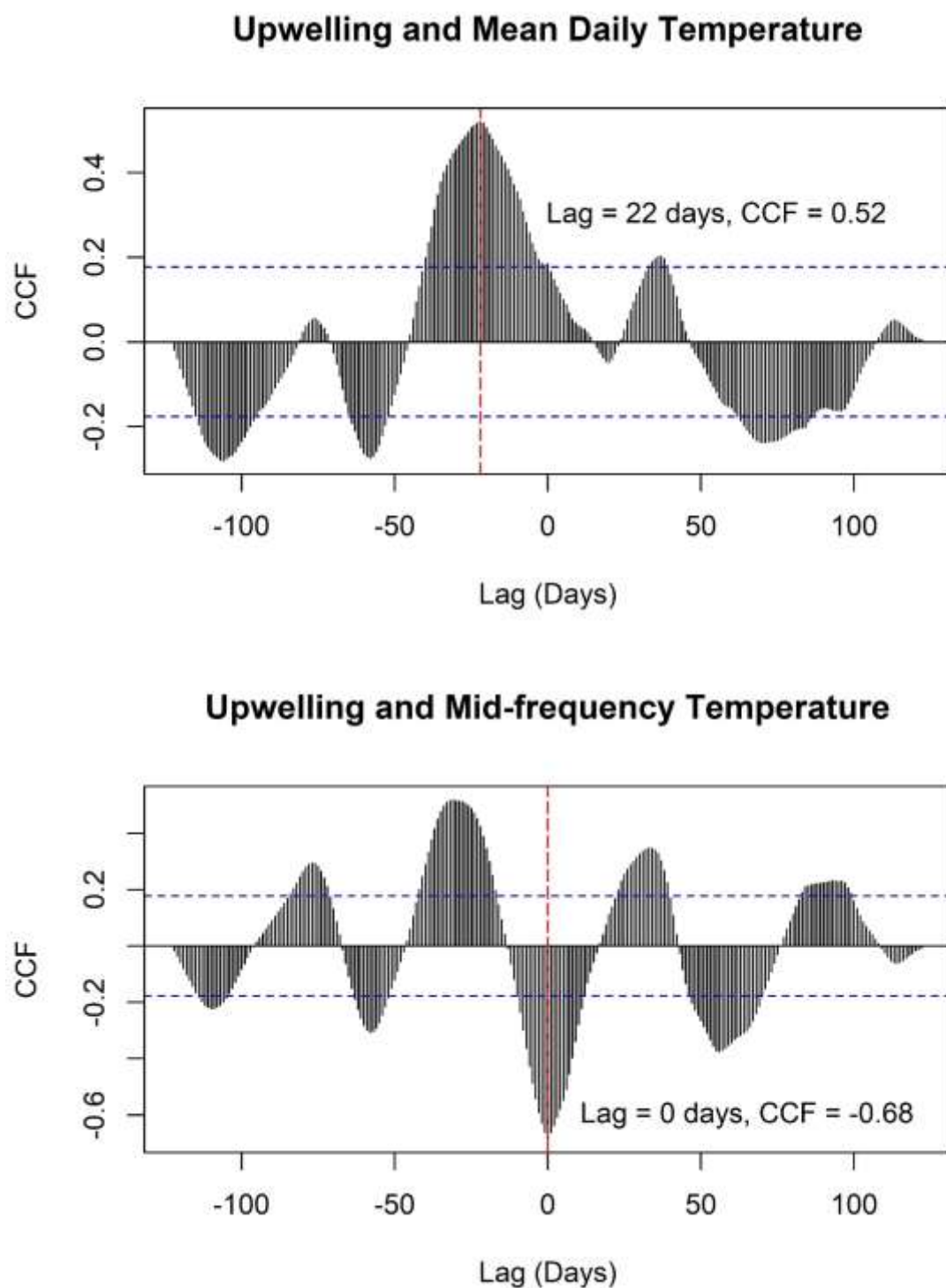
Figure S10. Correlations (CCFs) between a 17-day back-averaged upwelling index and average daily temperatures (top panel), and mid-frequency temperatures (bottom panel) at the deep location at Cable Island. Shown on each pane are the dominant lags and corresponding CCF value for each measure of temperature.
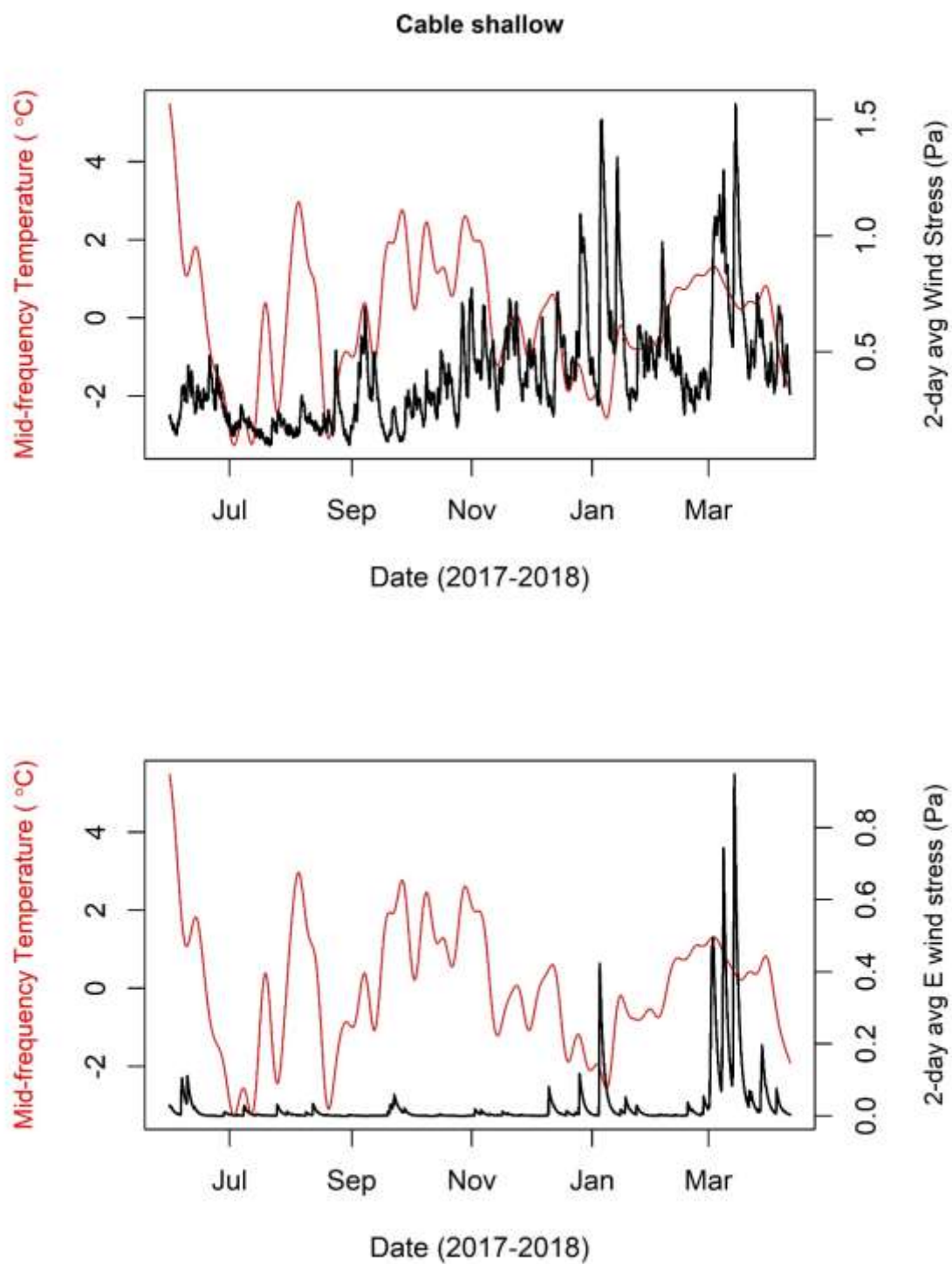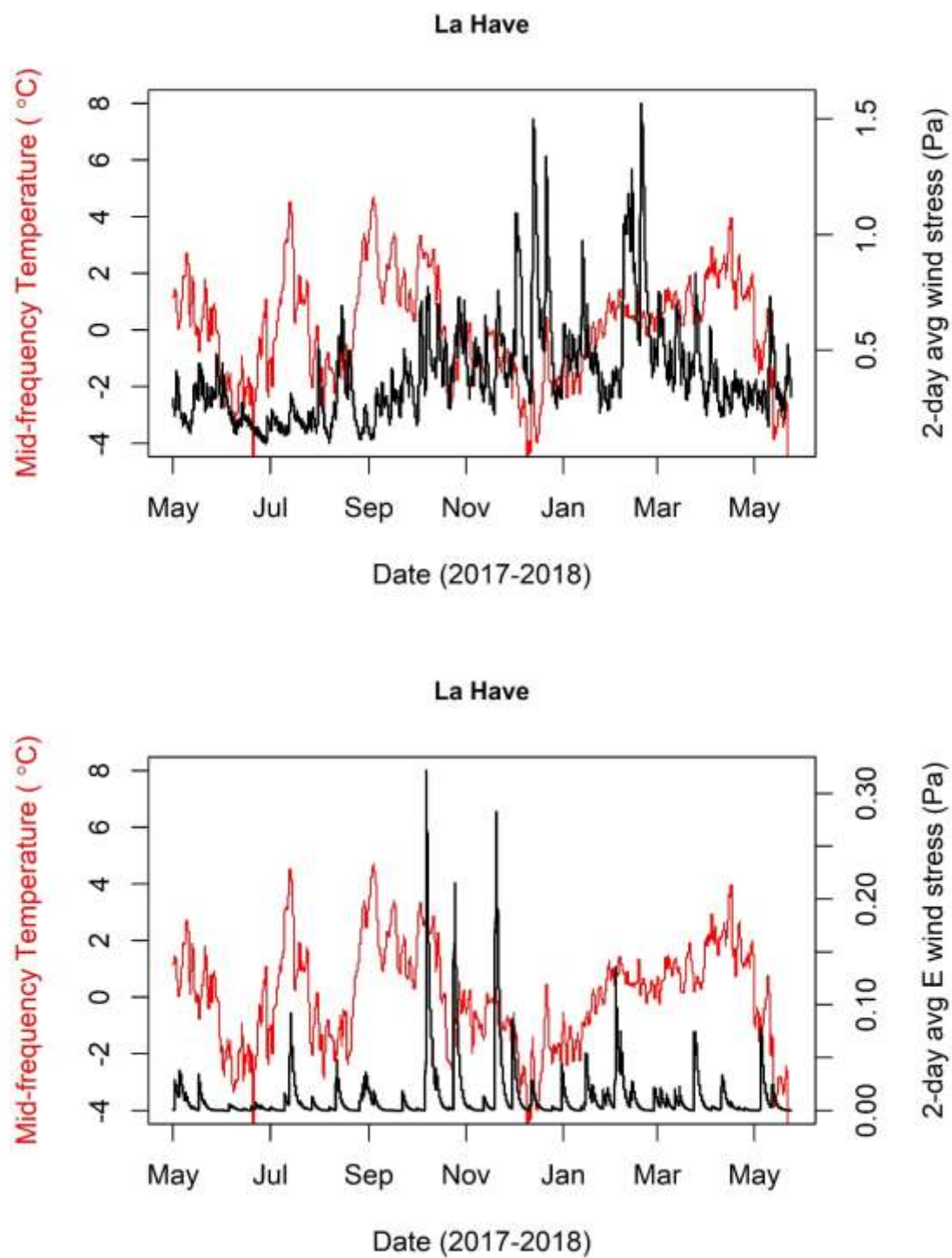
Cable shallow

Figure S11. 2-day back-averaged wind stress plotted against mid-frequency temperatures at the shallow location at Cable Island. The top panel shows total wind stress, while the bottom panel shows easterly wind stress.

2-day Wind Stress and Mid-frequency Temp

Lag = 68 hours, CCF = -0.07
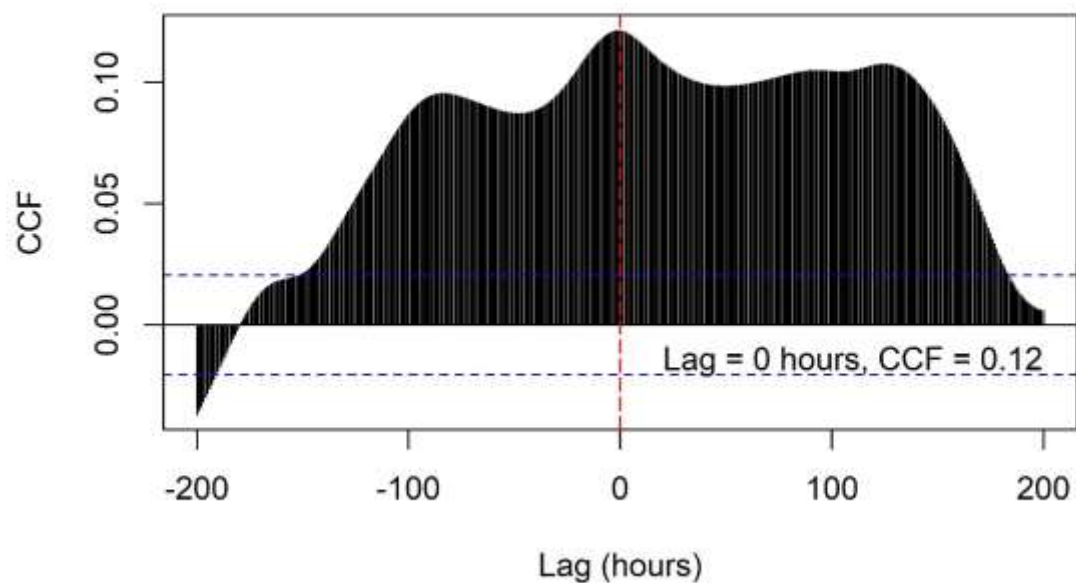
Lag (hours)

2-day E Wind Stress and Mid-frequency Temp

Lag (hours)
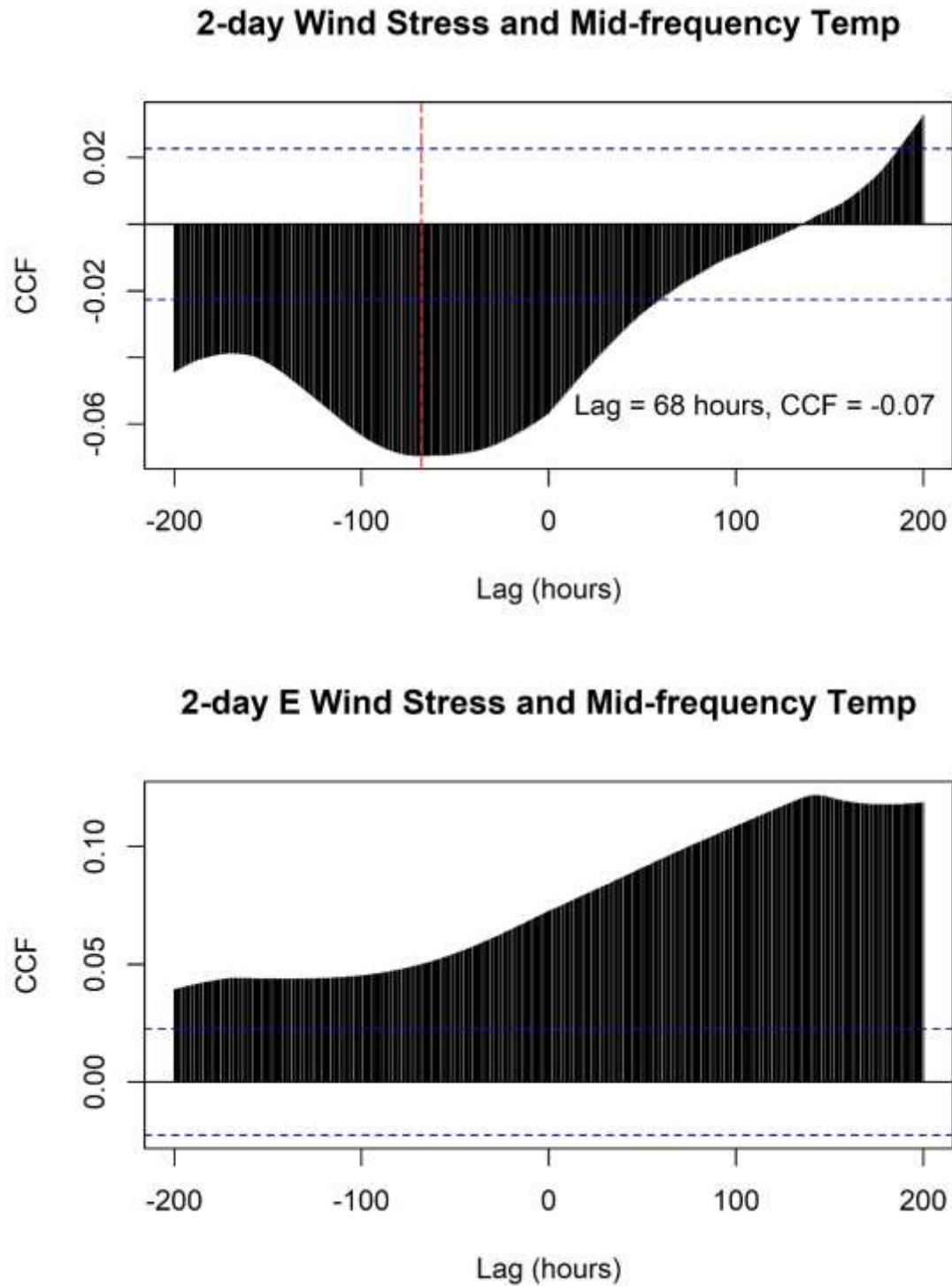
Figure S12. Correlations (CCFs) between a 2-day back-averaged wind stress and mid-frequency temperatures at the shallow location at Cable Island. The top panel shows total wind stress, while the bottom panel shows easterly wind stress. Shown on each pane are the dominant lags and corresponding CCF value for each measure of temperature.
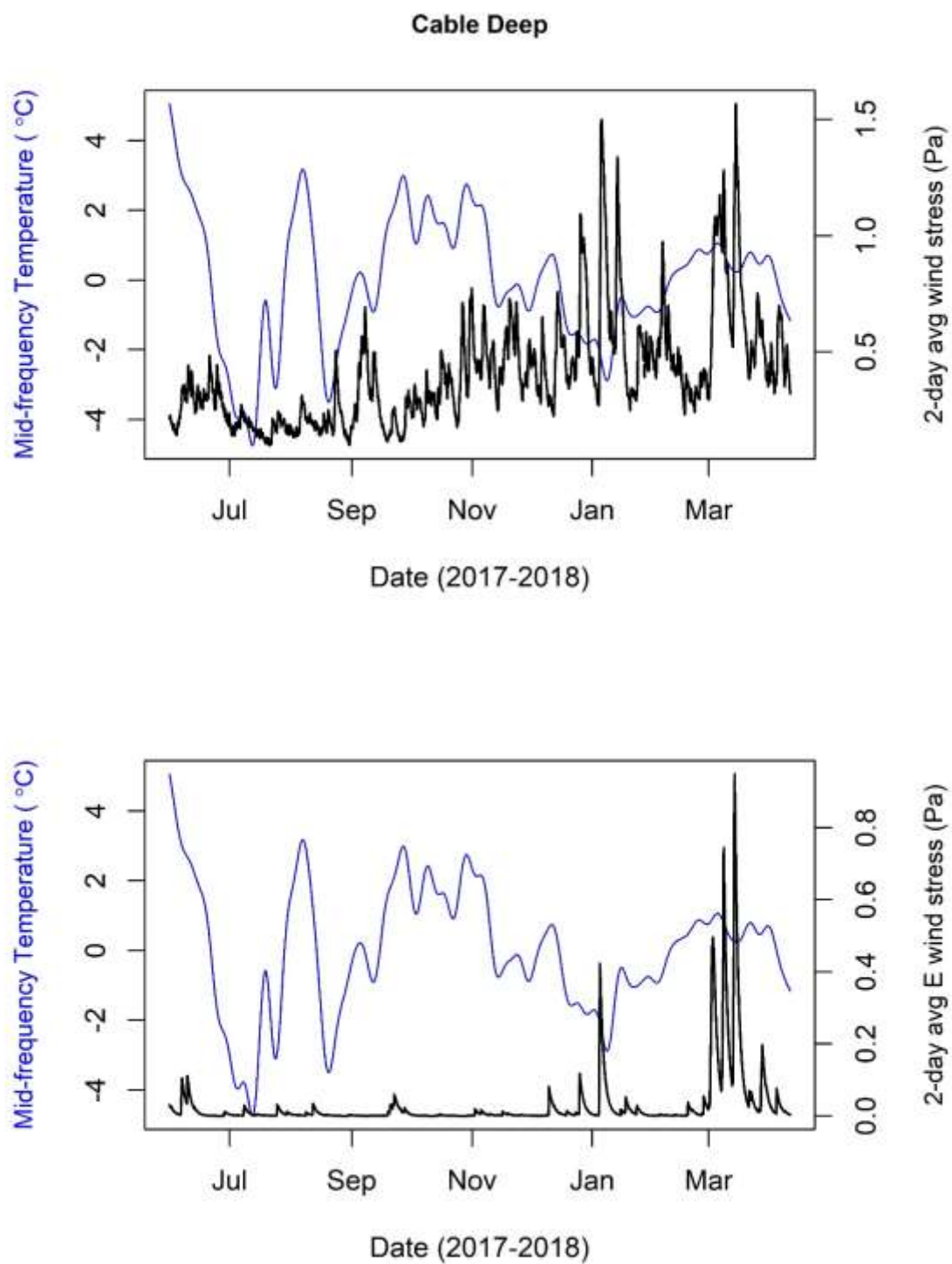
Figure S13. 2-day back-averaged wind stress plotted against mid-frequency temperatures at the deep location at Cable Island. The top panel shows total wind stress, while the bottom panel shows easterly wind stress.

2-day Wind Stress and Mid-frequency Temp

Lag = 77 hours, CCF = -0.06

2-day E Wind Stress and Mid-frequency Temp
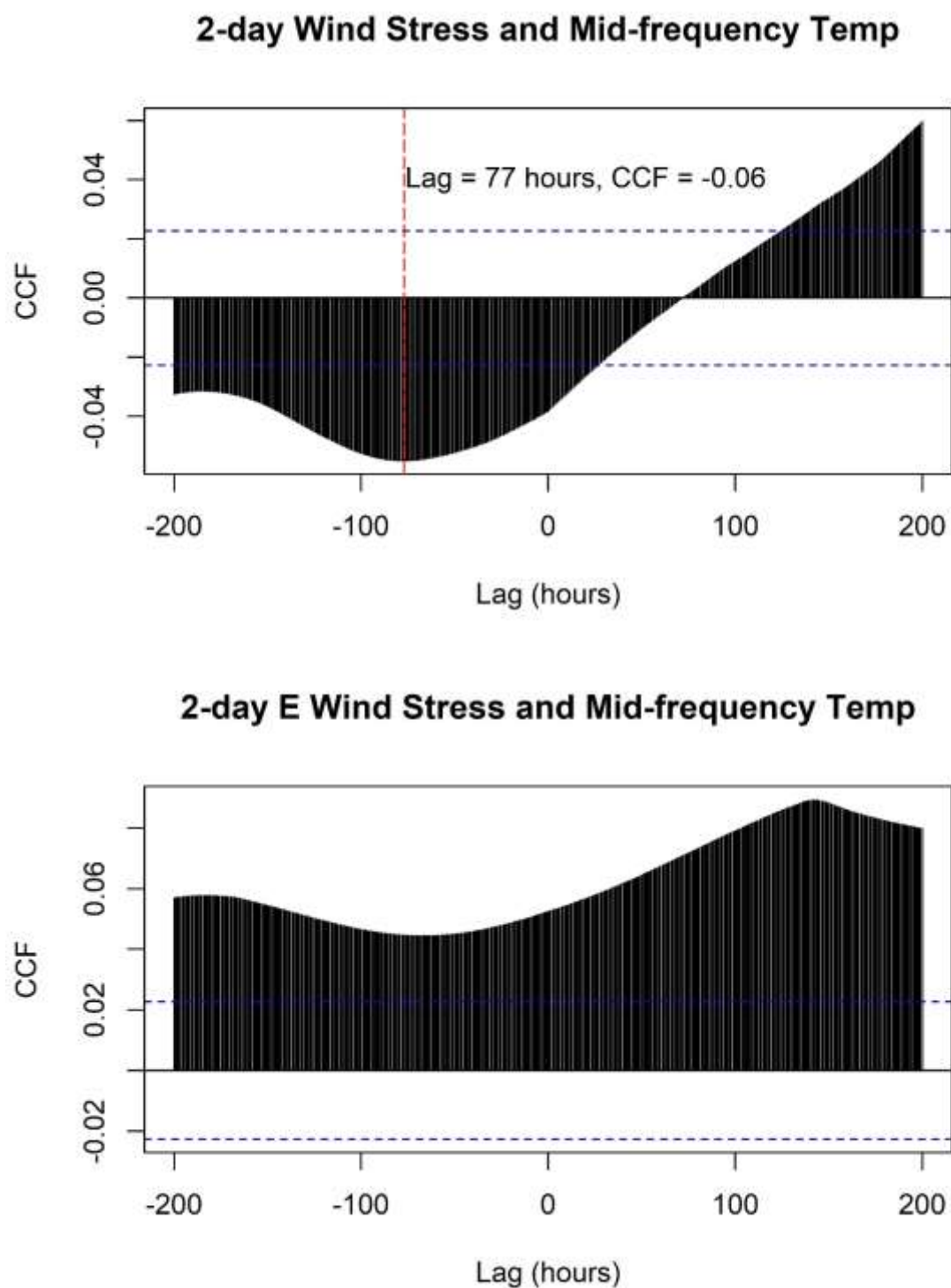
Figure S14. Correlations (CCFs) between a 17-day back-averaged wind stress and mid-frequency temperatures at the deep location at Cable Island. The top panel shows total wind stress, while the bottom panel shows easterly wind stress. Shown on each pane are the dominant lags and corresponding CCF value for each measure of temperature.

Croucher Island
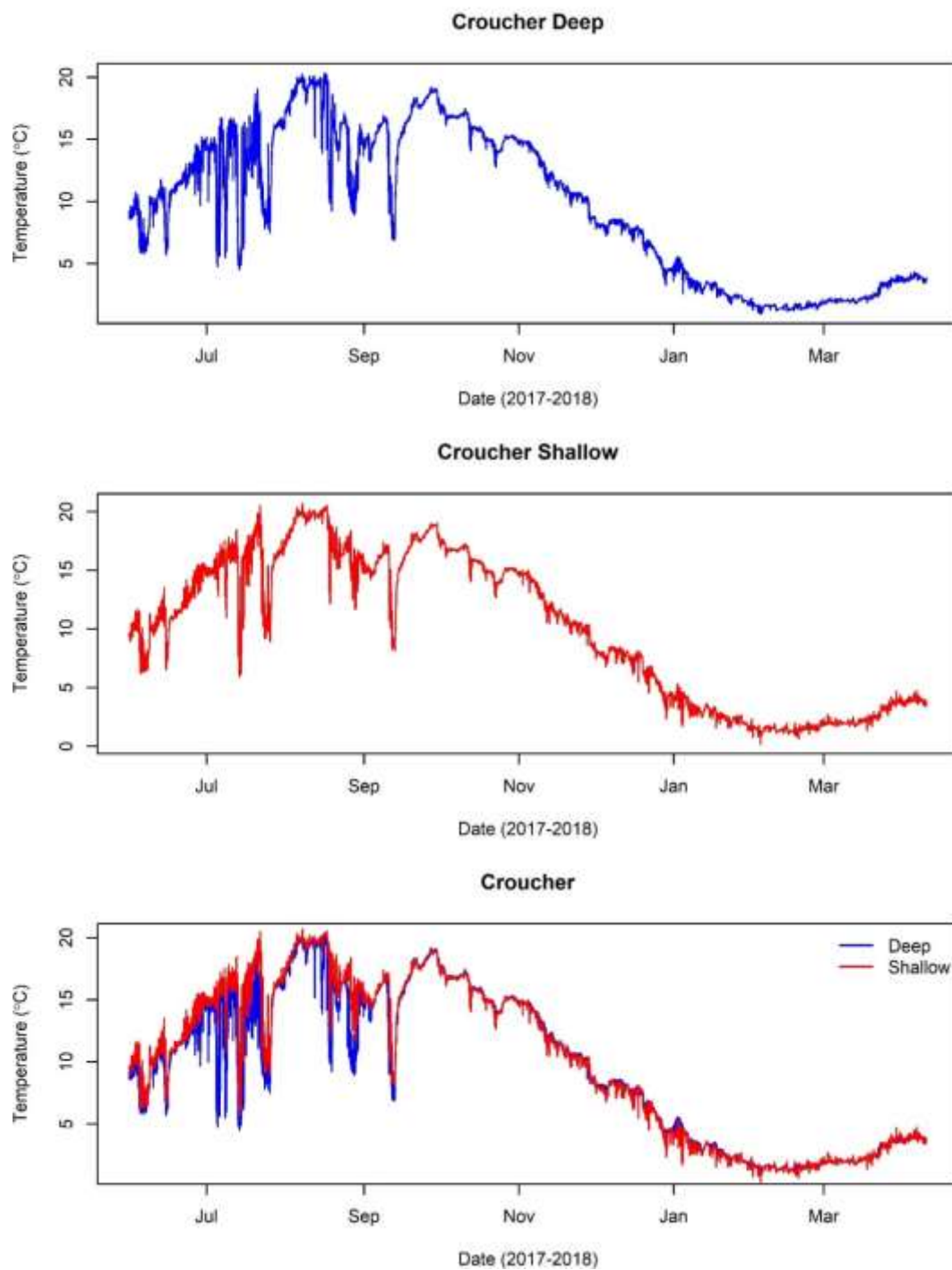
Figure S15. Temperature records at the deep and shallow locations at Croucher Island, recorded from May 31, 2017 to April 10, 2018.
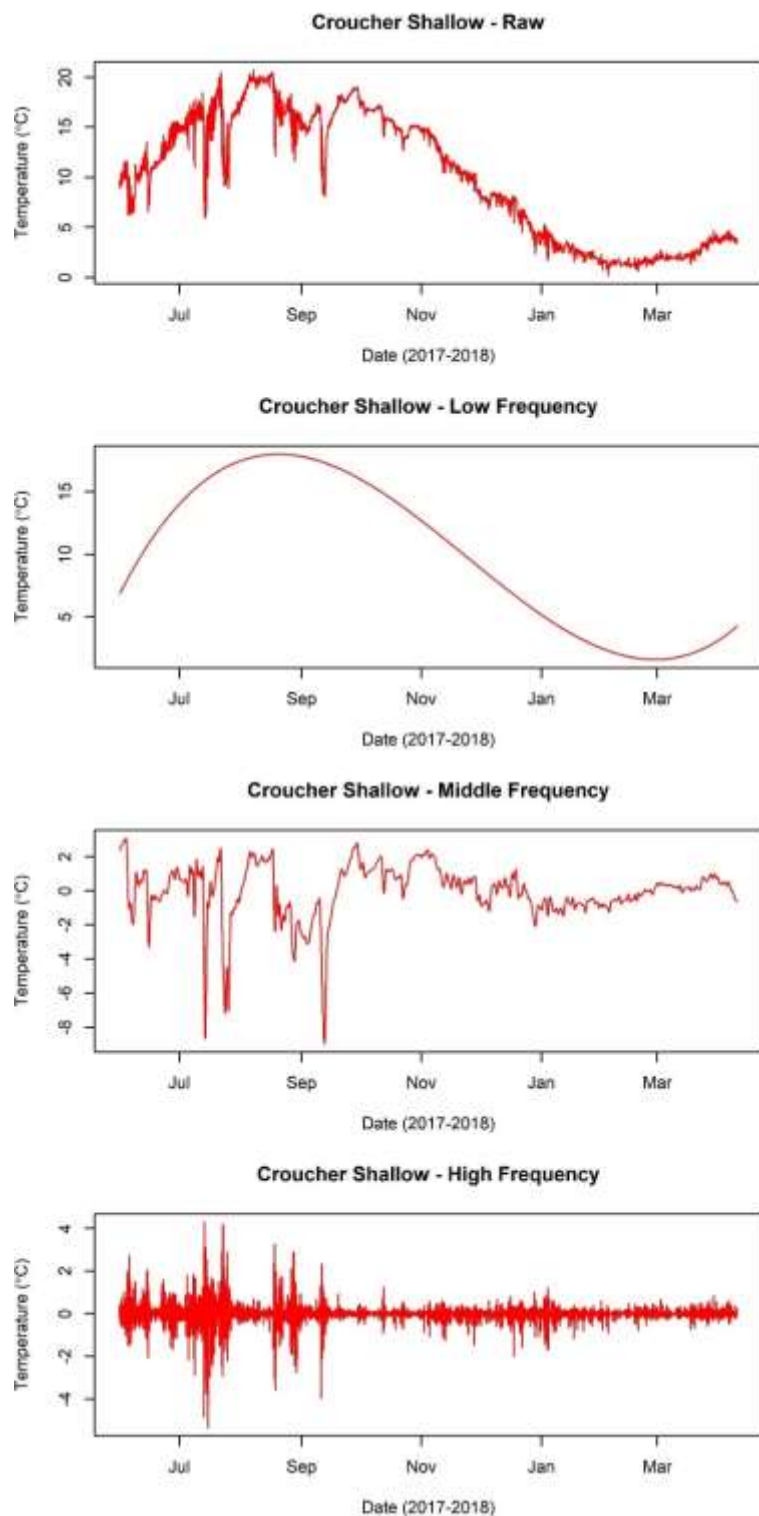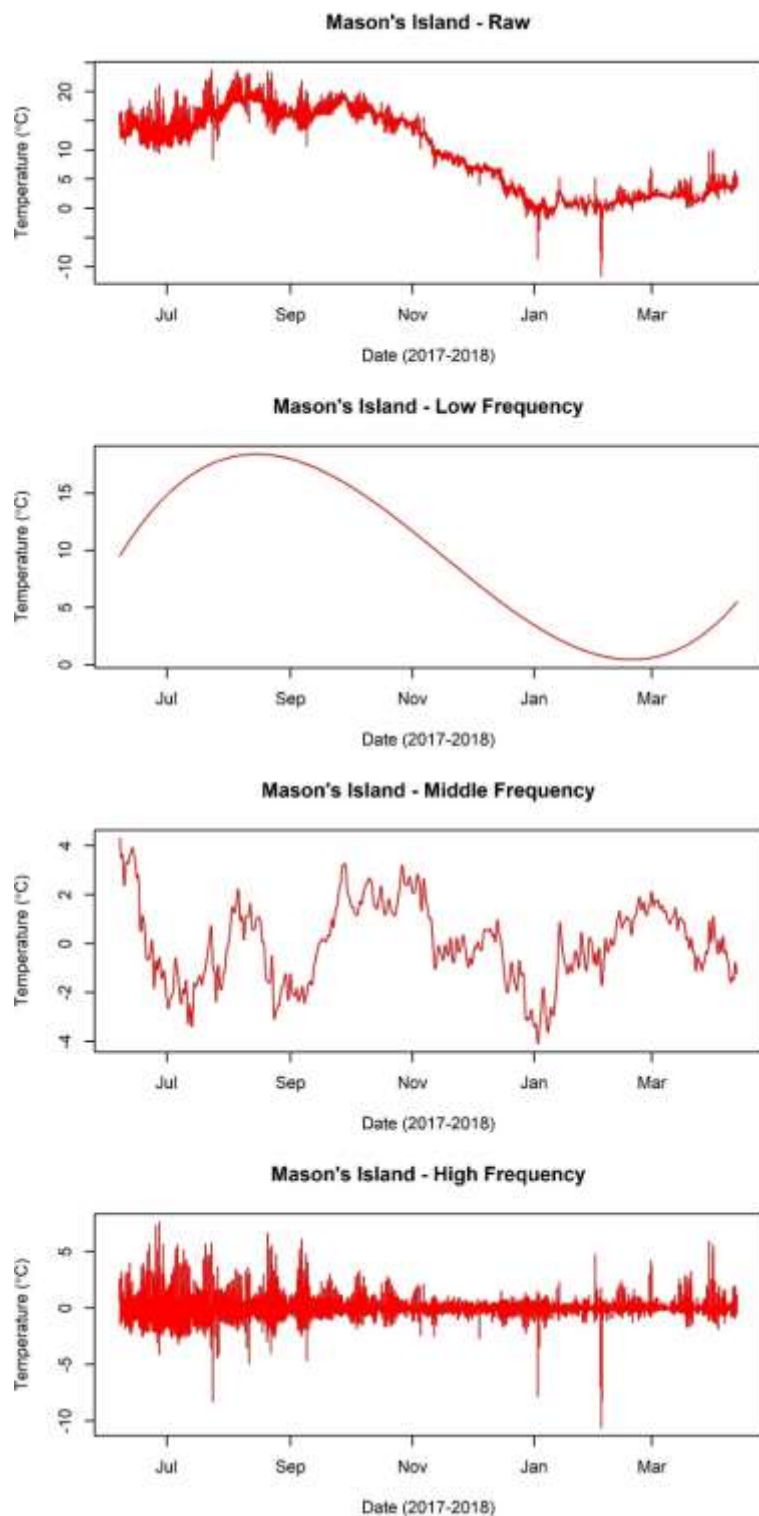
Figure S16. Raw temperatures (top panel), low (second panel), middle (third panel), and high frequency (bottom panel) temperature variability isolated at the shallow location at Croucher Island.
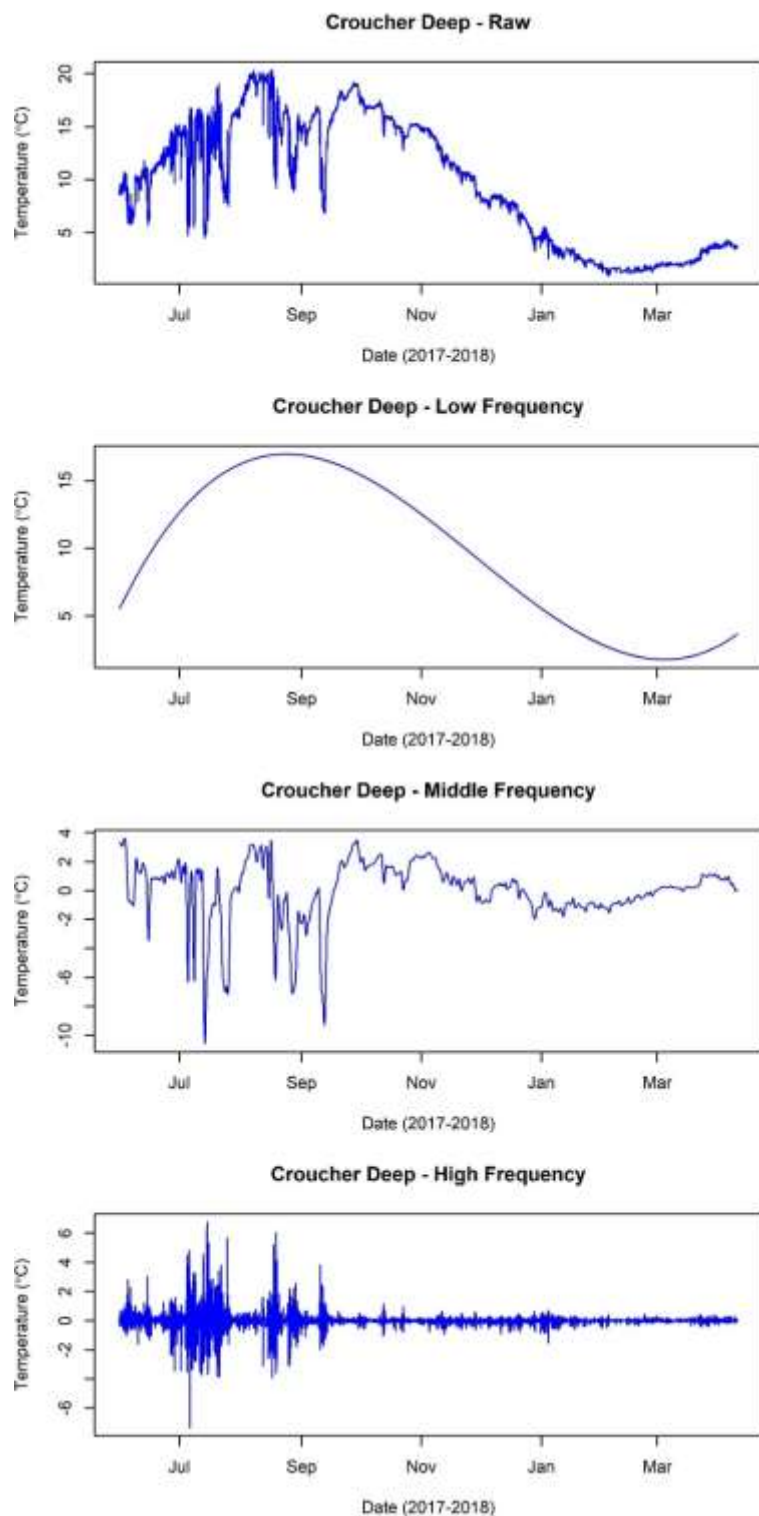
Figure S17. Raw temperatures (top panel), low (second panel), middle (third panel), and high frequency (bottom panel) temperature variability isolated at the deep location at Croucher Island.
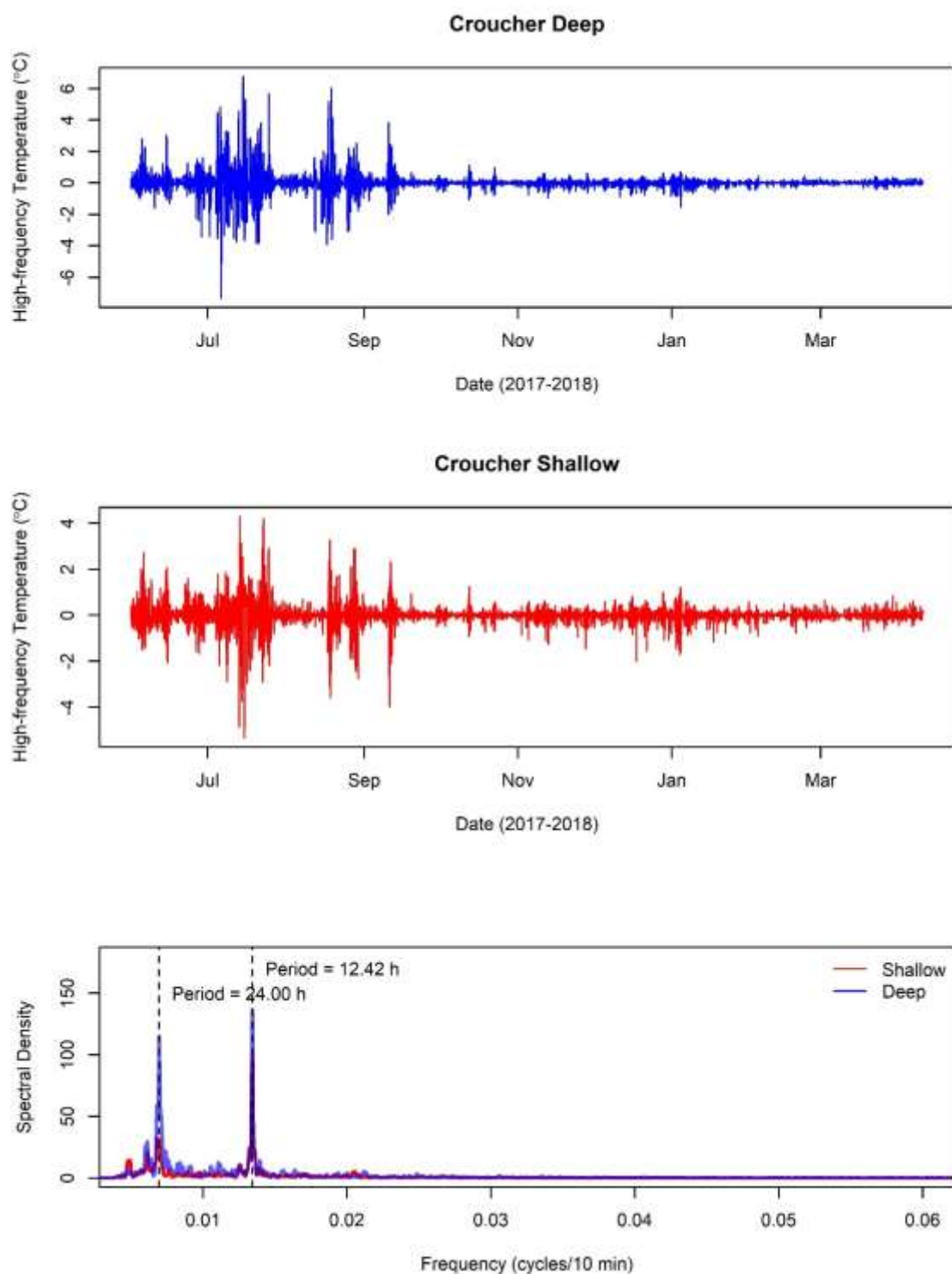
Figure S18. High frequency temperature changes at the shallow and deep locations at Croucher Island (top two panels). The bottom panel shows the results of a spectral analysis, with the dominant frequencies shown in dotted lines and the period shown in text.

Croucher Deep
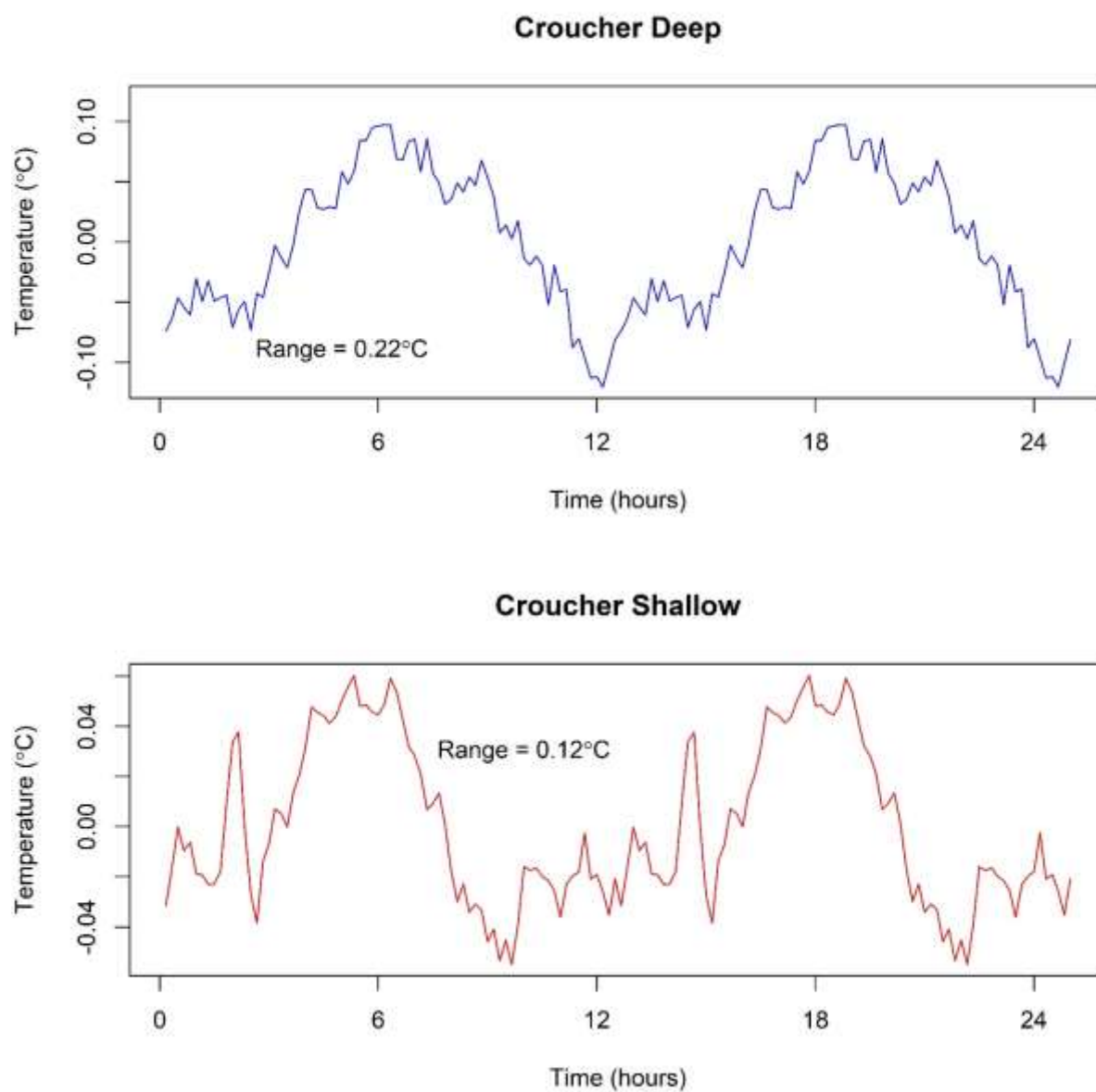
Croucher Shallow

Figure S19. Average temperature changes over the 12.42-hour tidal cycle at Croucher Island deep and shallow, calculated for the summer period (June-October 2017).

Croucher Deep
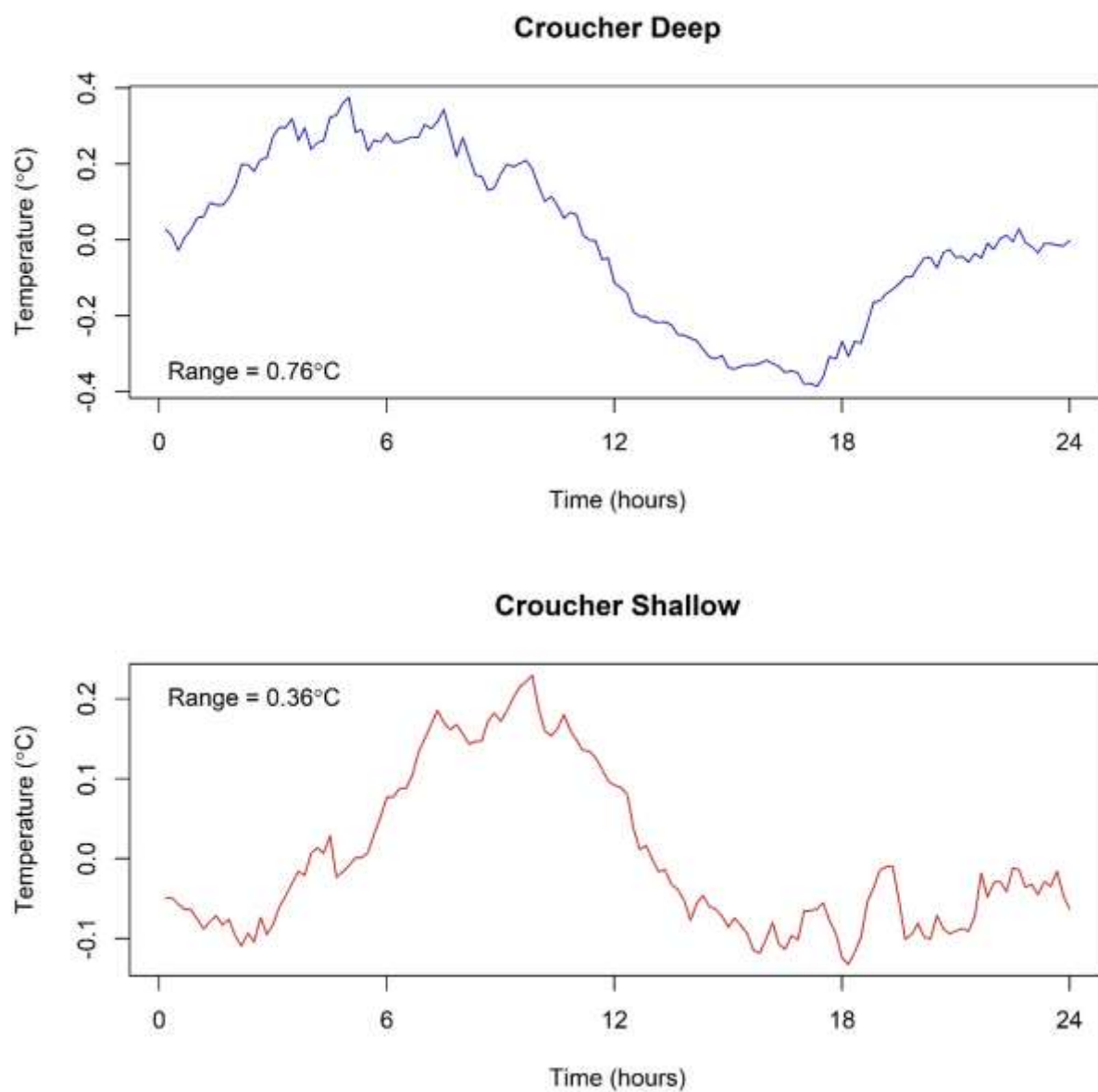
Croucher Shallow

Figure S20. Average temperature changes over the 24-hour daily heating and cooling cycle at Croucher Island deep and shallow, calculated for the summer period (June-October 2017).
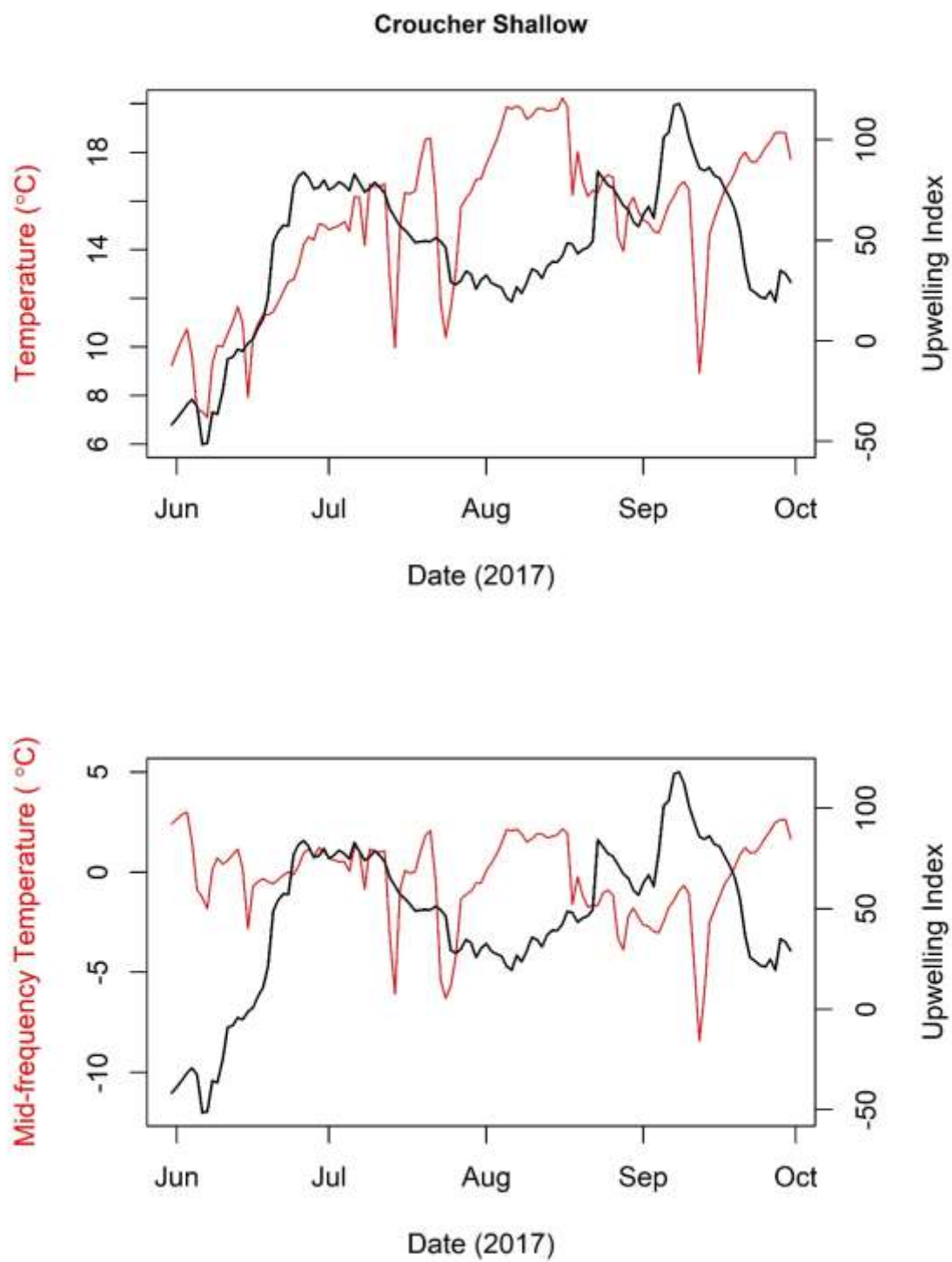
Figure S21. A 17-day back-averaged upwelling index plotted against average daily temperatures (top panel) and mid-frequency temperatures (bottom panel) at the shallow location at Croucher Island.
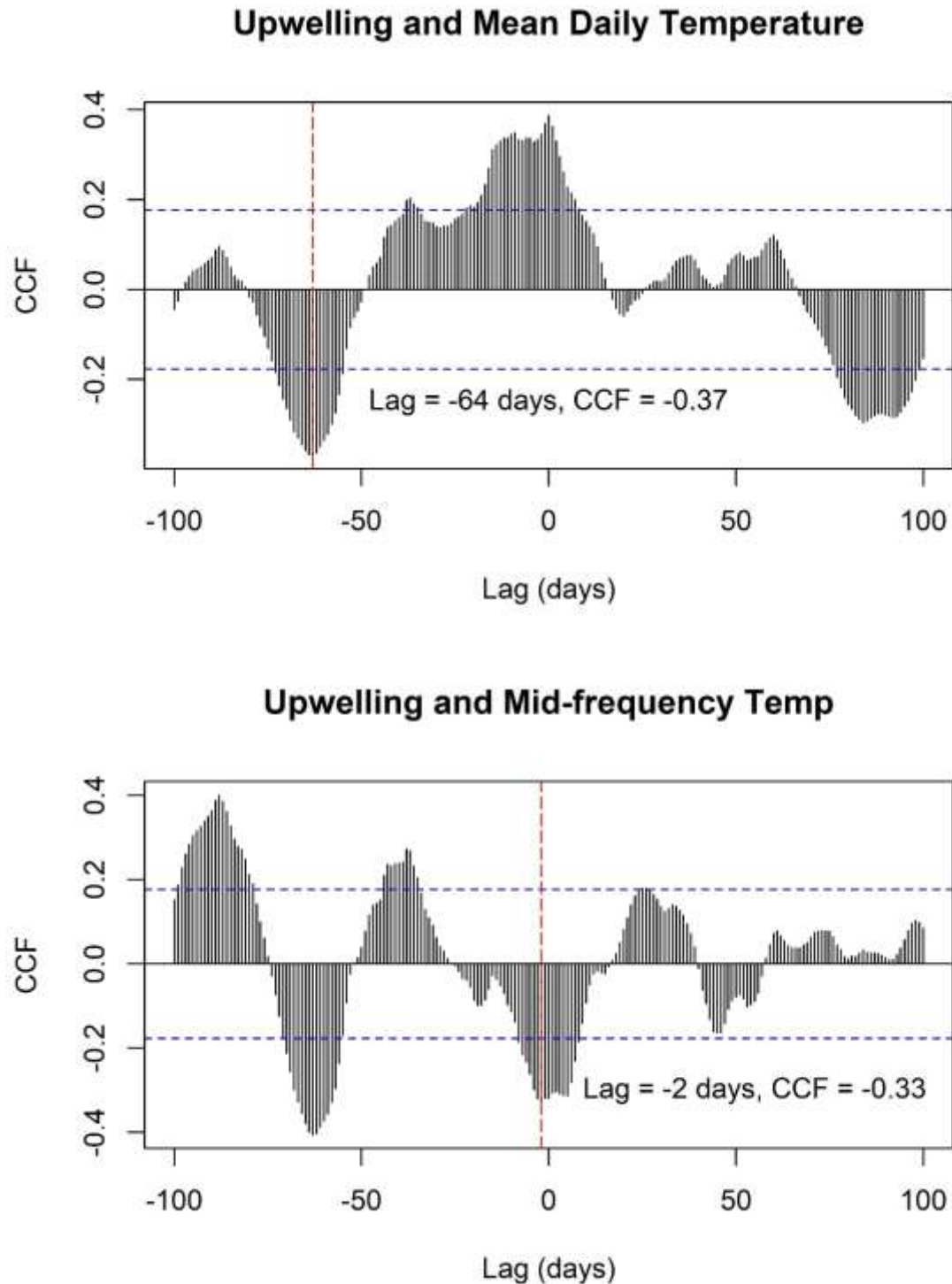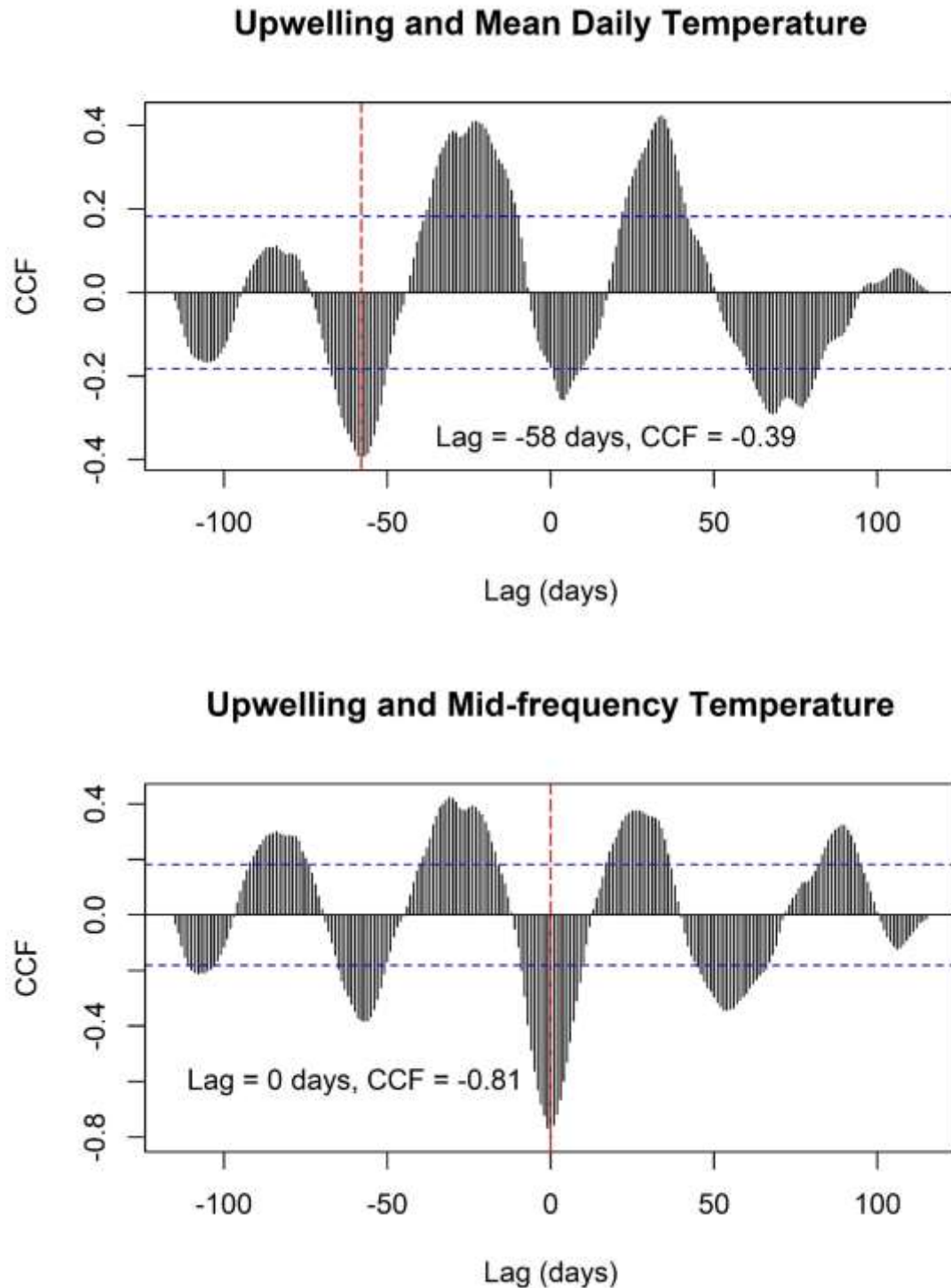
Figure S22. Correlations (CCFs) between a 17-day back-averaged upwelling index and average daily temperatures (top panel), and mid-frequency temperatures (bottom panel) at the shallow location at Croucher Island. Shown on each pane are the dominant lags and corresponding CCF value for each measure of temperature.
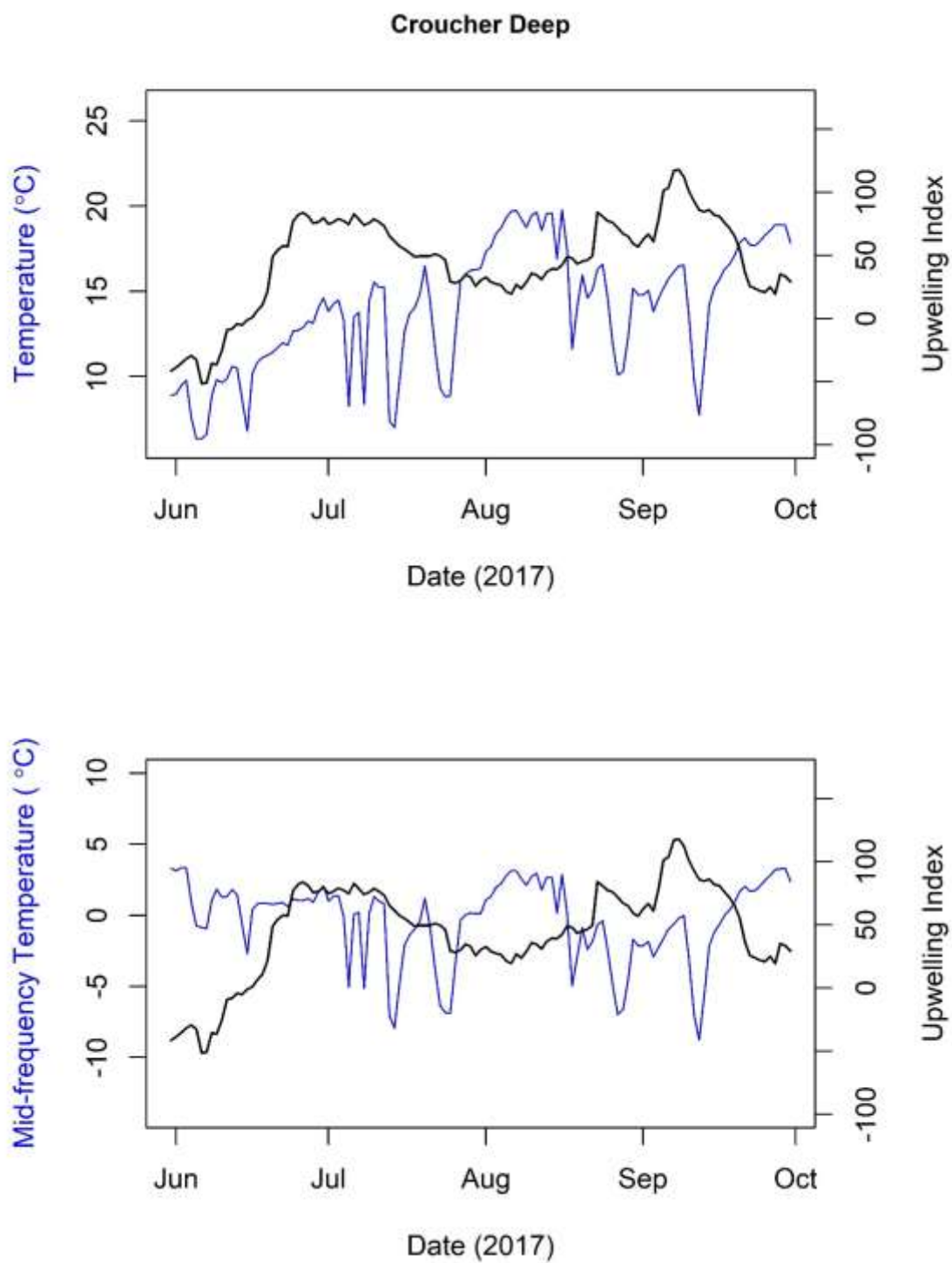
Figure S23. A 17-day back-averaged upwelling index plotted against average daily temperatures (top panel) and mid-frequency temperatures (bottom panel) at the deep location at Croucher Island.

Upwelling and Mean Daily Temperature

Upwelling and Mid-frequency Temperature
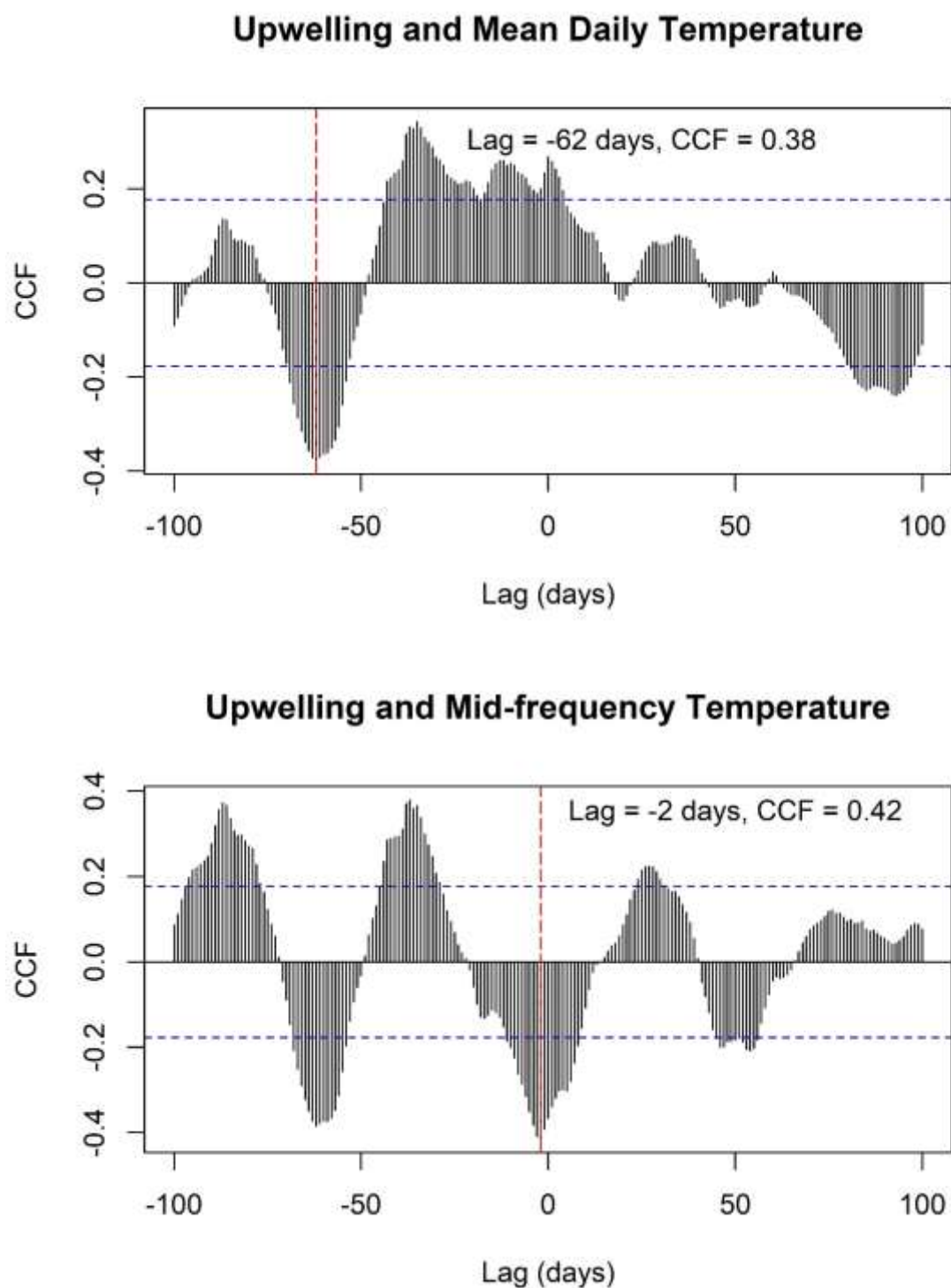
Figure S24. Correlations (CCFs) between a 17-day back-averaged upwelling index and average daily temperatures (top panel), and mid-frequency temperatures (bottom panel) at the deep location at Croucher Island. Shown on each pane are the dominant lags and corresponding CCF value for each measure of temperature.
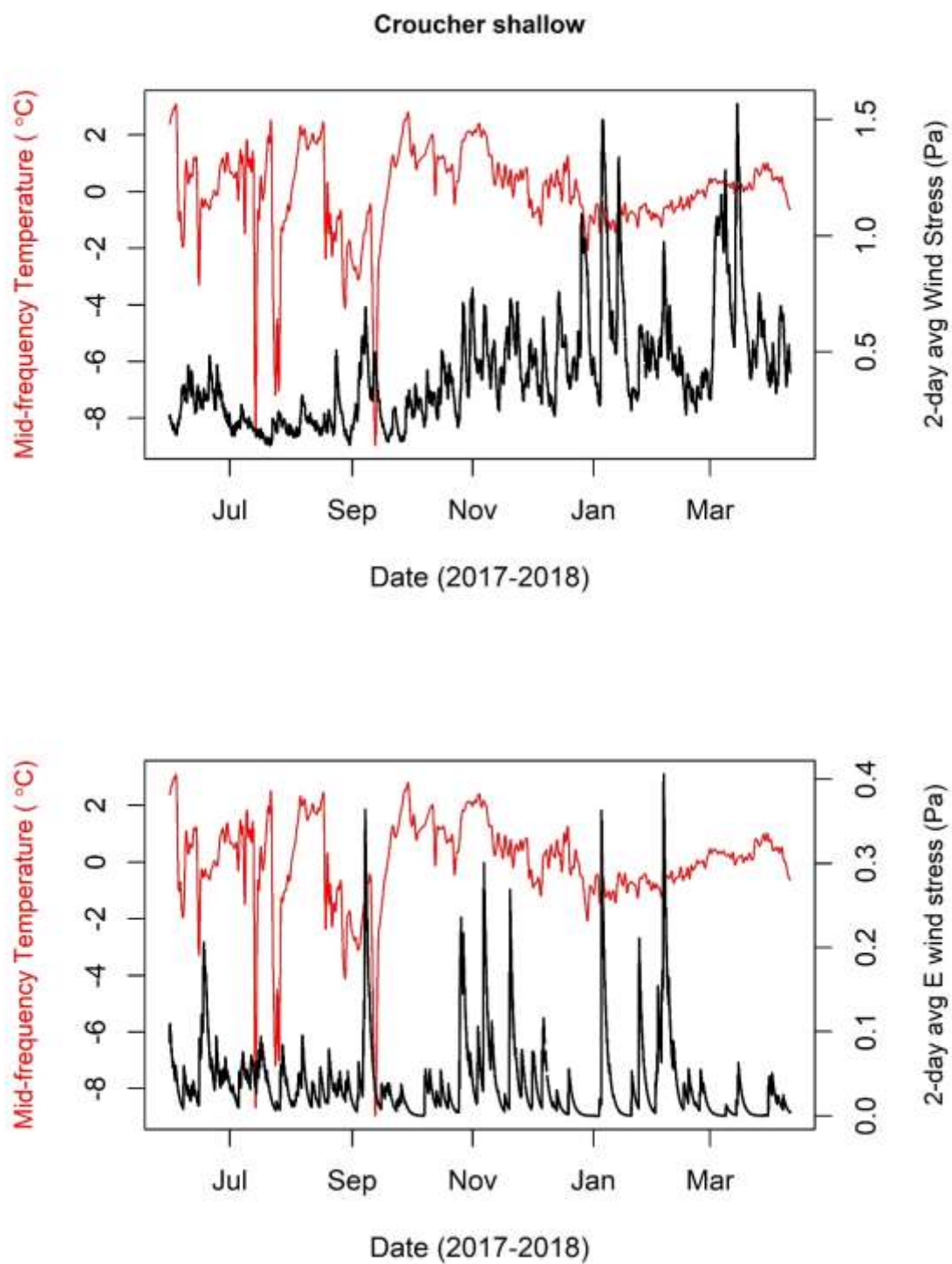
Croucher shallow

Figure S25. 2-day back-averaged wind stress plotted against mid-frequency temperatures at the shallow location at Croucher Island. The top panel shows total wind stress, while the bottom panel shows easterly wind stress.

2-day Wind Stress and Mid-frequency Temp

Lag = -173 hours, CCF = -0.05

2-day E Wind Stress and Mid-frequency Temp

Lag = -112 hours, CCF = -0.166
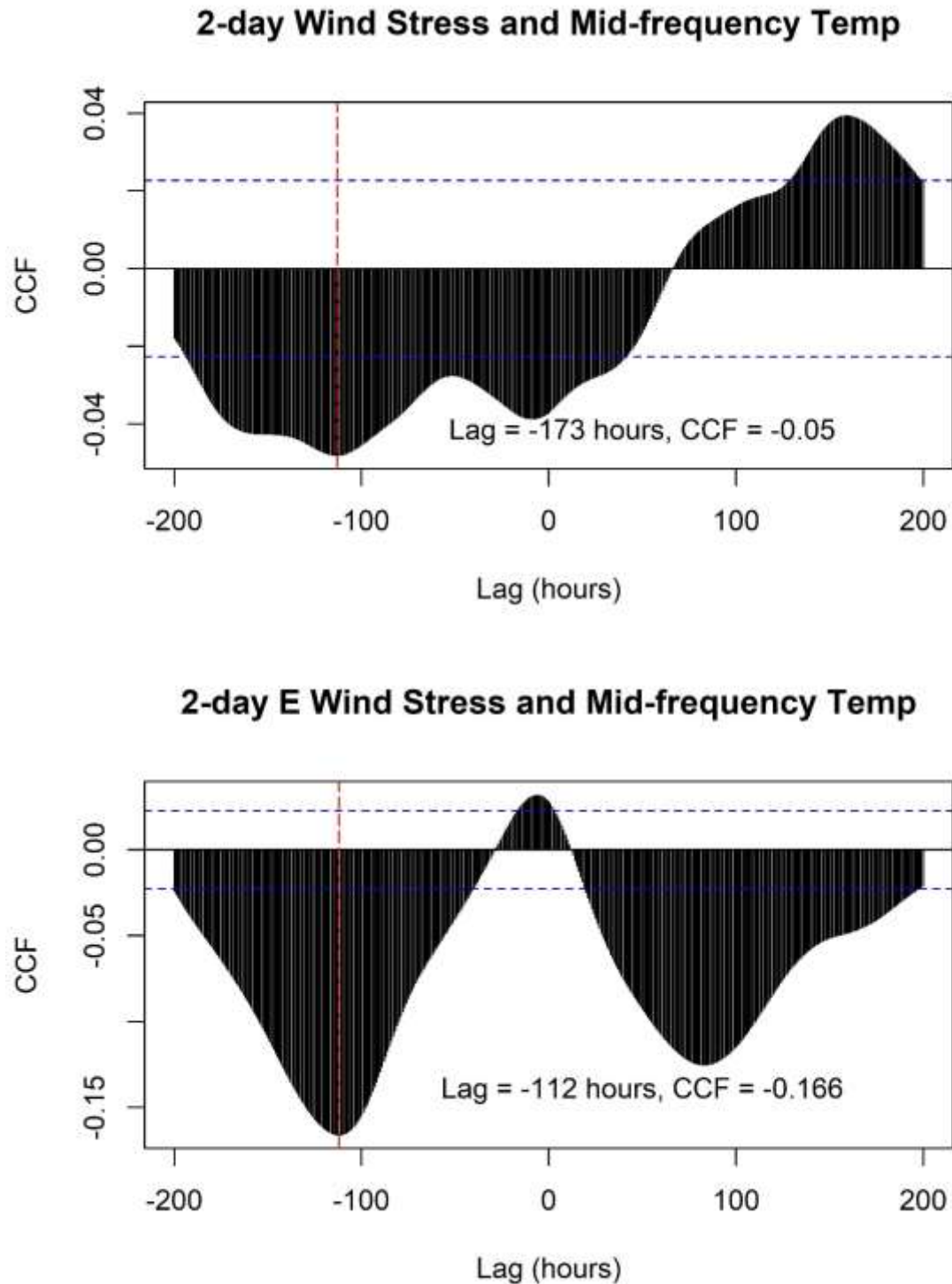
Figure S26. Correlations (CCFs) between a 2-day back-averaged wind stress and mid-frequency temperatures at the shallow location at Croucher Island. The top panel shows total wind stress, while the bottom panel shows easterly wind stress. Shown on each pane are the dominant lags and corresponding CCF value for each measure of temperature.
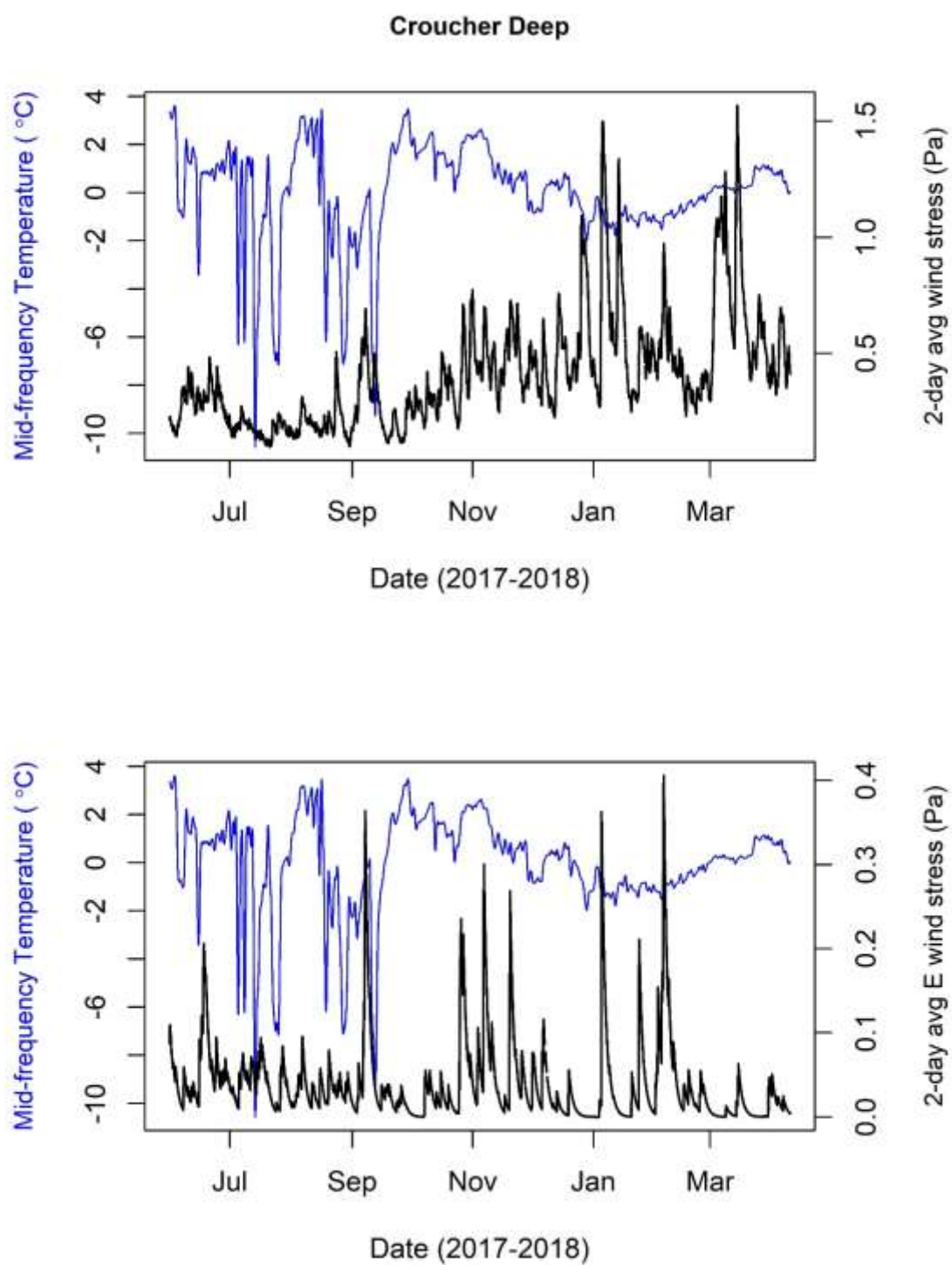
Croucher Deep

Figure S27. 2-day back-averaged wind stress plotted against mid-frequency temperatures at the deep location at Croucher Island. The top panel shows total wind stress, while the bottom panel shows easterly wind stress.

2-day Wind Stress and Mid-frequency Temp

Lag = -113 hours, CCF = -0.036

2-day E Wind Stress and Mid-frequency Temp

Lag = -115 hours, CCF = -0.148
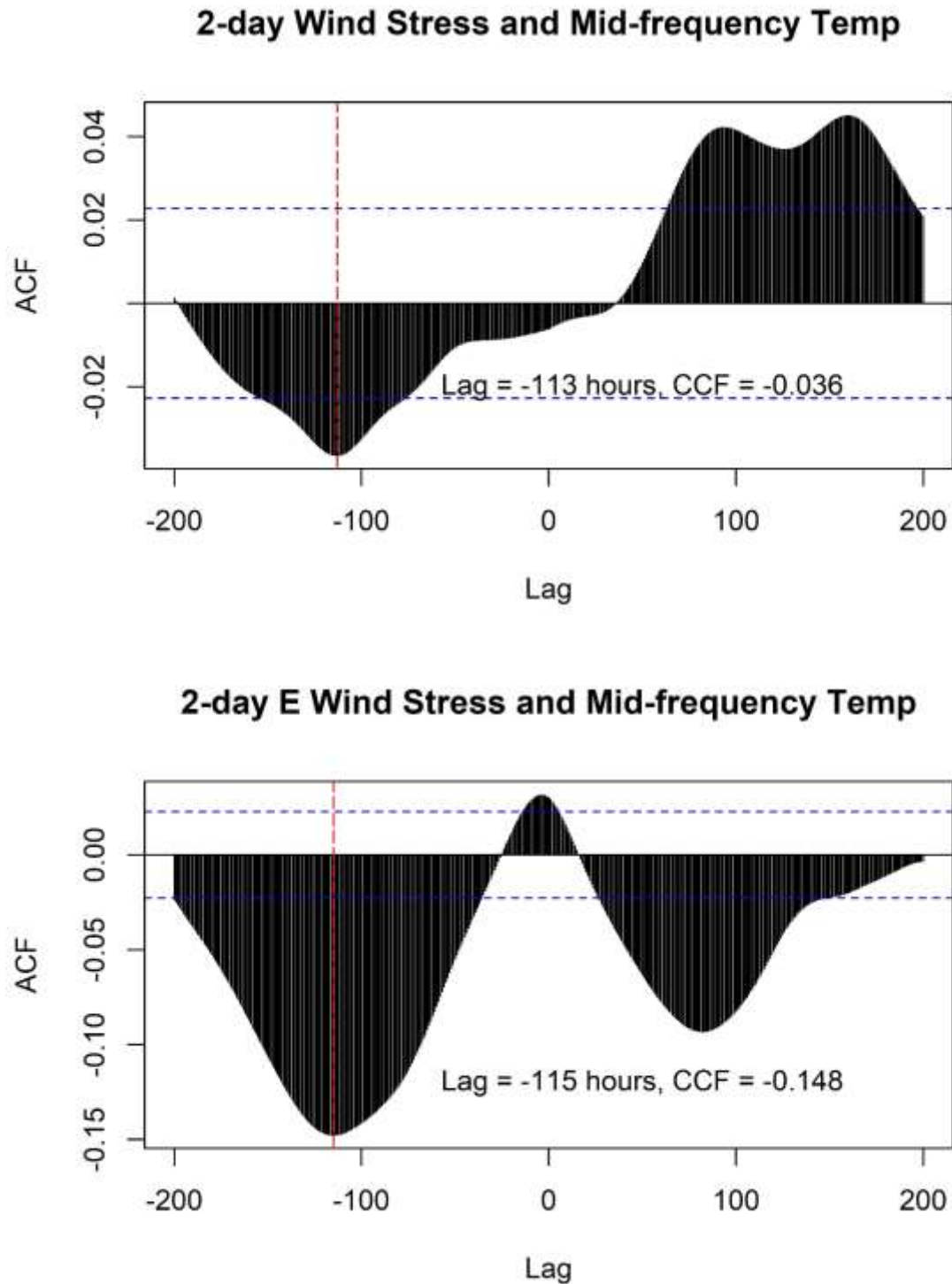
Figure S28. Correlations (CCFs) between a 2-day back-averaged wind stress and mid-frequency temperatures at the deep location at Croucher Island. The top panel shows total wind stress, while the bottom panel shows easterly wind stress. Shown on each pane are the dominant lags and corresponding CCF value for each measure of temperature.
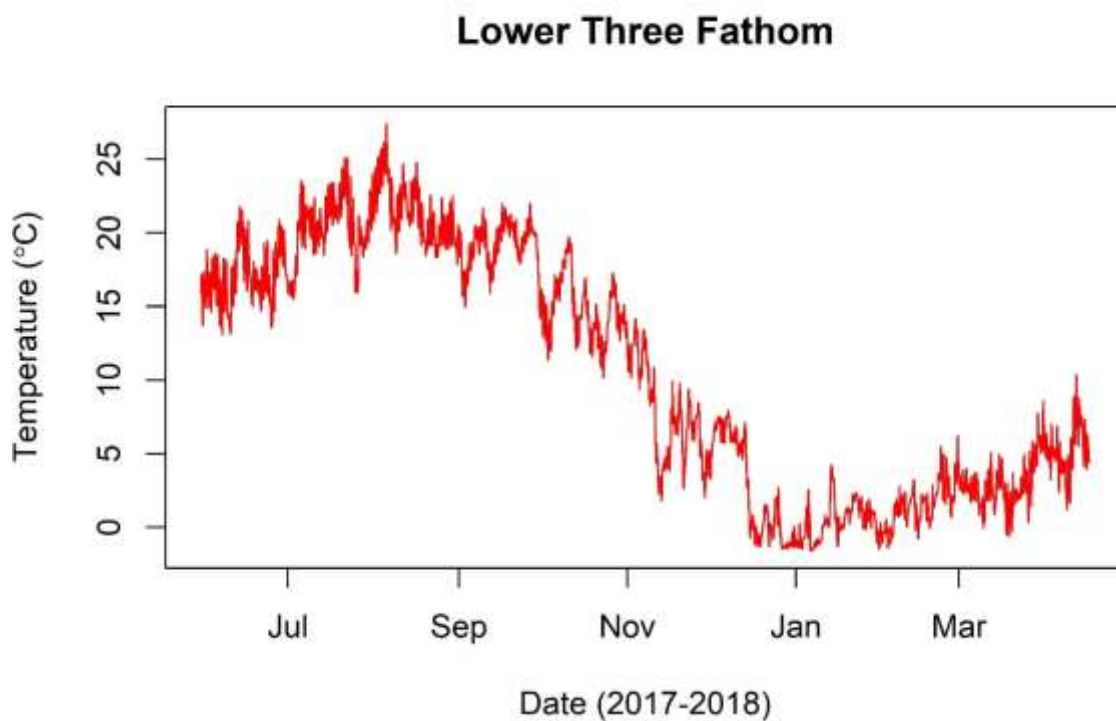
Lower Three Fathom

Figure S29. Temperature records at Lower Three Fathom, recorded from May 30, 2017 to April 17, 2018.
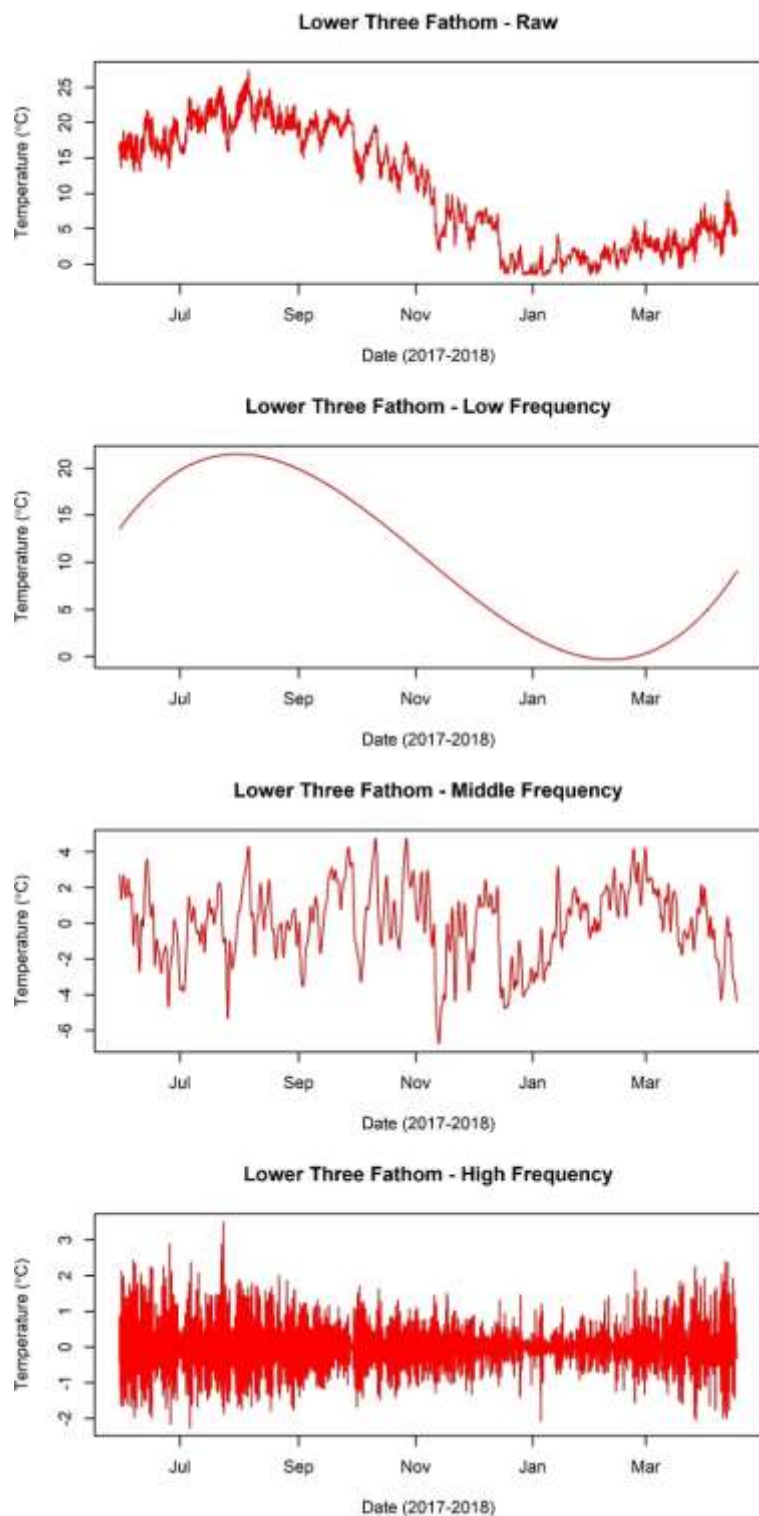
Figure S30. Raw temperatures (top panel), low (second panel), middle (third panel), and high frequency (bottom panel) temperature variability isolated at Lower Three Fathom.
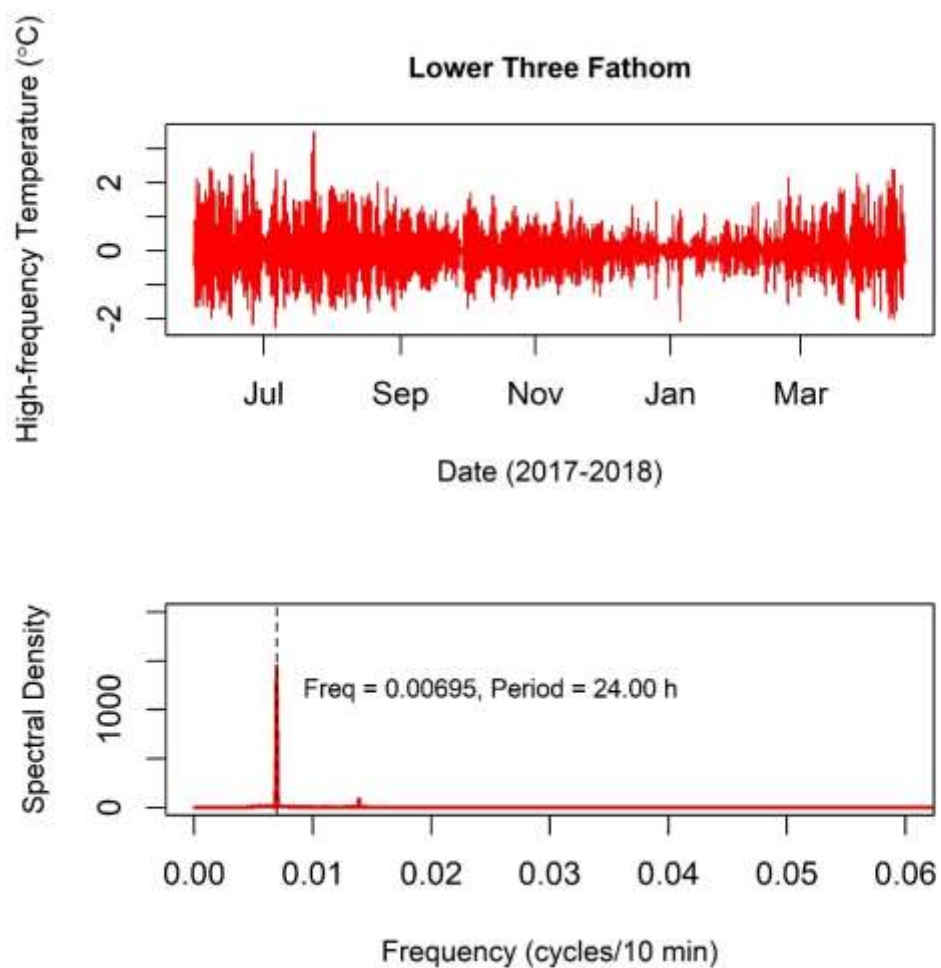
Figure S31. High frequency temperature changes at Lower Three Fathom. The bottom panel shows the results of a spectral analysis, with the dominant frequencies shown as a dotted line and the period shown in text.
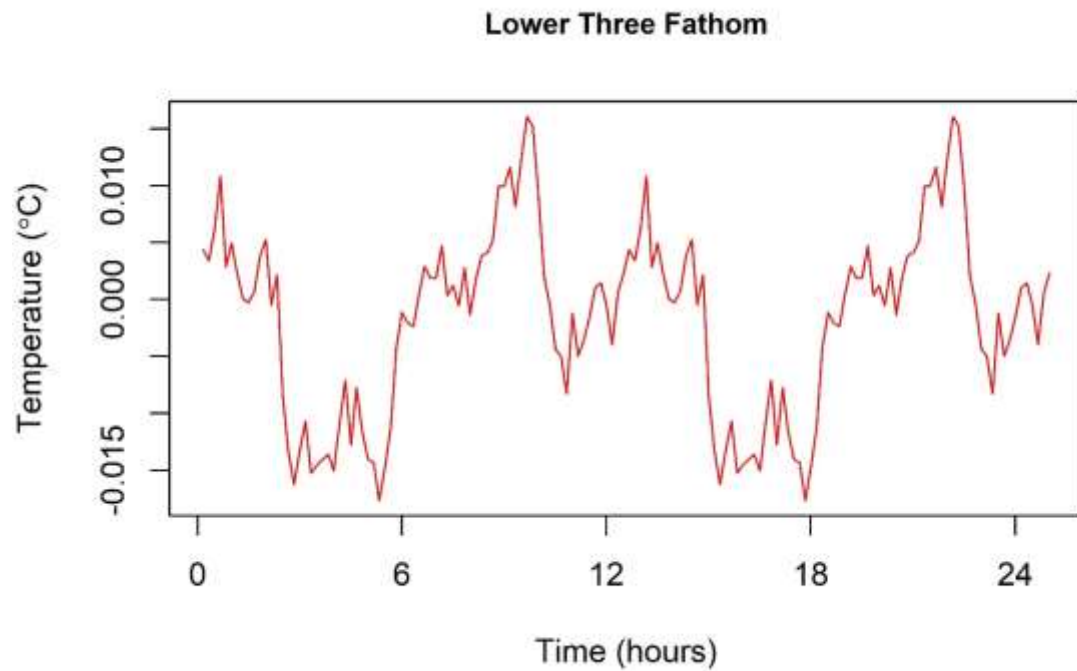
Lower Three Fathom

Figure S32. Average temperature changes over the 12.42-hour tidal cycle at Lower Three Fathom, calculated for the summer period (June-October 2017).
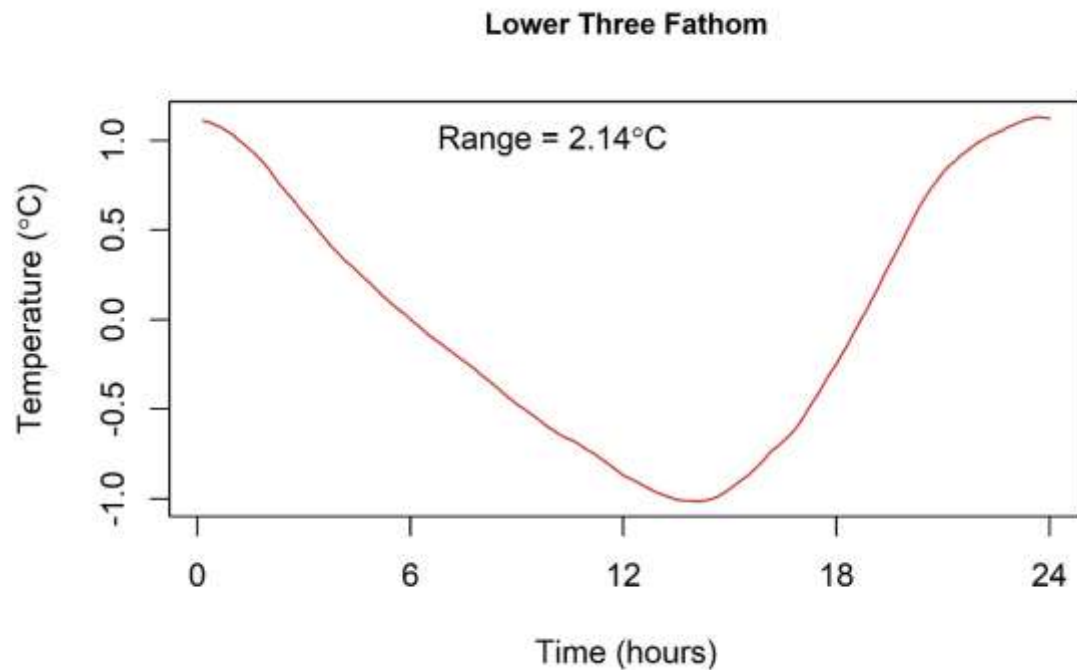
Lower Three Fathom

Figure S33. Average temperature changes over the 24-hour daily heating and cooling cycle at Lower Three Fathom, calculated for the summer period (June-October 2017).
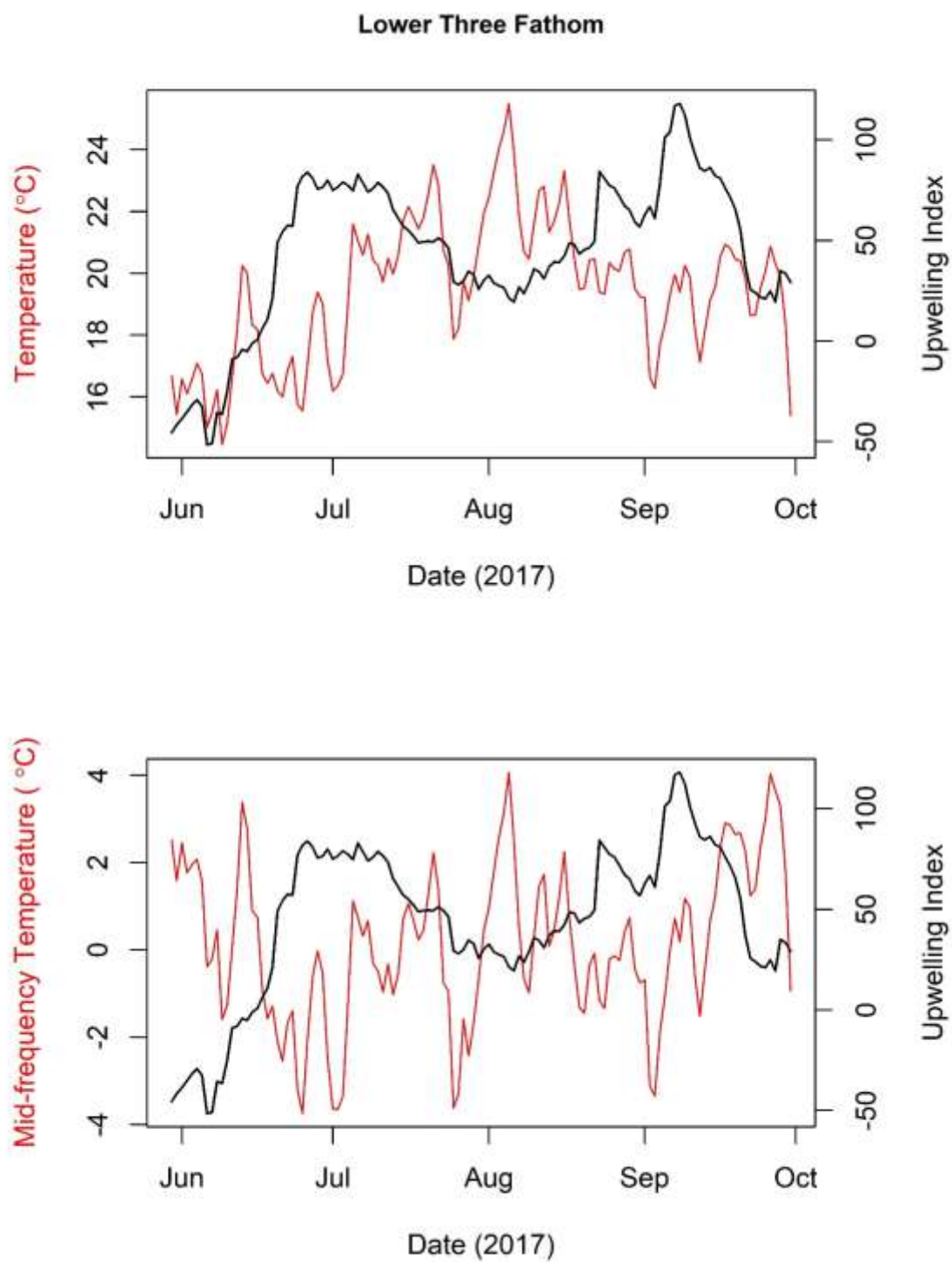
Figure S34. A 17-day back-averaged upwelling index plotted against average daily temperatures (top panel) and mid-frequency temperatures (bottom panel) at Lower Three Fathom.

Upwelling and Mean Daily Temperature

Lag = -61 days, CCF = 0.39

Upwelling and Mid-frequency Temperature

Lag = 0 days, CCF = -0.29
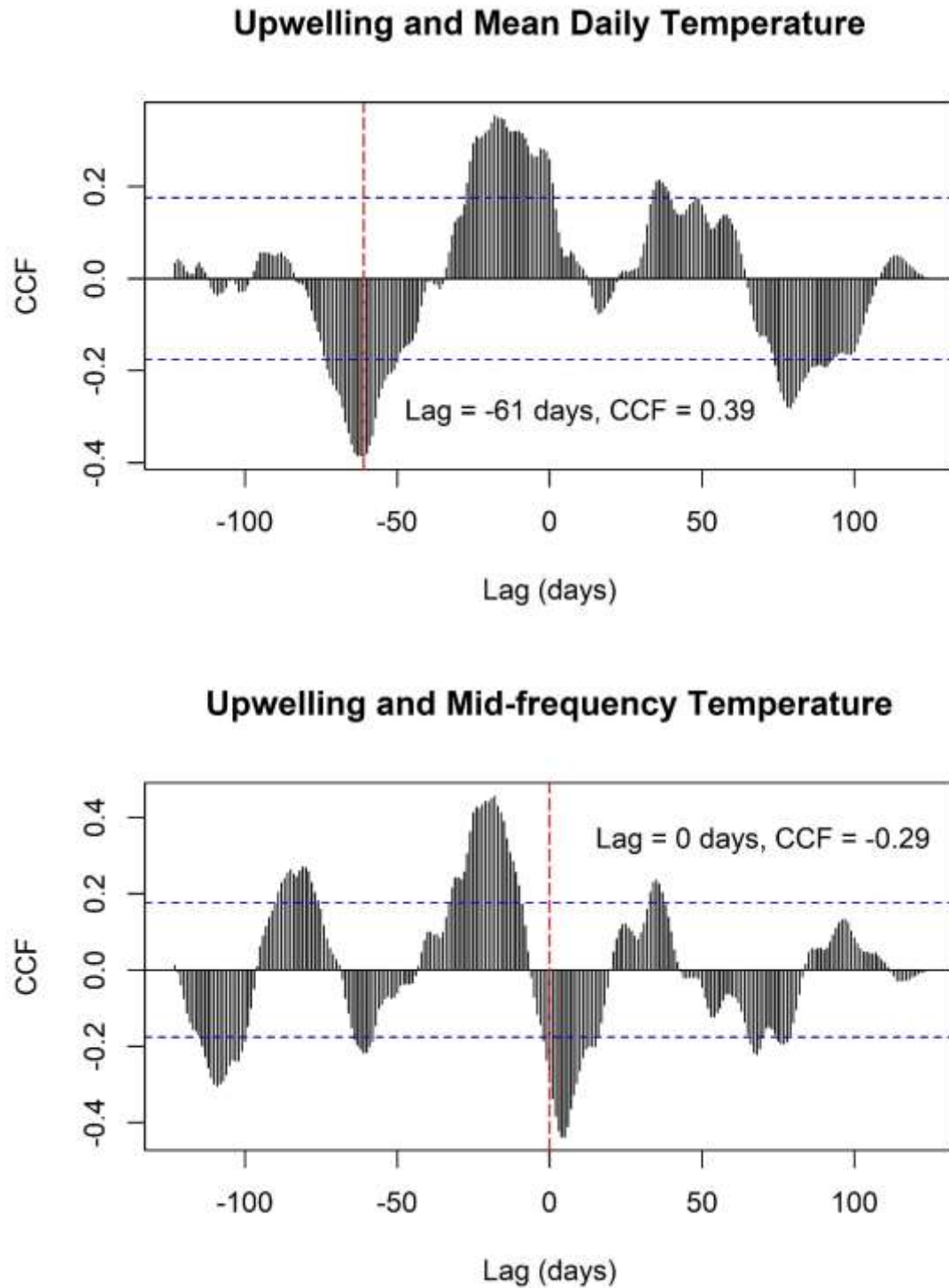
Figure S35. Correlations (CCFs) between a 17-day back-averaged upwelling index and average daily temperatures (top panel), and mid-frequency temperatures (bottom panel) at Lower Three Fathom. Shown on each pane are the dominant lags and corresponding CCF value for each measure of temperature.

Lower Three Fathom

Date (2017-2018)

Date (2017-2018)
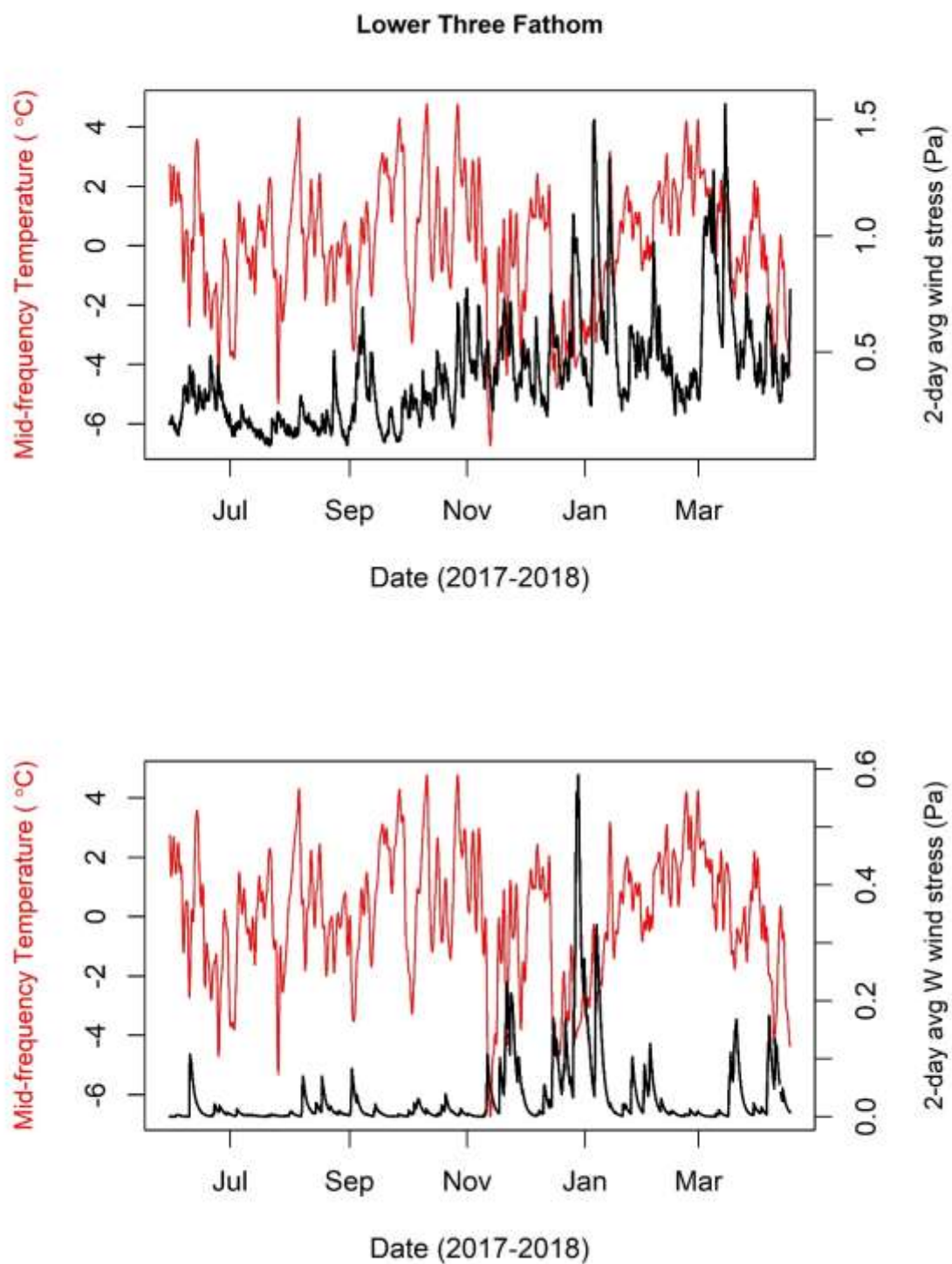
Figure S36. 2-day back-averaged wind stress plotted against mid-frequency temperatures at Lower Three Fathom. The top panel shows total wind stress, while the bottom panel shows westerly wind stress.

2-day Wind Stress and and Mid-frequency Temp

Lag = -36 hours, CCF = -0.16
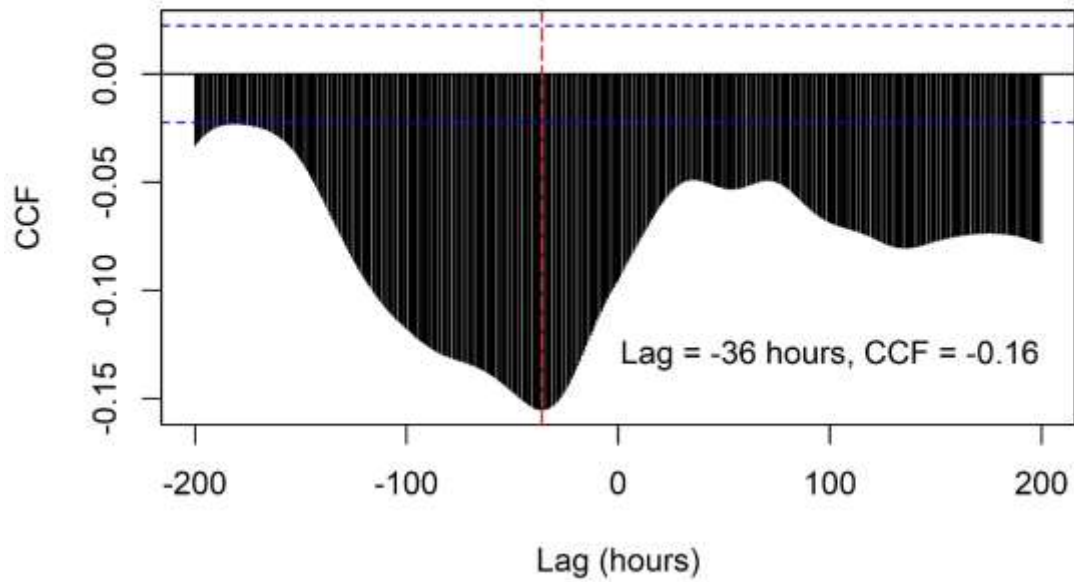
2-day W Wind Stress and Mid-frequency Temp

Lag = 0 hours, CCF = -0.45
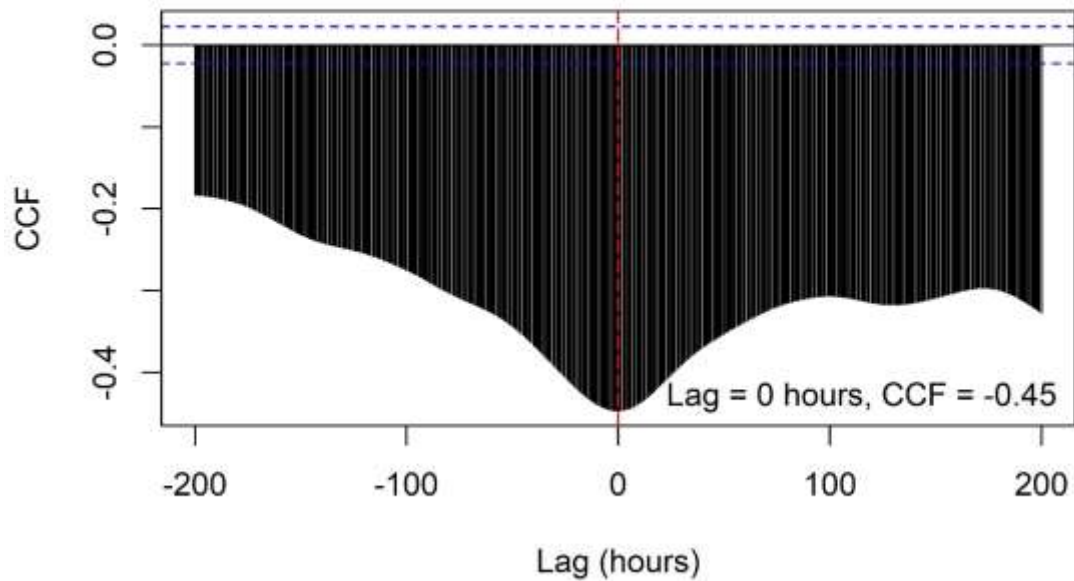
Figure S37. Correlations (CCFs) between a 2-day back-averaged wind stress and mid-frequency temperatures at Lower Three Fathom. The top panel shows total wind stress, while the bottom panel shows westerly wind stress. Shown on each pane are the dominant lags and corresponding CCF value for each measure of temperature.

La Have
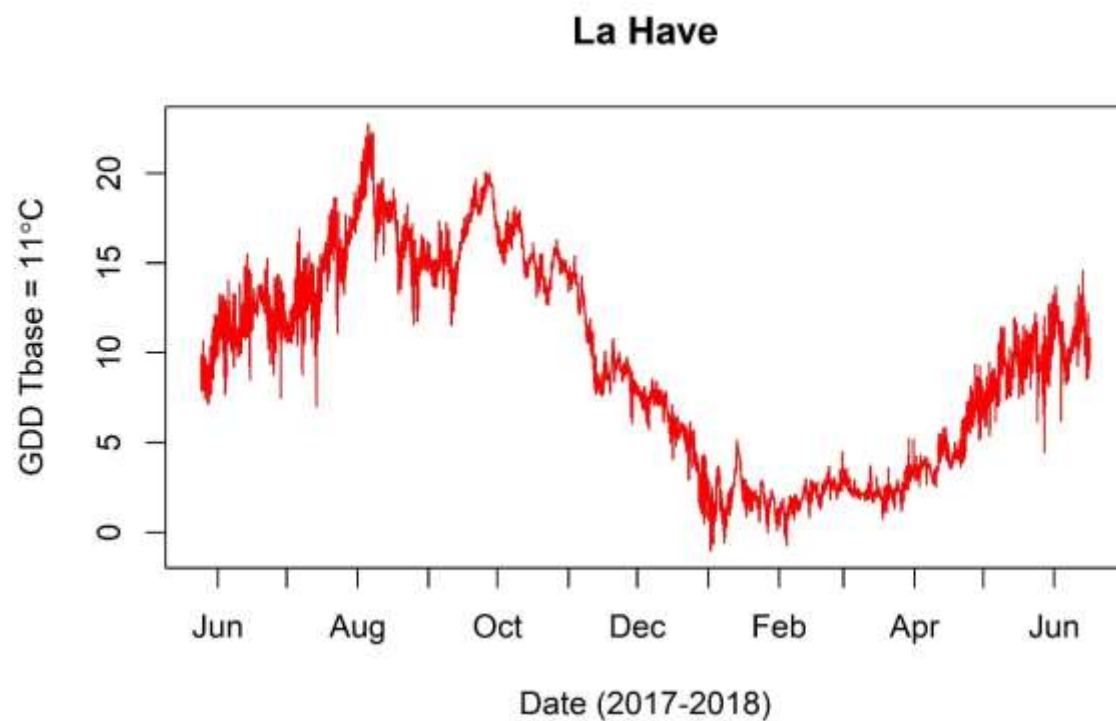
La Have

Figure S38. Temperature records at La Have, recorded from May 24, 2017 to June 16, 2018.

Figure S39. Raw temperatures (top panel), low (second panel), middle (third panel), and high frequency (bottom panel) temperature variability isolated at La Have.
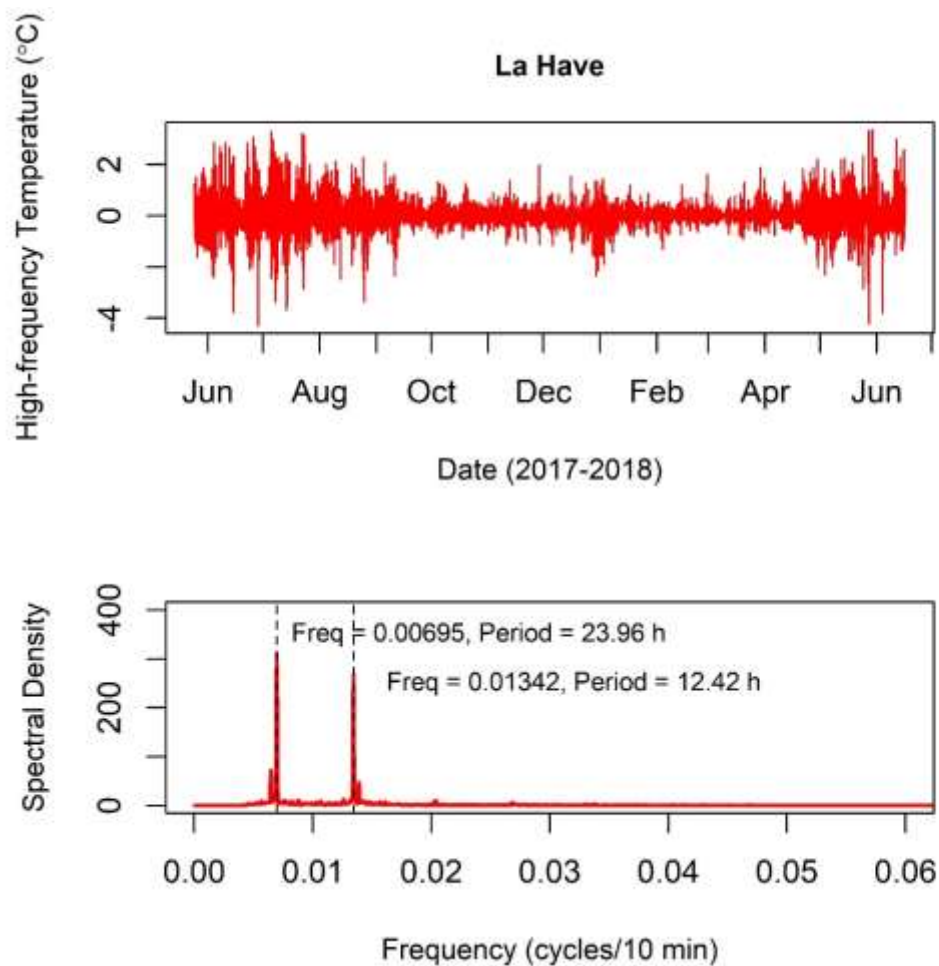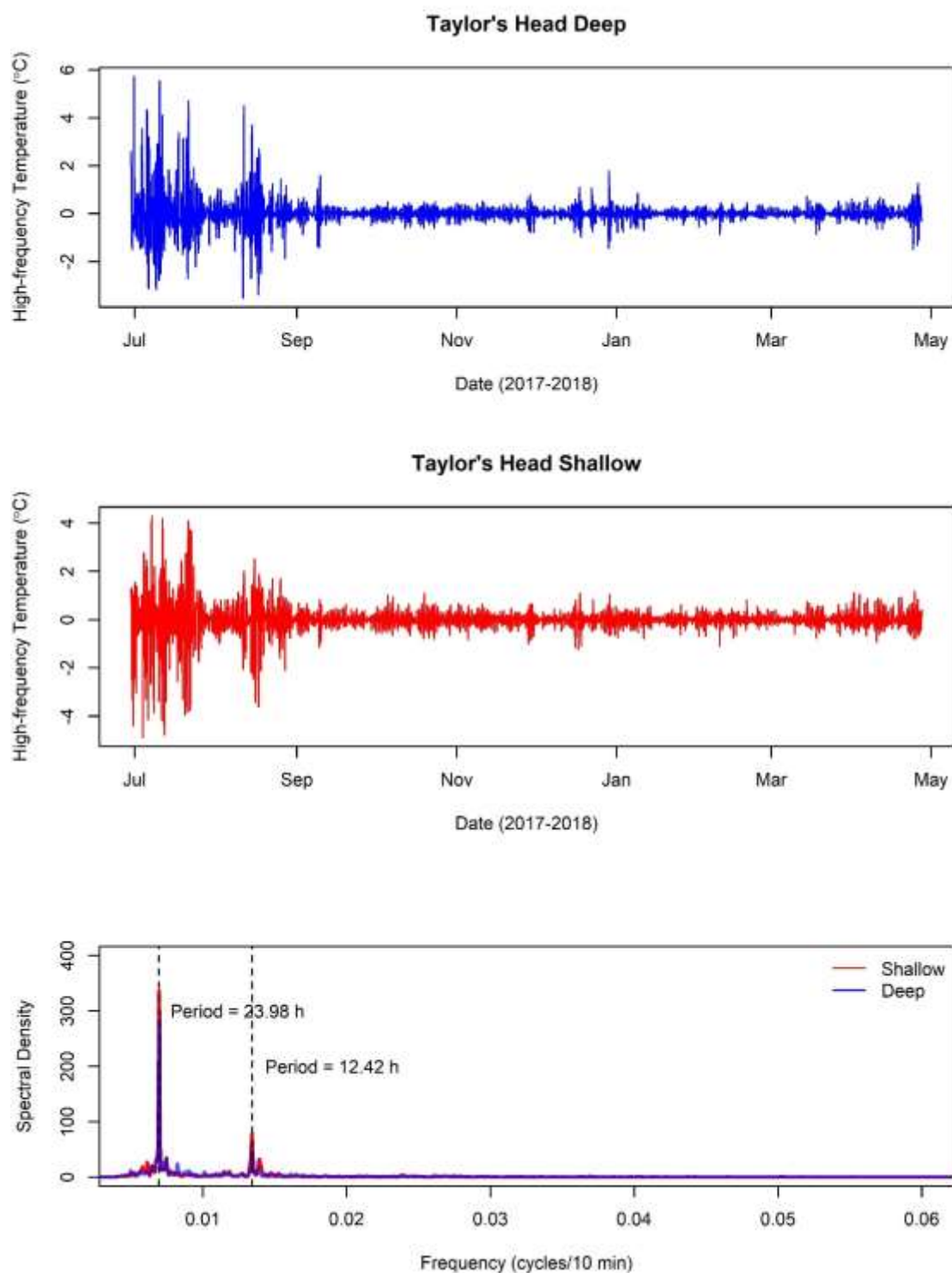
Figure S40. High frequency temperature changes at La Have. The bottom panel shows the results of a spectral analysis, with the dominant frequencies shown with dotted lines and the period shown in text.
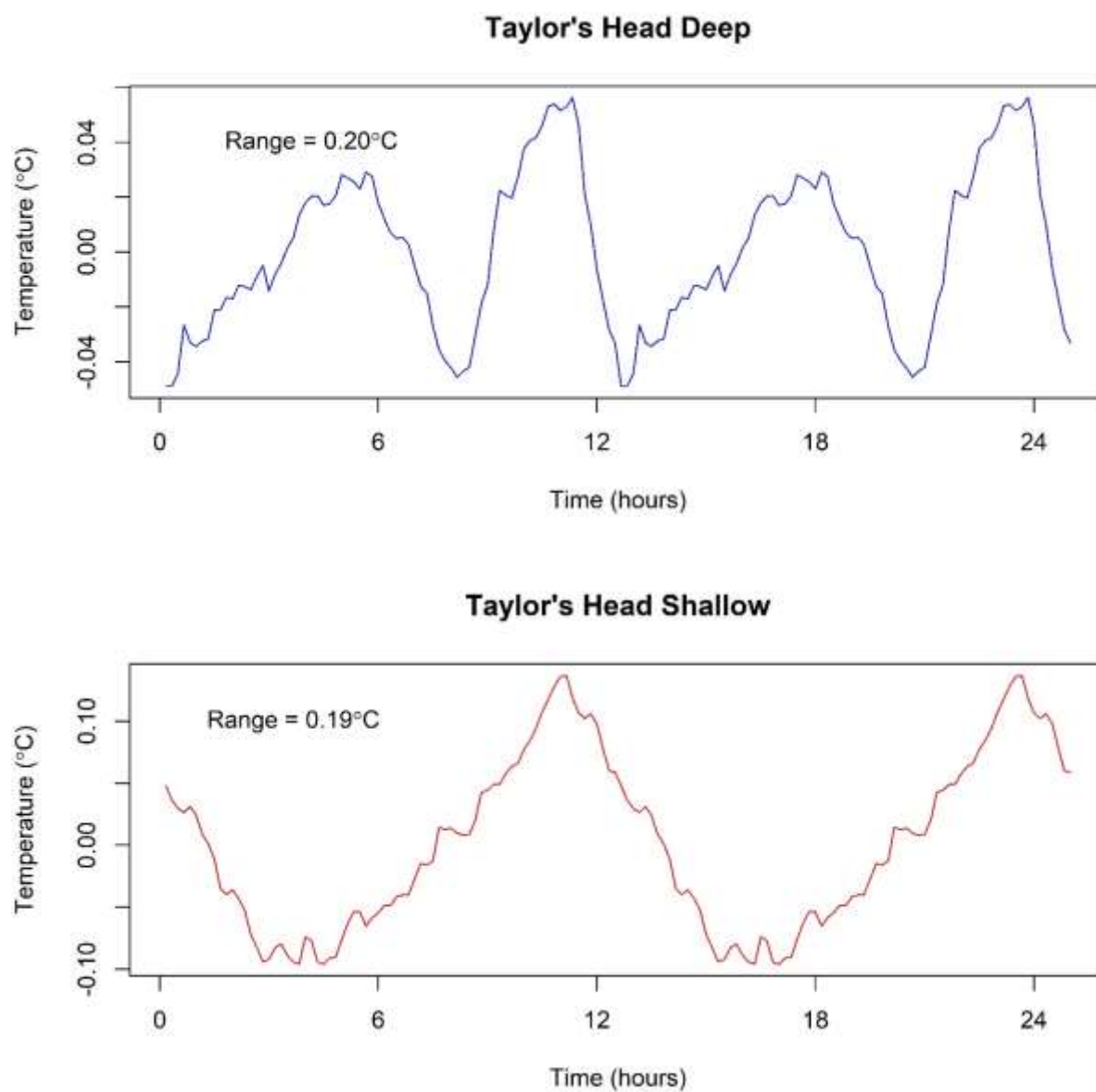
La Have

Figure S41. Average temperature changes over the 12.42-hour tidal cycle at La Have, calculated for the summer period (June-October 2017).
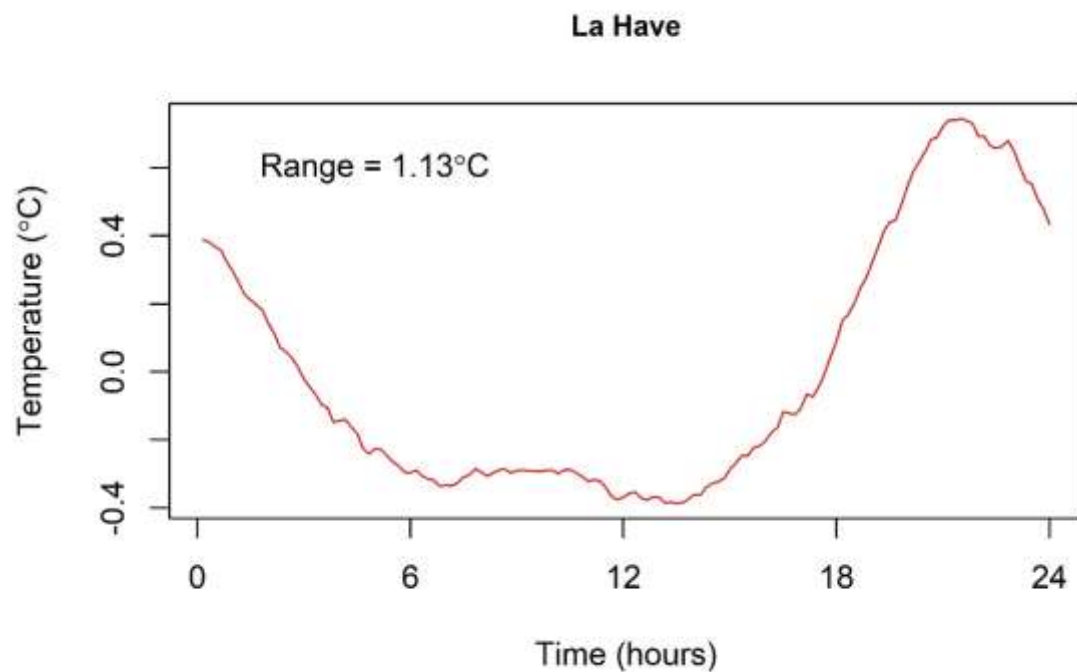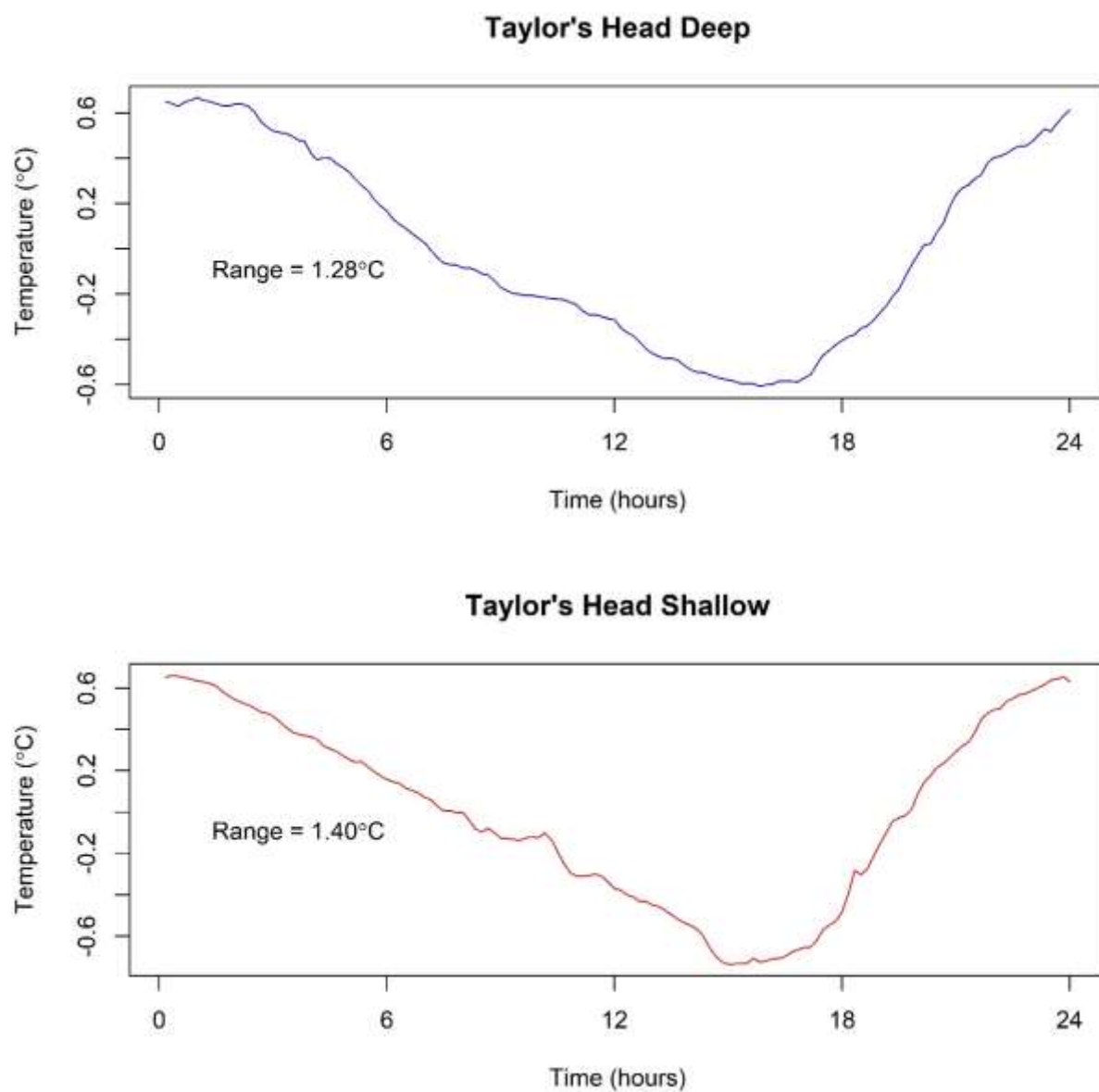
La Have

Figure S42. Average temperature changes over the 24-hour daily heating and cooling cycle at La Have, calculated for the summer period (June-October 2017).
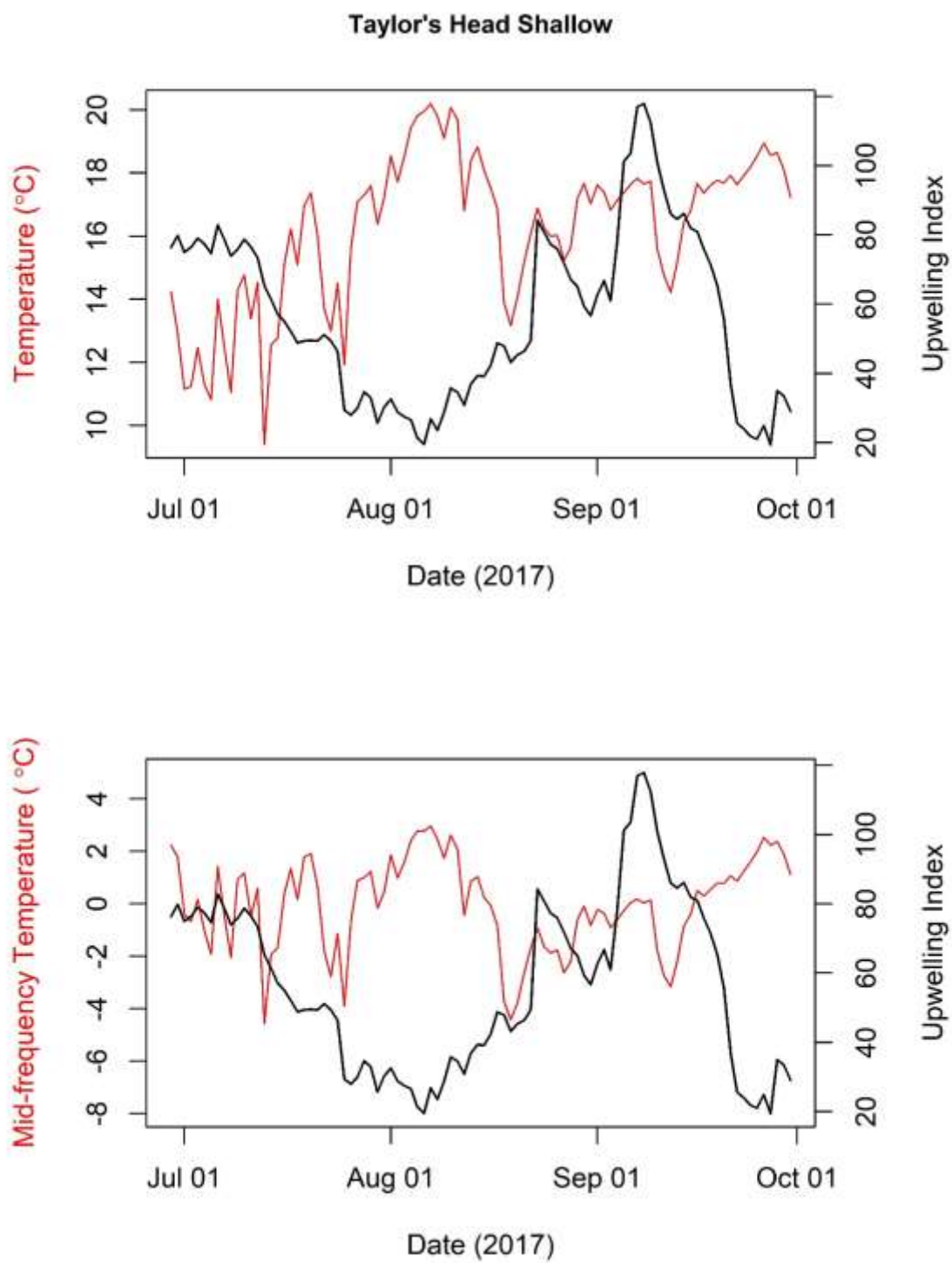
La Have

Figure S43. A 17-day back-averaged upwelling index plotted against average daily temperatures (top panel) and mid-frequency temperatures (bottom panel) at La Have.

Upwelling and Mean Daily Temperature

Lag = -27 days, CCF = 0.51

Upwelling and Mid-frequency Temperature
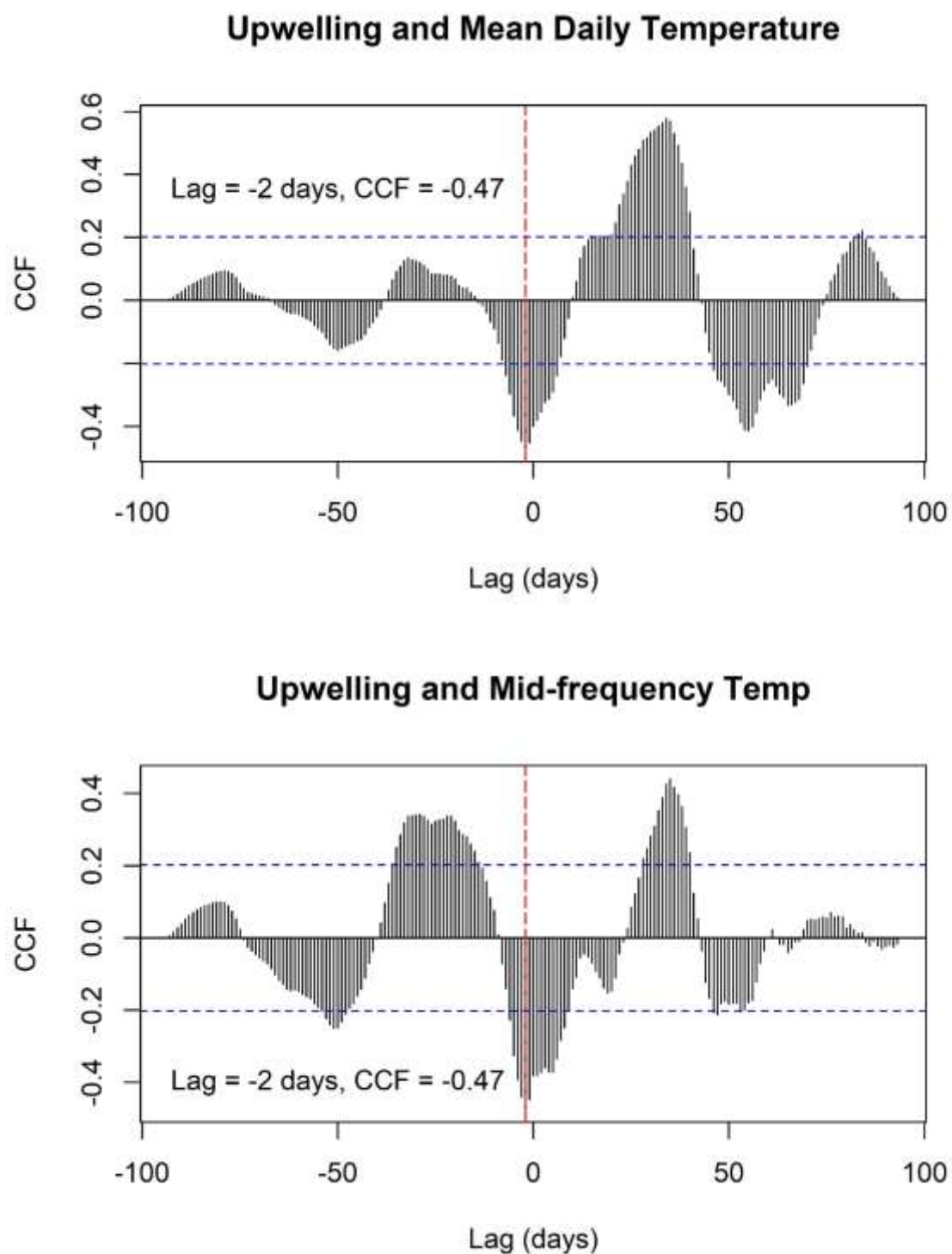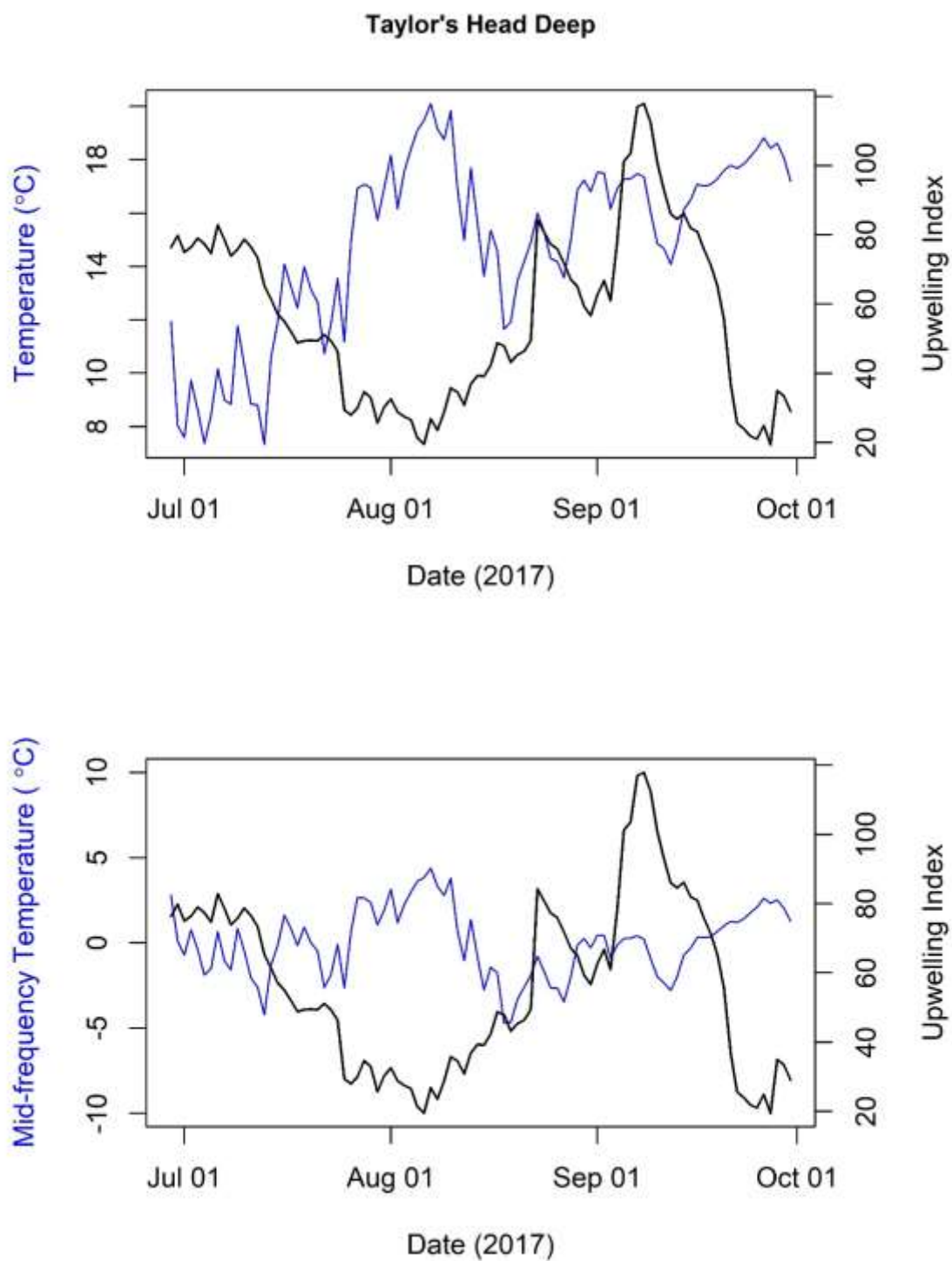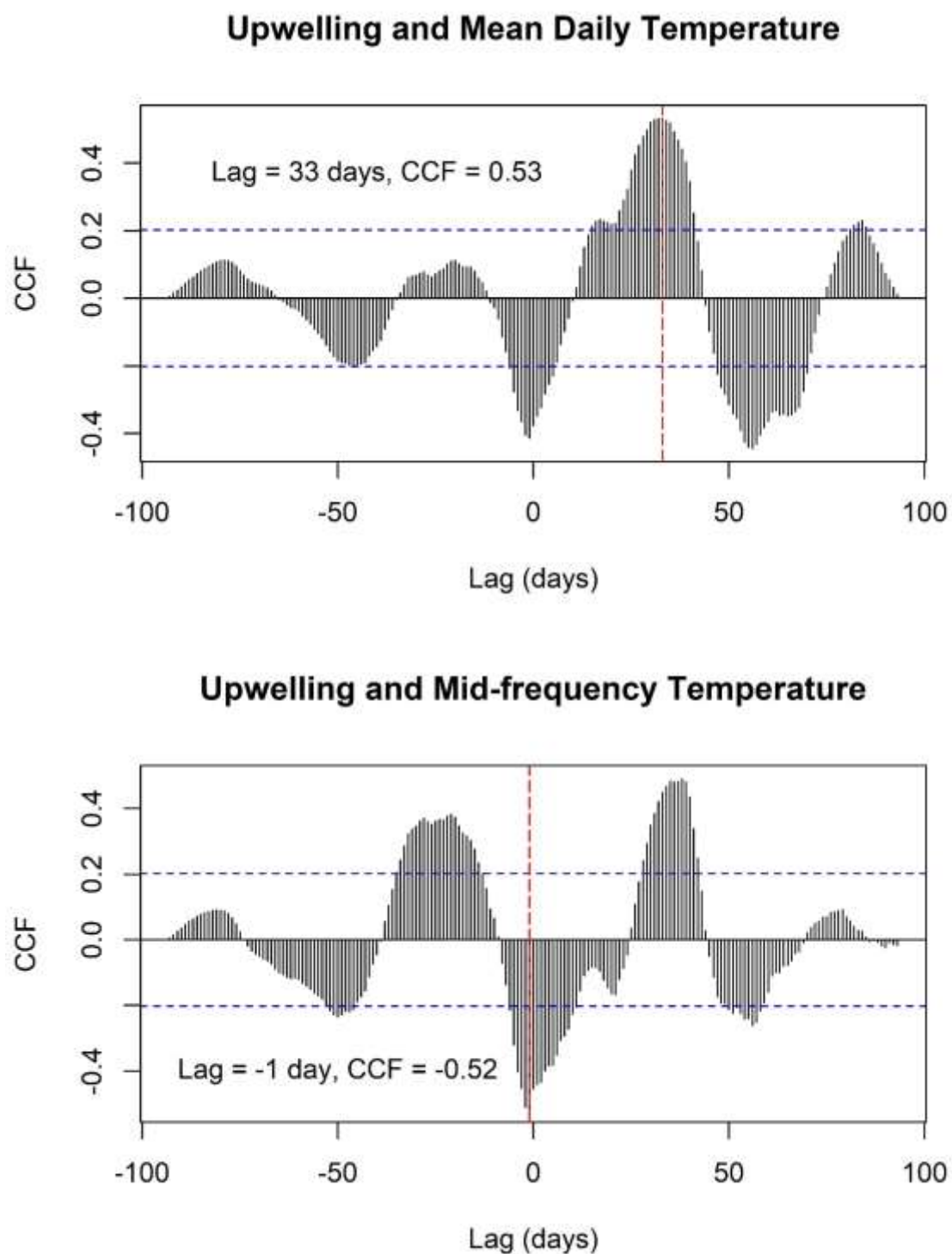

Lag = 0 days, CCF = -0.51

Figure S44. Correlations (CCFs) between a 17-day back-averaged upwelling index and average daily temperatures (top panel), and mid-frequency temperatures (bottom panel) at La Have. Shown on each panel are the dominant lags and corresponding CCF value for each measure of temperature.
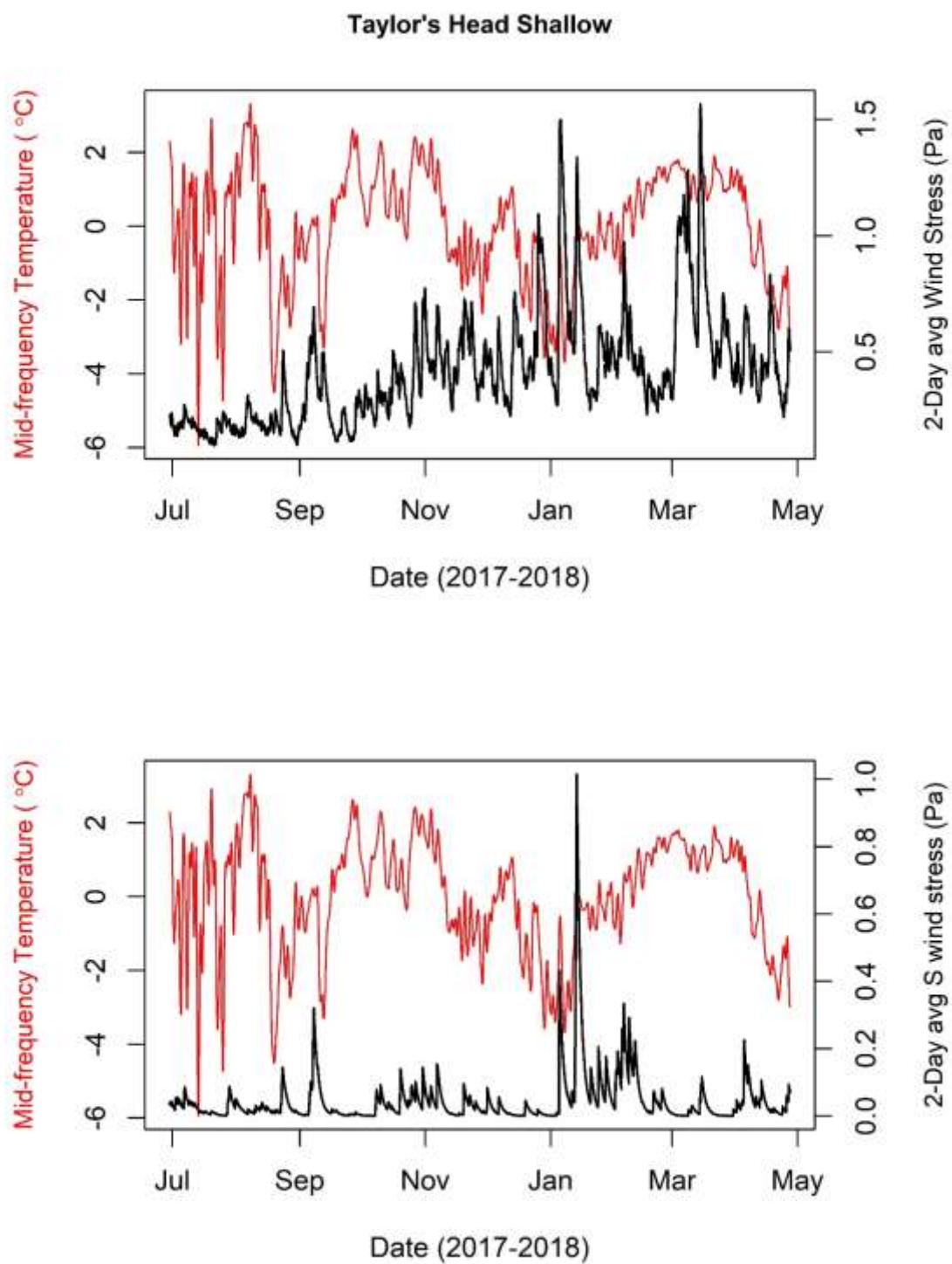
Figure S45. 2-day back-averaged wind stress plotted against mid-frequency temperatures at the shallow location at La Have. The top panel shows total wind stress, while the bottom panel shows easterly wind stress.

2-day Wind Stress and and Mid-frequency Temp

Lag = 48 hours, CCF = -0.201

2-day E Wind Stress and Mid-frequency Temp

Lag = 0 hours, CCF = 0.12
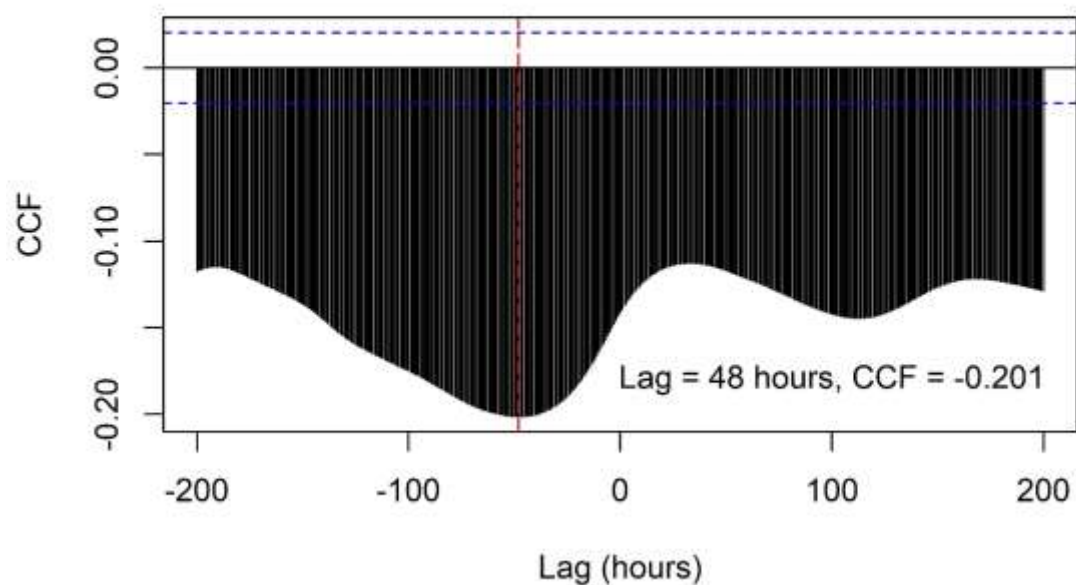
Figure S46. Correlations (CCFs) between a 2-day back-averaged wind stress and mid-frequency temperatures at La Have. The top panel shows total wind stress, while the bottom panel shows easterly wind stress. Shown on each pane are the dominant lags and corresponding CCF value for each measure of temperature.
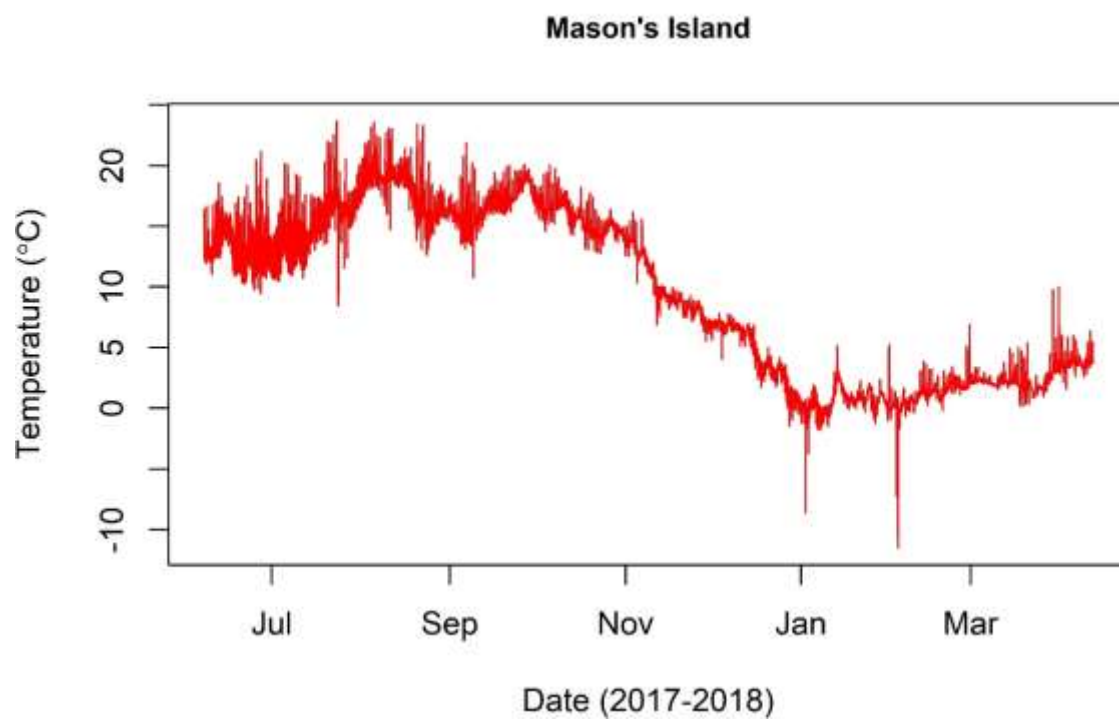
Mason's Island

Figure S47. Temperature records at Mason's Island, recorded from June 7, 2017 to April 12, 2018.

Figure S48. Raw temperatures (top panel), low (second panel), middle (third panel), and high frequency (bottom panel) temperature variability isolated at Mason's Island.
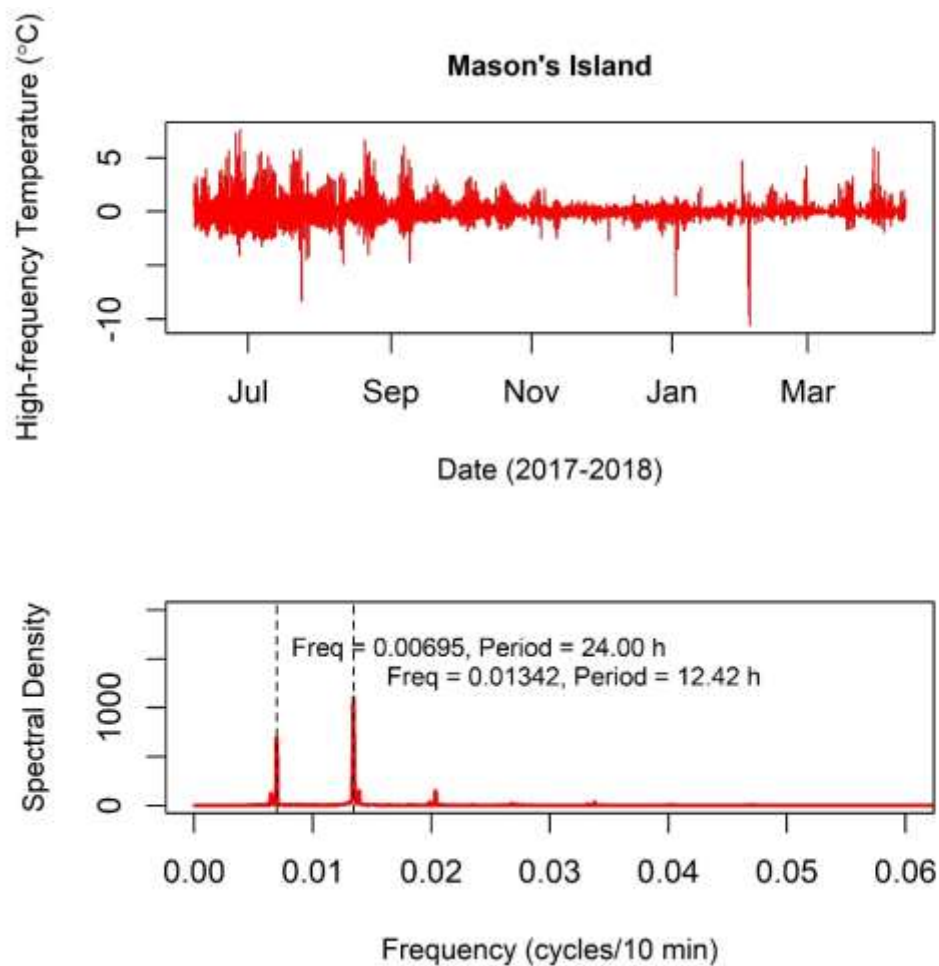
Figure S49. High frequency temperature changes at Mason's Island. The bottom panel shows the results of a spectral analysis, with the dominant frequencies shown with dotted lines and the period shown in text.
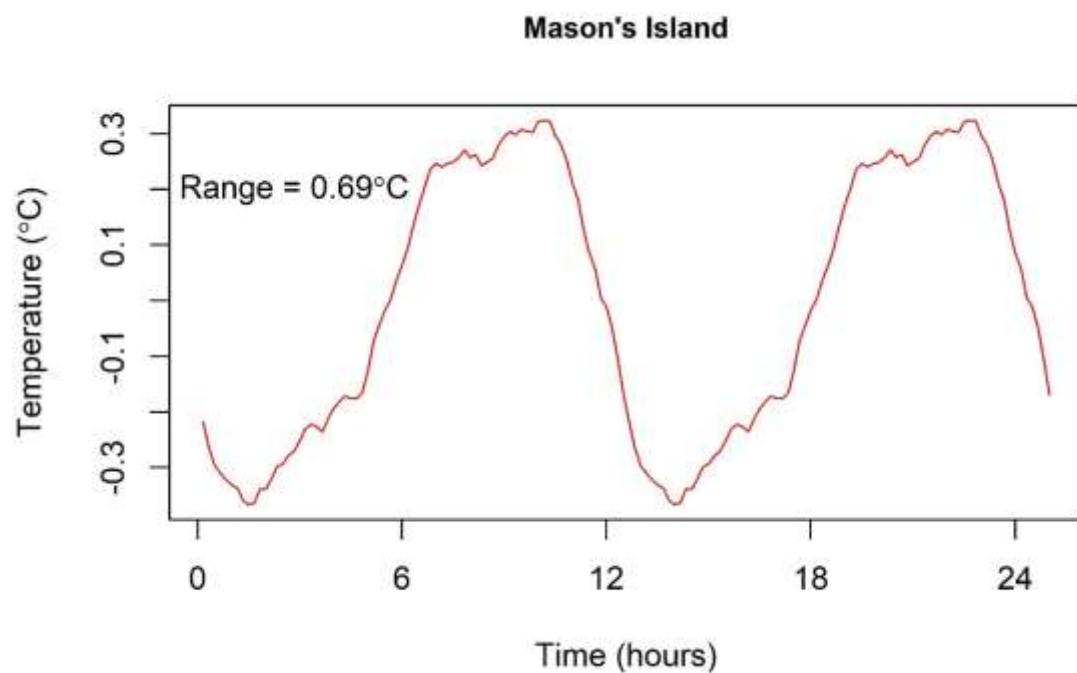
Mason's Island

Figure S50. Average temperature changes over the 12.42-hour tidal cycle at Mason's Island, calculated for the summer period (June-October 2017).
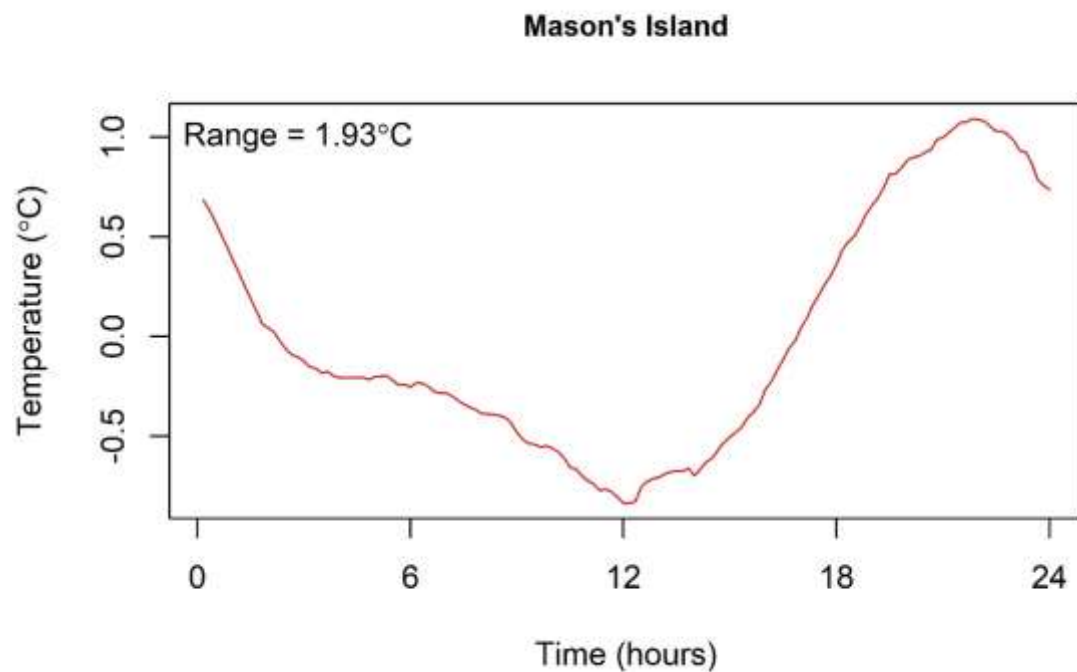
Mason's Island

Figure S51. Average temperature changes over the 24-hour daily heating and cooling cycle at Mason's Island, calculated for the summer period (June-October 2017).
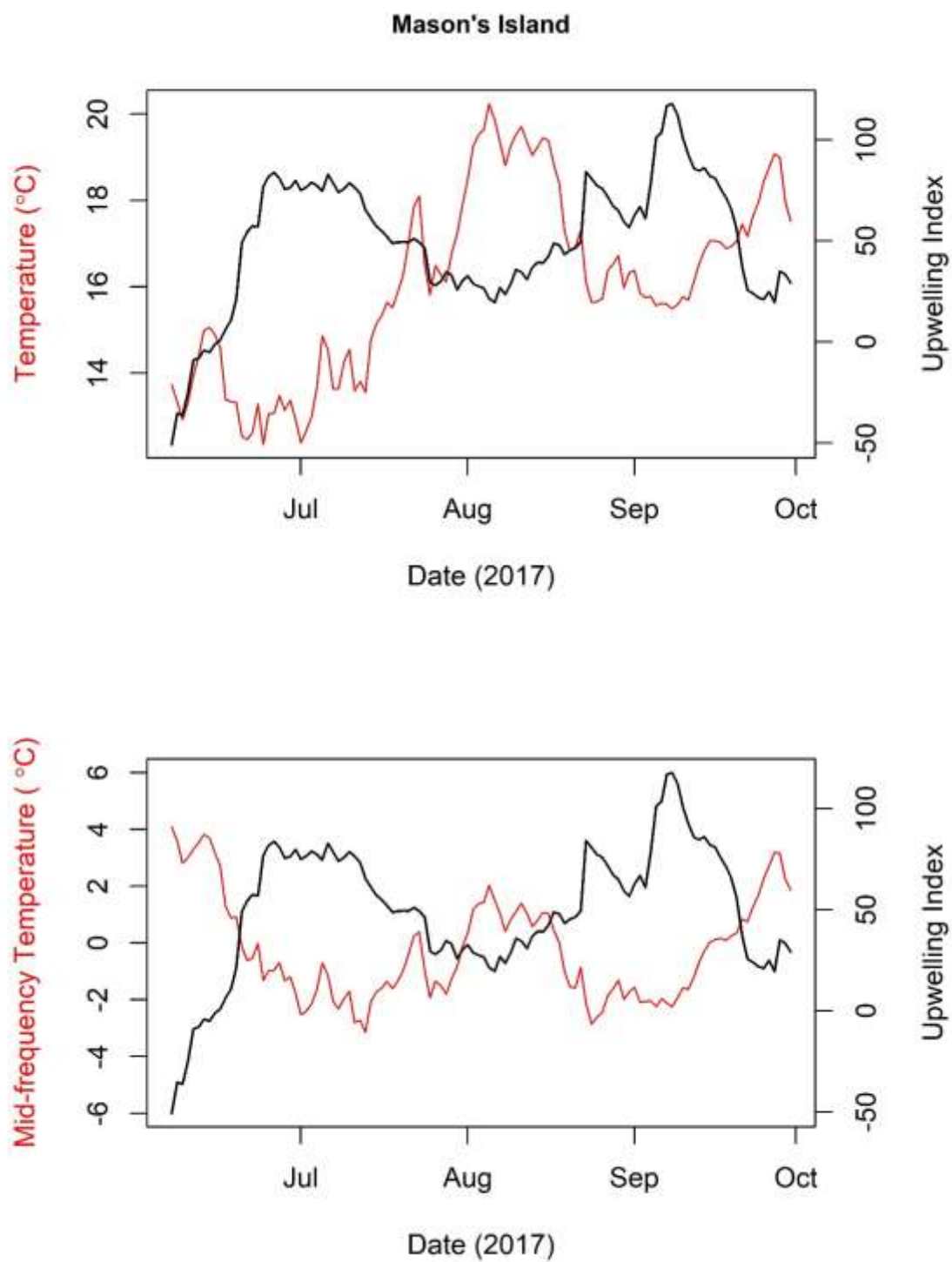
Mason's Island

Figure S52. A 17-day back-averaged upwelling index plotted against average daily temperatures (top panel) and mid-frequency temperatures (bottom panel) at Mason's Island.

Upwelling and Mean Daily Temperature

Lag = -58 days, CCF = -0.39

Upwelling and Mid-frequency Temperature

Lag = 0 days, CCF = -0.81

Figure S53. Correlations (CCFs) between a 17-day back-averaged upwelling index and average daily temperatures (top panel), and mid-frequency temperatures (bottom panel) at Mason's Island. Shown on each panel are the dominant lags and corresponding CCF value for each measure of temperature.
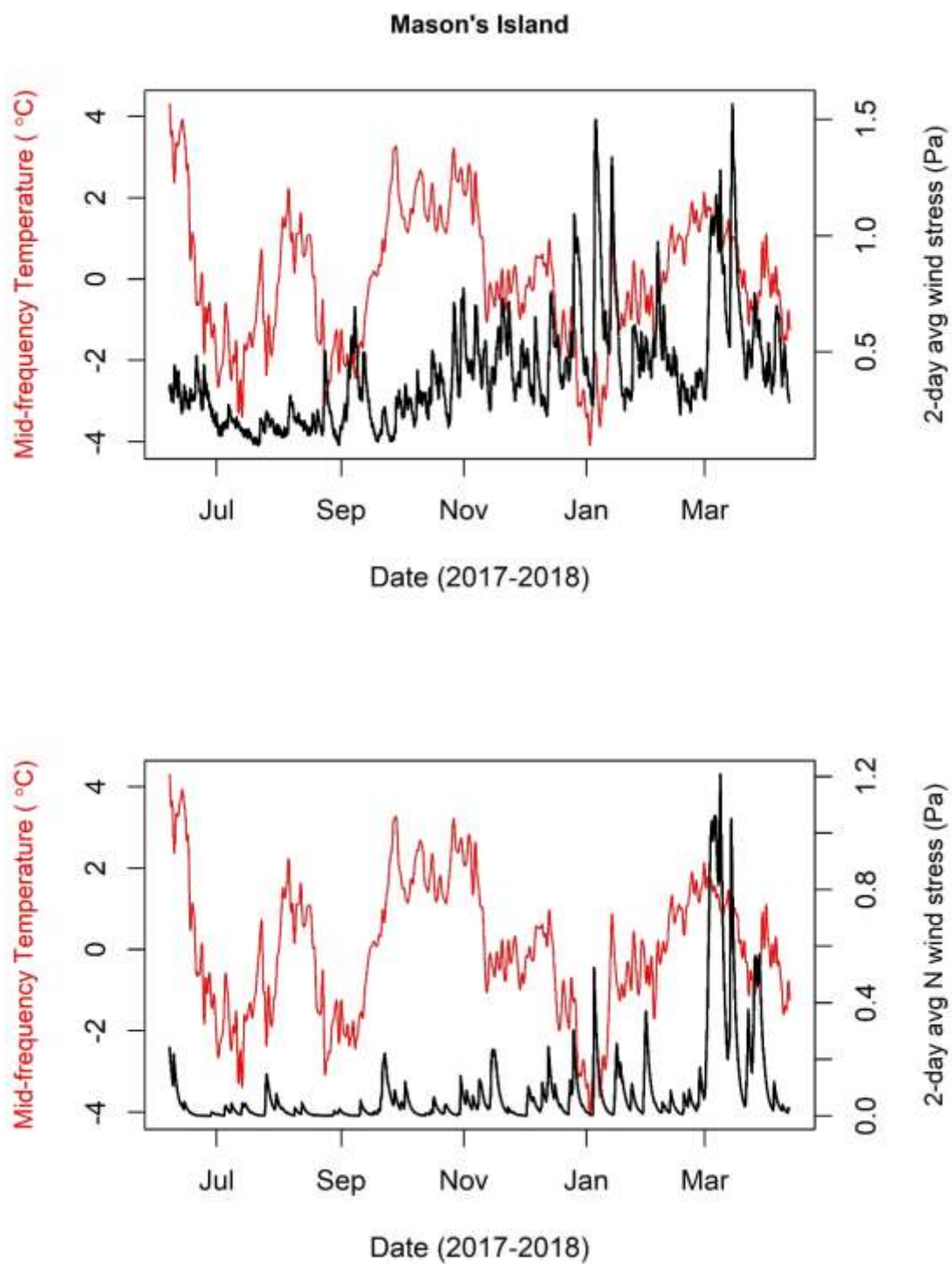
Mason's Island

Figure S54. 2-day back-averaged wind stress plotted against mid-frequency temperatures at the shallow location at Mason's Island. The top panel shows total wind stress, while the bottom panel shows northerly wind stress.

2-day Wind Stress and and Mid-frequency Temp

Lag = -50 hours, CCF = -0.09

CCF

Lag (hours)

2-day N Wind Stress and Mid-frequency Temp

CCF

Lag (hours)
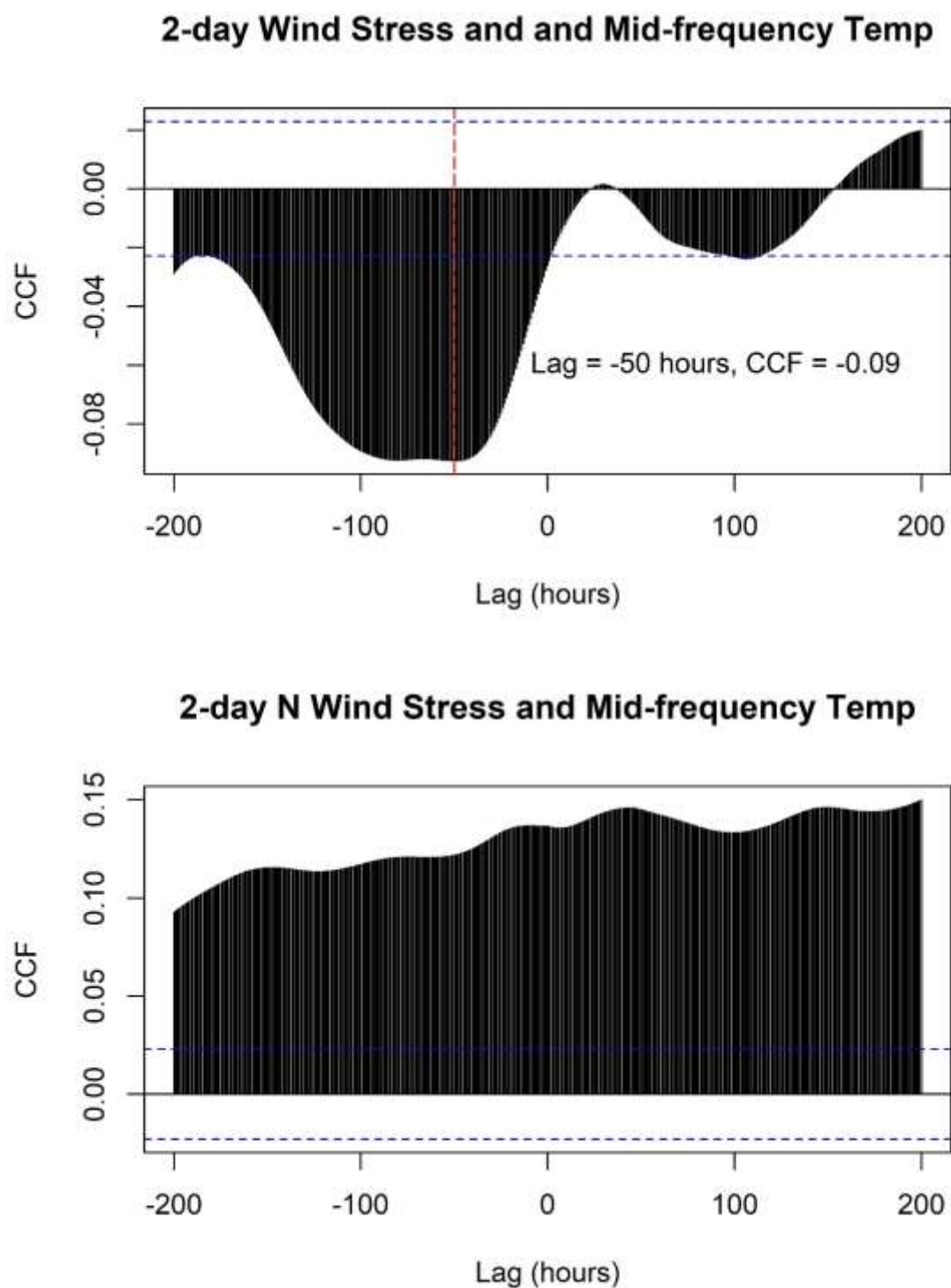
Figure S55. Correlations (CCFs) between a 2-day back-averaged wind stress and mid-frequency temperatures at Mason's Island. The top panel shows total wind stress, while the bottom panel shows northerly wind stress. Shown on each pane are the dominant lags and corresponding CCF value for each measure of temperature.
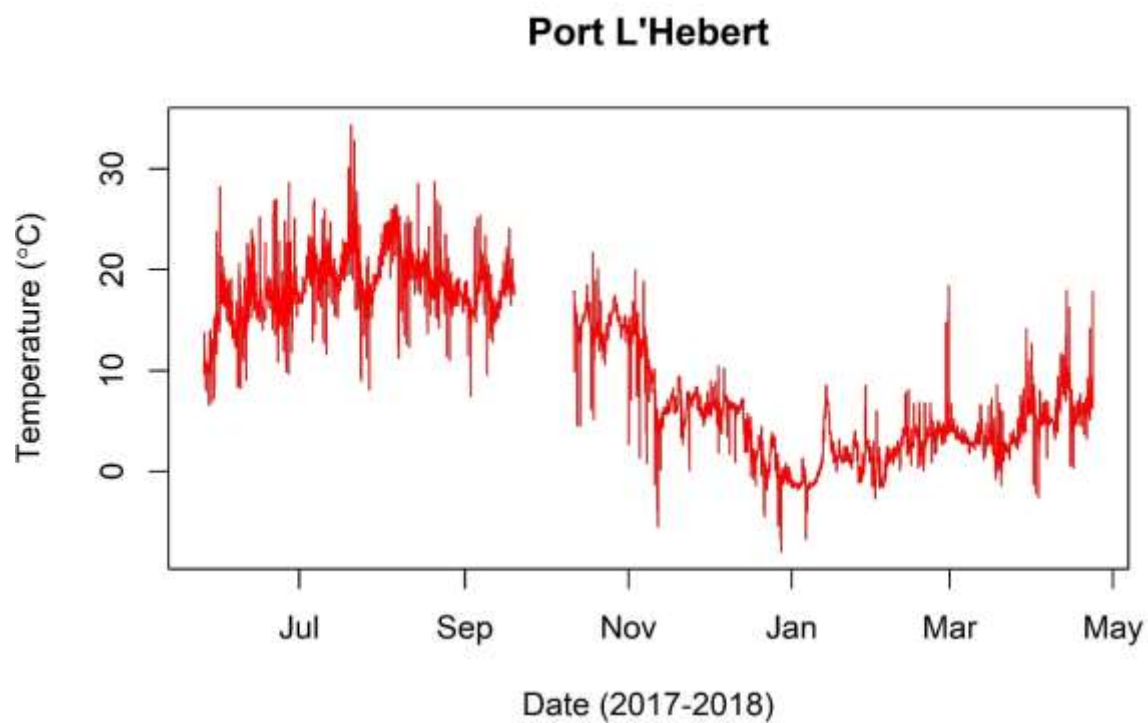
Port L'Hebert

Figure S56. Temperature records at Port L'Hebert, as recorded from May 26, 2017 to April 23, 2018.
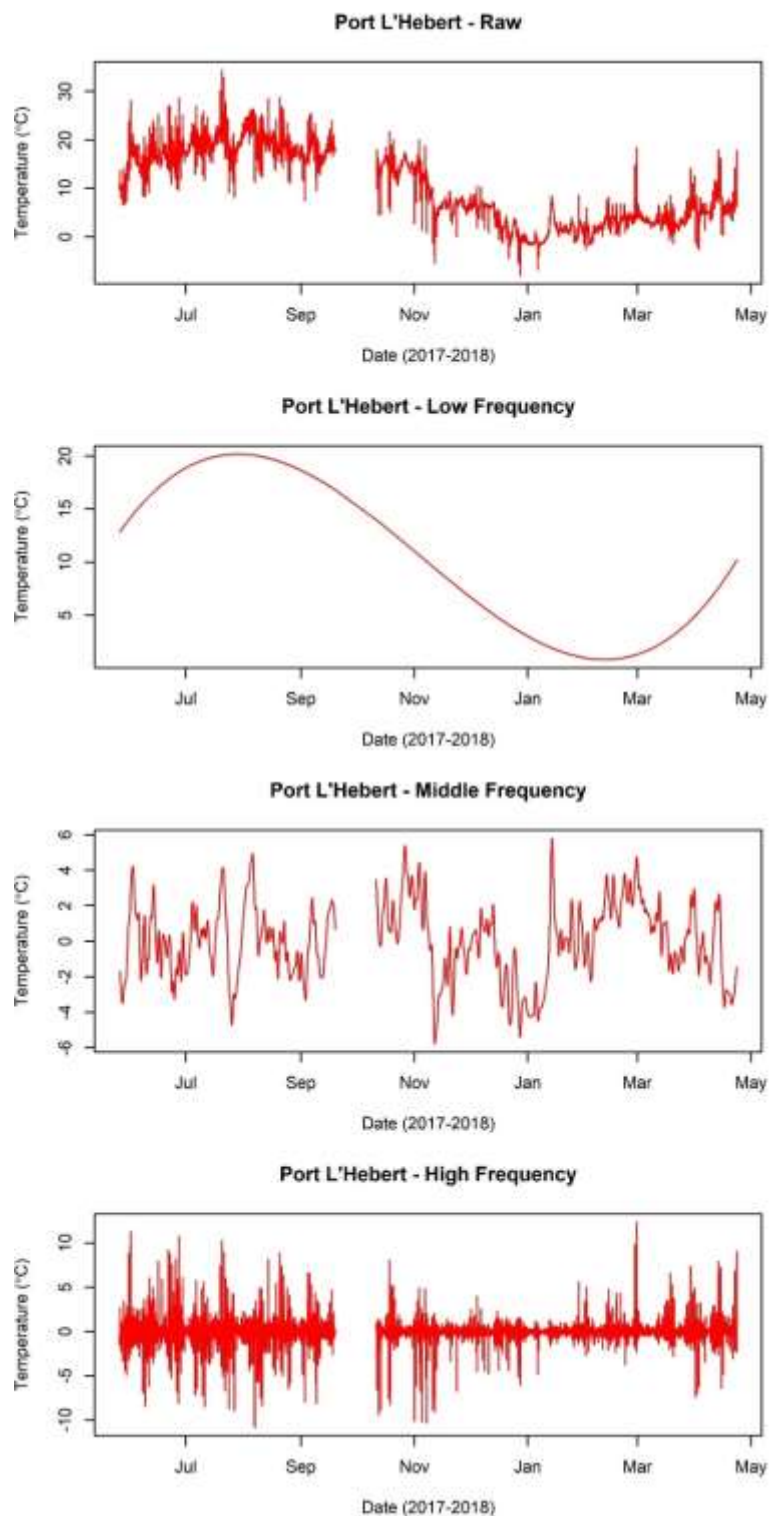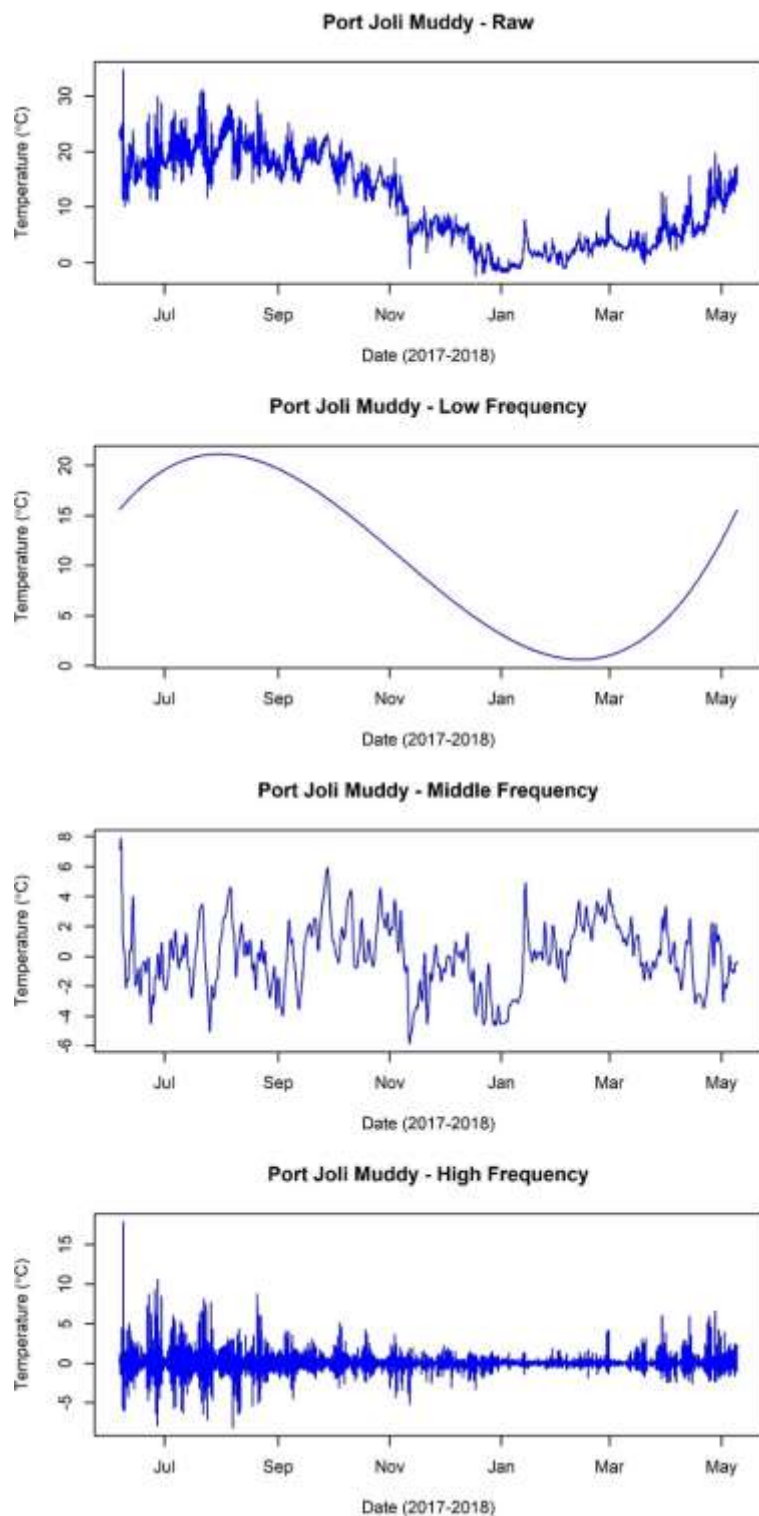
Figure S57. Raw temperatures (top panel), low (second panel), middle (third panel), and high frequency (bottom panel) temperature variability isolated at Port L'Hebert.
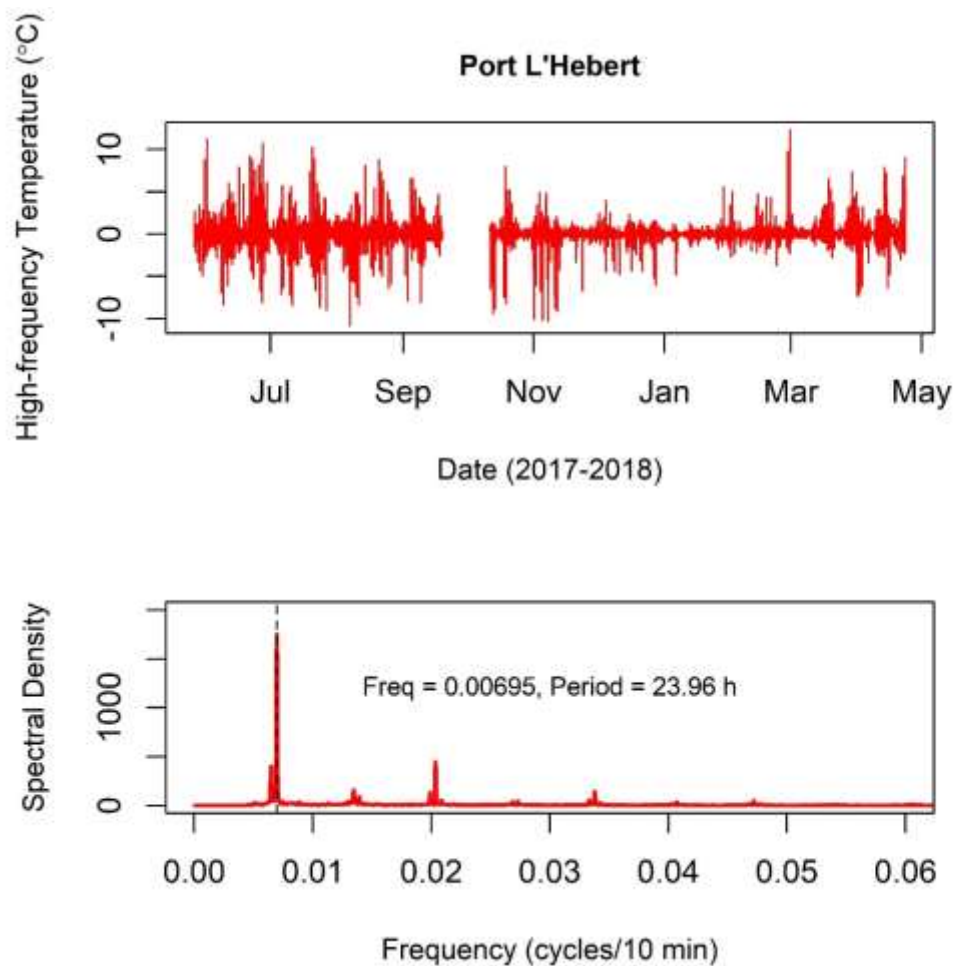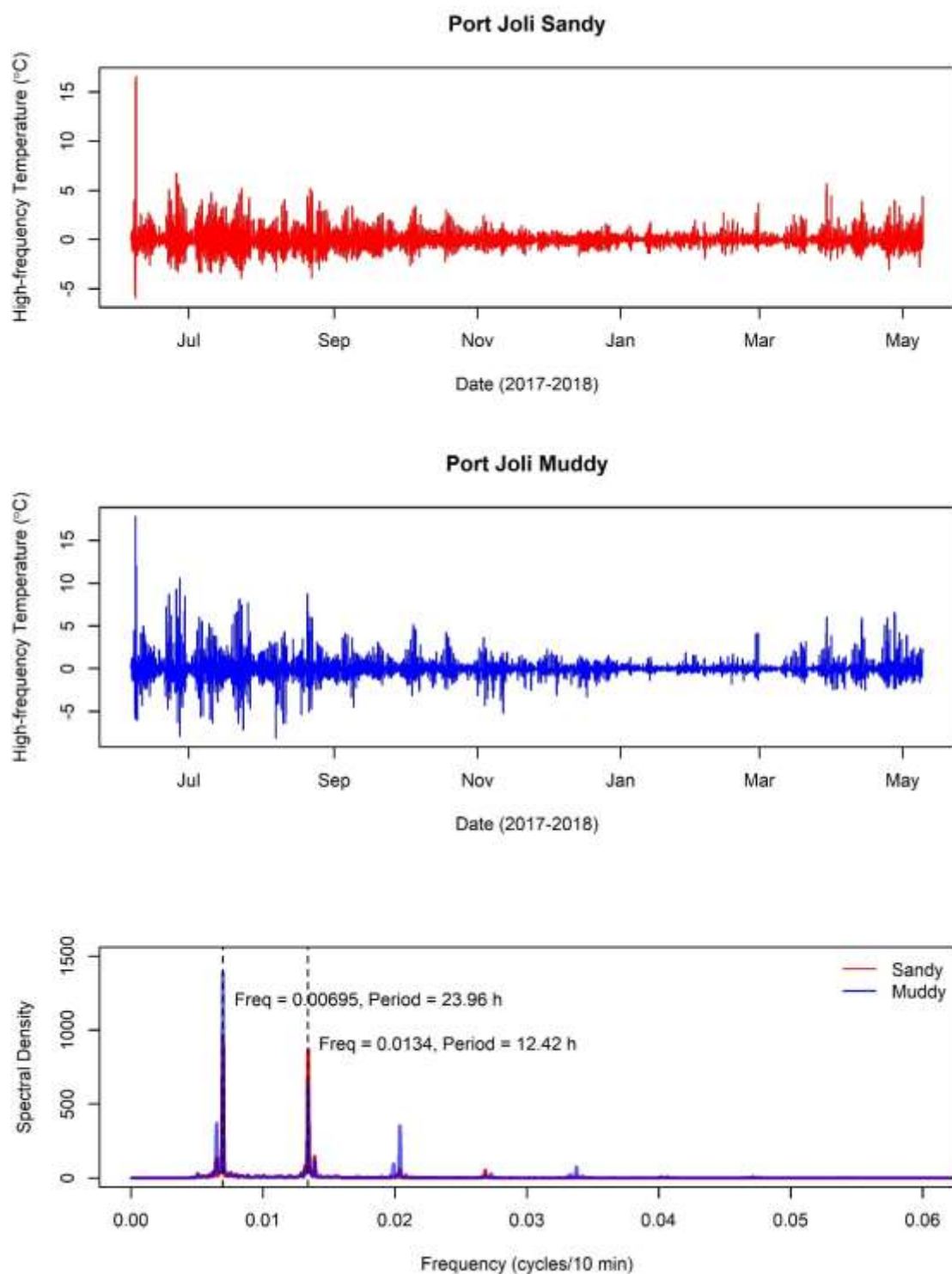
Figure S58. High frequency temperature changes at Port L'Hebert. The bottom panel shows the results of a spectral analysis, with the dominant frequencies shown with dotted lines and the period shown in text.
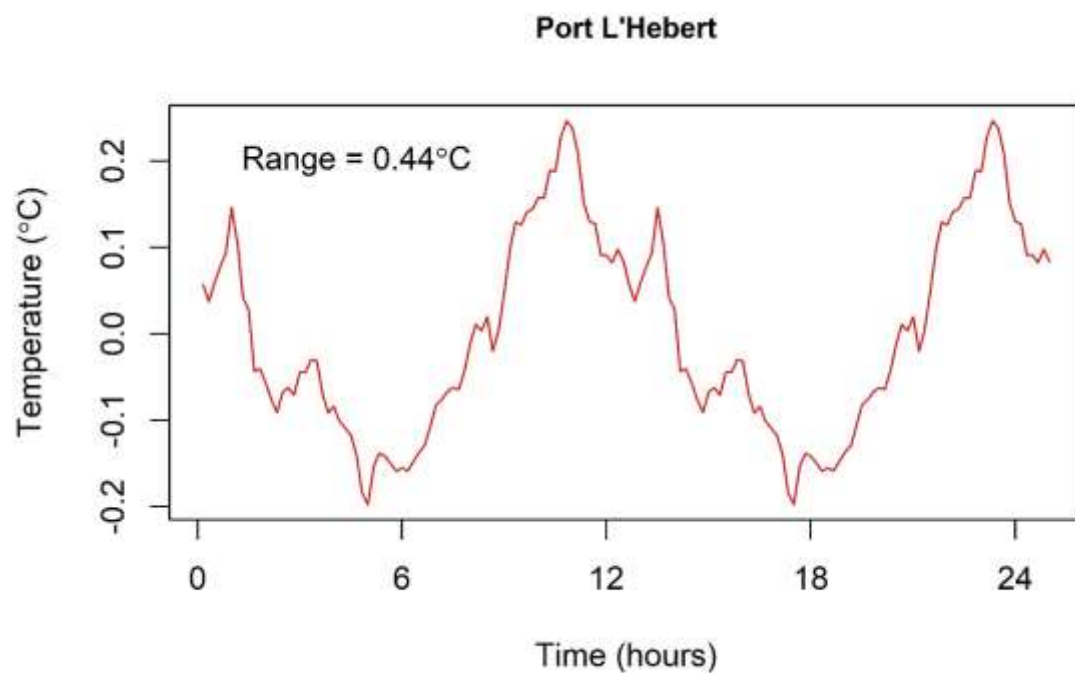
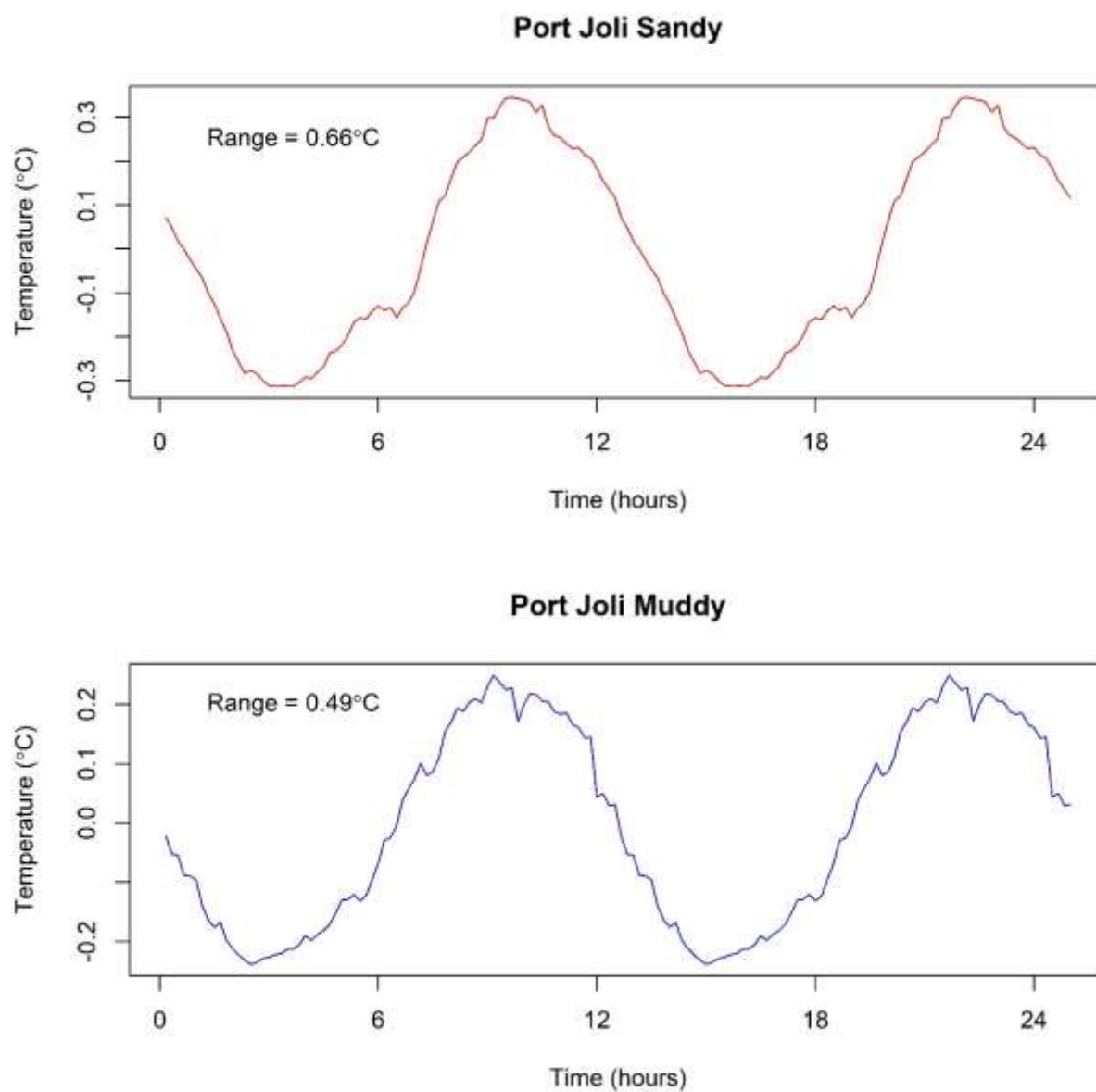**Port L'Hebert**

Figure S59. Average temperature changes over the 12.42-hour tidal cycle at Port L'Hebert, calculated for the summer period (June-October 2017).
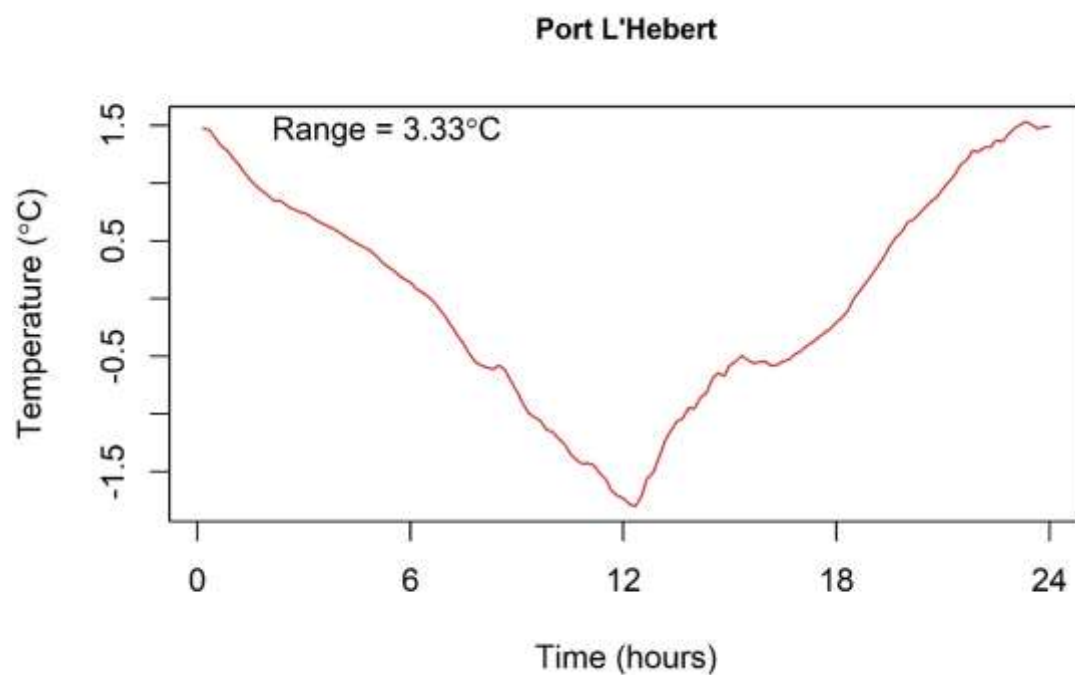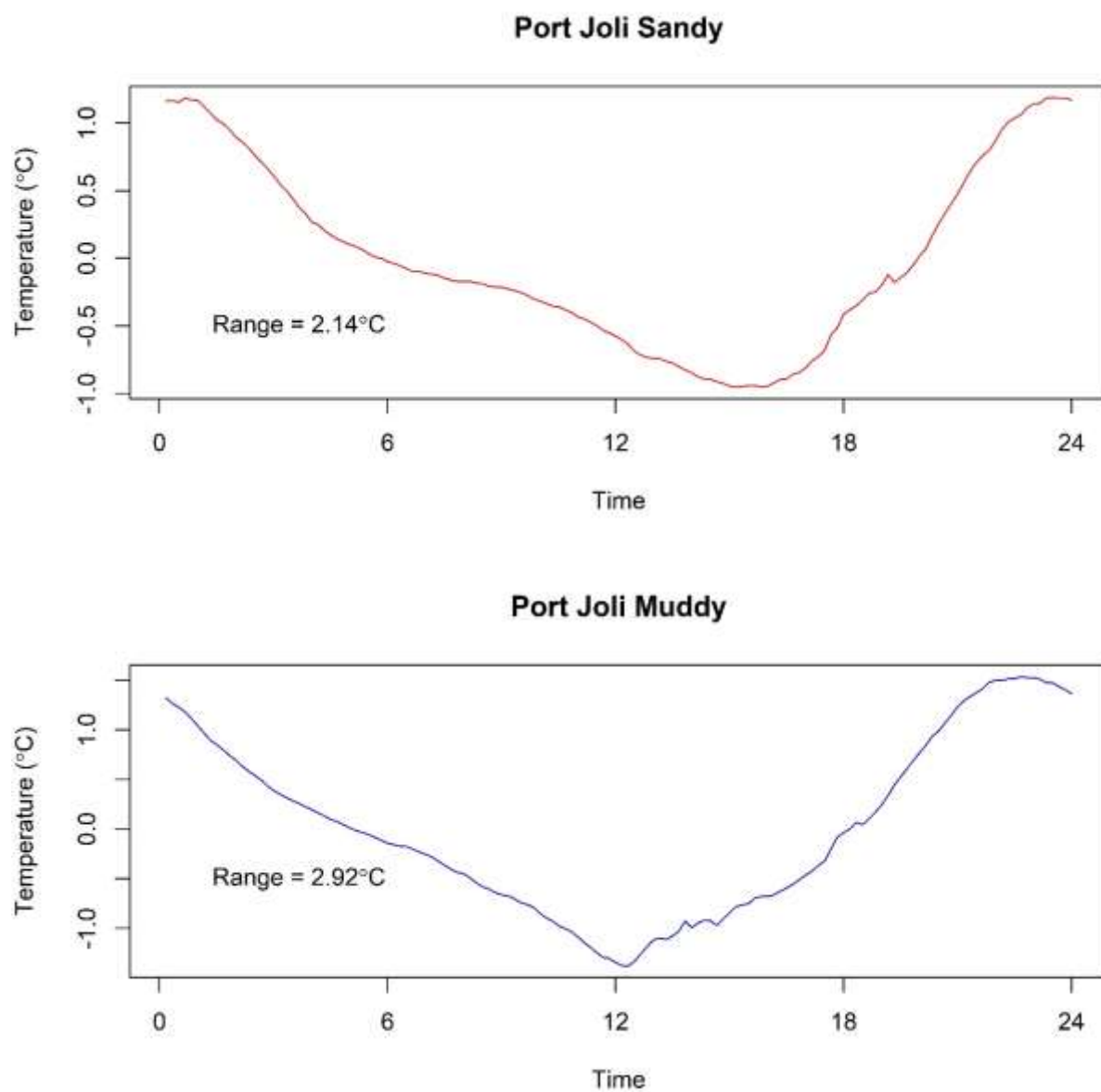
Port L'Hebert

Figure S60. Average temperature changes over the 24-hour daily heating and cooling cycle at Port L'Hebert, calculated for the summer period (June-October 2017).
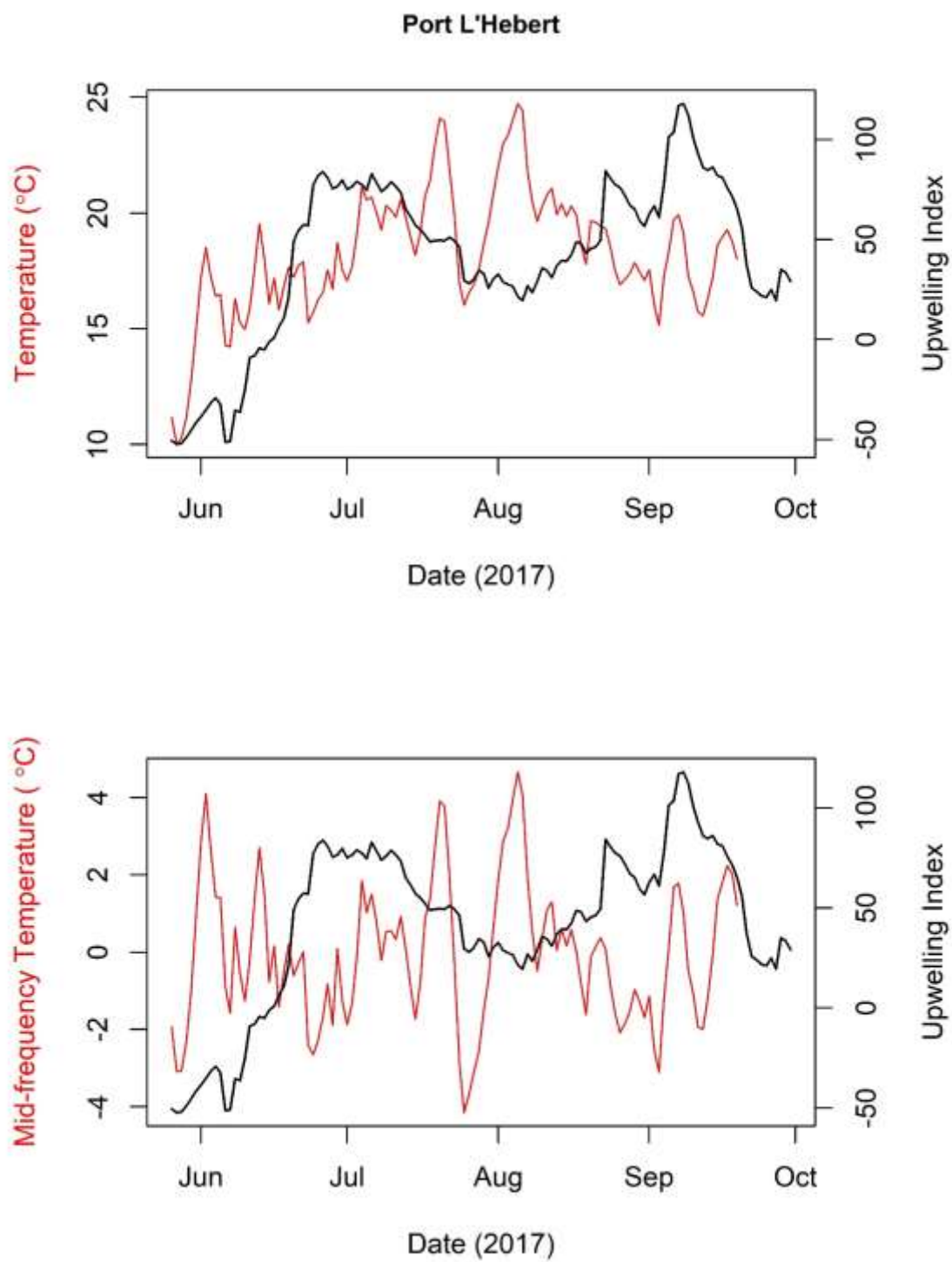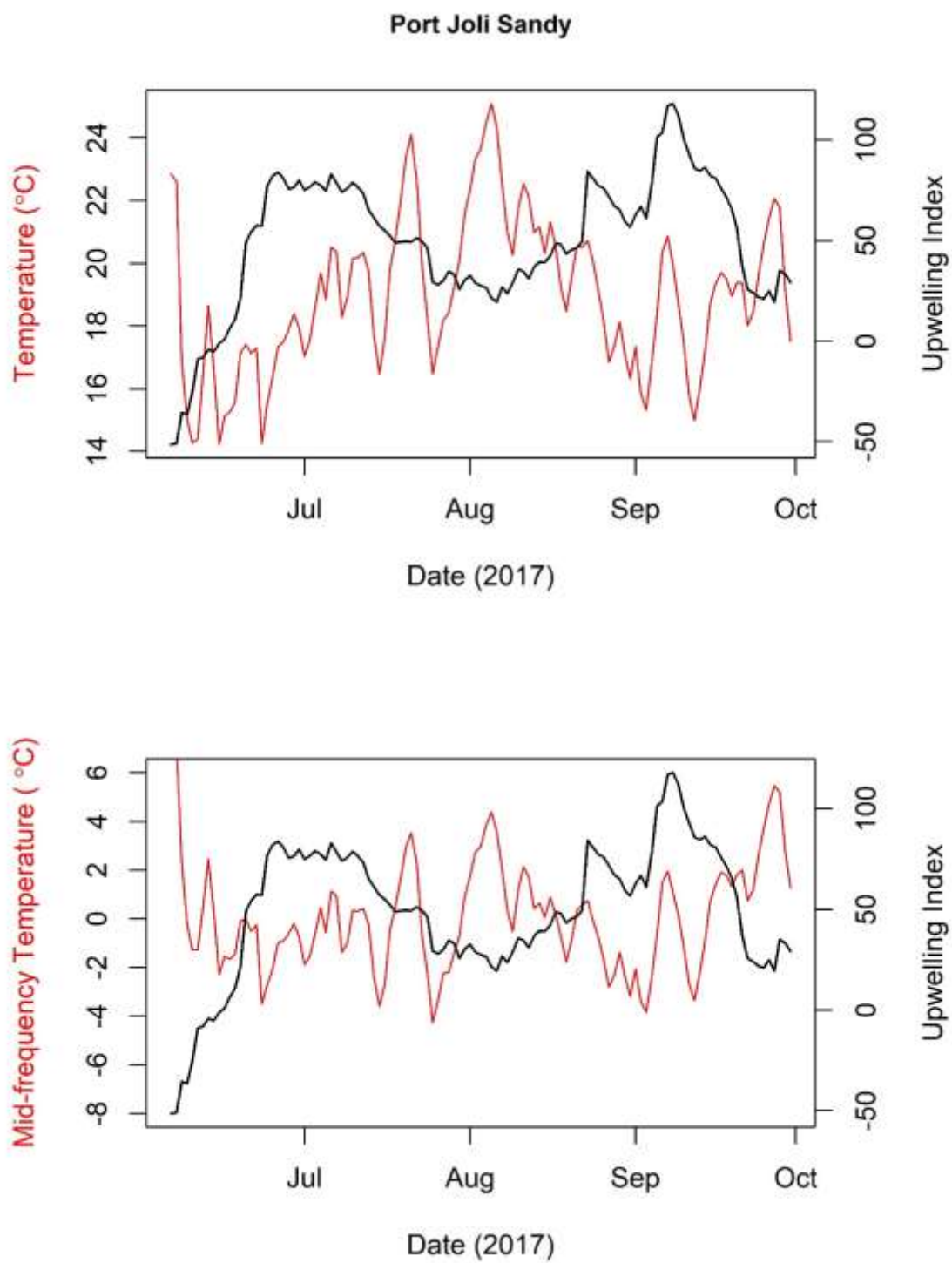
Port L'Hebert

Figure S61. A 17-day back-averaged upwelling index plotted against average daily temperatures (top panel) and mid-frequency temperatures (bottom panel) at Port L'Hebert.

Upwelling and Mean Daily Temperature

Lag = -66 days, CCF = 0.41

Upwelling and Mid-frequency Temperature
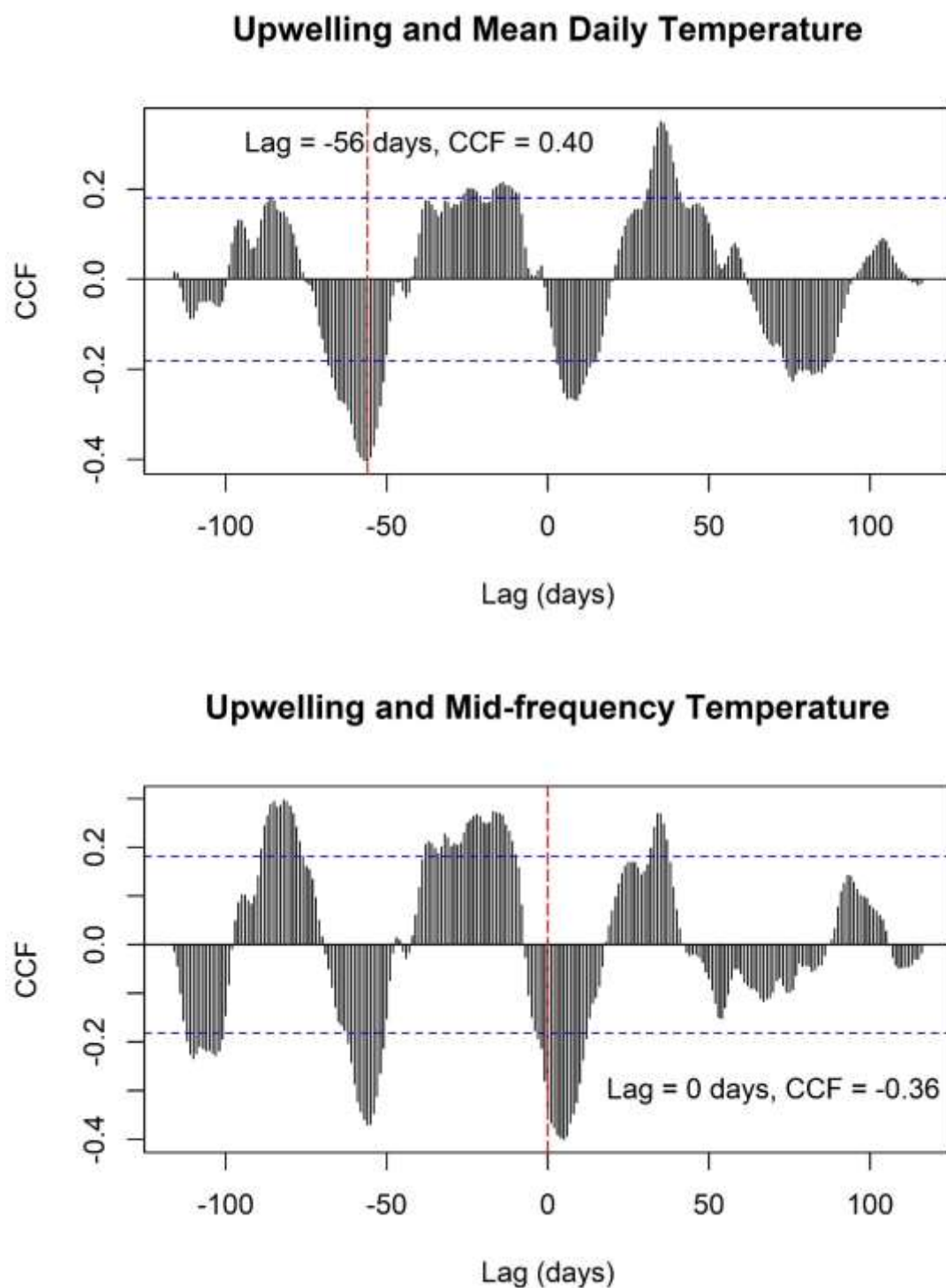

Lag = -4 days, CCF = -0.20
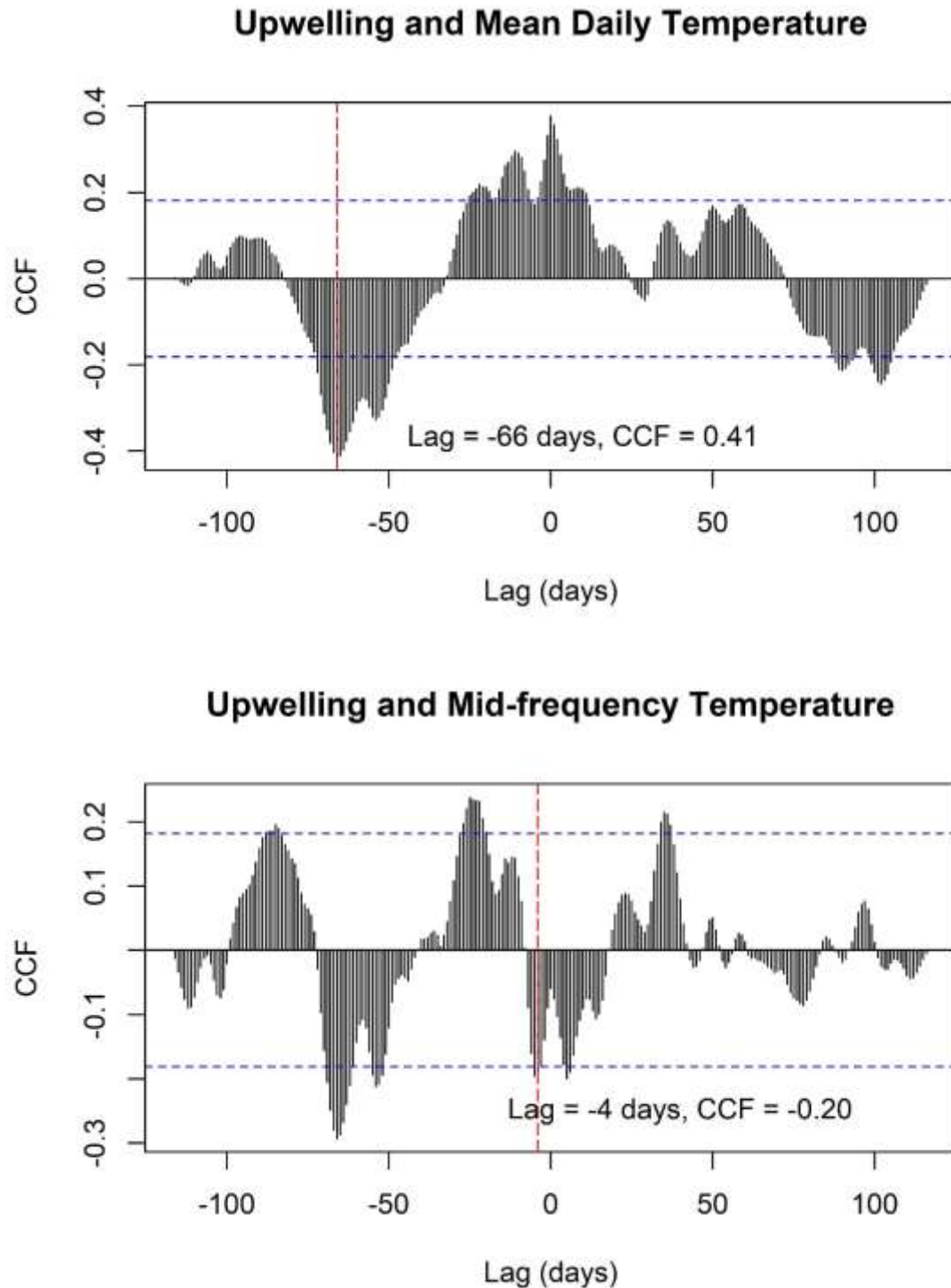
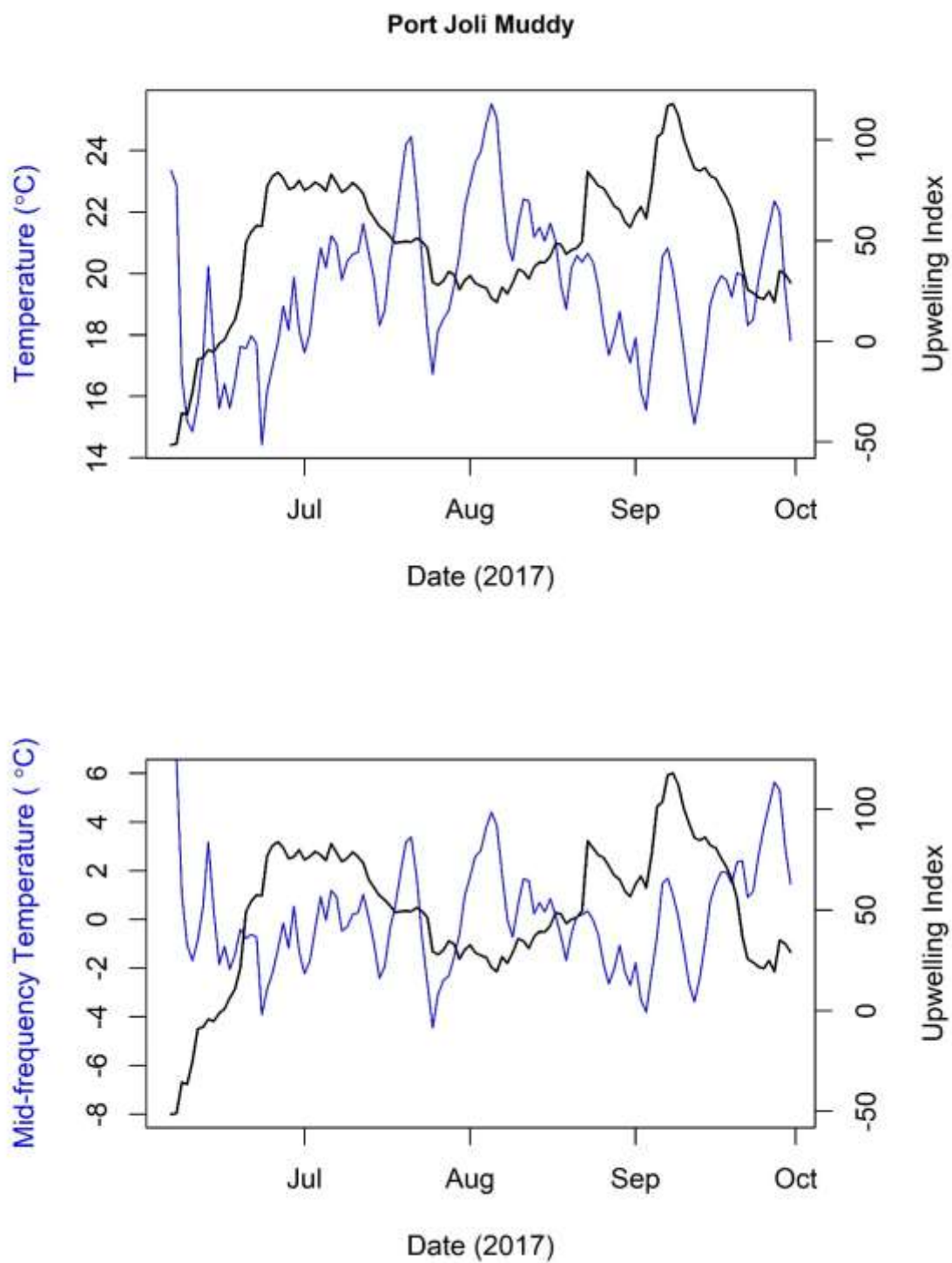Figure S62. Correlations (CCFs) between a 17-day back-averaged upwelling index and average daily temperatures (top panel), and mid-frequency temperatures (bottom panel) at Port L'Hebert. Shown on each panel are the dominant lags and corresponding CCF value for each measure of temperature.
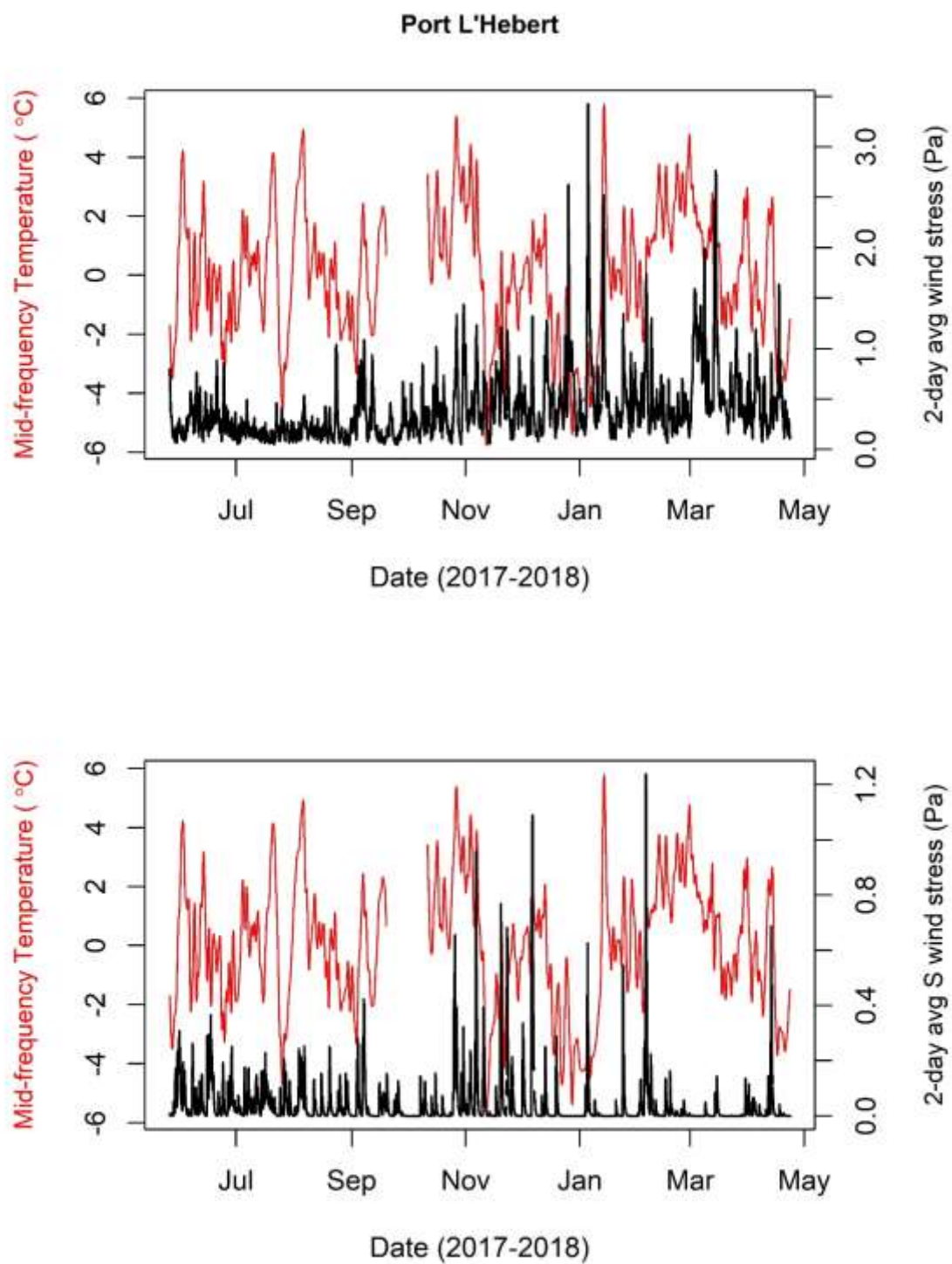
Port L'Hebert

Figure S63. 2-day back-averaged wind stress plotted against mid-frequency temperatures at the shallow location at Port L'Hebert. The top panel shows total wind stress, while the bottom panel shows southerly wind stress.
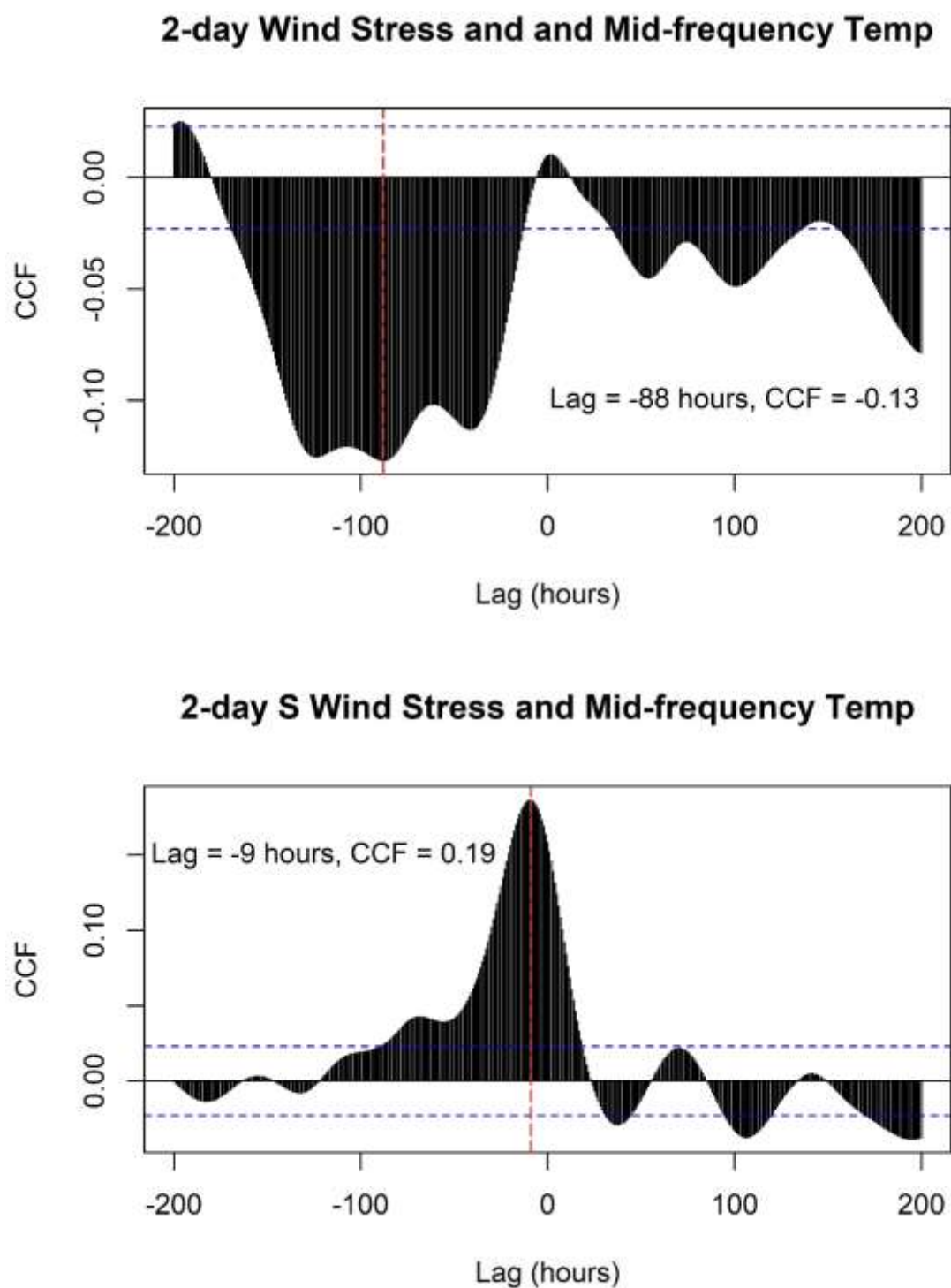
Figure S64. Correlations (CCFs) between a 2-day back-averaged wind stress and mid-frequency temperatures at Port L'Hebert. The top panel shows total wind stress, while the bottom panel shows southerly wind stress. Shown on each pane are the dominant lags and corresponding CCF value for each measure of temperature.
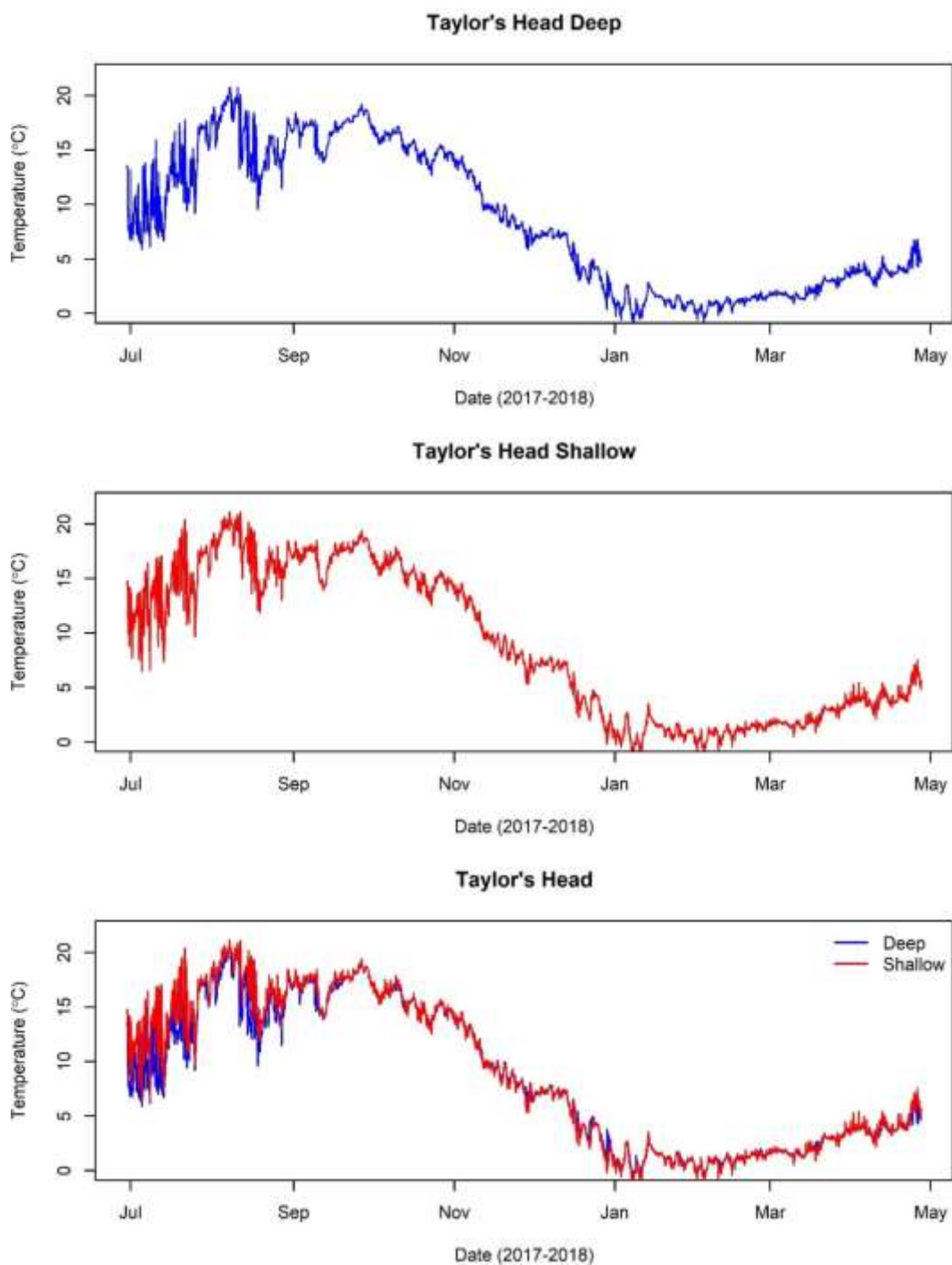
Taylor's Head

Figure S65. Temperature records at the deep and shallow locations at Taylor's Head, recorded from May 31, 2017 to April 11, 2018.
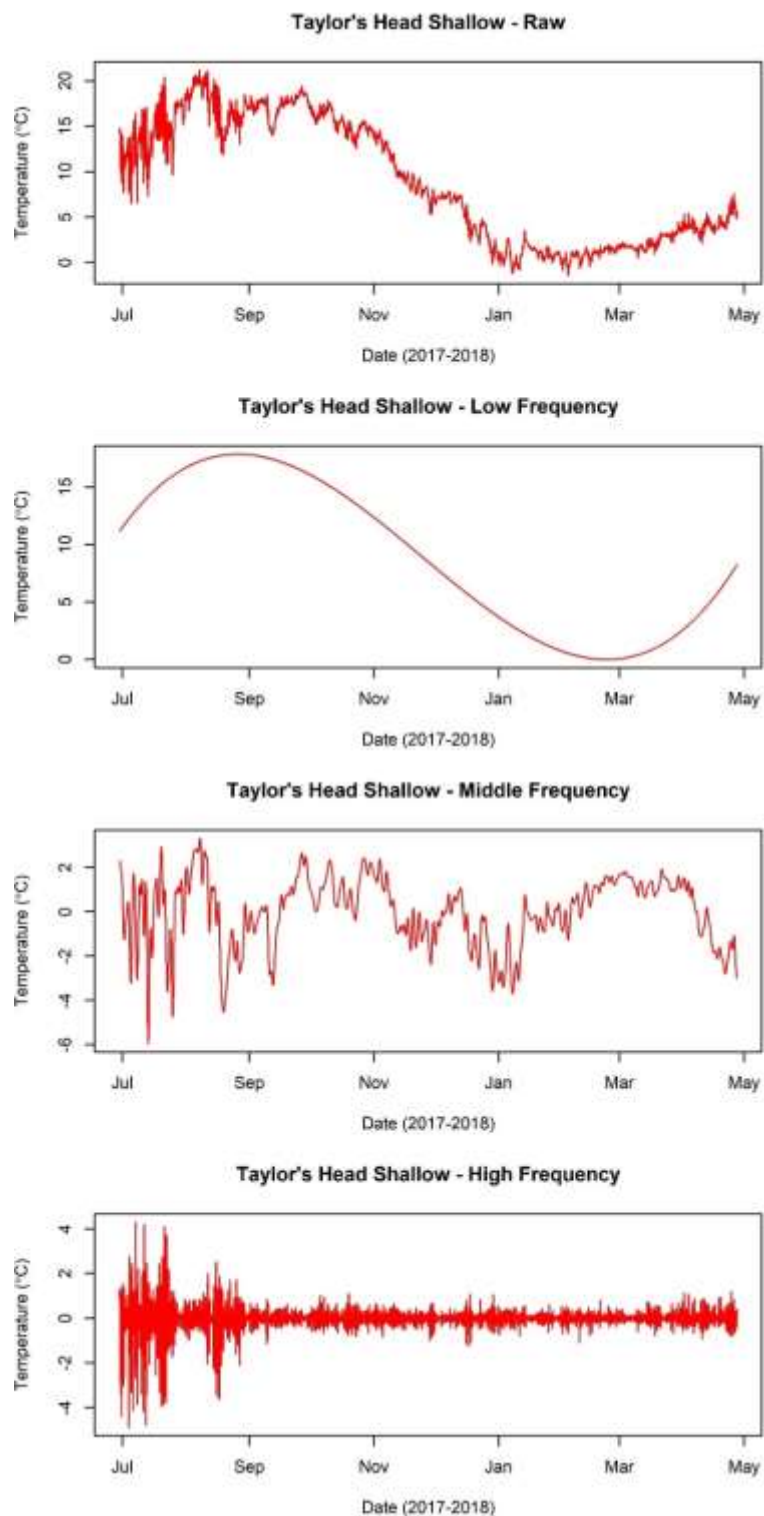
Figure S66. Raw temperatures (top panel), low (second panel), middle (third panel), and high frequency (bottom panel) temperature variability isolated at the shallow location at Taylor's Head.
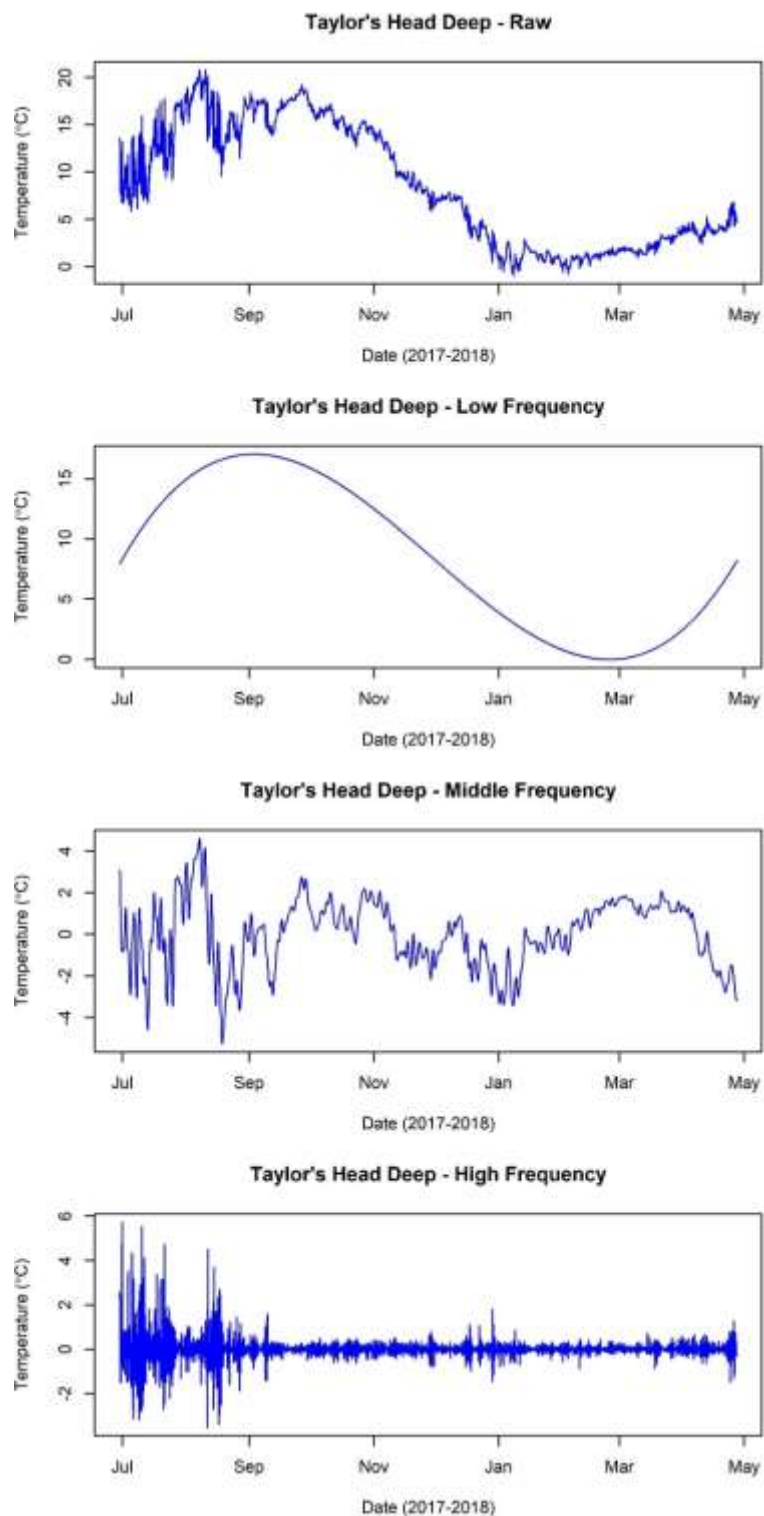
Figure S67. Raw temperatures (top panel), low (second panel), middle (third panel), and high frequency (bottom panel) temperature variability isolated at the deep location at Taylor's Head.

Figure S68. High frequency temperature changes at the shallow and deep locations at Taylor's Head (top two panels). The bottom panel shows the results of a spectral analysis, with the dominant frequencies shown in dotted lines and the period shown in text.

Figure S69. Average temperature changes over the 12.42-hour tidal cycle at Taylor's Head deep and shallow, calculated for the summer period (June-October 2017).

Taylor's Head Deep

Taylor's Head Shallow

Figure S70. Average temperature changes over the 24-hour daily heating and cooling cycle at Taylor's Head deep and shallow, calculated for the summer period (June-October 2017).

Taylor's Head Shallow

Figure S71. A 17-day back-averaged upwelling index plotted against average daily temperatures (top panel) and mid-frequency temperatures (bottom panel) at the shallow location at Taylor's Head.

Upwelling and Mean Daily Temperature

Lag = -2 days, CCF = -0.47

Upwelling and Mid-frequency Temp

Lag = -2 days, CCF = -0.47

Figure S72. Correlations (CCFs) between a 17-day back-averaged upwelling index and average daily temperatures (top panel), and mid-frequency temperatures (bottom panel) at the shallow location at Taylor's Head. Shown on each pane are the dominant lags and corresponding CCF value for each measure of temperature.

Figure S73. A 17-day back-averaged upwelling index plotted against average daily temperatures (top panel) and mid-frequency temperatures (bottom panel) at the deep location at Taylor's Head.

Upwelling and Mean Daily Temperature

Lag = 33 days, CCF = 0.53

Upwelling and Mid-frequency Temperature

Lag = -1 day, CCF = -0.52

Figure S74. Correlations (CCFs) between a 17-day back-averaged upwelling index and average daily temperatures (top panel), and mid-frequency temperatures (bottom panel) at the deep location at Taylor's Head. Shown on each pane are the dominant lags and corresponding CCF value for each measure of temperature.

Figure S75. 2-day back-averaged wind stress plotted against mid-frequency temperatures at the shallow location at Taylor's Head. The top panel shows total wind stress, while the bottom panel shows southerly wind stress.
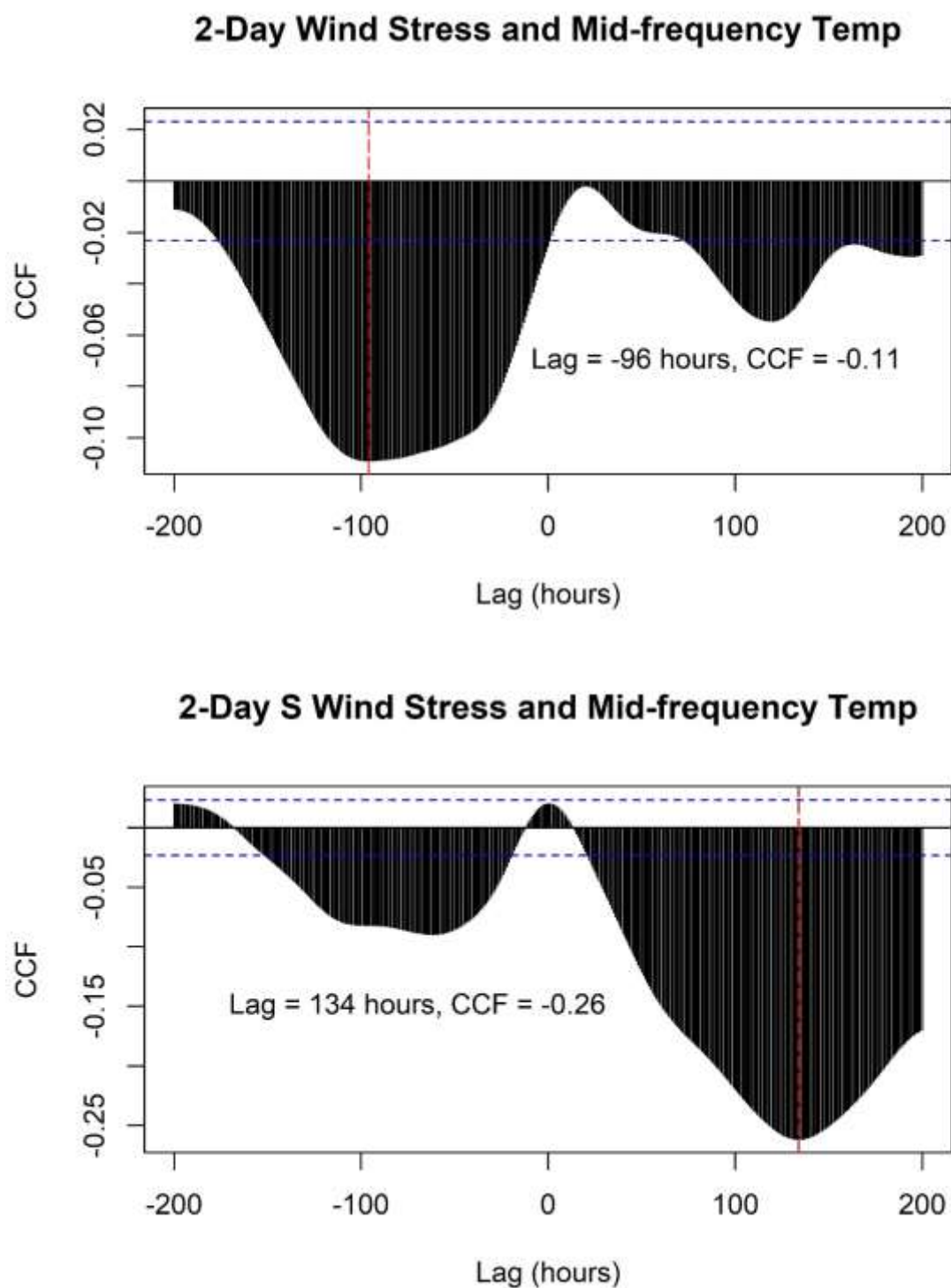
Figure S76. Correlations (CCFs) between a 2-day back-averaged wind stress and mid-frequency temperatures at the shallow location at Taylor's Head. The top panel shows total wind stress, while the bottom panel shows southerly wind stress. Shown on each pane are the dominant lags and corresponding CCF value for each measure of temperature.
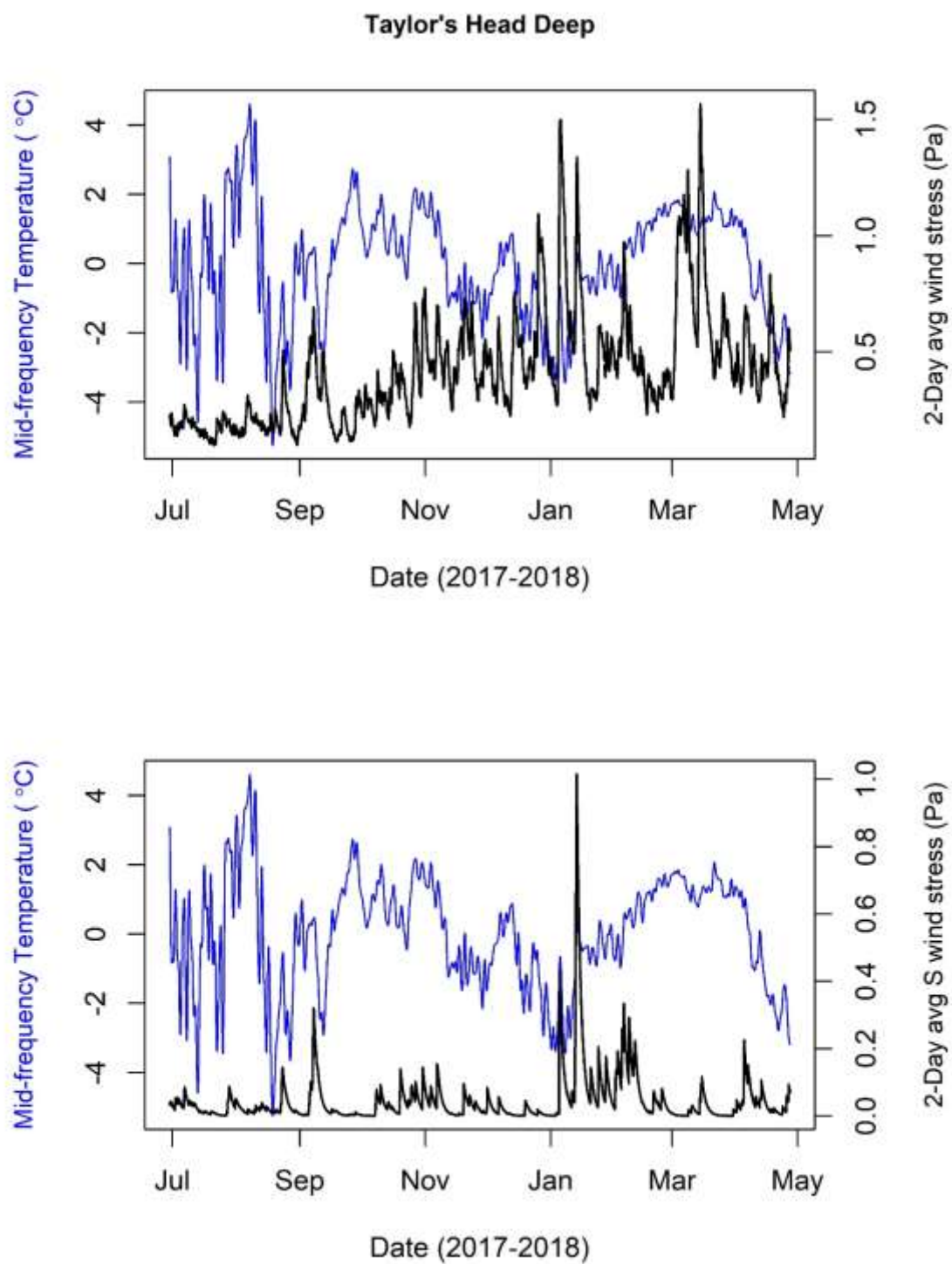
Taylor's Head Deep

Figure S77. 2-day back-averaged wind stress plotted against mid-frequency temperatures at the deep location at Taylor's Head. The top panel shows total wind stress, while the bottom panel shows southerly wind stress.

2-Day Wind Stress and Mid-frequency Temp

Lag = -110 hours, CCF = -0.11

2-Day S Wind Stress and Mid-frequency Temp

Lag = 134 hours, CCF = -0.24
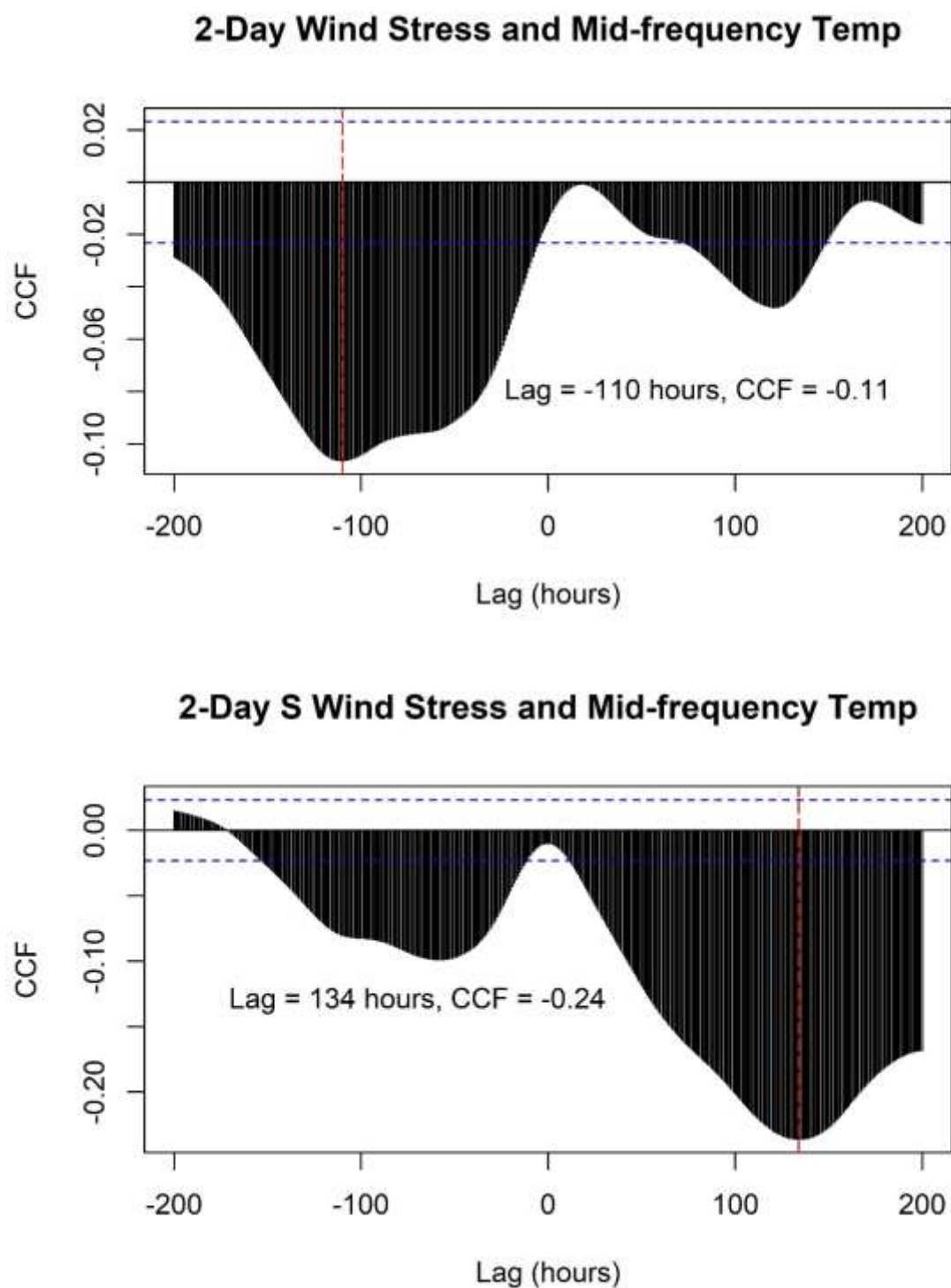
Figure S78. Correlations (CCFs) between a 2-day back-averaged wind stress and mid-frequency temperatures at the deep location at Taylor's Head. The top panel shows total wind stress, while the bottom panel shows southerly wind stress. Shown on each pane are the dominant lags and corresponding CCF value for each measure of temperature.

Port Joli

Port Joli Sandy

Port Joli Muddy
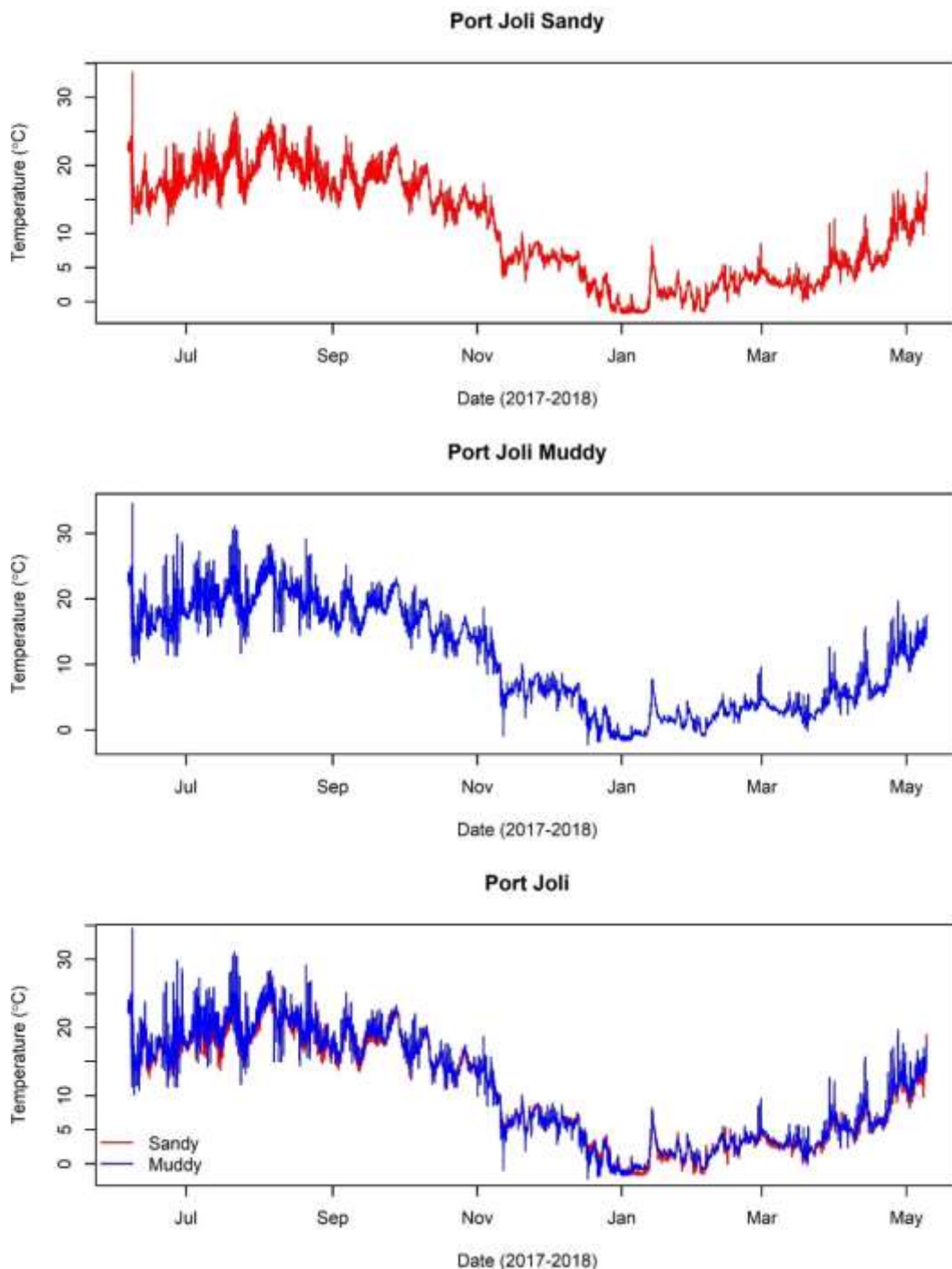
Port Joli

Figure S79. Temperature records at the sandy and muddy locations at Port Joli, recorded from June 6, 2017 to May 9, 2018.
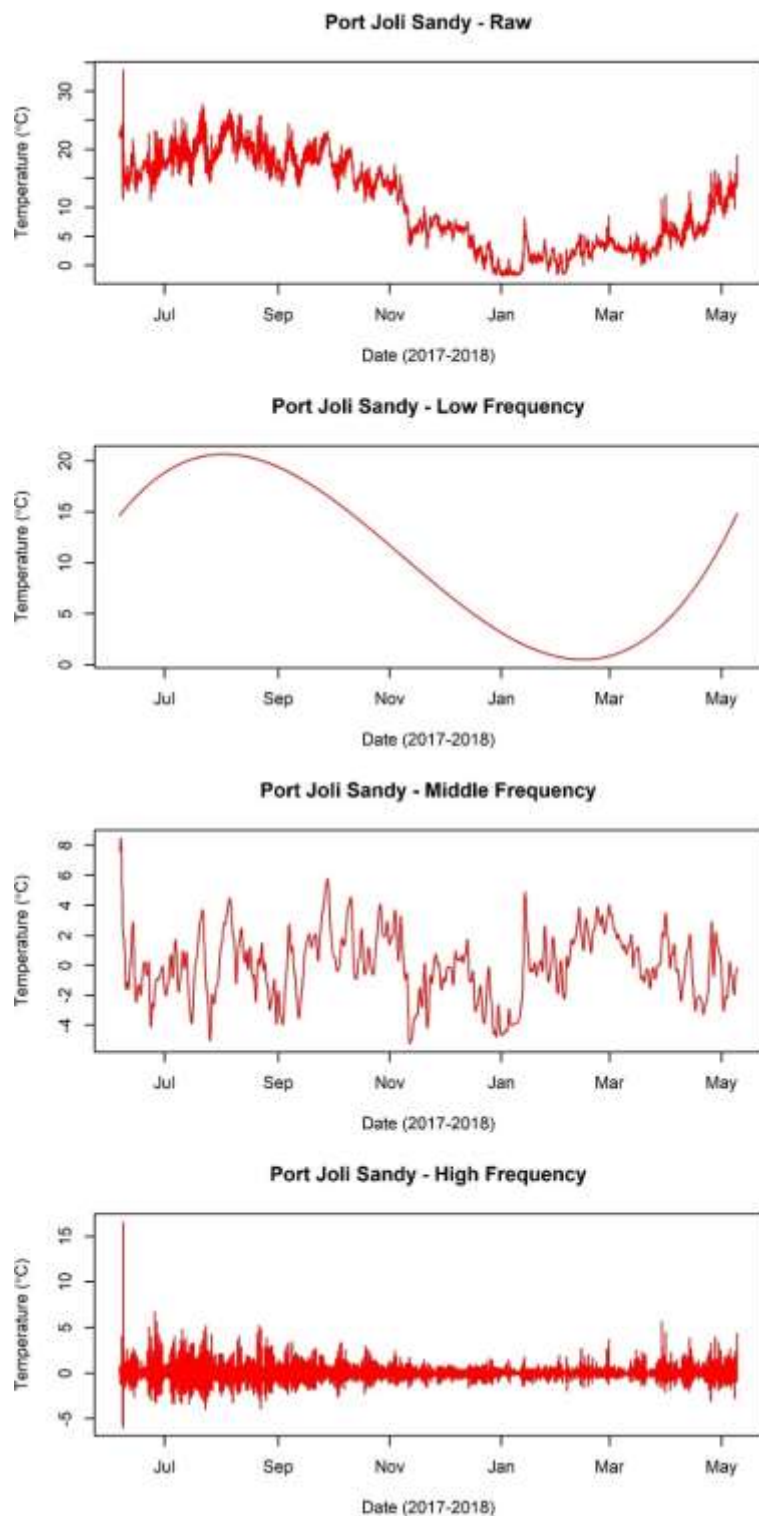
Figure S80. Raw temperatures (top panel), low (second panel), middle (third panel), and high frequency (bottom panel) temperature variability isolated at the sandy location at Port Joli.

Figure S81. Raw temperatures (top panel), low (second panel), middle (third panel), and high frequency (bottom panel) temperature variability isolated at the muddy location at Port Joli.

Figure S82. High frequency temperature changes at the sandy and muddy locations at Port Joli (top two panels). The bottom panel shows the results of a spectral analysis, with the dominant frequencies shown in dotted lines and the period shown in text.

Port Joli Sandy

Port Joli Muddy

Figure S83. Average temperature changes over the 12.42-hour tidal cycle at Port Joli sandy and muddy, calculated for the summer period (June-October 2017).

Port Joli Sandy

Port Joli Muddy

Figure S84. Average temperature changes over the 24-hour daily heating and cooling cycle at Port Joli sandy and muddy, calculated for the summer period (June-October 2017).

Port Joli Sandy

Figure S85. A 17-day back-averaged upwelling index plotted against average daily temperatures (top panel) and mid-frequency temperatures (bottom panel) at the sandy location at Port Joli.

Figure S86. Correlations (CCFs) between a 17-day back-averaged upwelling index and average daily temperatures (top panel), and mid-frequency temperatures (bottom panel) at the sandy location at Port Joli. Shown on each pane are the dominant lags and corresponding CCF value for each measure of temperature.

Port Joli Muddy

Figure S87. A 17-day back-averaged upwelling index plotted against average daily temperatures (top panel) and mid-frequency temperatures (bottom panel) at the muddy location at Port Joli.

Upwelling and Mean Daily Temperature

Lag = -57 days, CCF = -0.40

Upwelling and Mid-frequency Temp

Lag = 0 days, CCF = -0.33
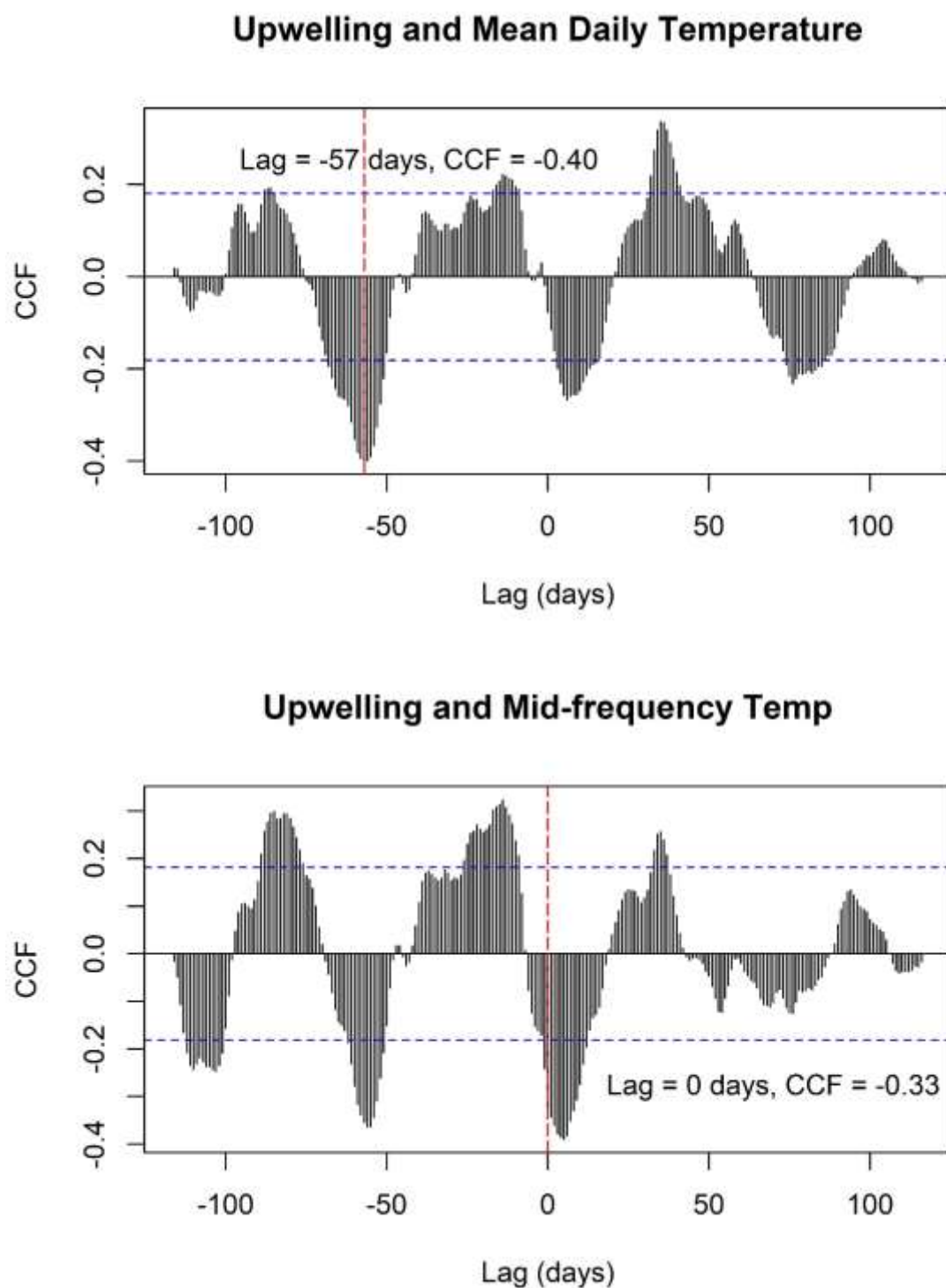
Figure S88. Correlations (CCFs) between a 17-day back-averaged upwelling index and average daily temperatures (top panel), and mid-frequency temperatures (bottom panel) at the muddy location at Port Joli. Shown on each pane are the dominant lags and corresponding CCF value for each measure of temperature.
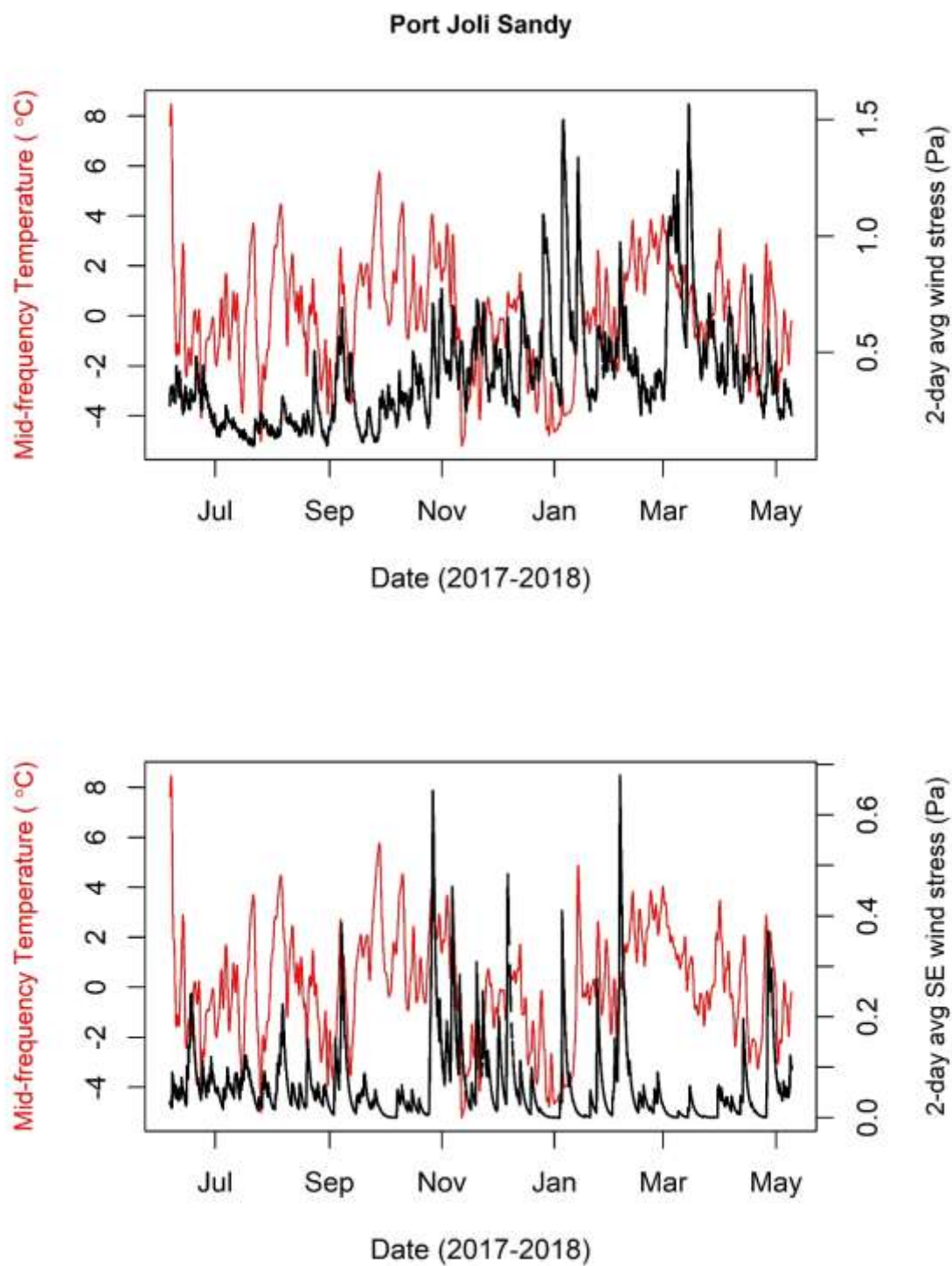
Figure S89. 2-day back-averaged wind stress plotted against mid-frequency temperatures at the sandy location at Port Joli. The top panel shows total wind stress, while the bottom panel shows southeasterly wind stress.
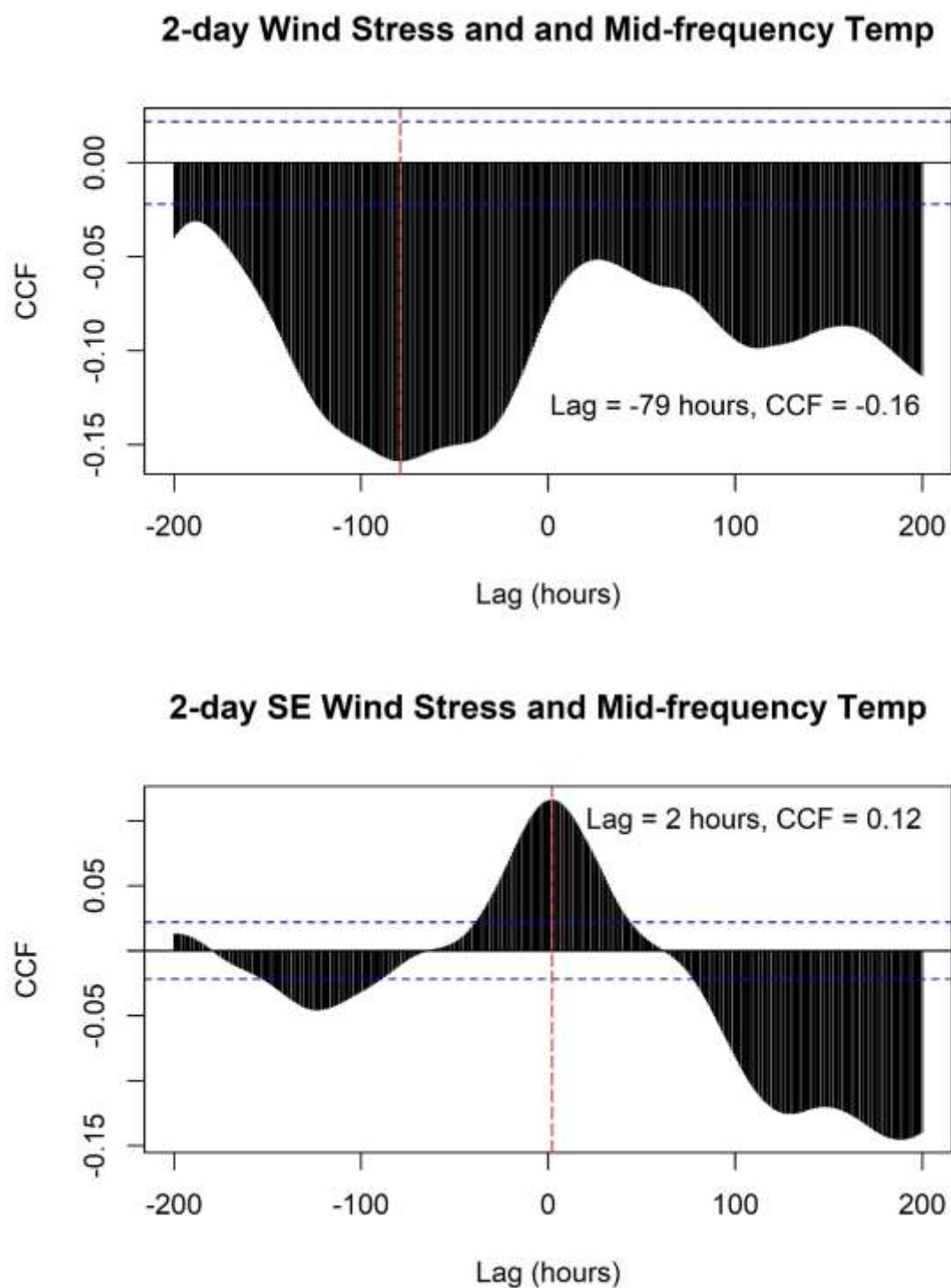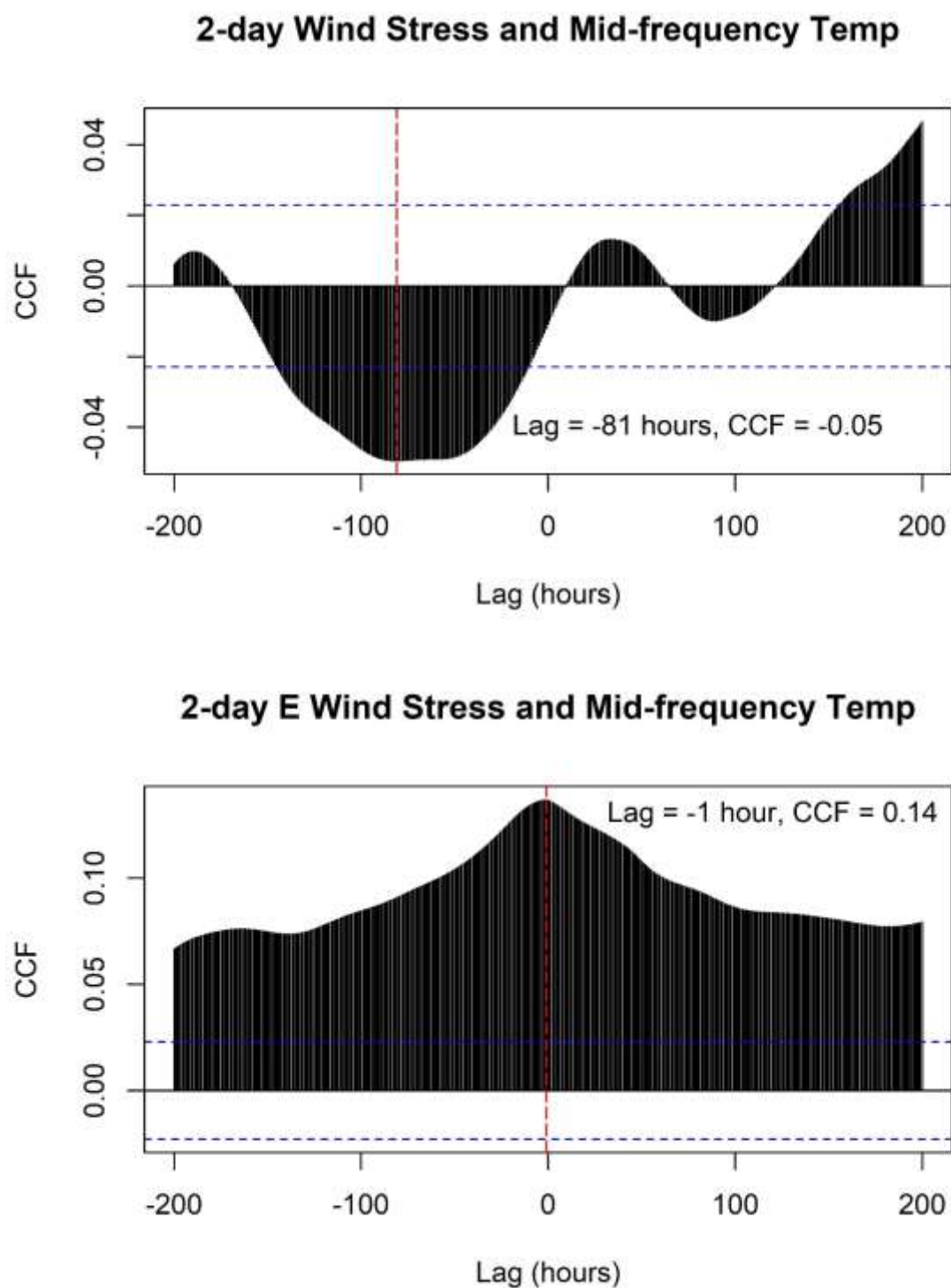
Figure S90. Correlations (CCFs) between a 2-day back-averaged wind stress and mid-frequency temperatures at the sandy location at Port Joli. The top panel shows total wind stress, while the bottom panel shows southeasterly wind stress. Shown on each pane are the dominant lags and corresponding CCF value for each measure of temperature.
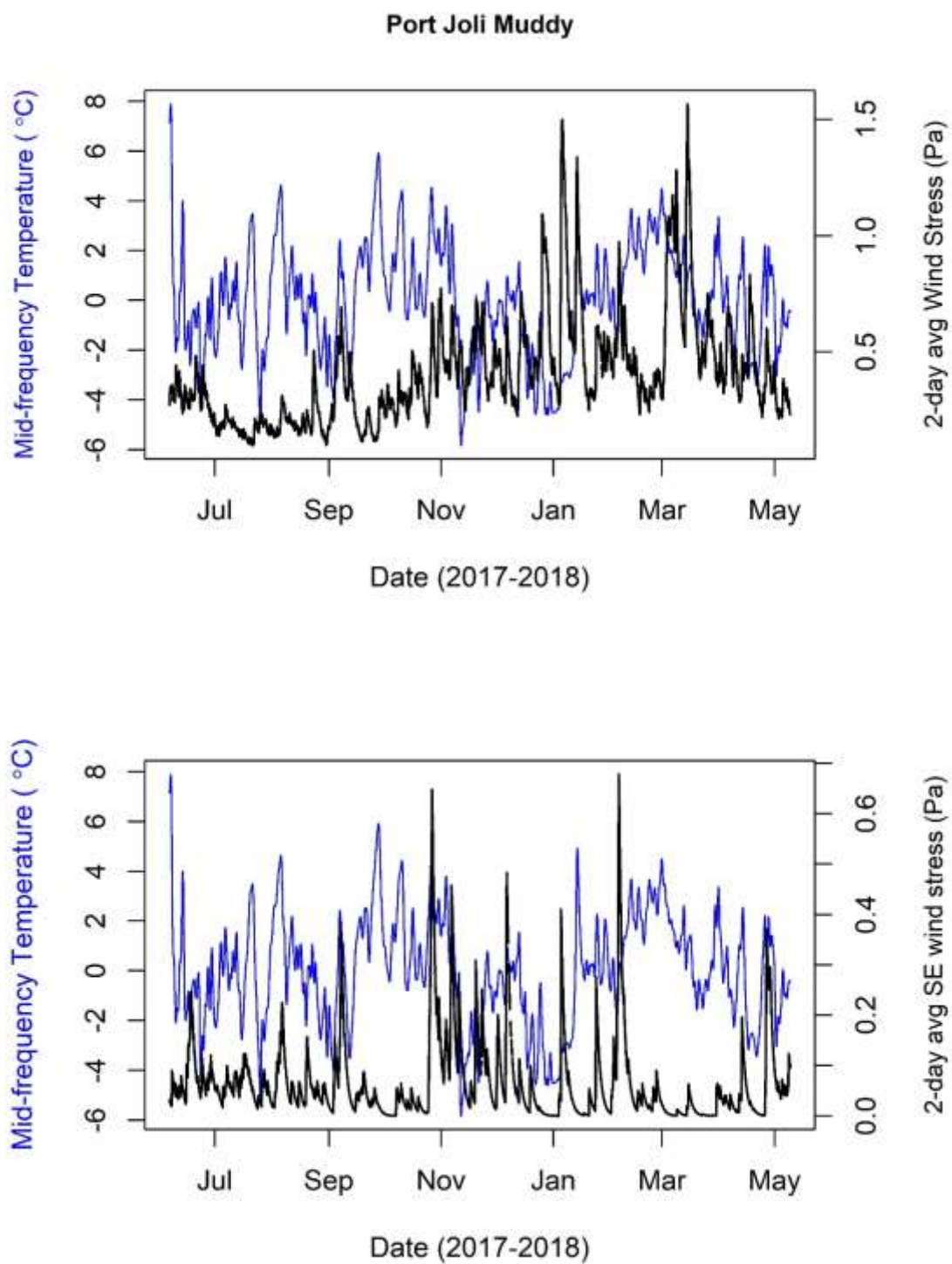
Port Joli Muddy

Figure S91. 2-day back-averaged wind stress plotted against mid-frequency temperatures at the muddy location at Port Joli. The top panel shows total wind stress, while the bottom panel shows southeasterly wind stress.

2-day Wind Stress and Mid-frequency Temp

Lag = -85 hours, CCF = -0.16

2-day SE Wind Stress and Mid-frequency Temp

Lag = 1 hour, CCF = 0.113
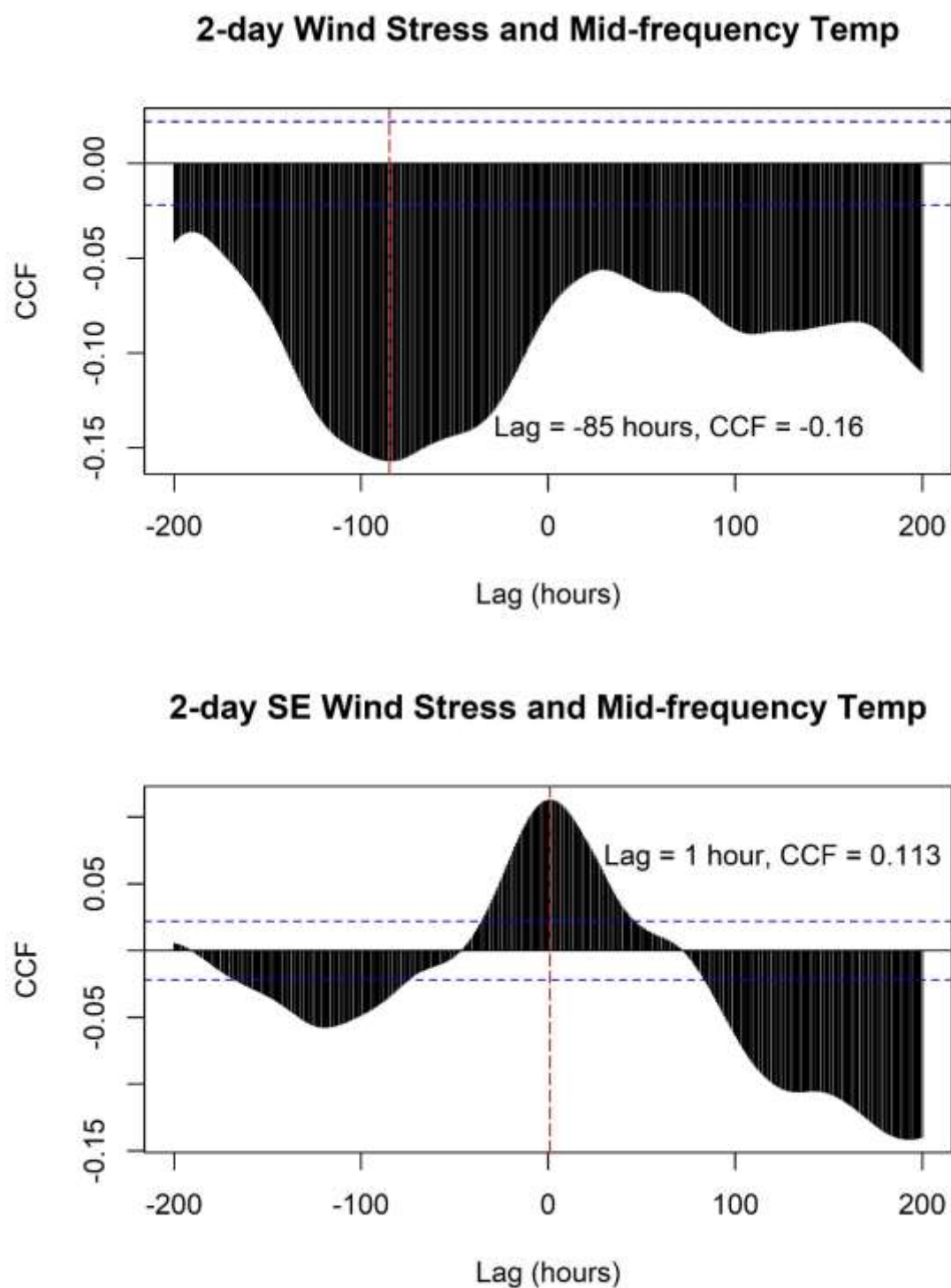
Figure S92. Correlations (CCFs) between a 2-day back-averaged wind stress and mid-frequency temperatures at the muddy location at Port Joli. The top panel shows total wind stress, while the bottom panel shows southeasterly wind stress. Shown on each pane are the dominant lags and corresponding CCF value for each measure of temperature.

Sacrifice Island

Sacrifice Deep

Sacrifice Shallow
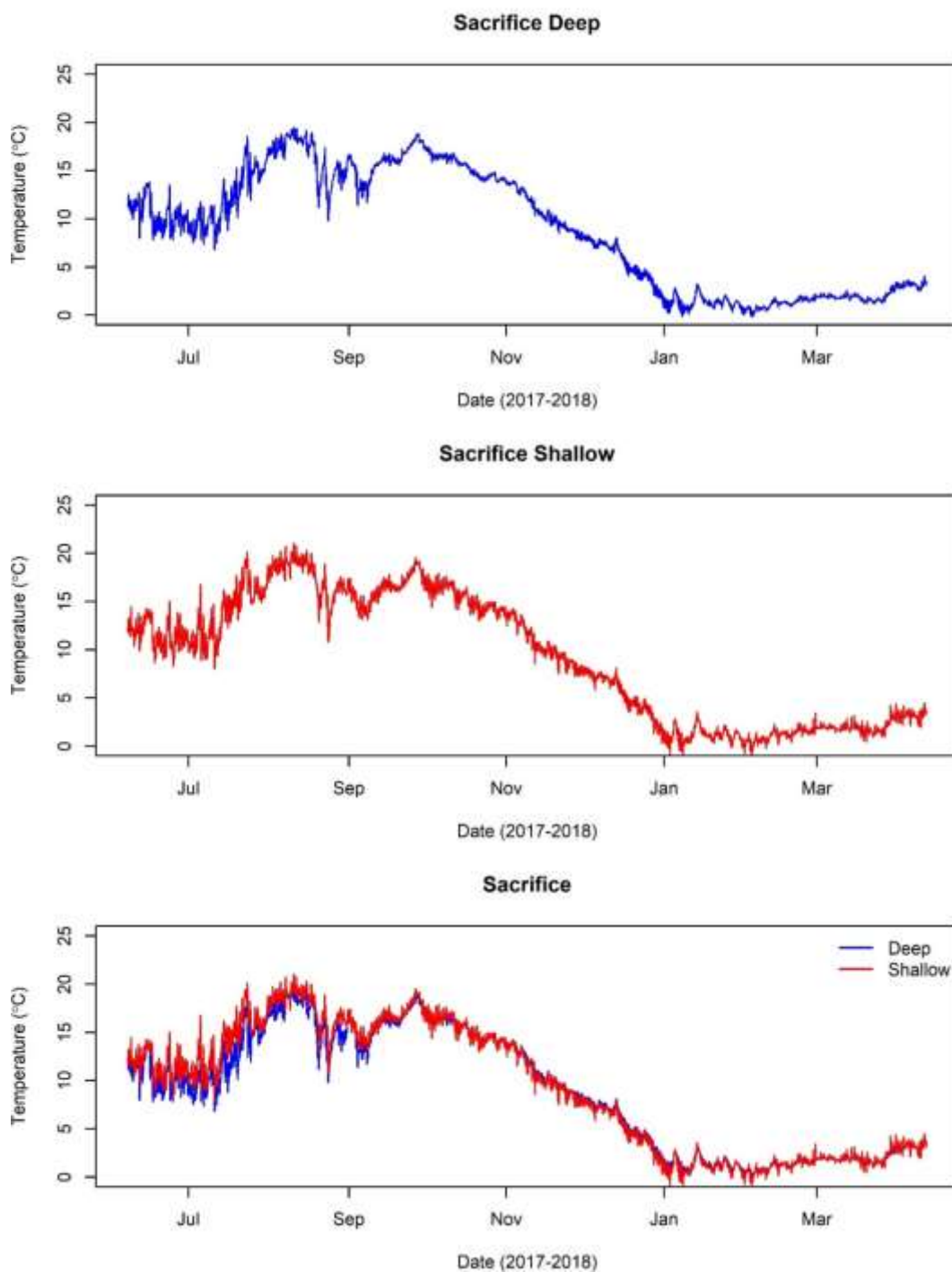
Sacrifice

Figure S93. Temperature records at the deep and shallow locations at Sacrifice Island, recorded from June 6, 2017 to May 9, 2018.
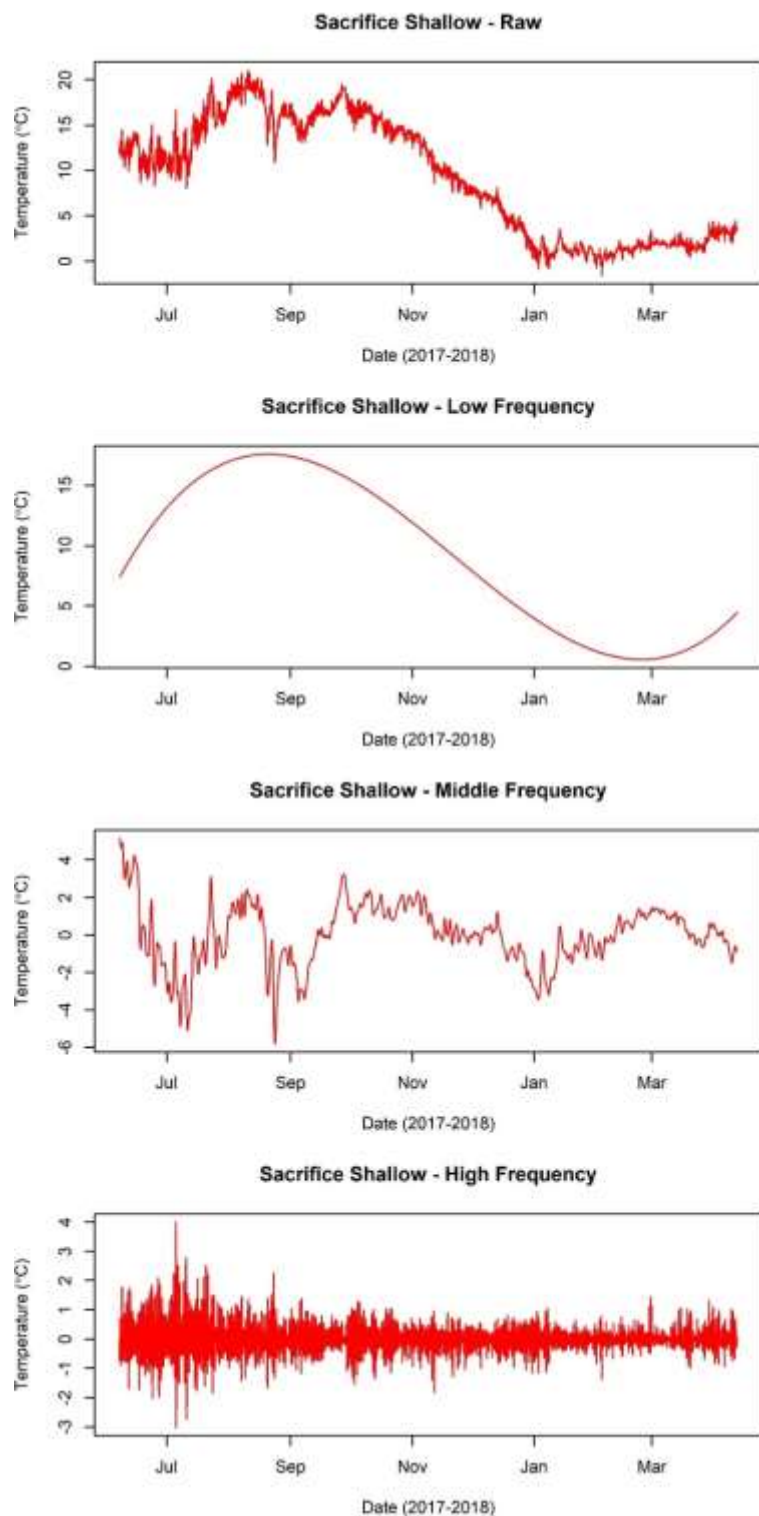
Figure S94. Raw temperatures (top panel), low (second panel), middle (third panel), and high frequency (bottom panel) temperature variability isolated at the shallow location at Sacrifice Island.
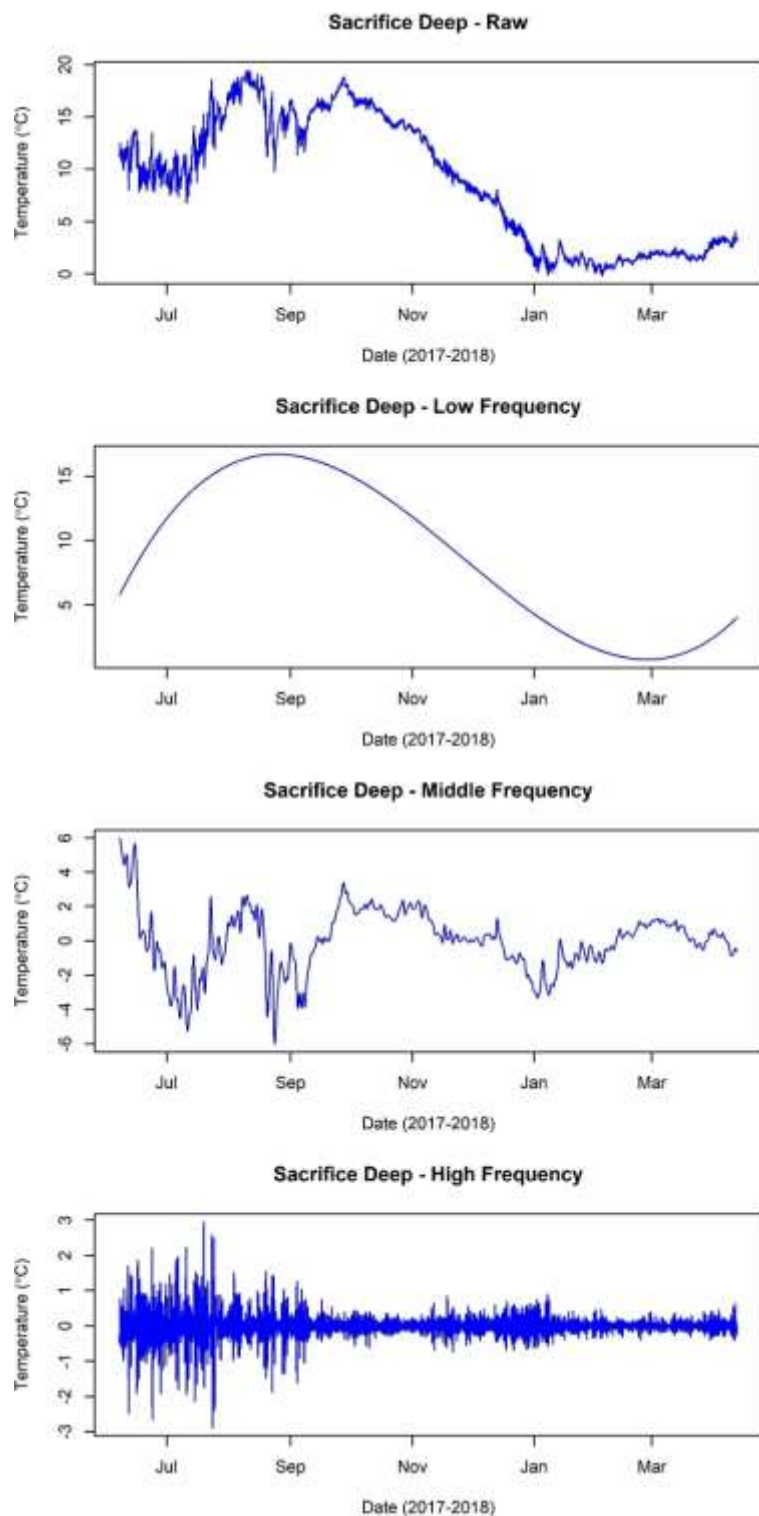
Figure S95. Raw temperatures (top panel), low (second panel), middle (third panel), and high frequency (bottom panel) temperature variability isolated at the deep location at Sacrifice Island.
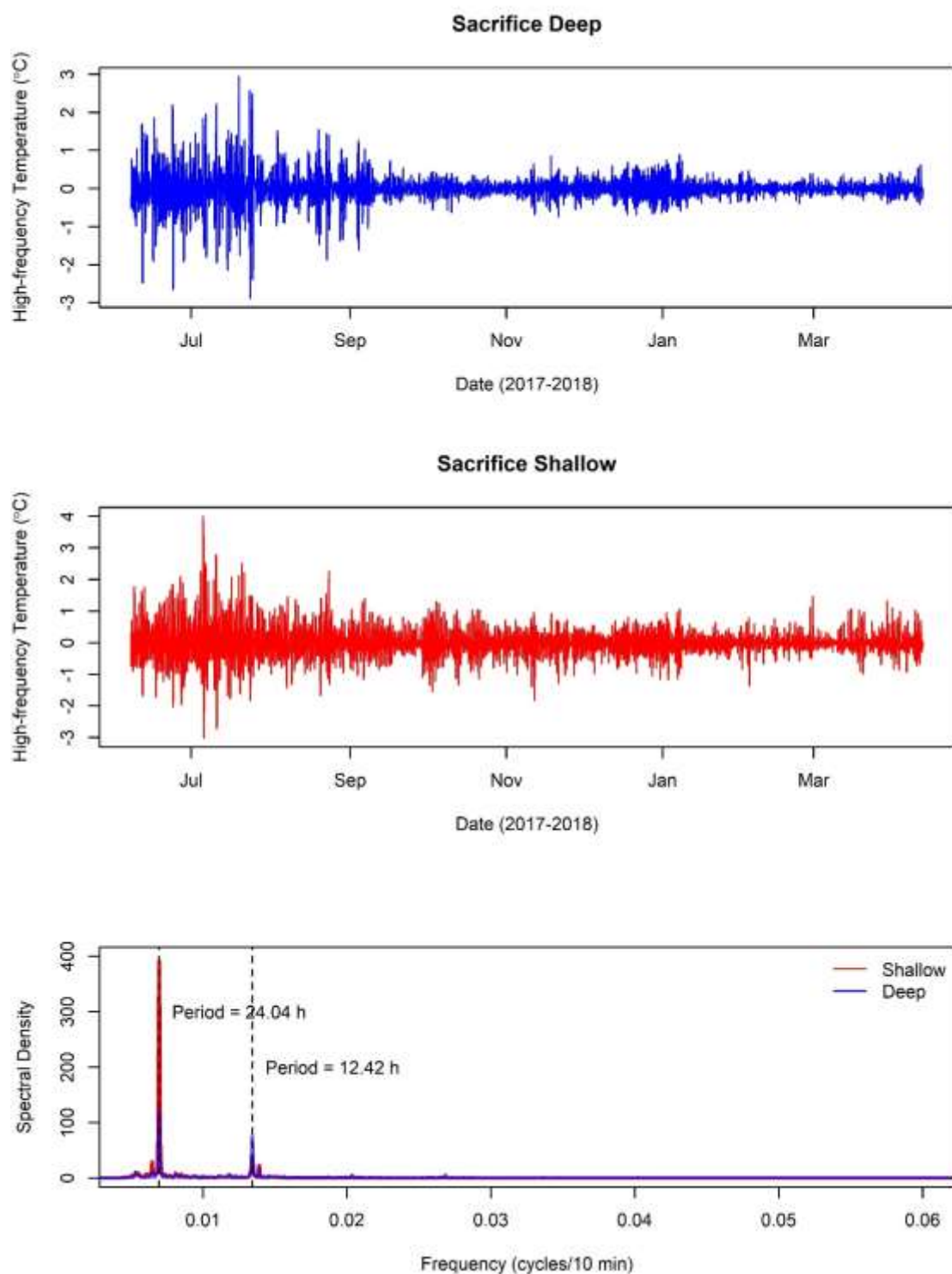
Figure S96. High frequency temperature changes at the deep and shallow locations at Sacrifice Island (top two panels). The bottom panel shows the results of a spectral analysis, with the dominant frequencies shown in dotted lines and the period shown in text.

Sacrifice Deep
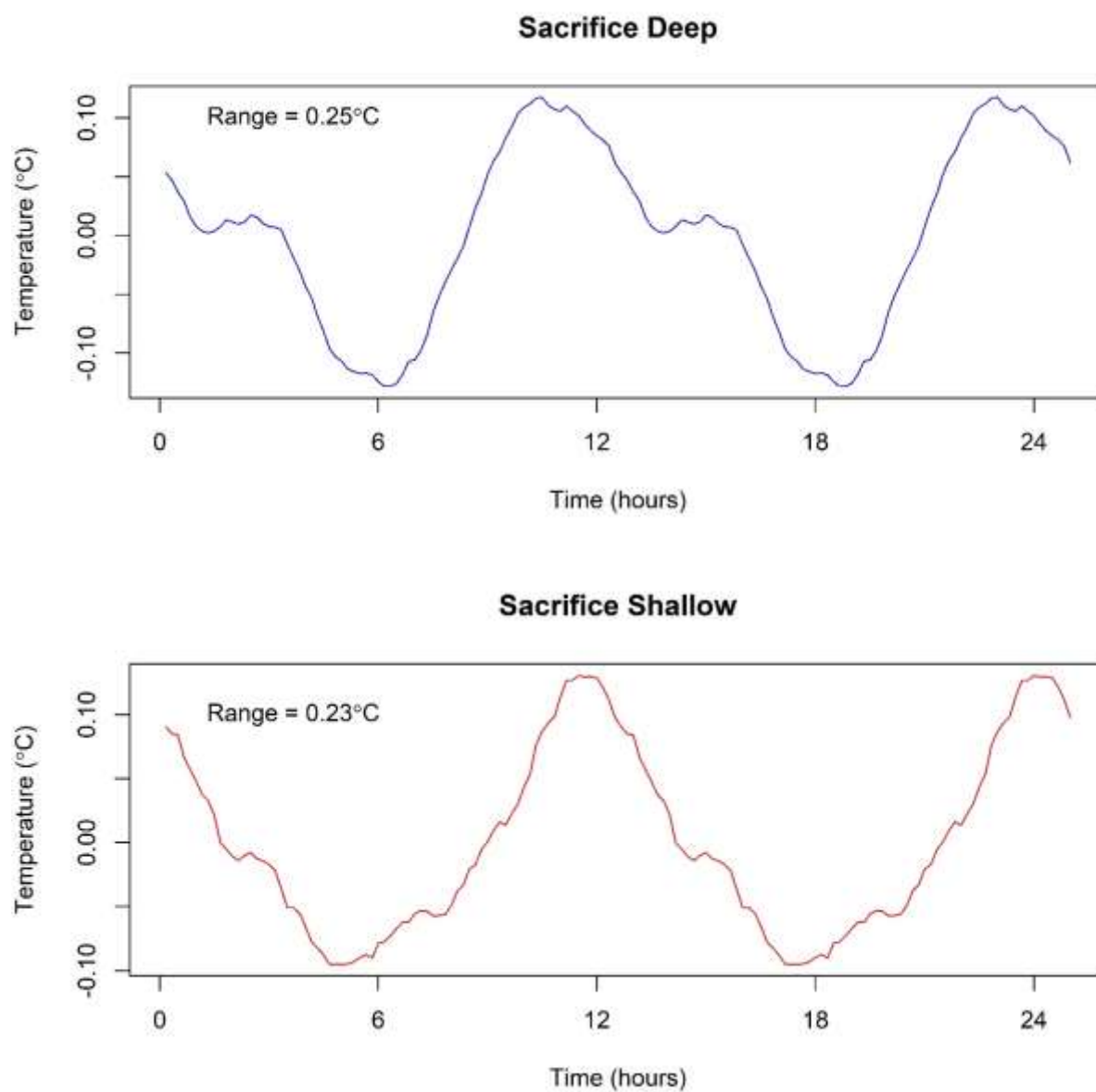
Sacrifice Shallow

Figure S97. Average temperature changes over the 12.42-hour tidal cycle at Sacrifice Island shallow and deep, calculated for the summer period (June-October 2017).
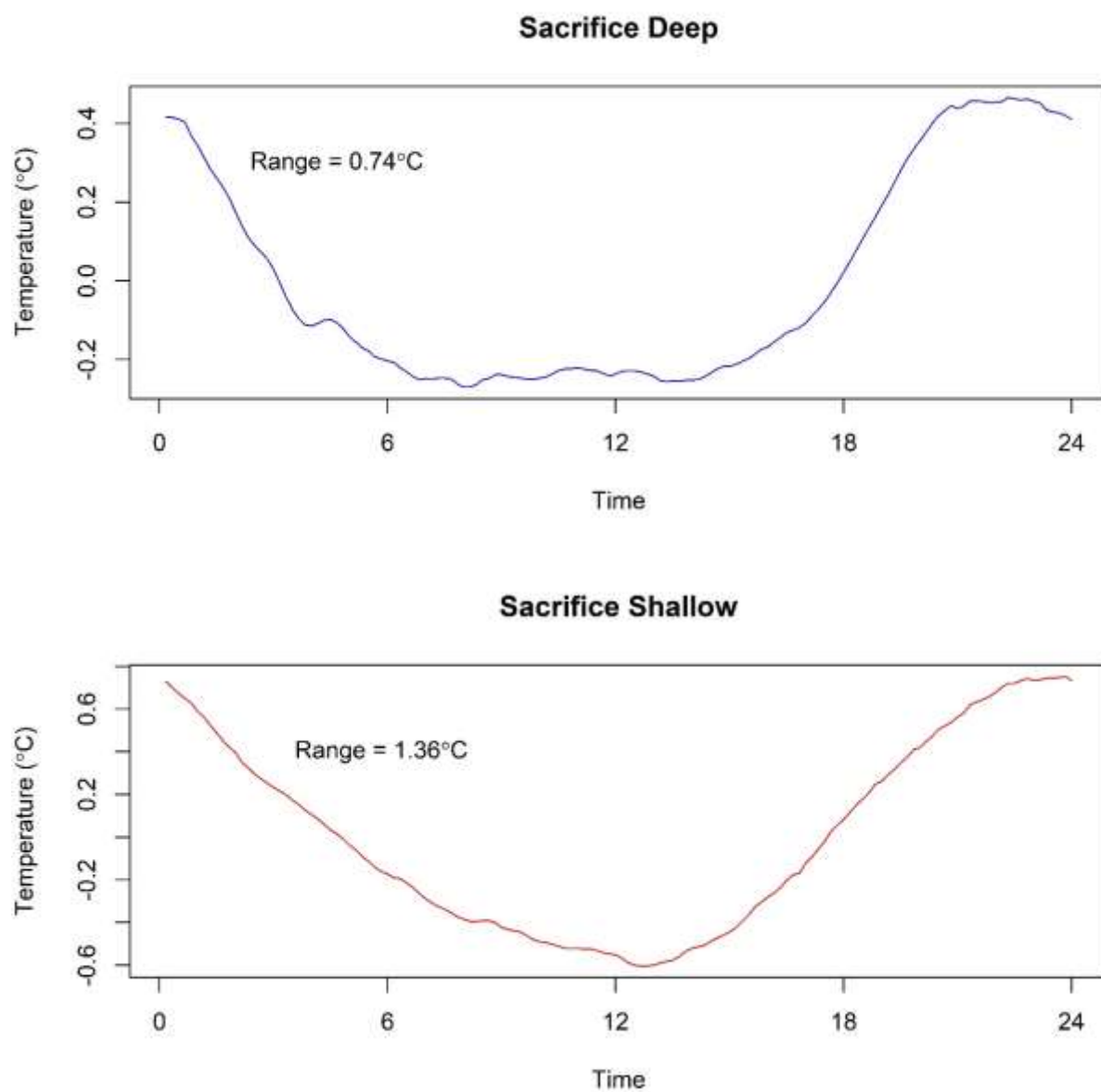
Figure S98. Average temperature changes over the 24-hour daily heating and cooling cycle at Sacrifice Island shallow and deep, calculated for the summer period (June-October 2017).
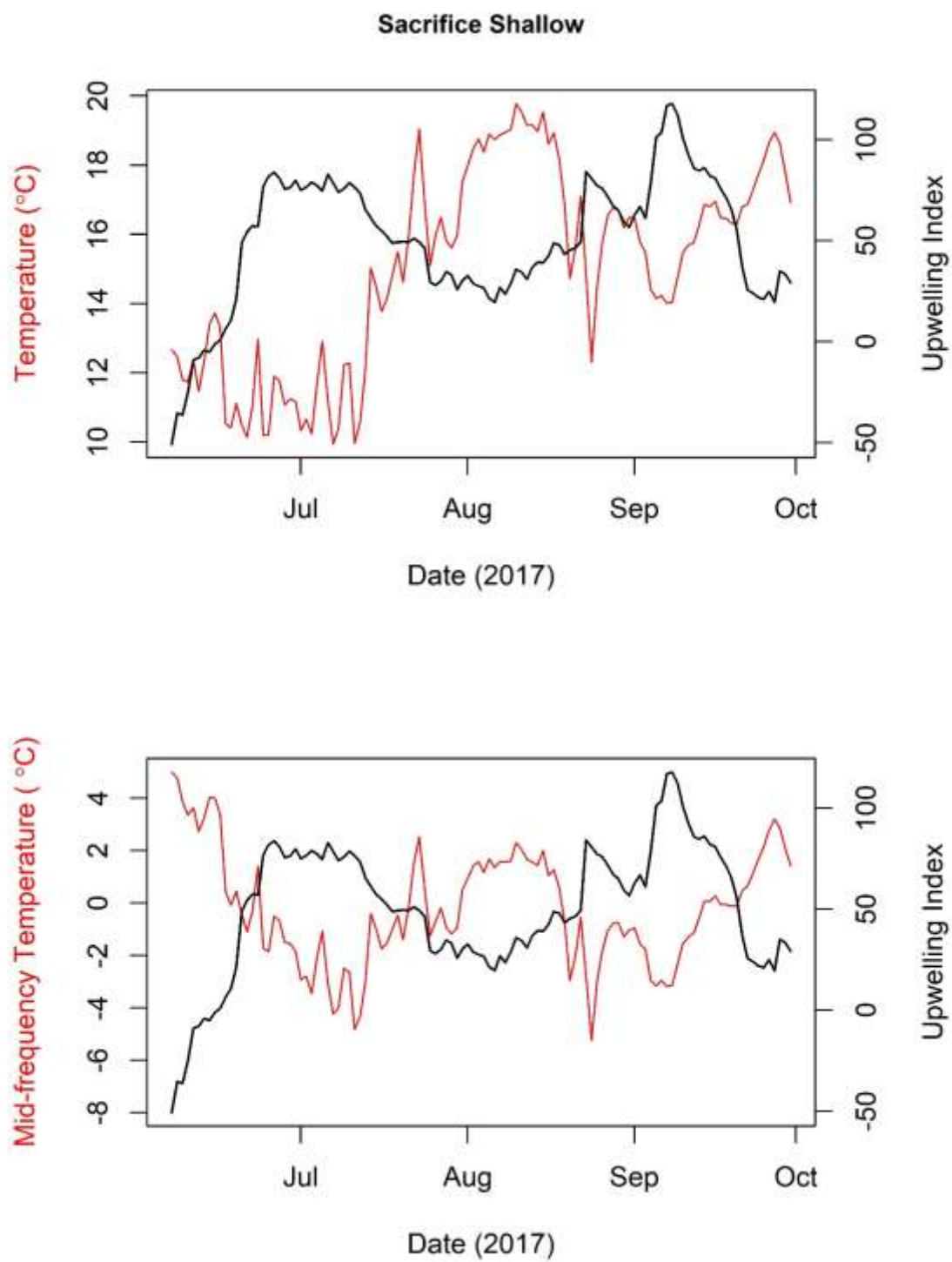
Figure S99. A 17-day back-averaged upwelling index plotted against average daily temperatures (top panel) and mid-frequency temperatures (bottom panel) at the shallow location at Sacrifice Island.
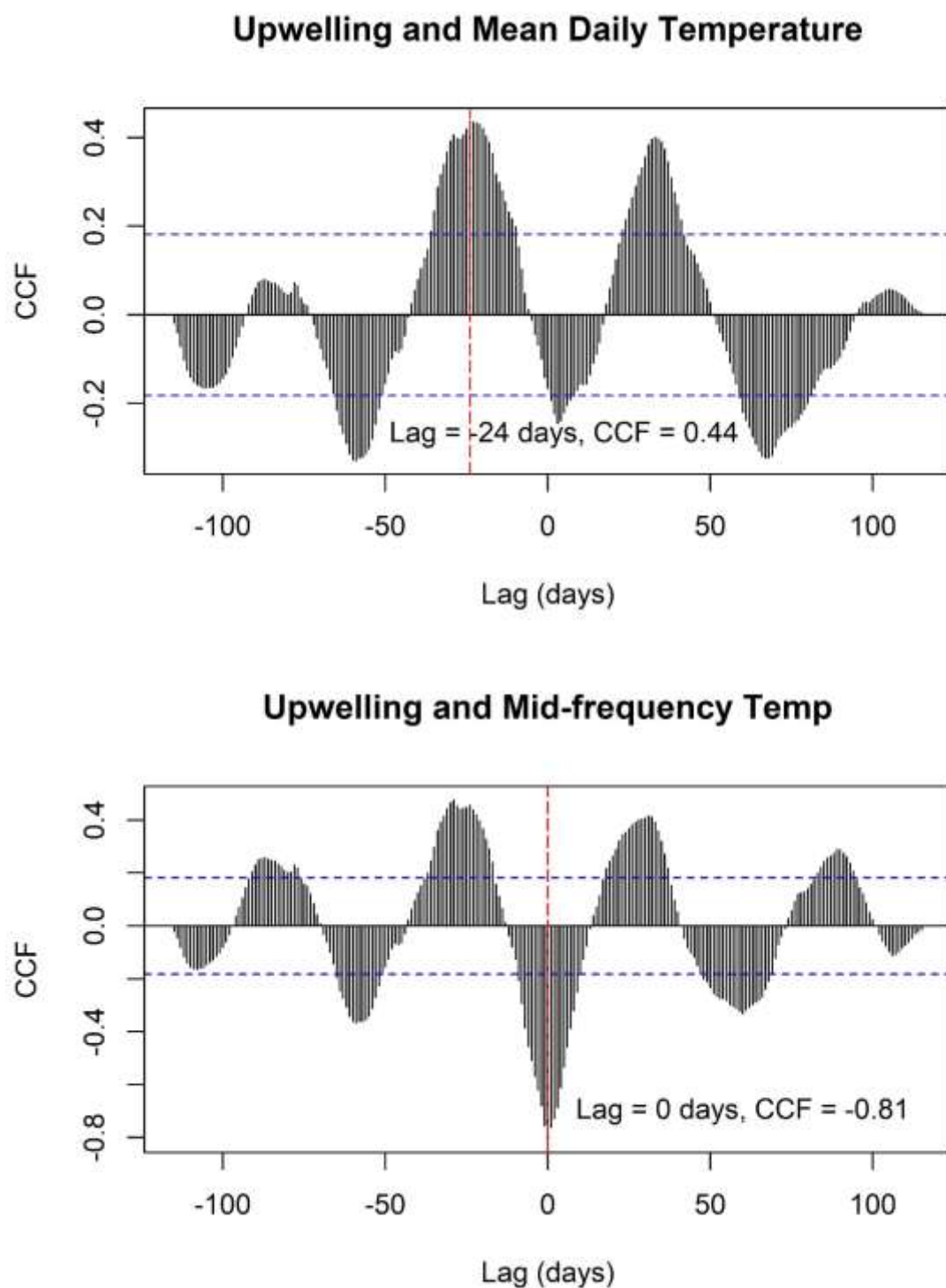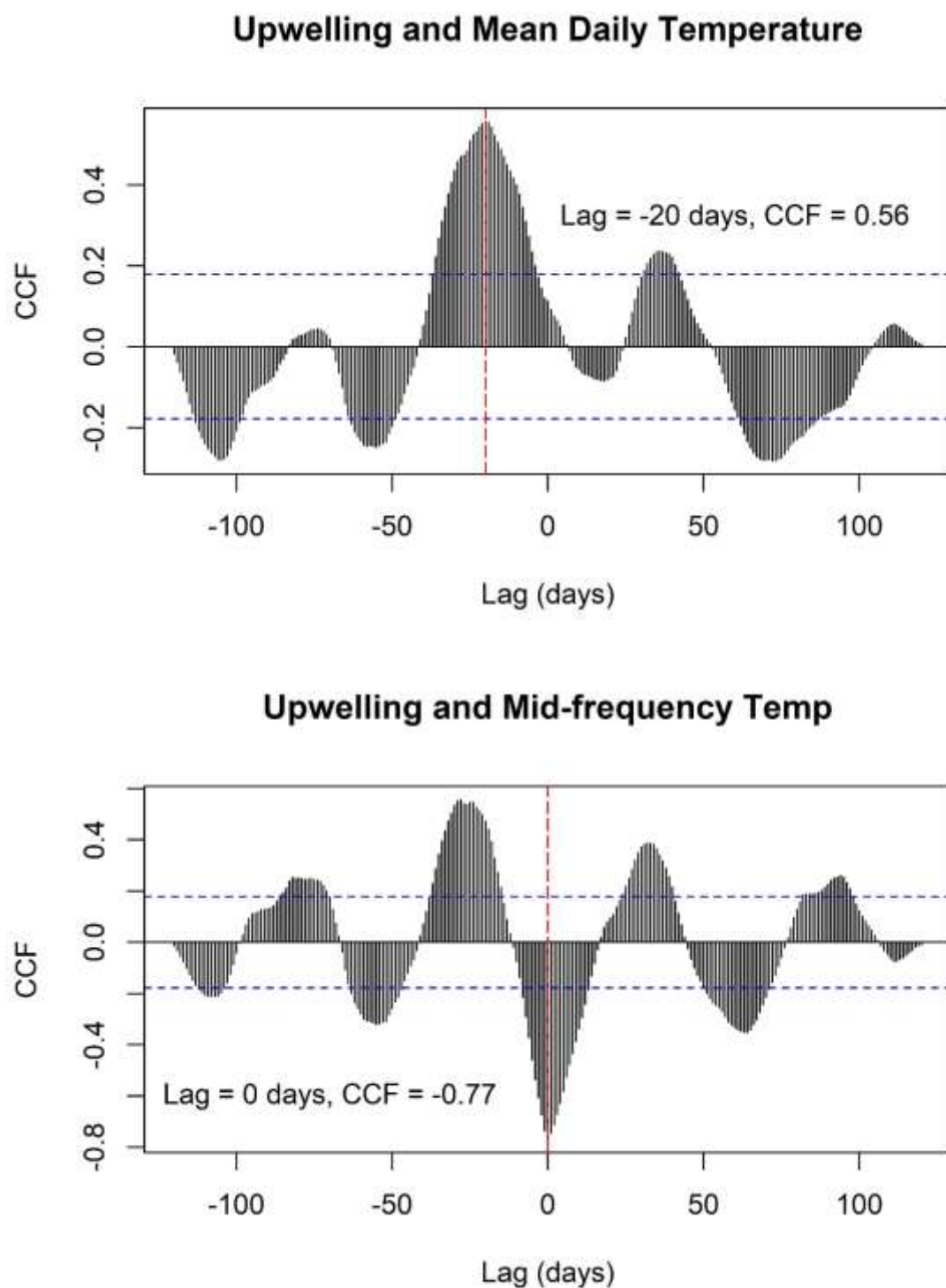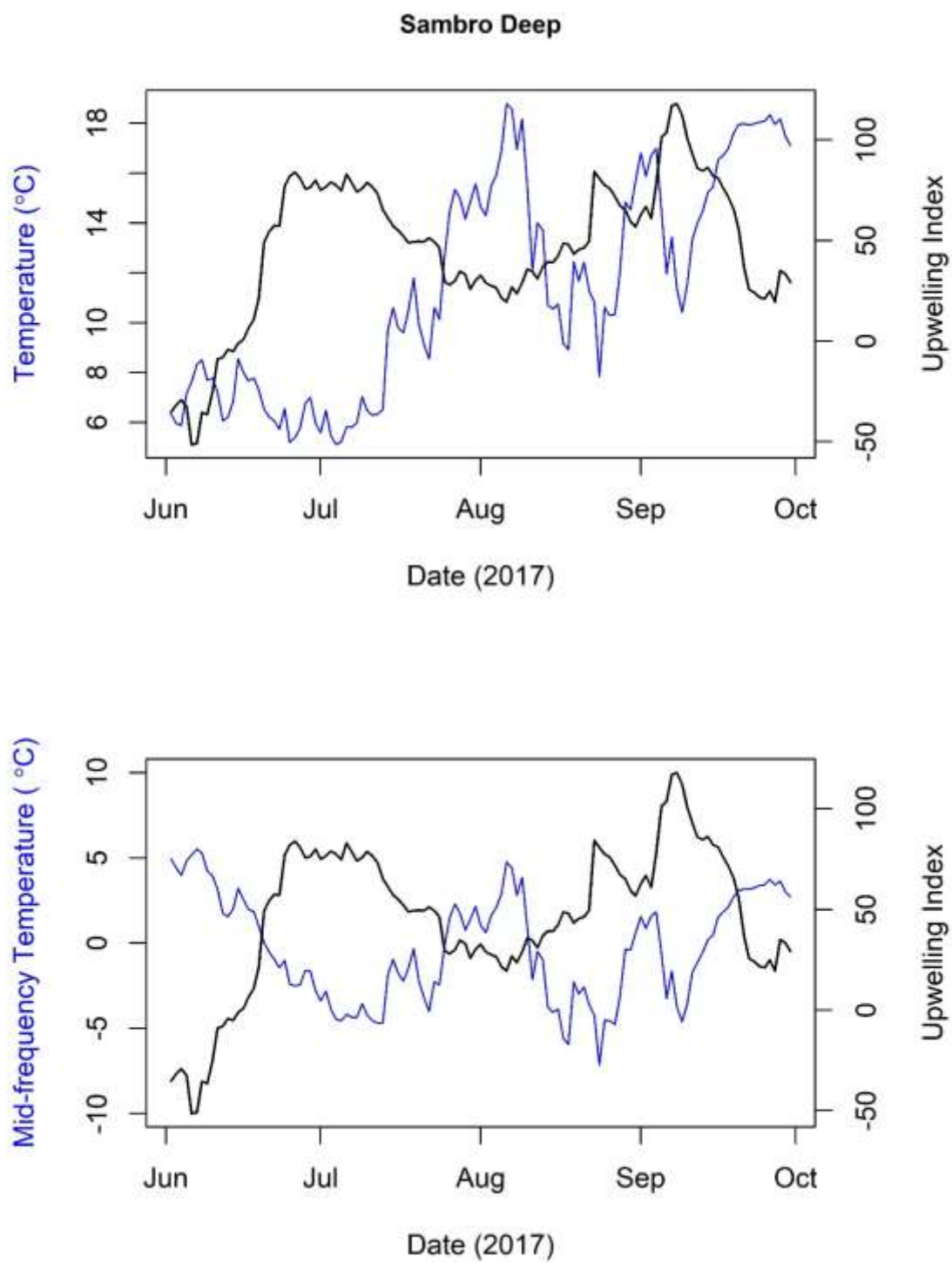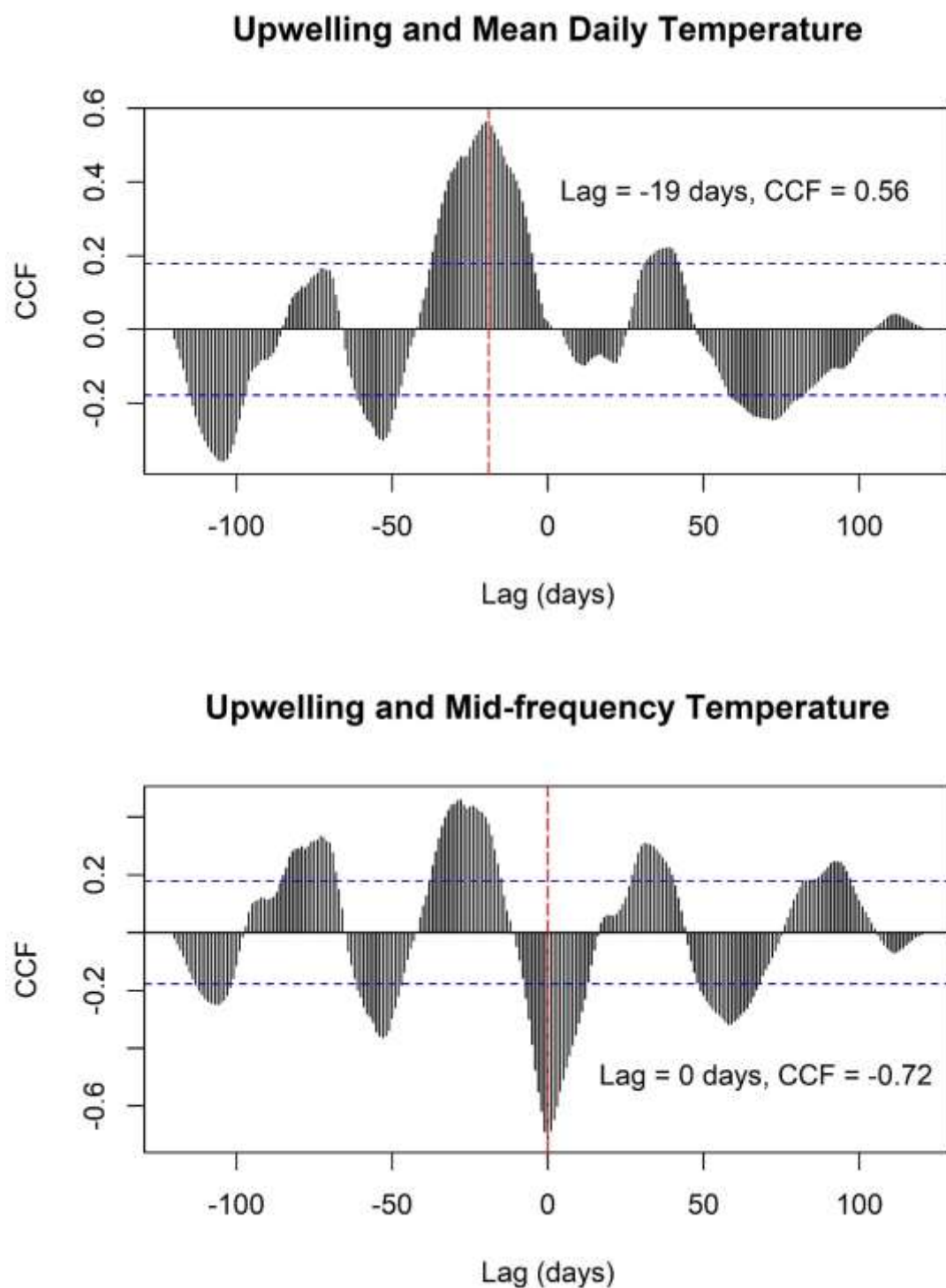
Figure S100. Correlations (CCFs) between a 17-day back-averaged upwelling index and average daily temperatures (top panel), and mid-frequency temperatures (bottom panel) at the shallow location at Sacrifice Island. Shown on each pane are the dominant lags and corresponding CCF value for each measure of temperature.
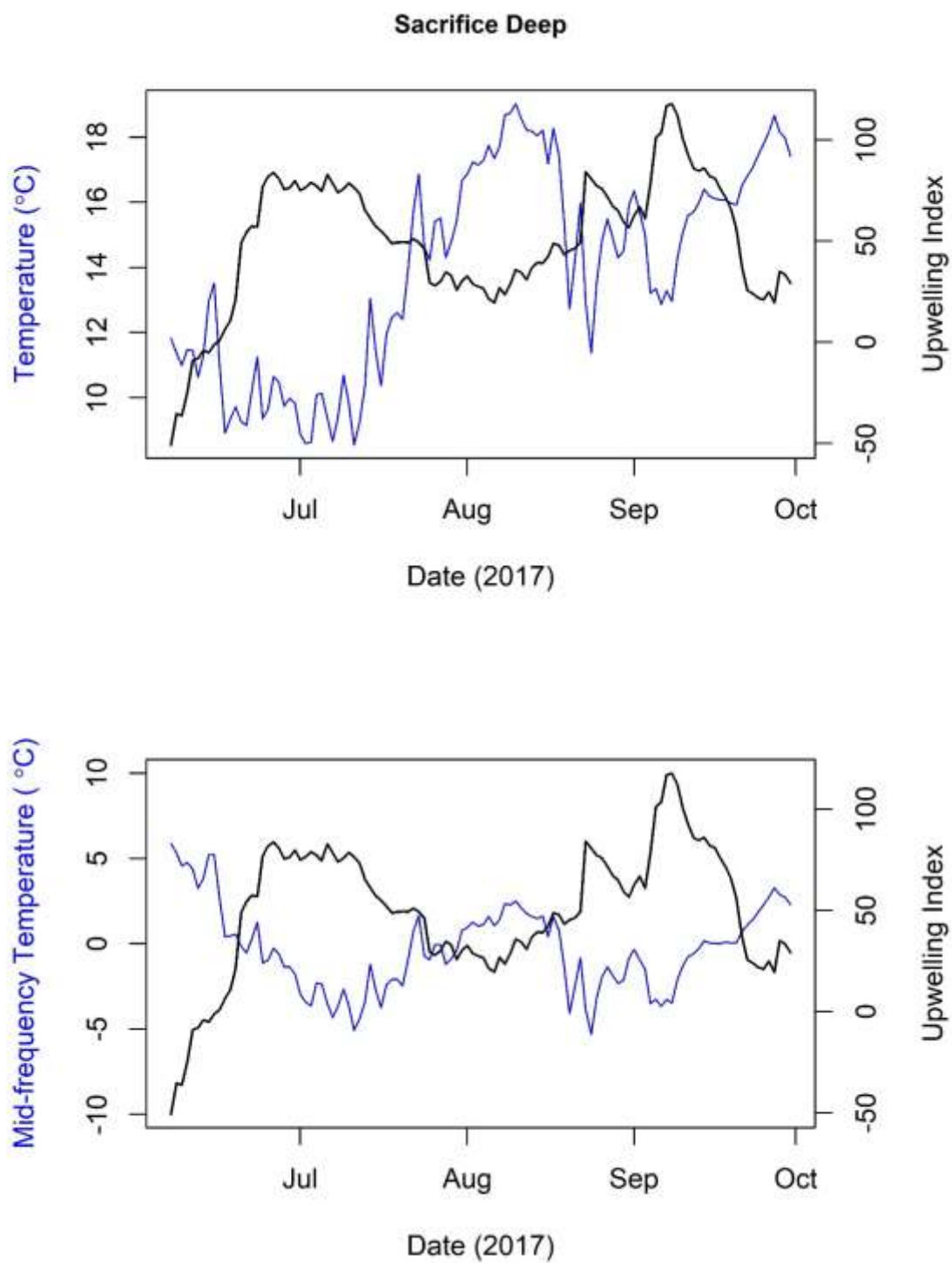
Figure S101. A 17-day back-averaged upwelling index plotted against average daily temperatures (top panel) and mid-frequency temperatures (bottom panel) at the deep location at Sacrifice Island.
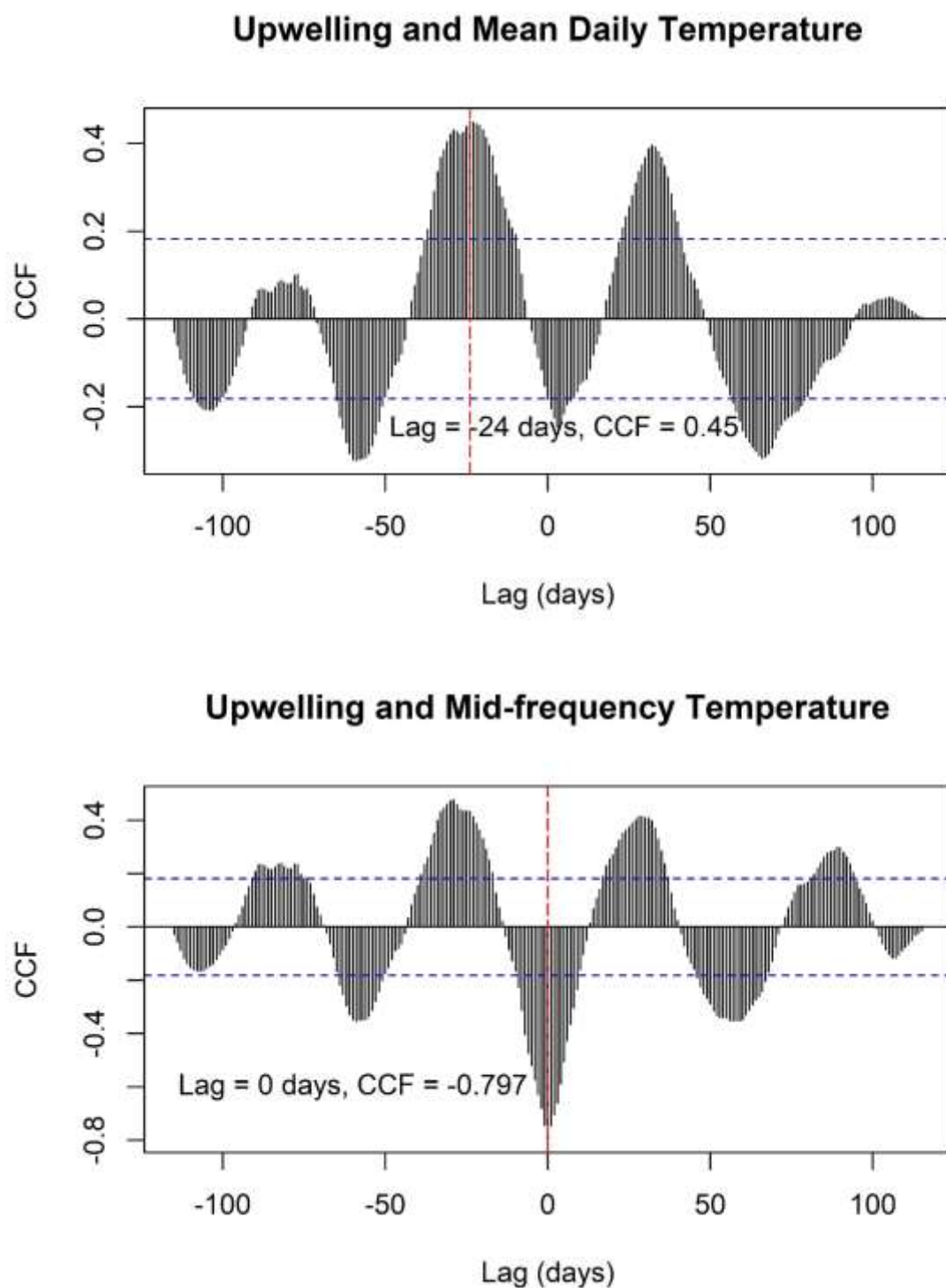
Figure S102. Correlations (CCFs) between a 17-day back-averaged upwelling index and average daily temperatures (top panel), and mid-frequency temperatures (bottom panel) at the deep location at Sacrifice Island. Shown on each pane are the dominant lags and corresponding CCF value for each measure of temperature.
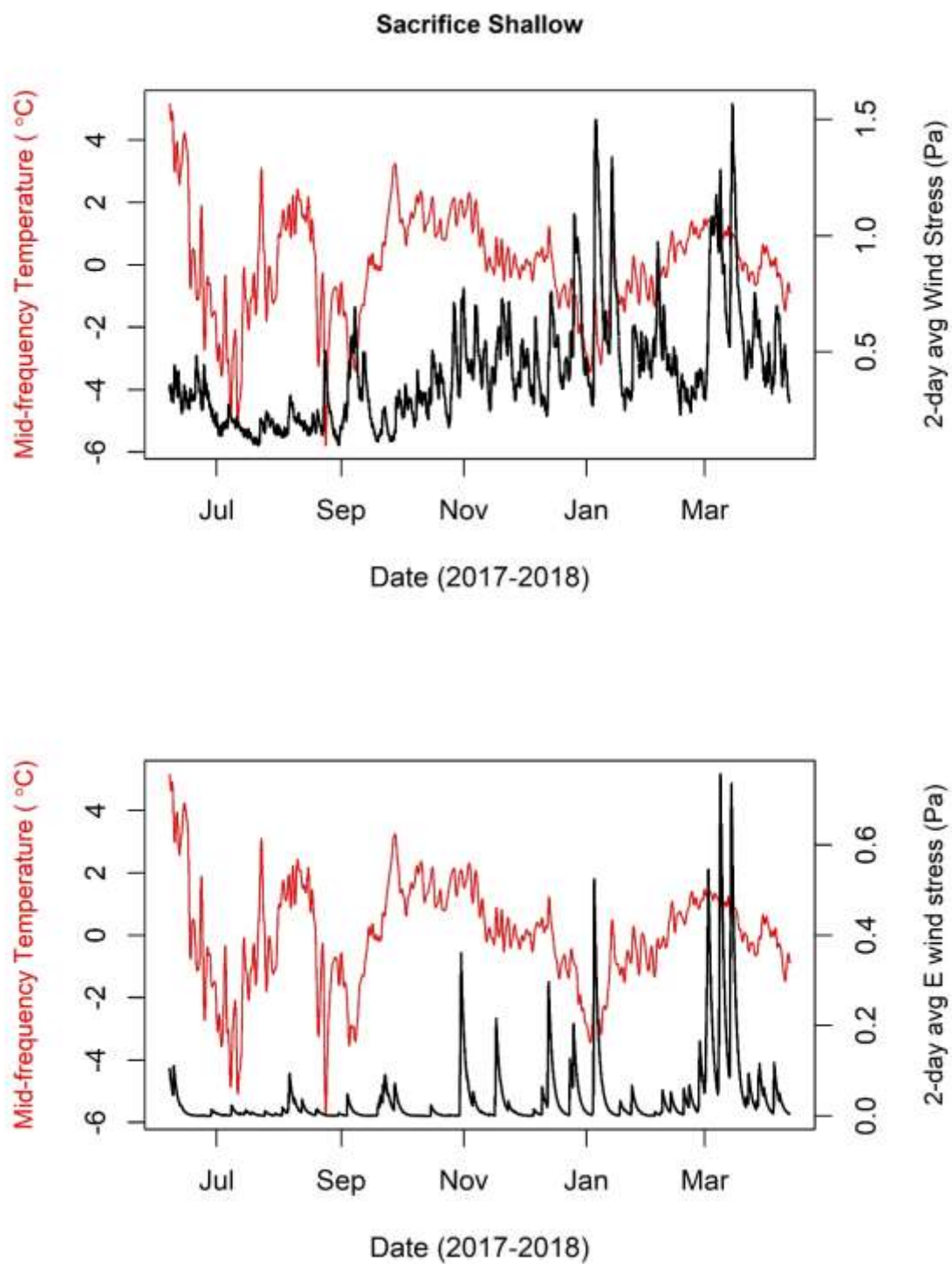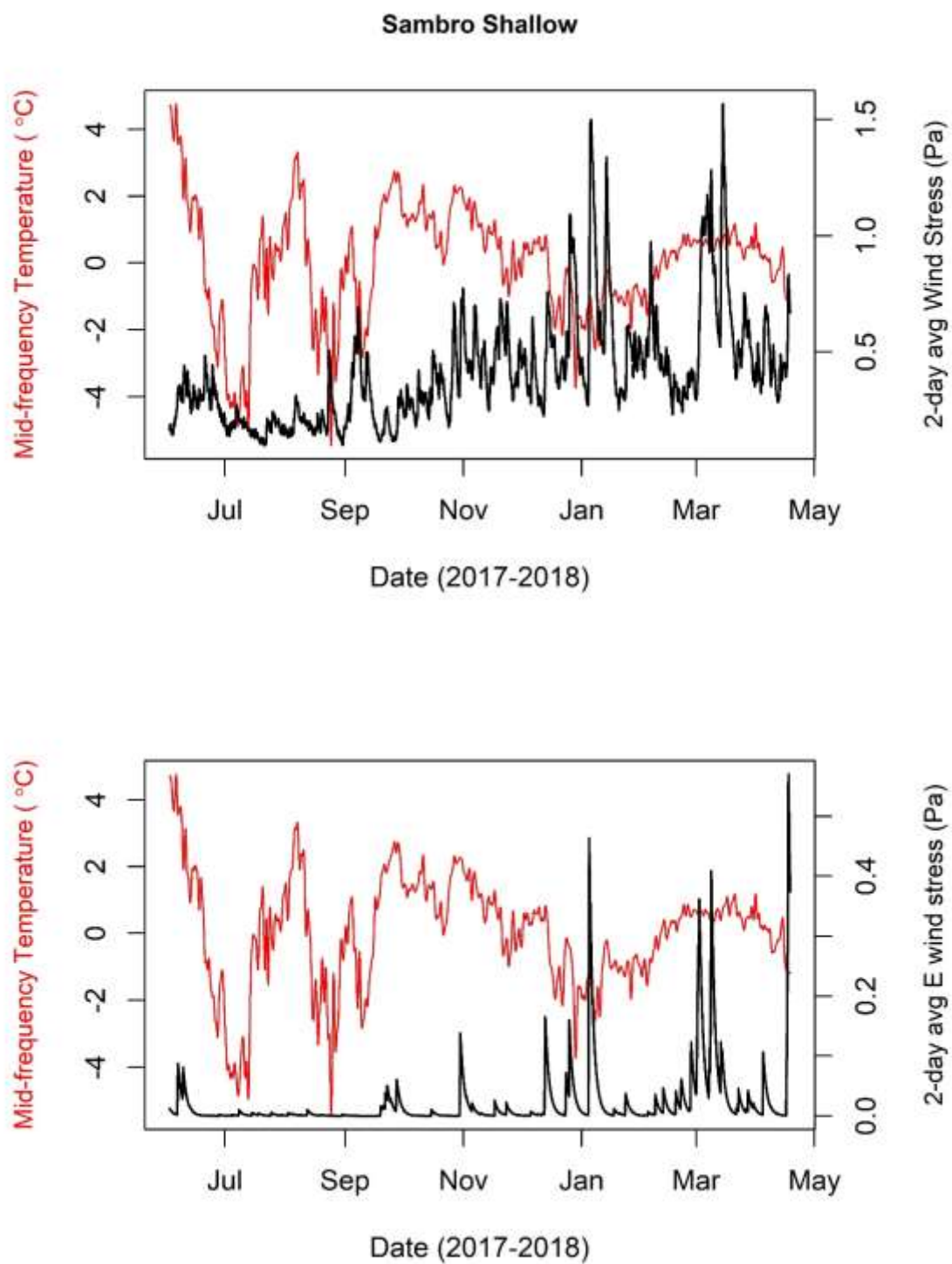
Figure S103. 2-day back-averaged wind stress plotted against mid-frequency temperatures at the shallow location at Sacrifice Island. The top panel shows total wind stress, while the bottom panel shows easterly wind stress.
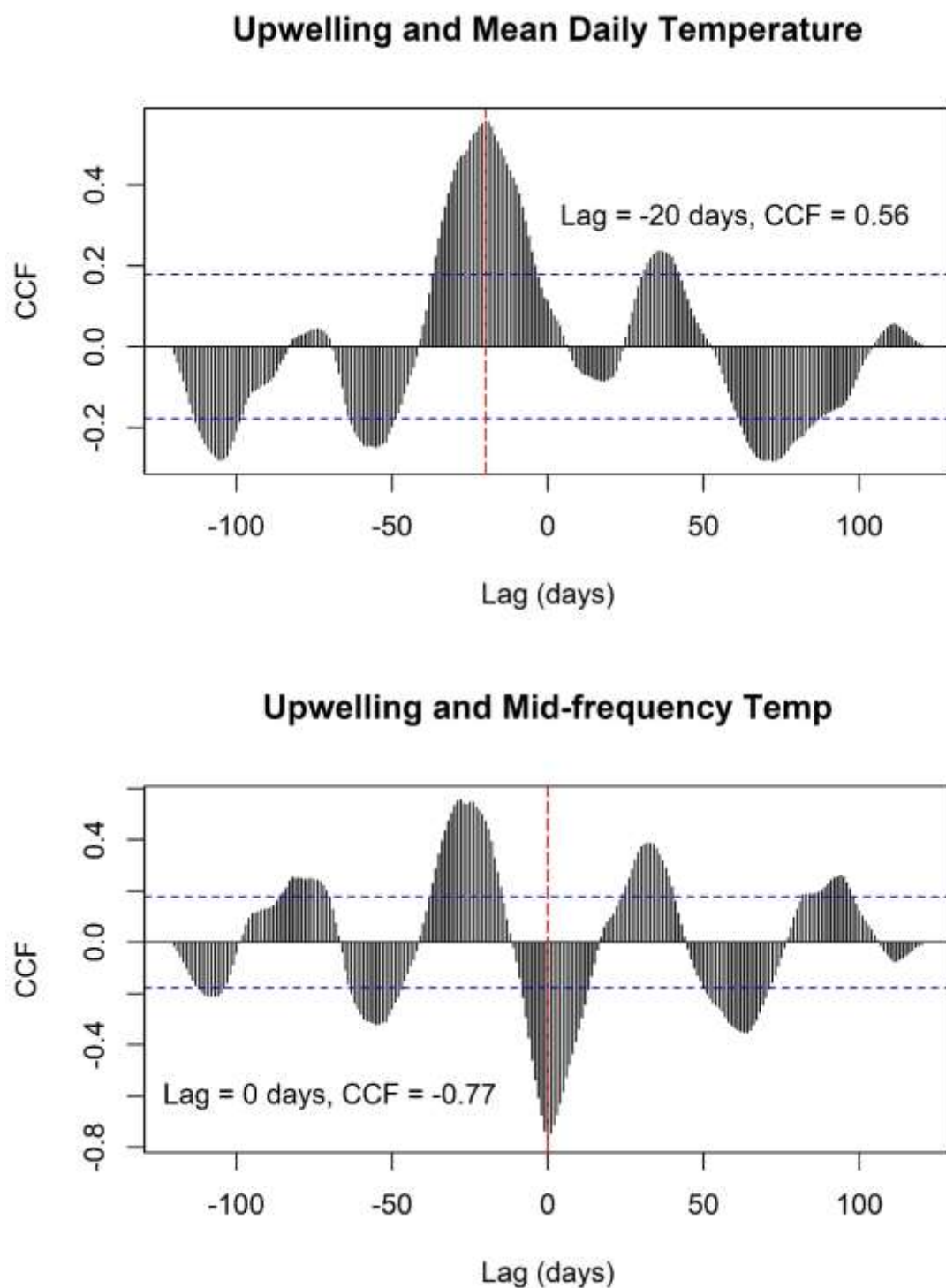
2-day Wind Stress and Mid-frequency Temp

Lag = -78 hours, CCF = -0.08

2-day E Wind Stress and Mid-frequency Temp

Lag = 0 days, CCF = 0.15
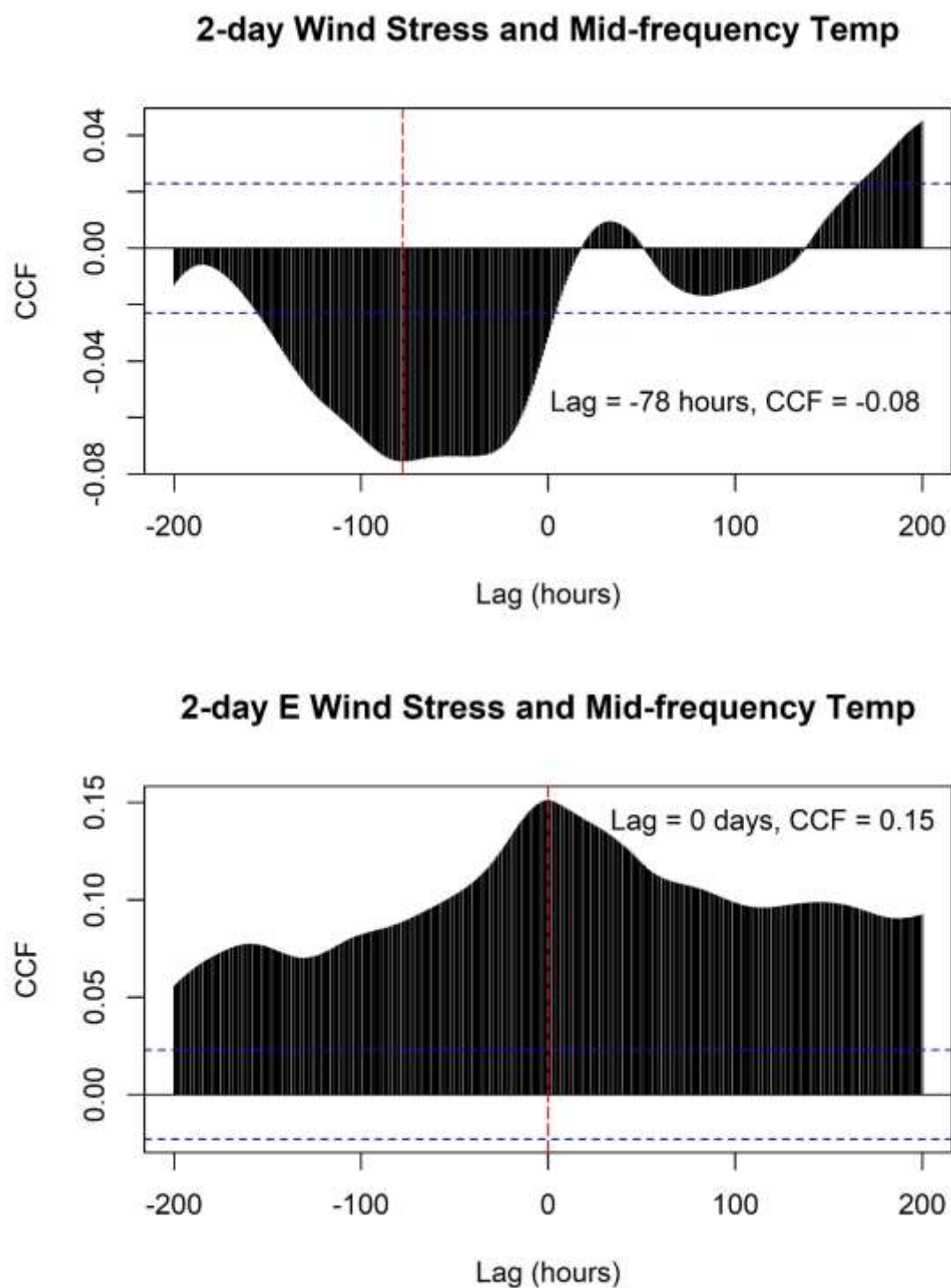
Figure S104. Correlations (CCFs) between a 2-day back-averaged wind stress and mid-frequency temperatures at the shallow location at Sacrifice Island. The top panel shows total wind stress, while the bottom panel shows easterly wind stress. Shown on each pane are the dominant lags and corresponding CCF value for each measure of temperature.
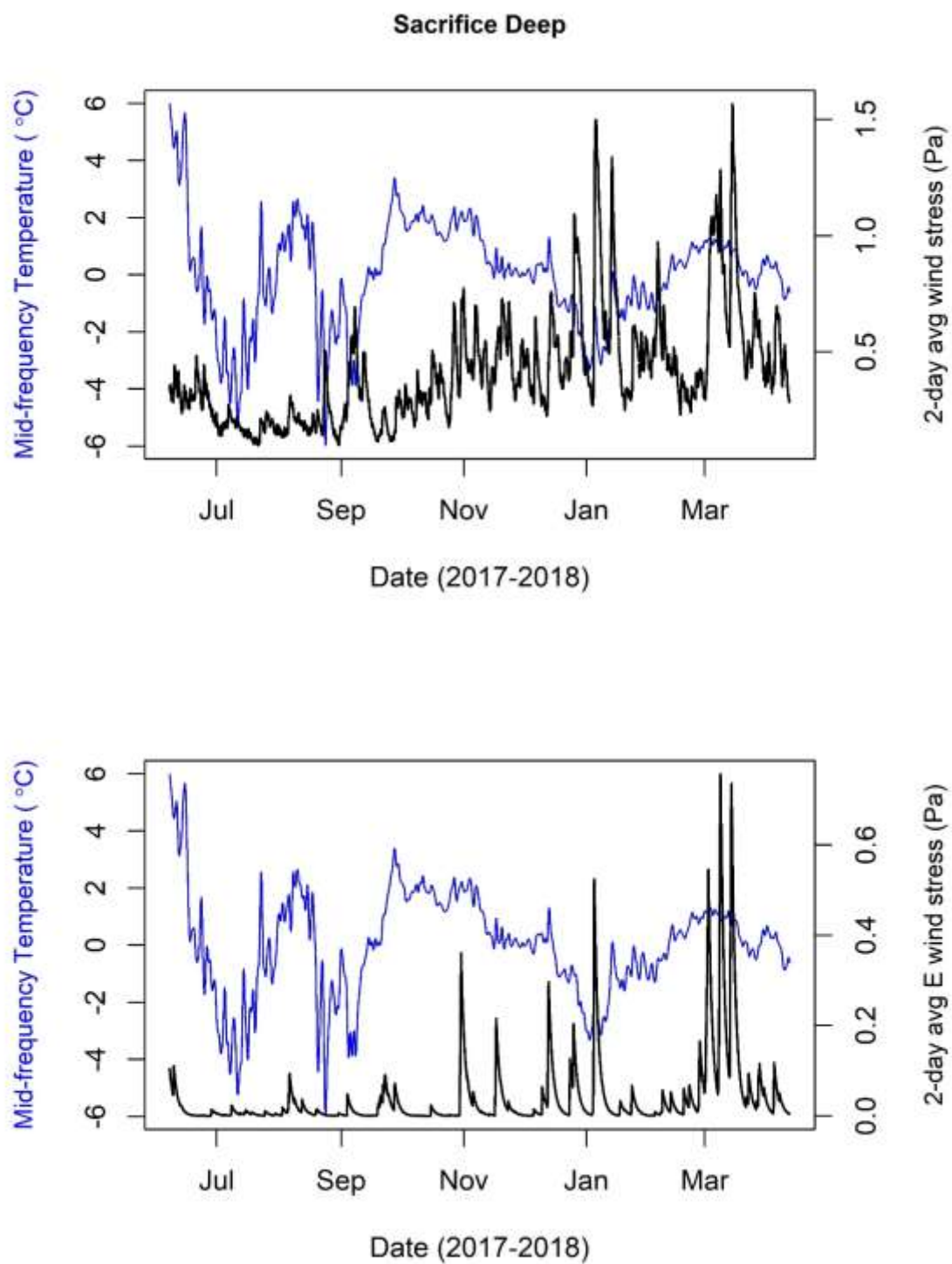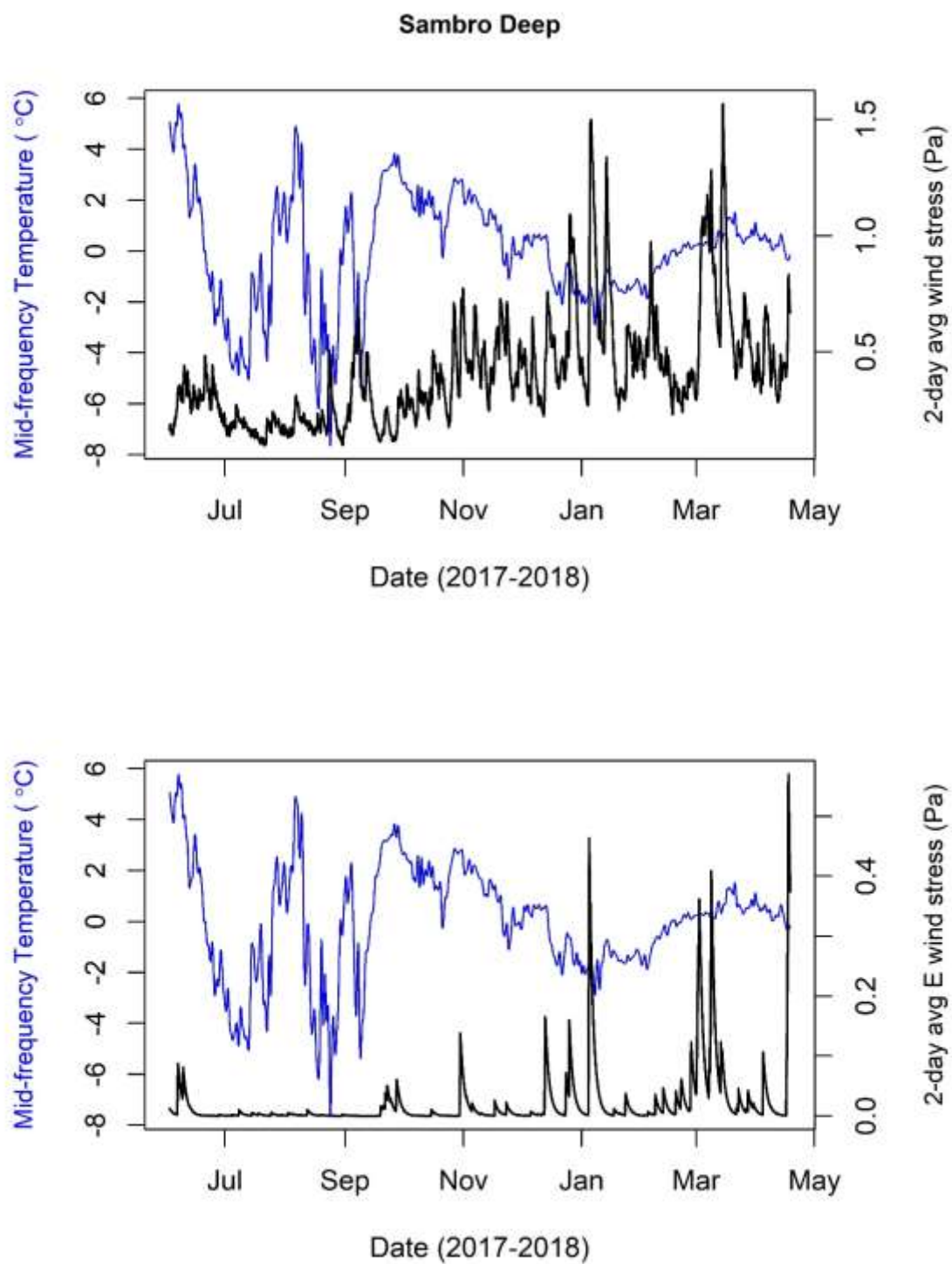
Sacrifice Deep

Figure S105. 2-day back-averaged wind stress plotted against mid-frequency temperatures at the deep location at Sacrifice Island. The top panel shows total wind stress, while the bottom panel shows easterly wind stress.
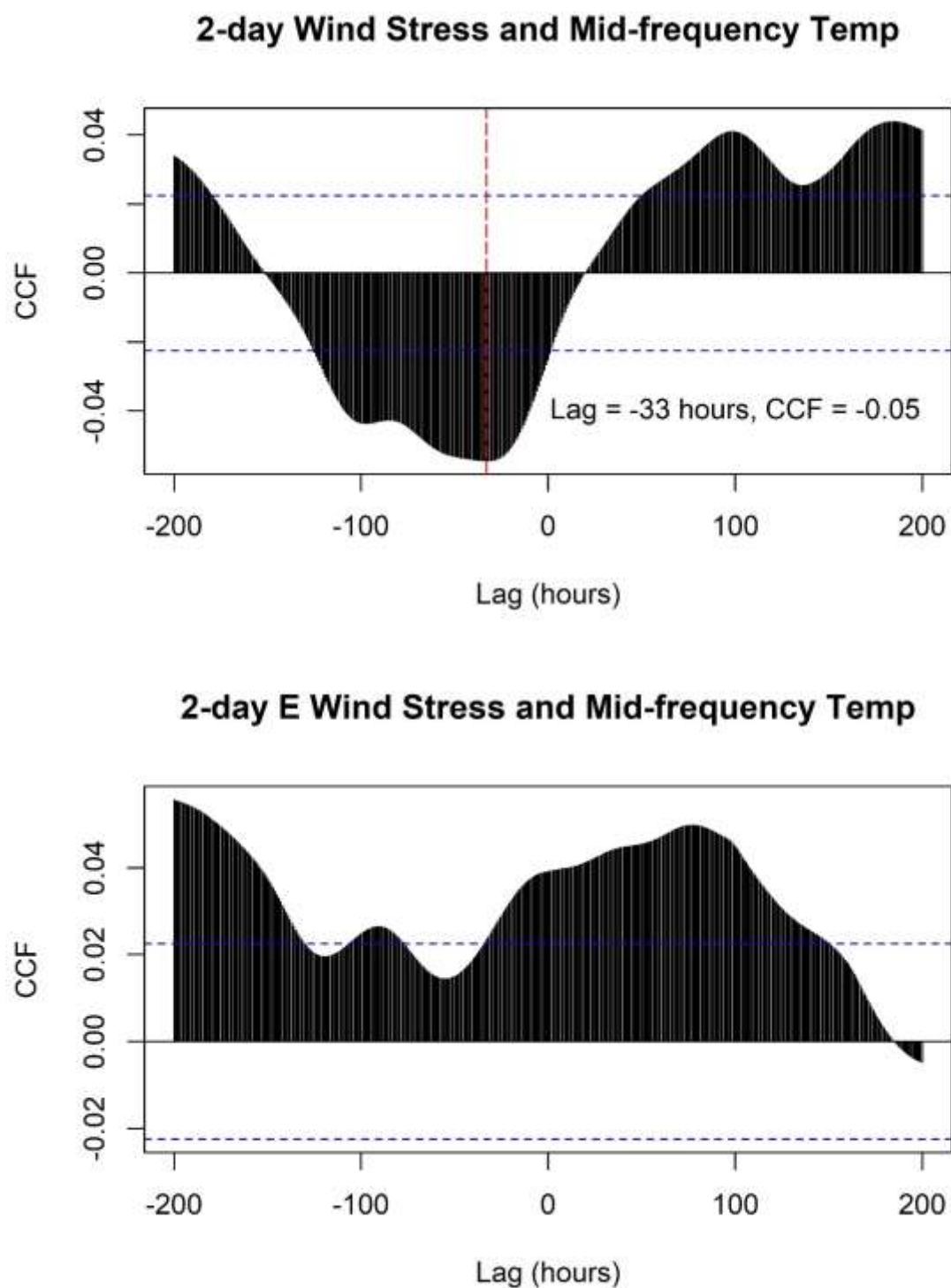
Figure S106. Correlations (CCFs) between a 2-day back-averaged wind stress and mid-frequency temperatures at the deep location at Sacrifice Island. The top panel shows total wind stress, while the bottom panel shows easterly wind stress. Shown on each pane are the dominant lags and corresponding CCF value for each measure of temperature.

Sambro Island

Sambro Deep

Sambro Shallow
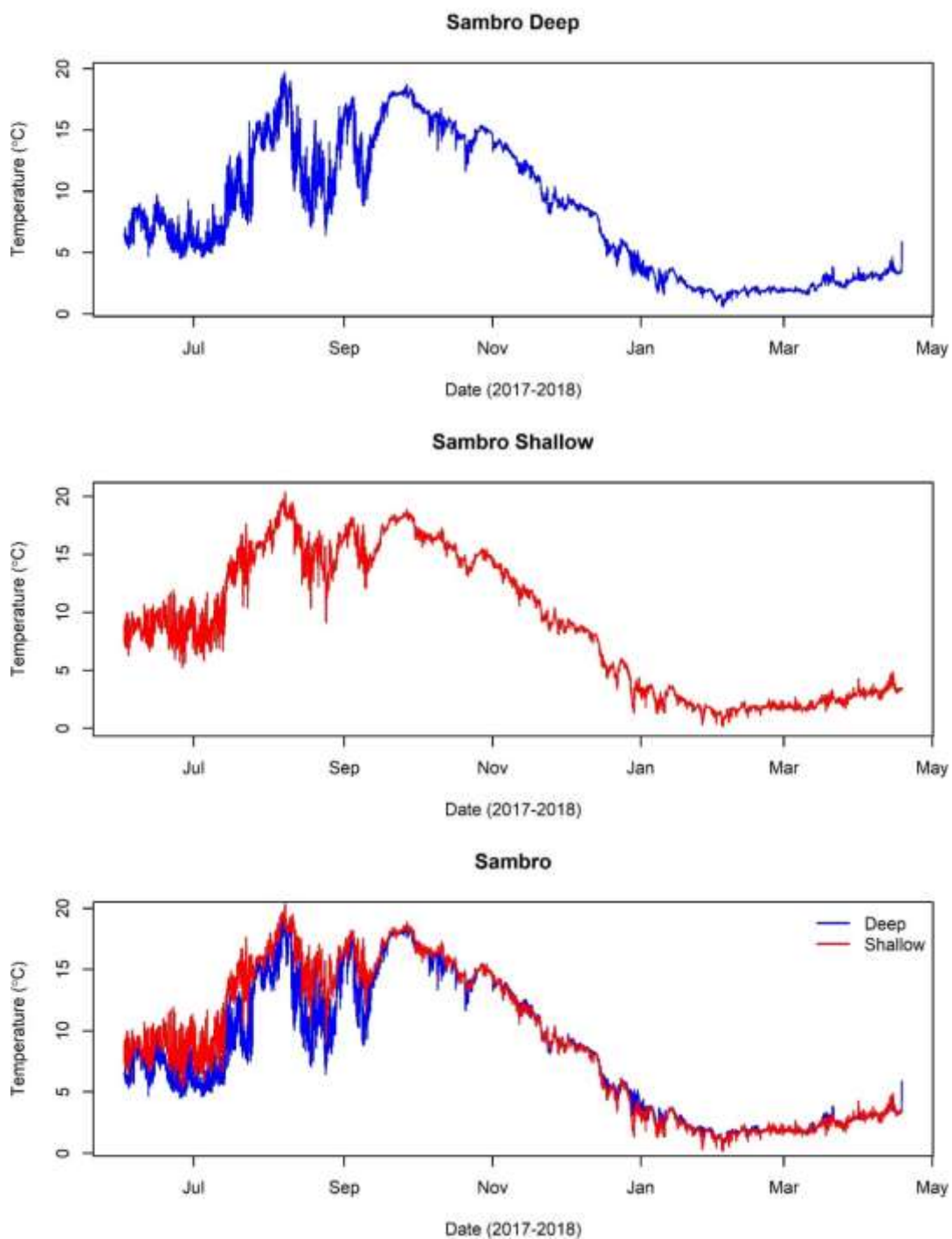
Sambro

Figure S107. Temperature records at the deep and shallow locations at Sambro Island, recorded from June 2, 2017 to April 18, 2018.
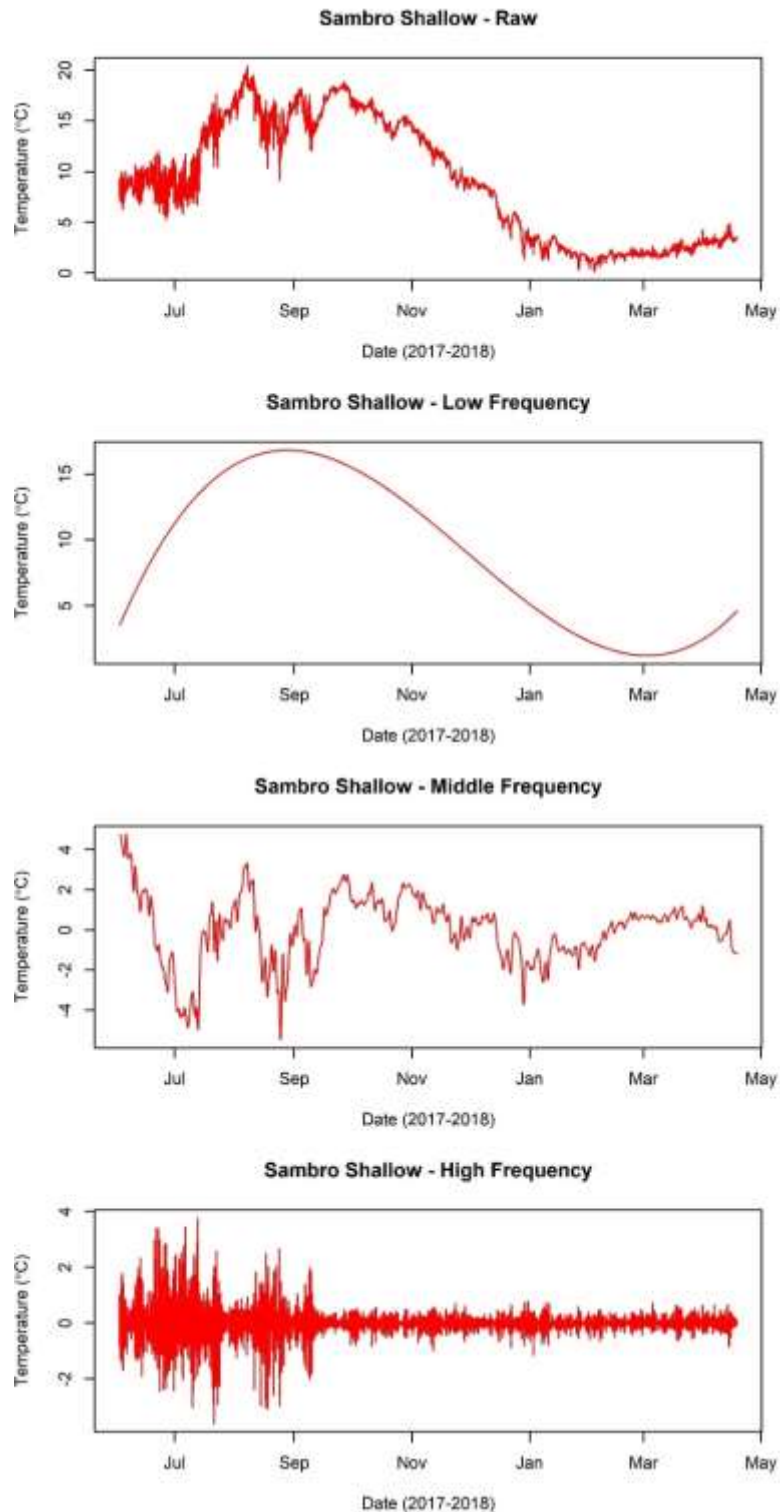
Figure S108. Raw temperatures (top panel), low (second panel), middle (third panel), and high frequency (bottom panel) temperature variability isolated at the shallow location at Sambro Island.
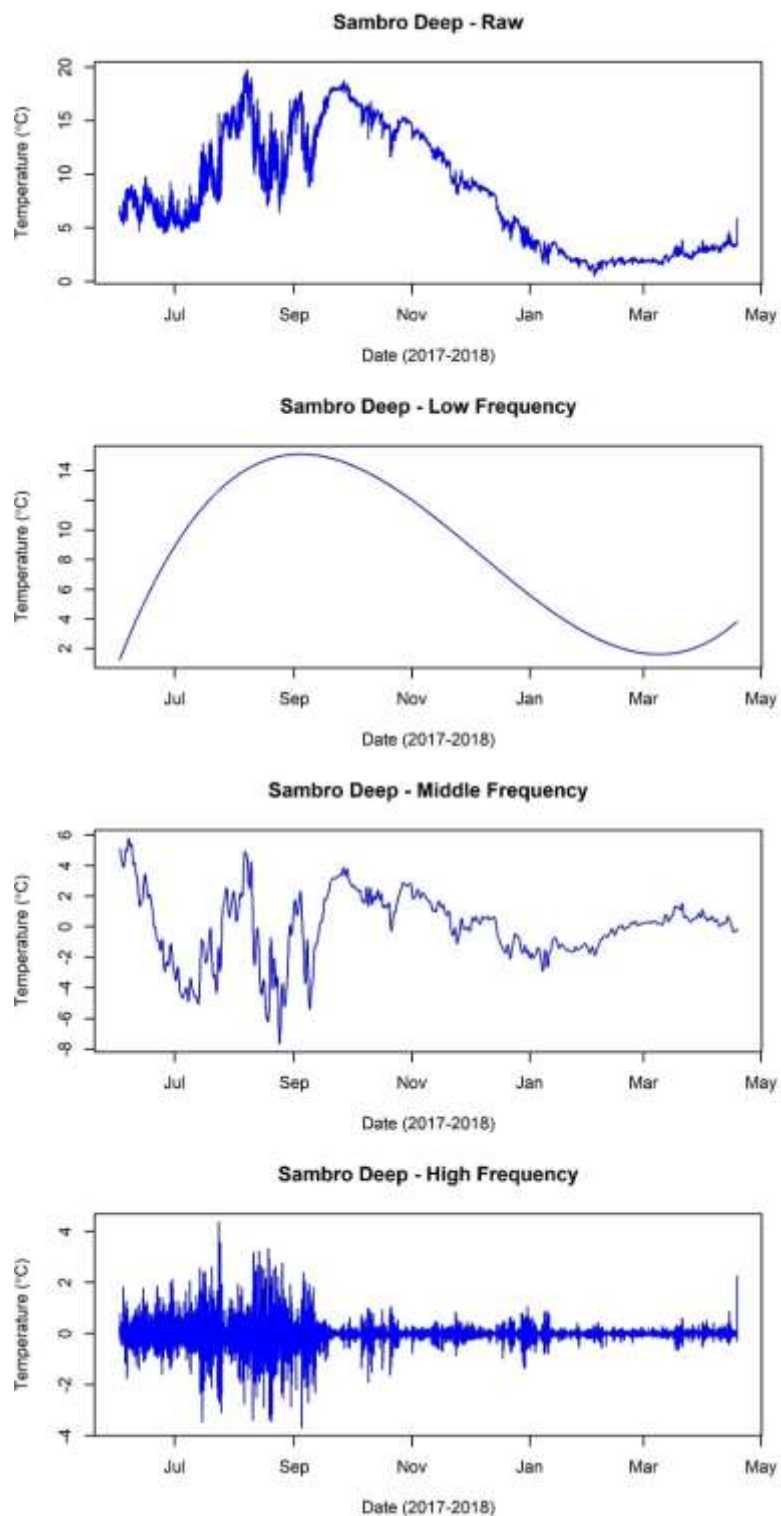
Figure S109. Raw temperatures (top panel), low (second panel), middle (third panel), and high frequency (bottom panel) temperature variability isolated at the deep location at Sambro Island.
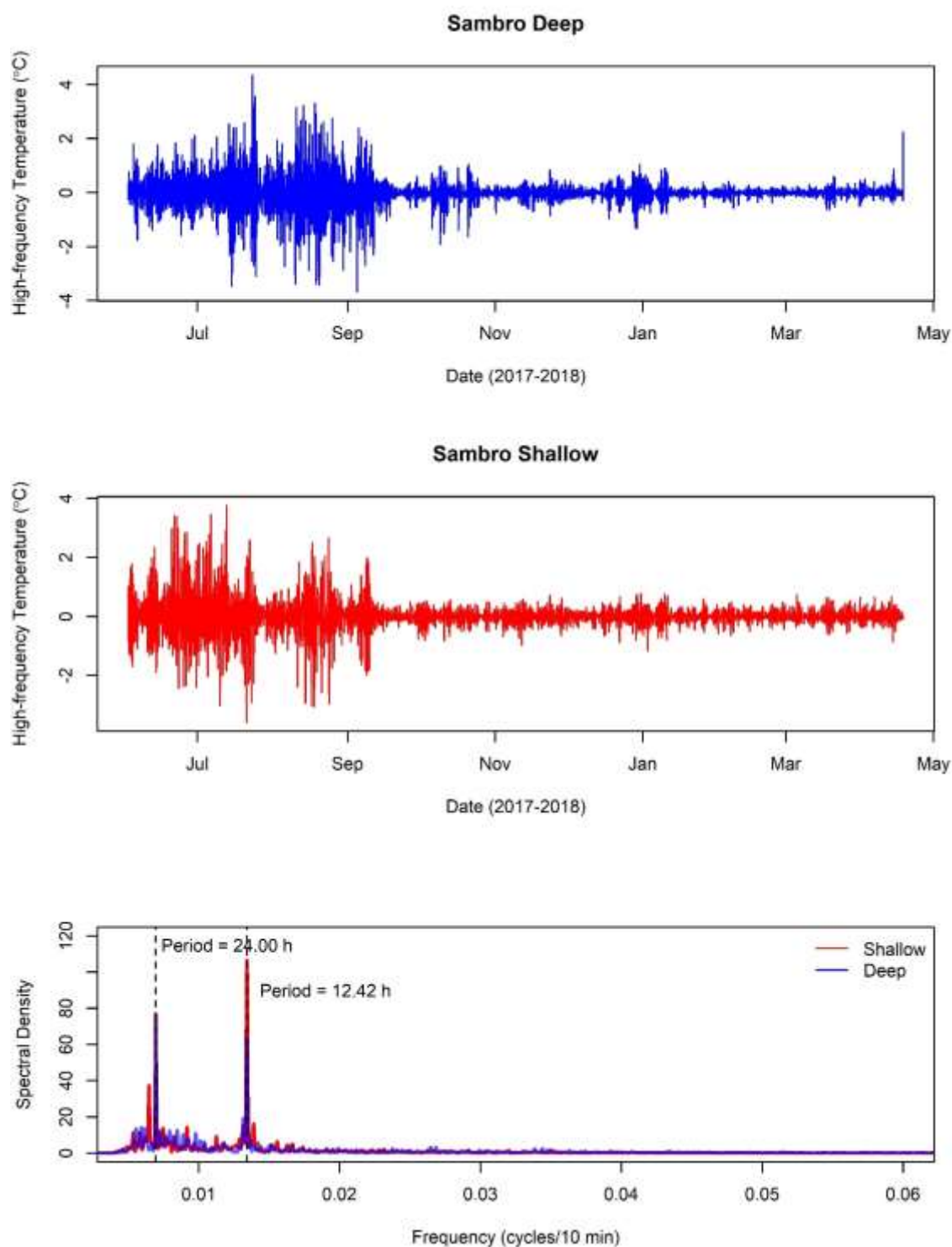
Figure S110. High frequency temperature changes at the deep and shallow locations at Sambro Island (top two panels). The bottom panel shows the results of a spectral analysis, with the dominant frequencies shown in dotted lines and the period shown in text.

Sambro Deep

Range = 0.20°C

Sambro Shallow

Range = 0.19°C
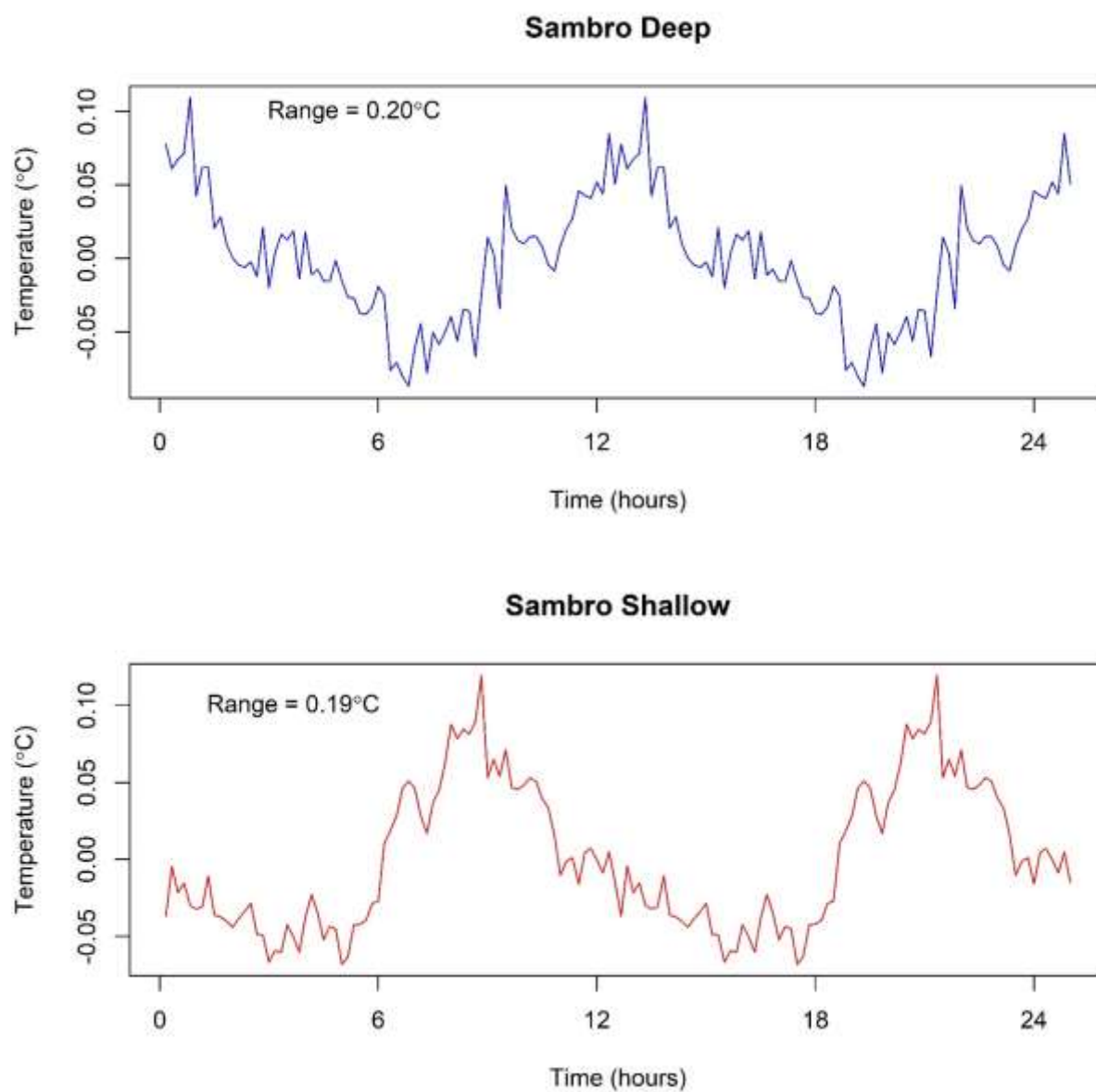
Figure S111. Average temperature changes over the 12.42-hour tidal cycle at Sambro Island shallow and deep, calculated for the summer period (June-October 2017).

Sambro Deep
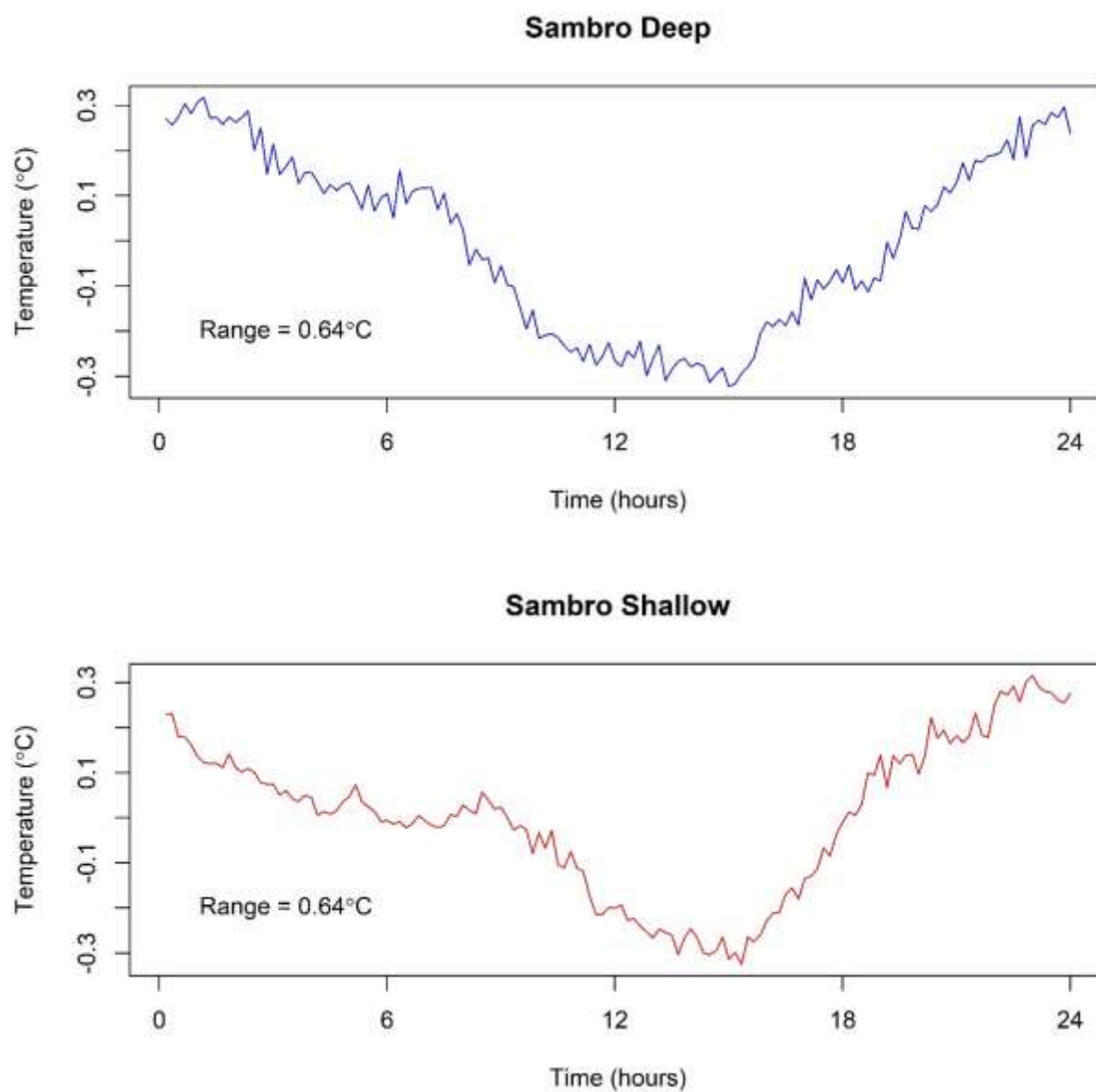
Sambro Shallow

Figure S112. Average temperature changes over the 24-hour daily heating and cooling cycle at Sambro Island shallow and deep, calculated for the summer period (June-October 2017).
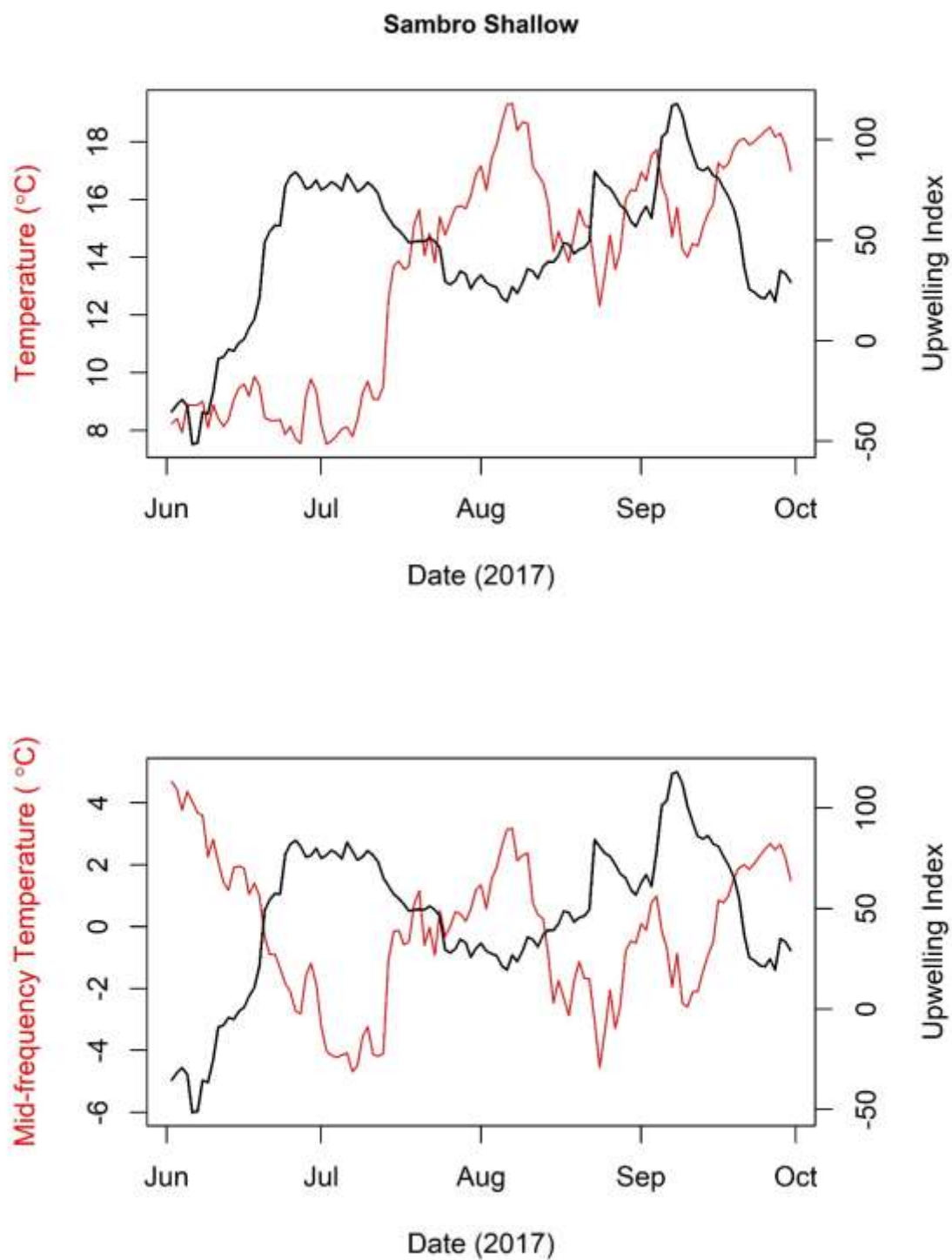
Figure S113. A 17-day back-averaged upwelling index plotted against average daily temperatures (top panel) and mid-frequency temperatures (bottom panel) at the shallow location at Sambro Island.

Figure S114. Correlations (CCFs) between a 17-day back-averaged upwelling index and average daily temperatures (top panel), and mid-frequency temperatures (bottom panel) at the shallow location at Sambro. Shown on each pane are the dominant lags and corresponding CCF value for each measure of temperature.

Sambro Deep

Figure S115. A 17-day back-averaged upwelling index plotted against average daily temperatures (top panel) and mid-frequency temperatures (bottom panel) at the deep location at Sambro Island.

Figure S116. Correlations (CCFs) between a 17-day back-averaged upwelling index and average daily temperatures (top panel), and mid-frequency temperatures (bottom panel) at the deep location at Sambro Island. Shown on each pane are the dominant lags and corresponding CCF value for each measure of temperature.

Figure S117. 2-day back-averaged wind stress plotted against mid-frequency temperatures at the shallow location at Sambro Island. The top panel shows total wind stress, while the bottom panel shows easterly wind stress.

Upwelling and Mean Daily Temperature

Lag = -20 days, CCF = 0.56

Upwelling and Mid-frequency Temp

Lag = 0 days, CCF = -0.77

Figure S118. Correlations (CCFs) between a 2-day back-averaged wind stress and mid-frequency temperatures at the shallow location at Sambro Island. The top panel shows total wind stress, while the bottom panel shows easterly wind stress. Shown on each pane are the dominant lags and corresponding CCF value for each measure of temperature.

Figure S119. 2-day back-averaged wind stress plotted against mid-frequency temperatures at the deep location at Sambro Island. The top panel shows total wind stress, while the bottom panel shows easterly wind stress.

2-day Wind Stress and Mid-frequency Temp

Lag = -33 hours, CCF = -0.05

2-day E Wind Stress and Mid-frequency Temp

Figure S120. Correlations (CCFs) between a 2-day back-averaged wind stress and mid-frequency temperatures at the deep location at Sambro Island. The top panel shows total wind stress, while the bottom panel shows easterly wind stress. Shown on each pane are the dominant lags and corresponding CCF value for each measure of temperature.
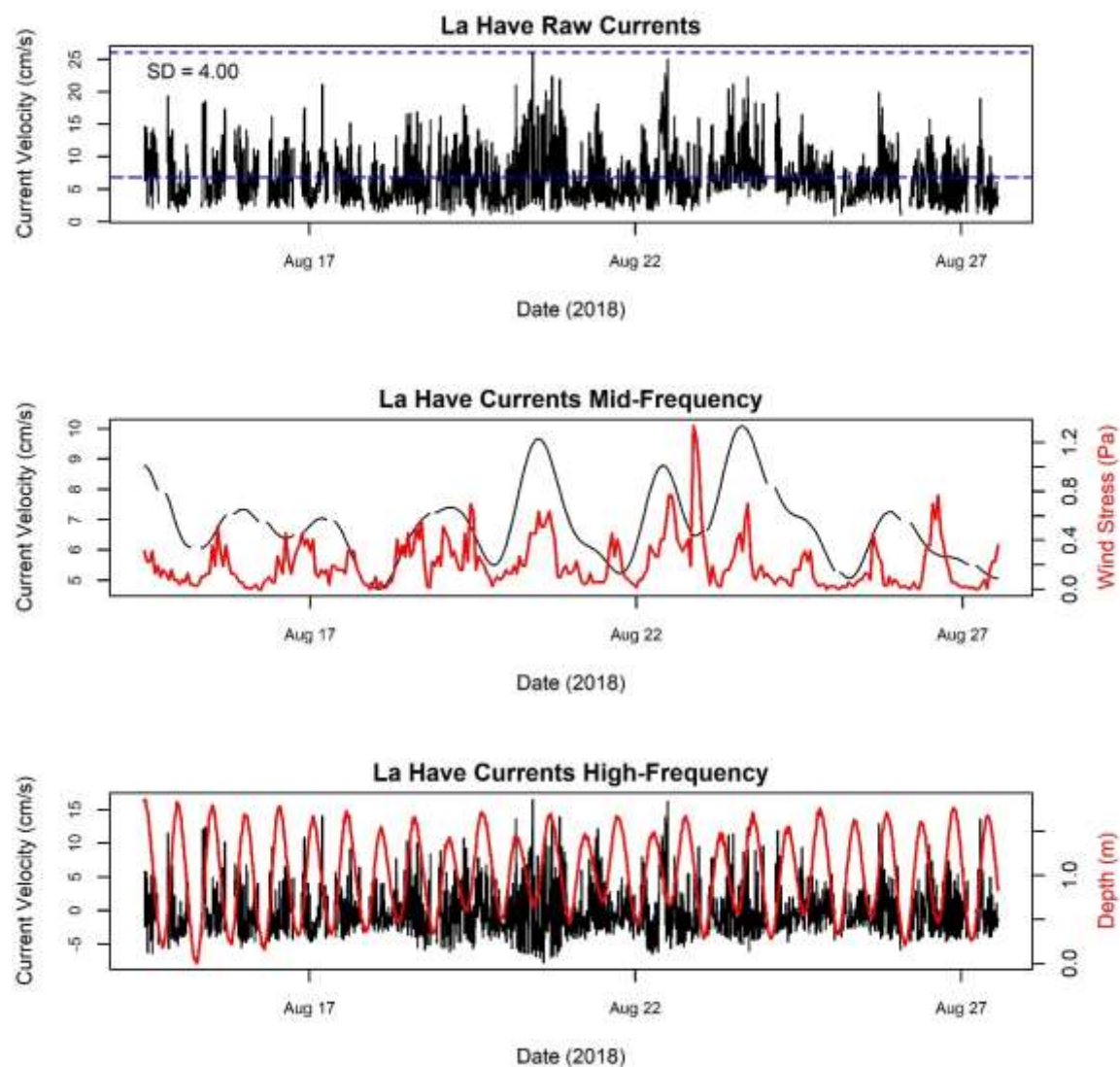
Currents

Cable Island
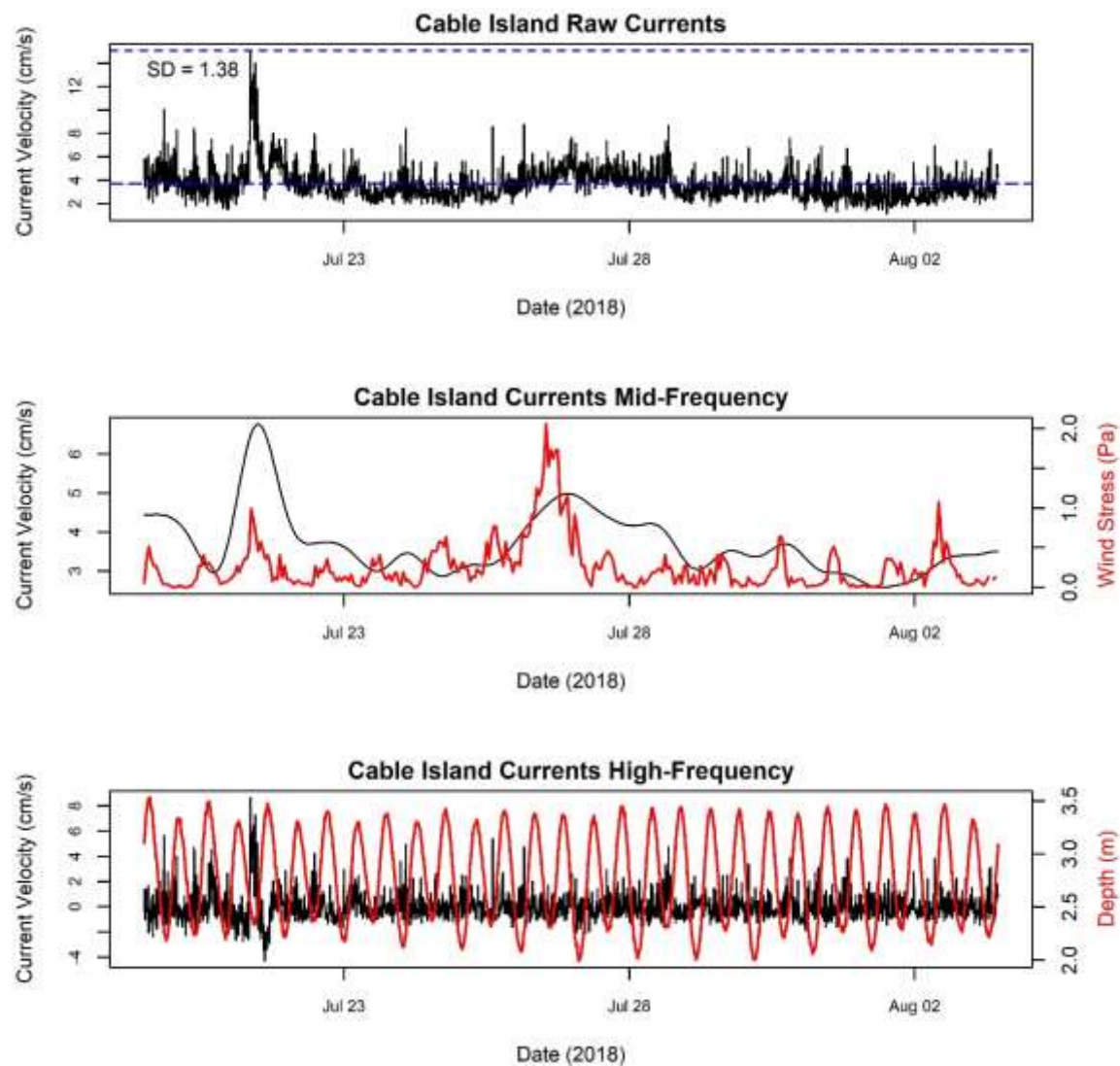
Figure S121. Raw current velocities (top panel) at Cable Island, and current velocities split into a mid-frequency band (middle panel, signals > 24 hours) and a high-frequency band (bottom panel, signals < 24 hours). Total wind stress is overlaid in red on mid-frequency current velocities, while depth is overlaid on high-frequency current velocities.

Cable Island Depth

Time = 12.41 hours

Cable Island High-Frequency Currents

Time = 15.00 hours

Cross-Spectrum

Time = 12.41 hours, Coh = 0.55
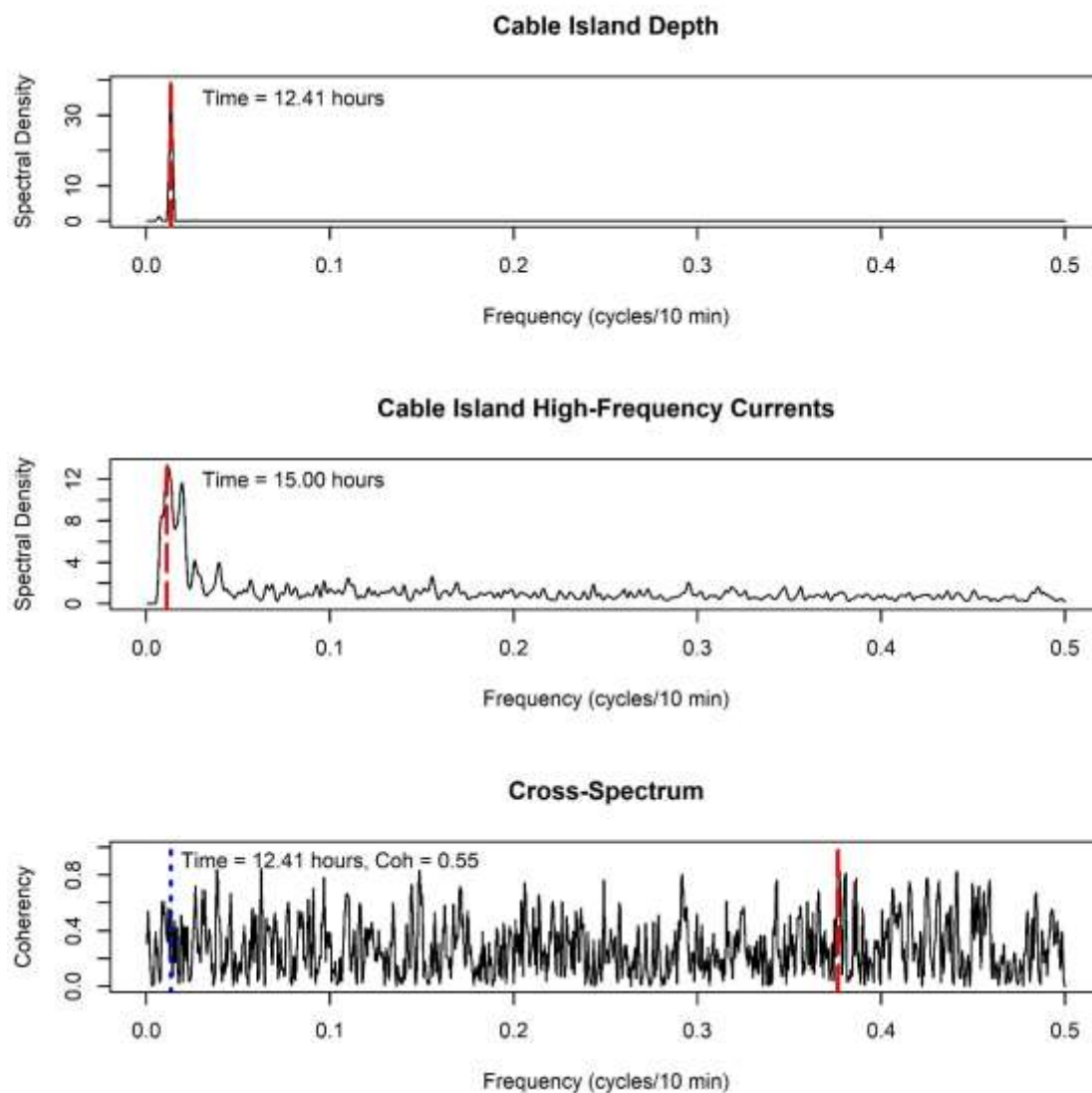
Figure S122. Spectral signatures of depth (top panel) and current (middle panel) time series at Cable Island. Bottom shows the coherency between time series at different frequencies. The red dotted line shows the frequency at which the highest coherency is observed, while the blue dotted line shows the frequency with the highest coherency between time series within the band of frequencies associated with the diurnal tidal constituents (0.126-0.144, 11.6-12.9 hours).
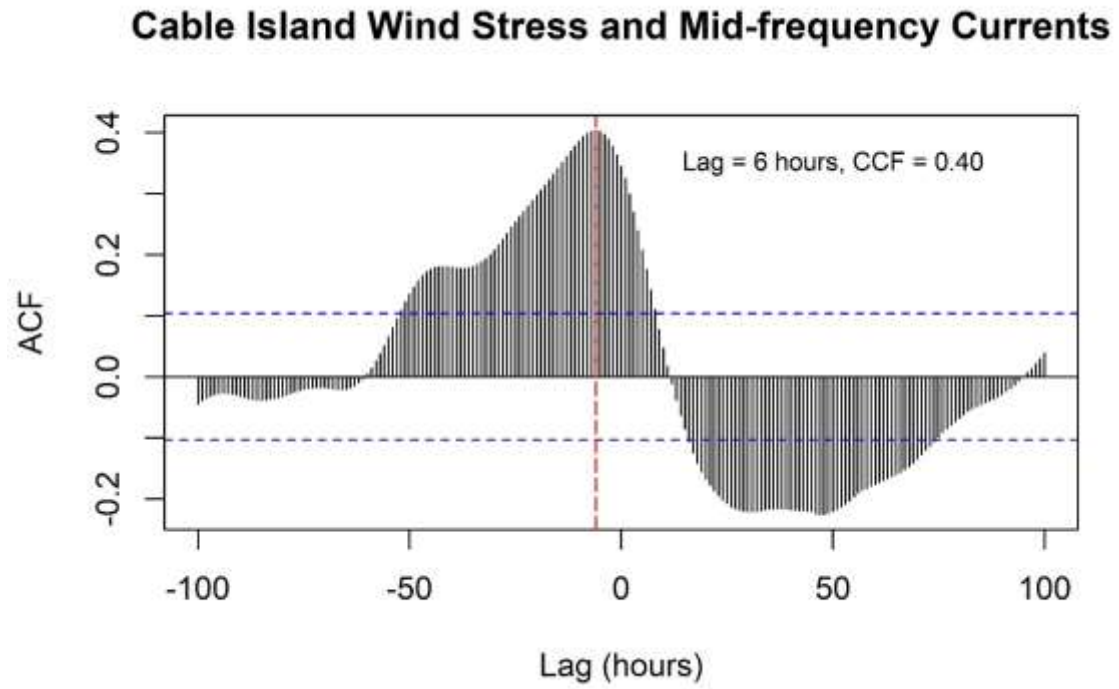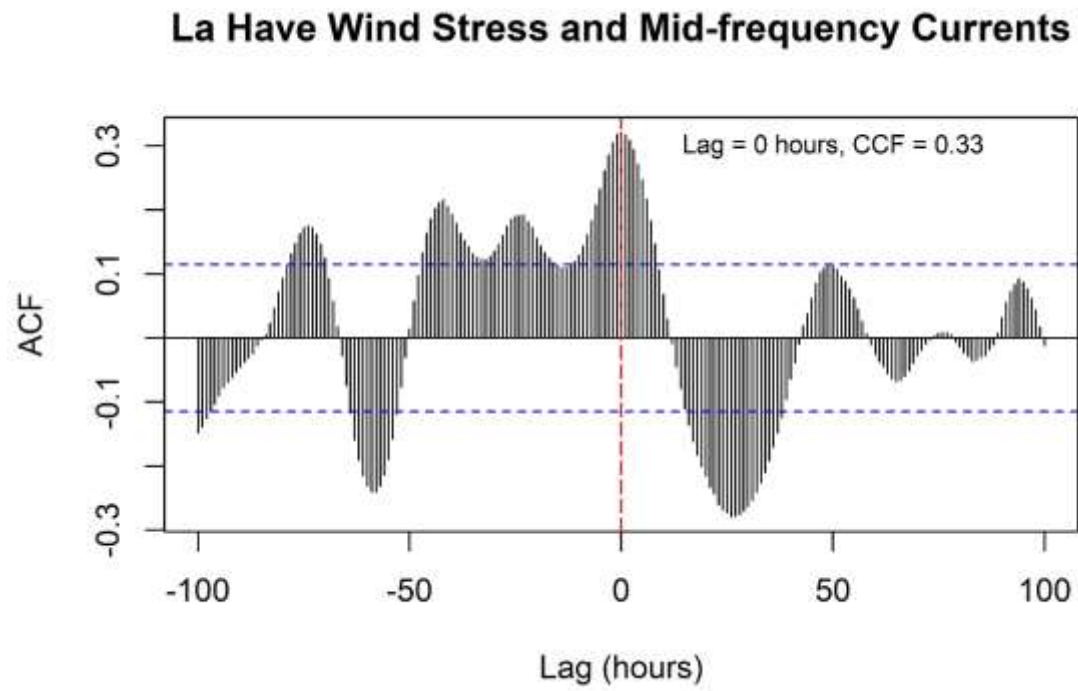
Figure S123. Cross correlation between wind stress and changes in currents in the middle-frequency band (>24 hours) at Cable Island. The lag with the highest correlation is shown with a red dotted line.
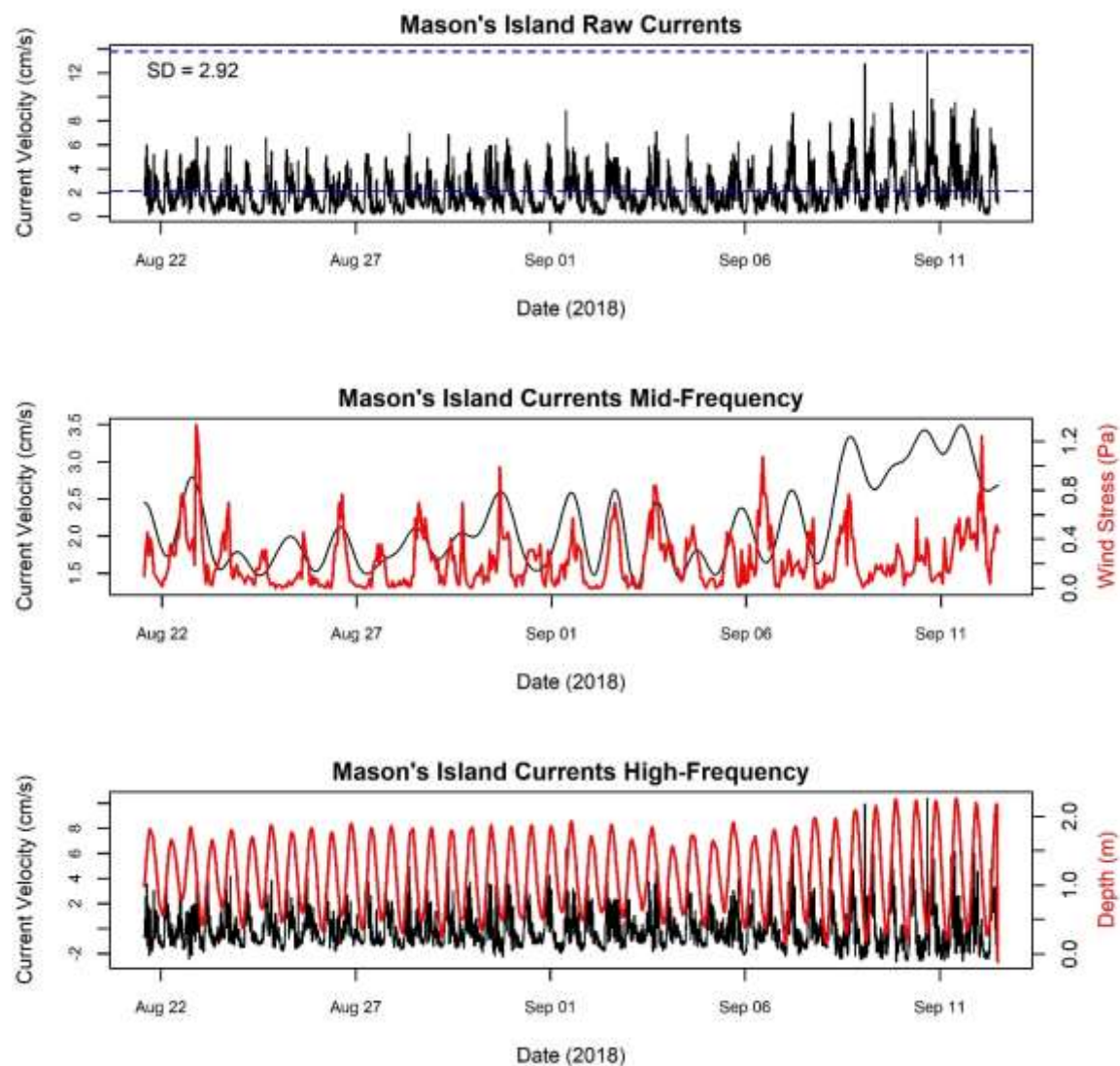
Croucher Island
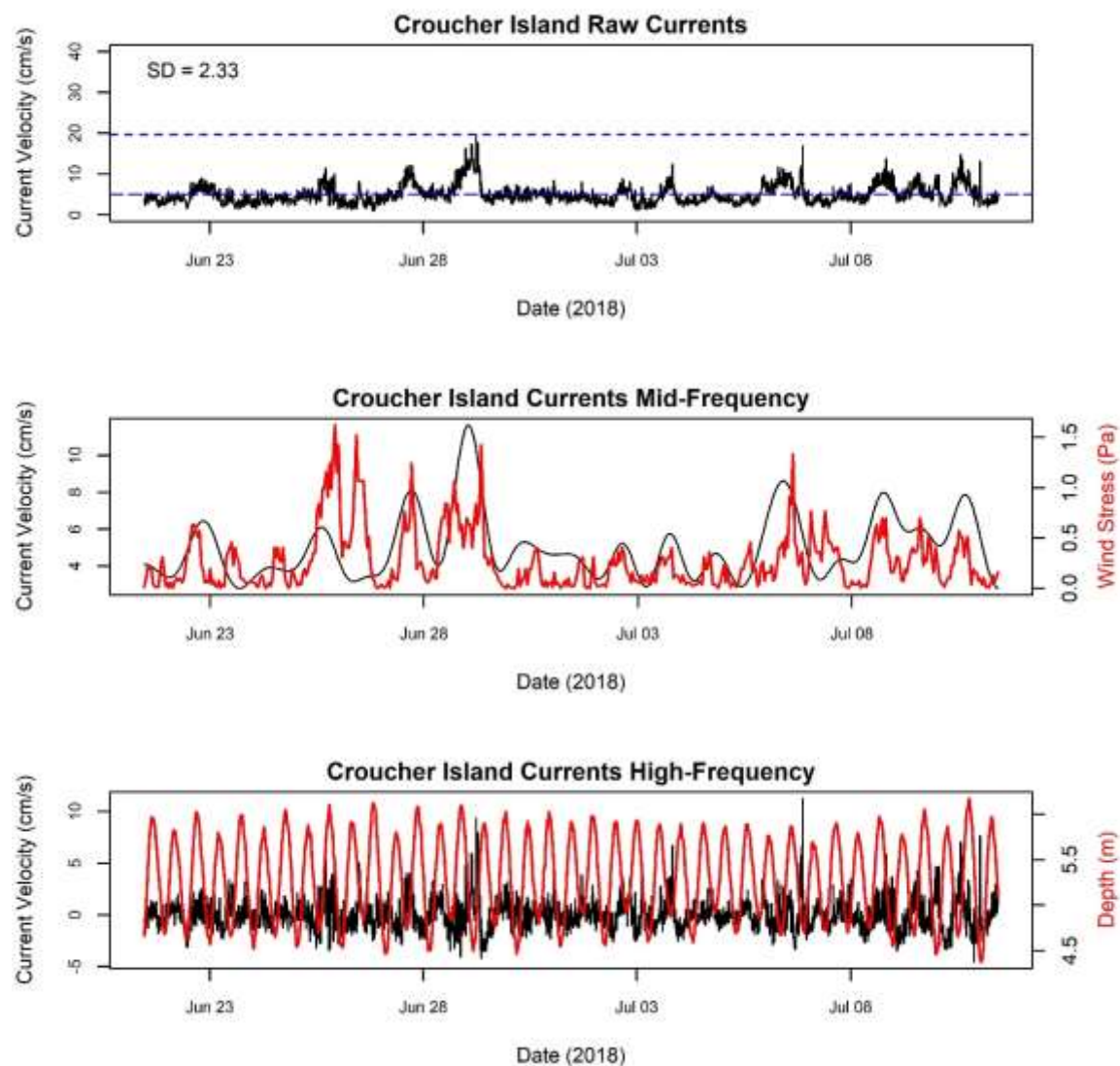
Figure S124. Raw current velocities (top panel) at Croucher Island, and current velocities split into a mid-frequency band (middle panel, signals > 24 hours) and a high-frequency band (bottom panel, signals < 24 hours). Total wind stress is overlaid in red on mid-frequency current velocities, while depth is overlaid on high-frequency current velocities.

Croucher Island Depth

Croucher Island High-Frequency Currents

Cross-Spectrum
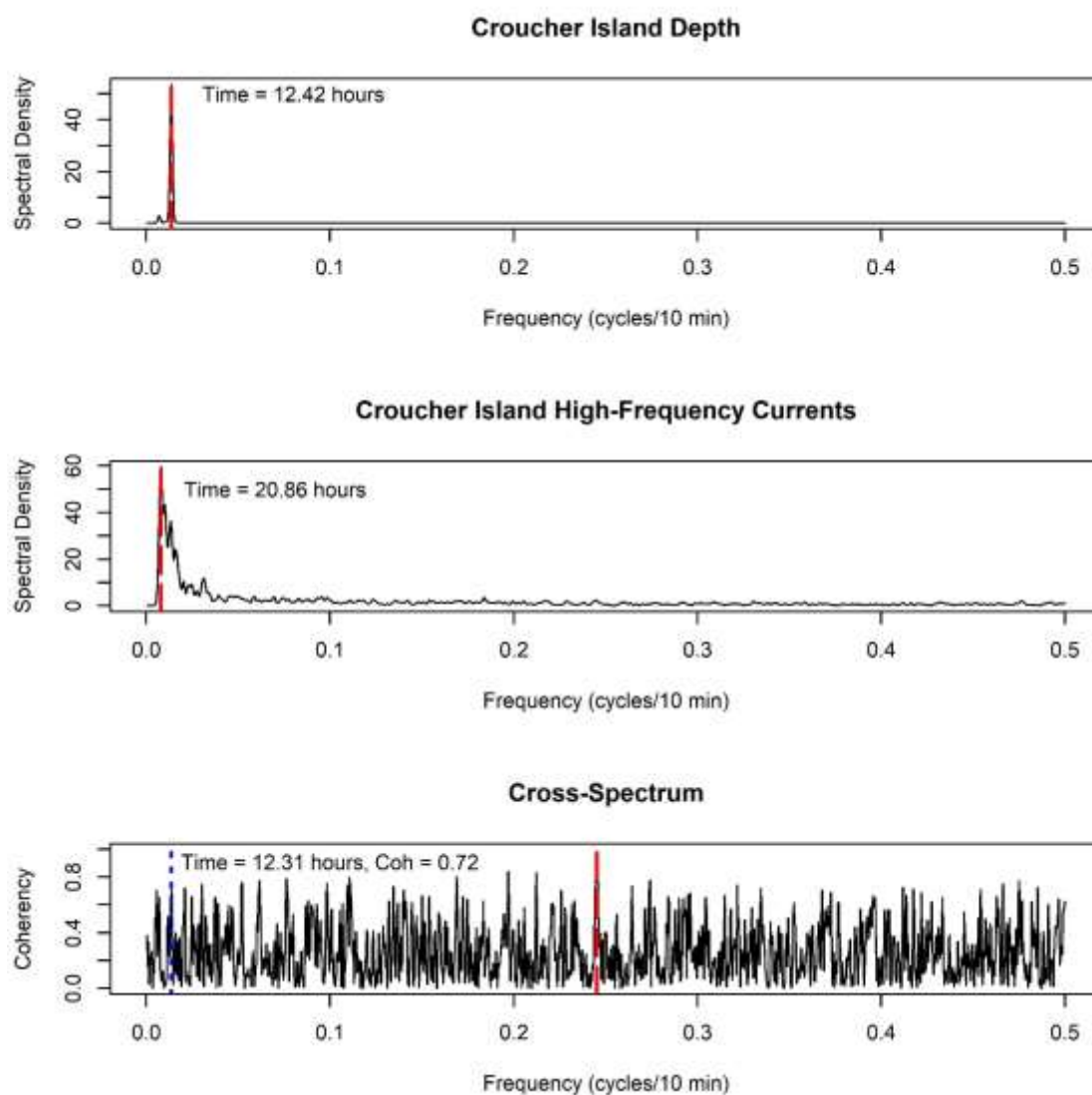
Figure S125. Spectral signatures of depth (top panel) and current (middle panel) time series at Croucher Island. Bottom shows the coherency between time series at different frequencies. The red dotted line shows the frequency at which the highest coherency is observed, while the blue dotted line shows the frequency with the highest coherency between time series within the band of frequencies associated with the diurnal tidal constituents (0.126-0.144, 11.6-12.9 hours).
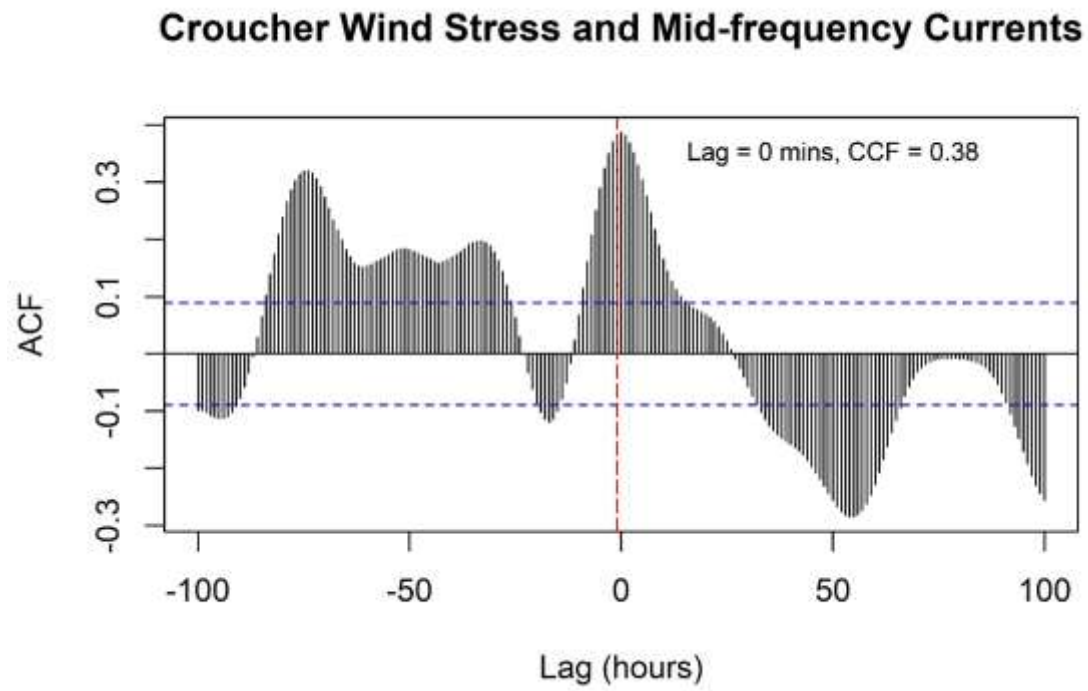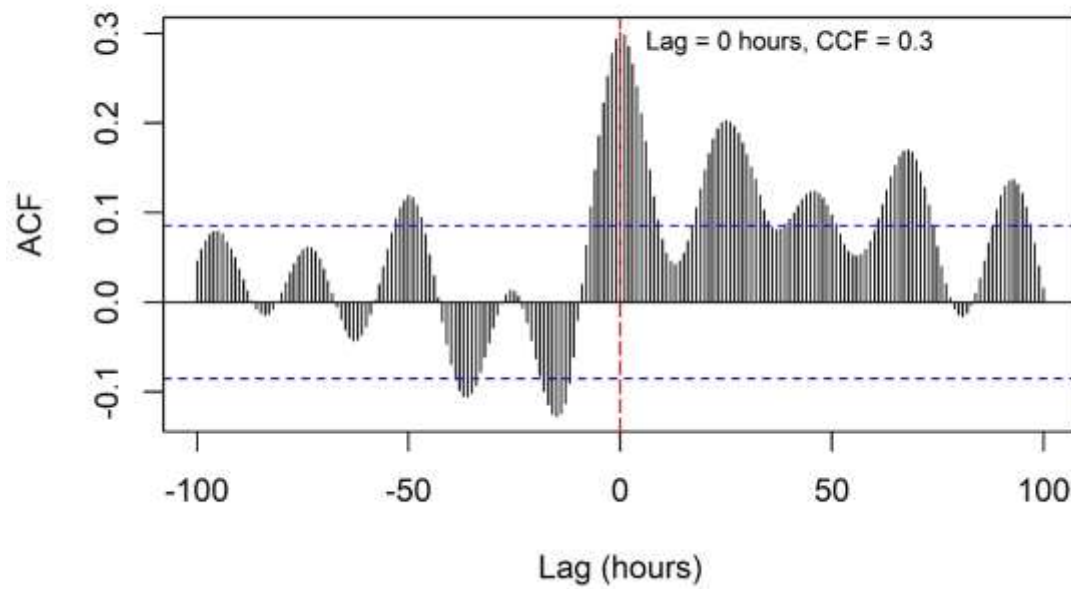
Figure S126. Cross correlation between wind stress and changes in currents in the middle-frequency band (>24 hours) at Croucher Island. The lag with the highest correlation is shown with a red dotted line.
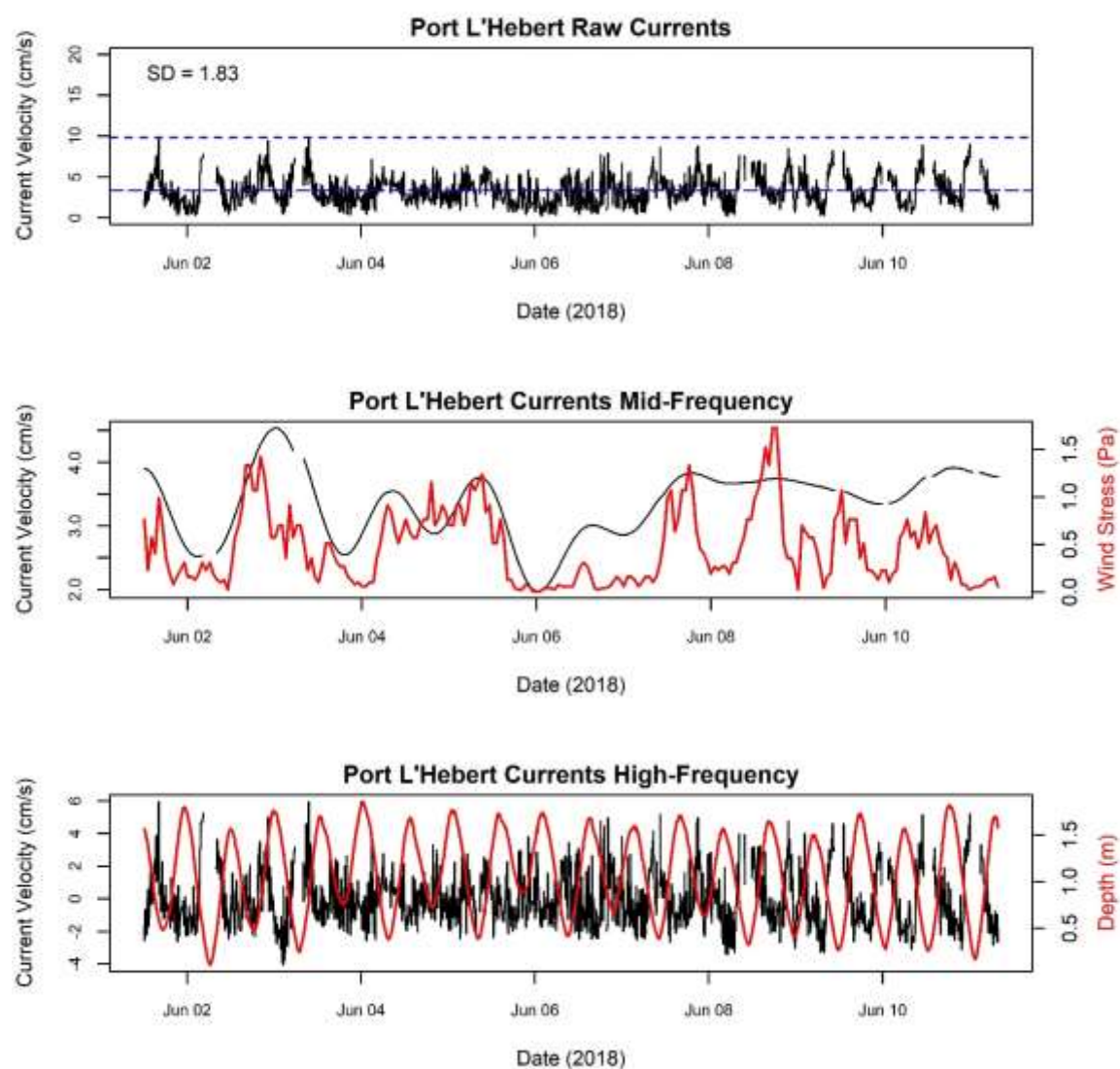
Lower Three Fathom
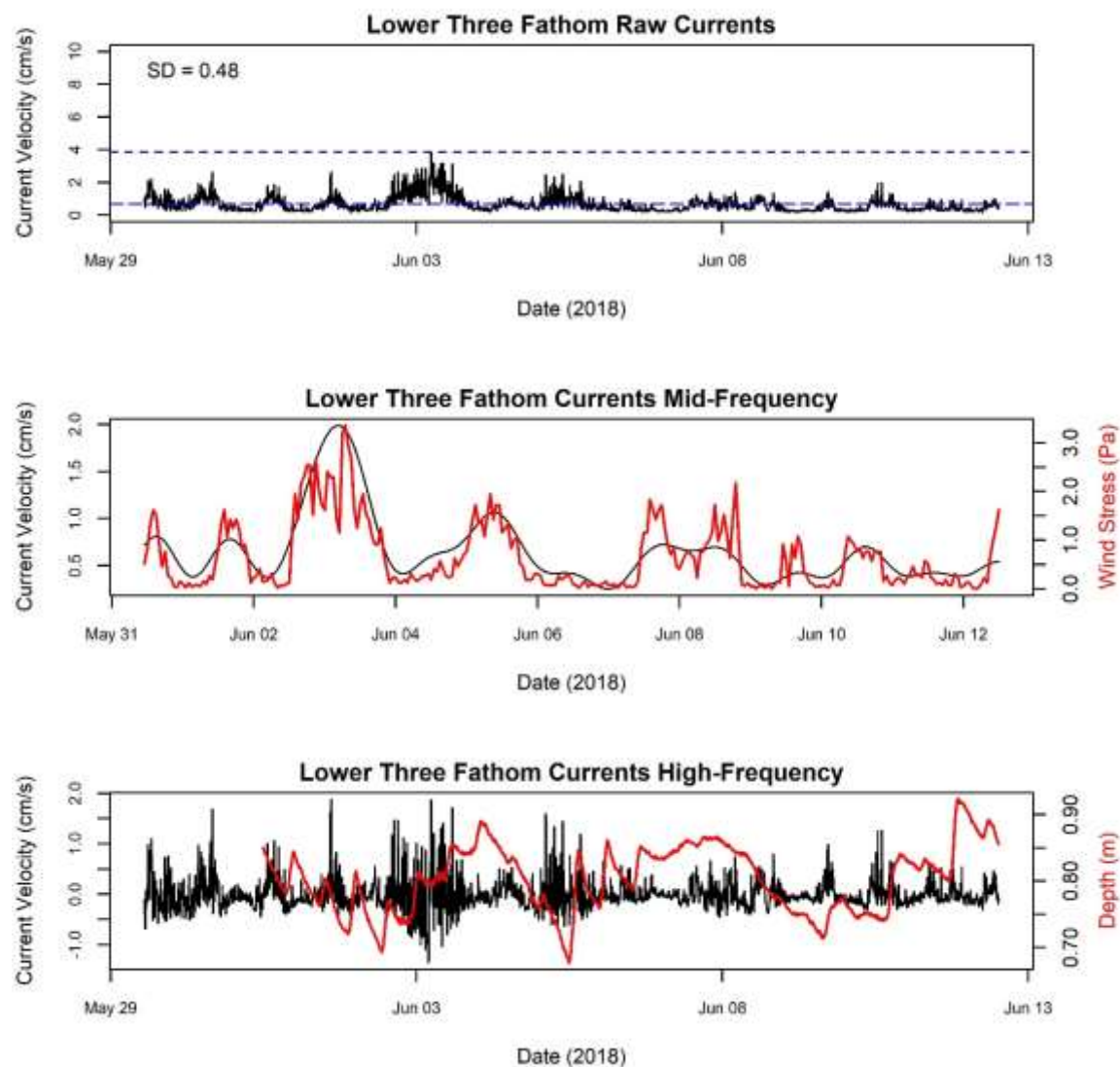
Figure S127. Raw current velocities (top panel) at Lower Three Fathom, and current velocities split into a mid-frequency band (middle panel, signals > 24 hours) and a high-frequency band (bottom panel, signals < 24 hours). Total wind stress is overlaid in red on mid-frequency current velocities, while depth is overlaid on high-frequency current velocities.

Lower Three Fathom Depth

Lower Three Fathom High-Frequency Currents

Cross-Spectrum
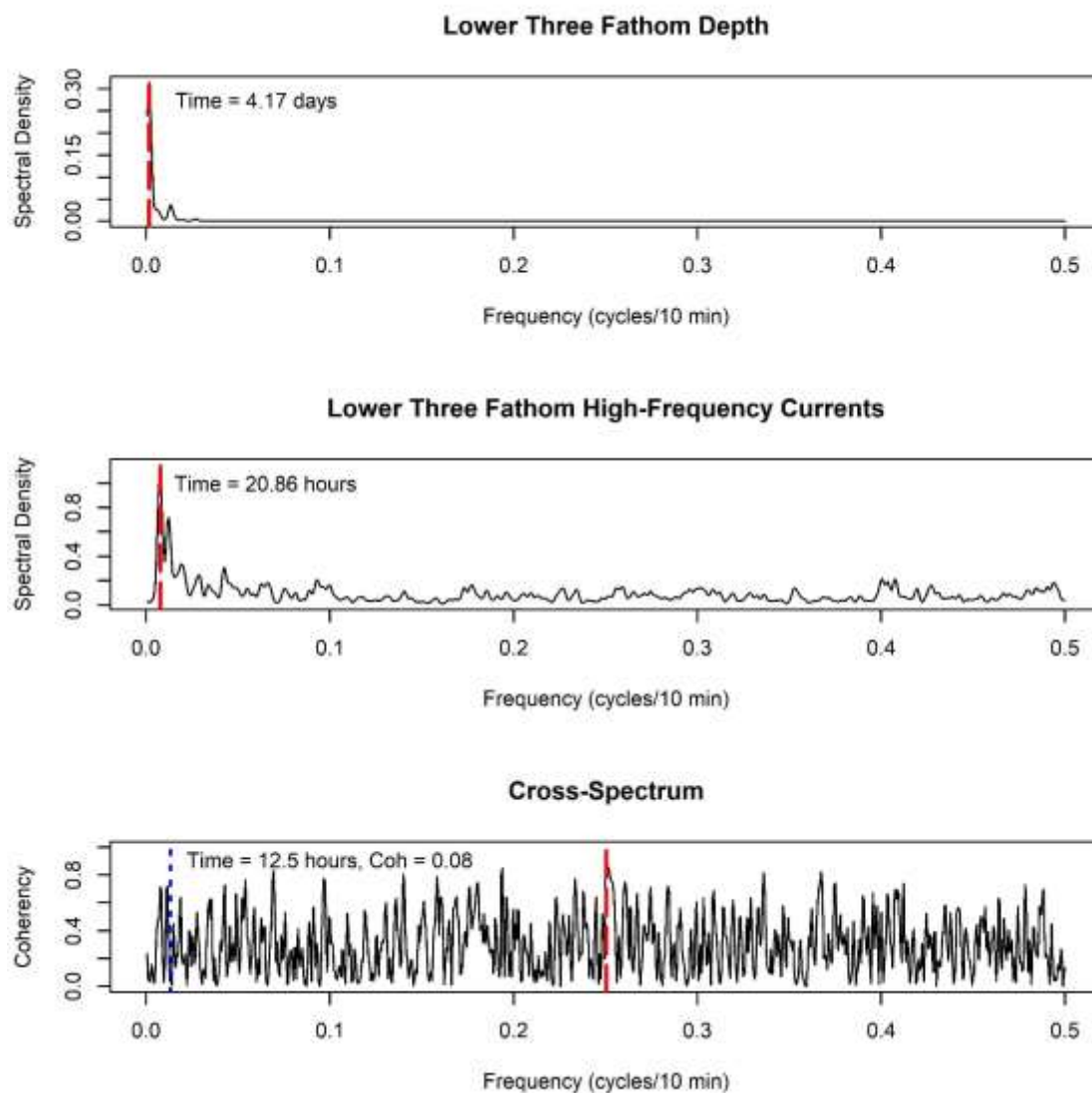
Figure S128. Spectral signatures of depth (top panel) and current (middle panel) time series at Lower Three Fathom. Bottom shows the coherency between time series at different frequencies. The red dotted line shows the frequency at which the highest coherency is observed, while the blue dotted line shows the frequency with the highest coherency between time series within the band of frequencies associated with the diurnal tidal constituents (0.126-0.144, 11.6-12.9 hours).

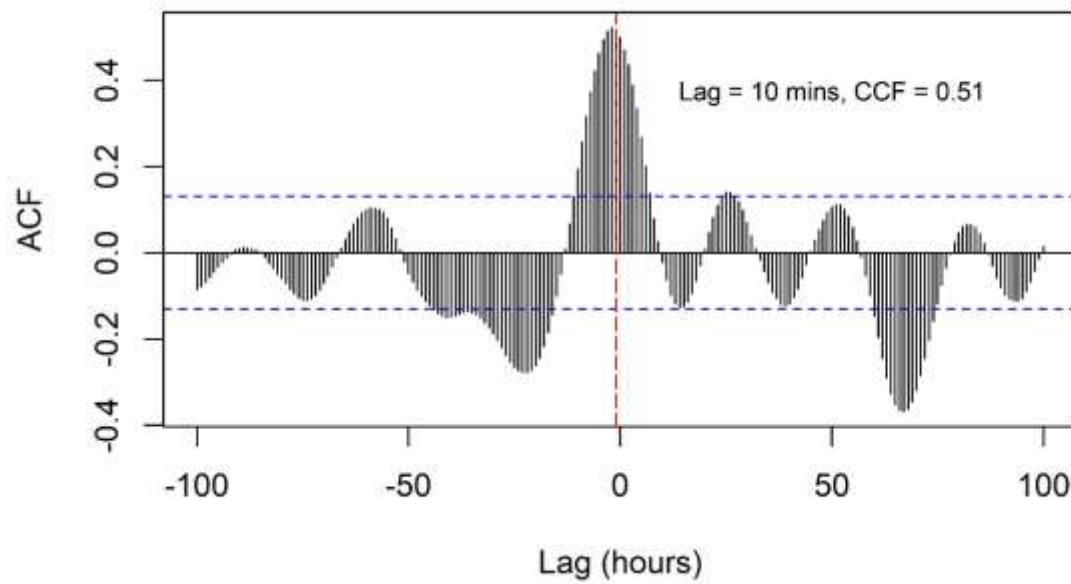## Lower Three Fathom Wind Stress and Mid-frequency Curren
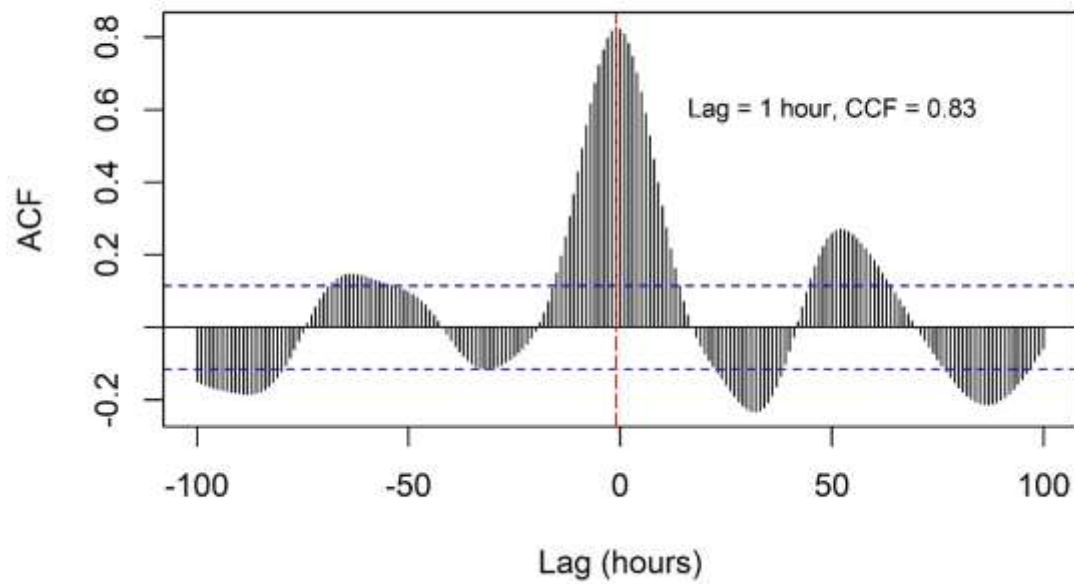
Figure S129. Cross correlation between wind stress and changes in currents in the middle-frequency band (>24 hours) at Lower Three Fathom. The lag with the highest correlation is shown with a red dotted line.
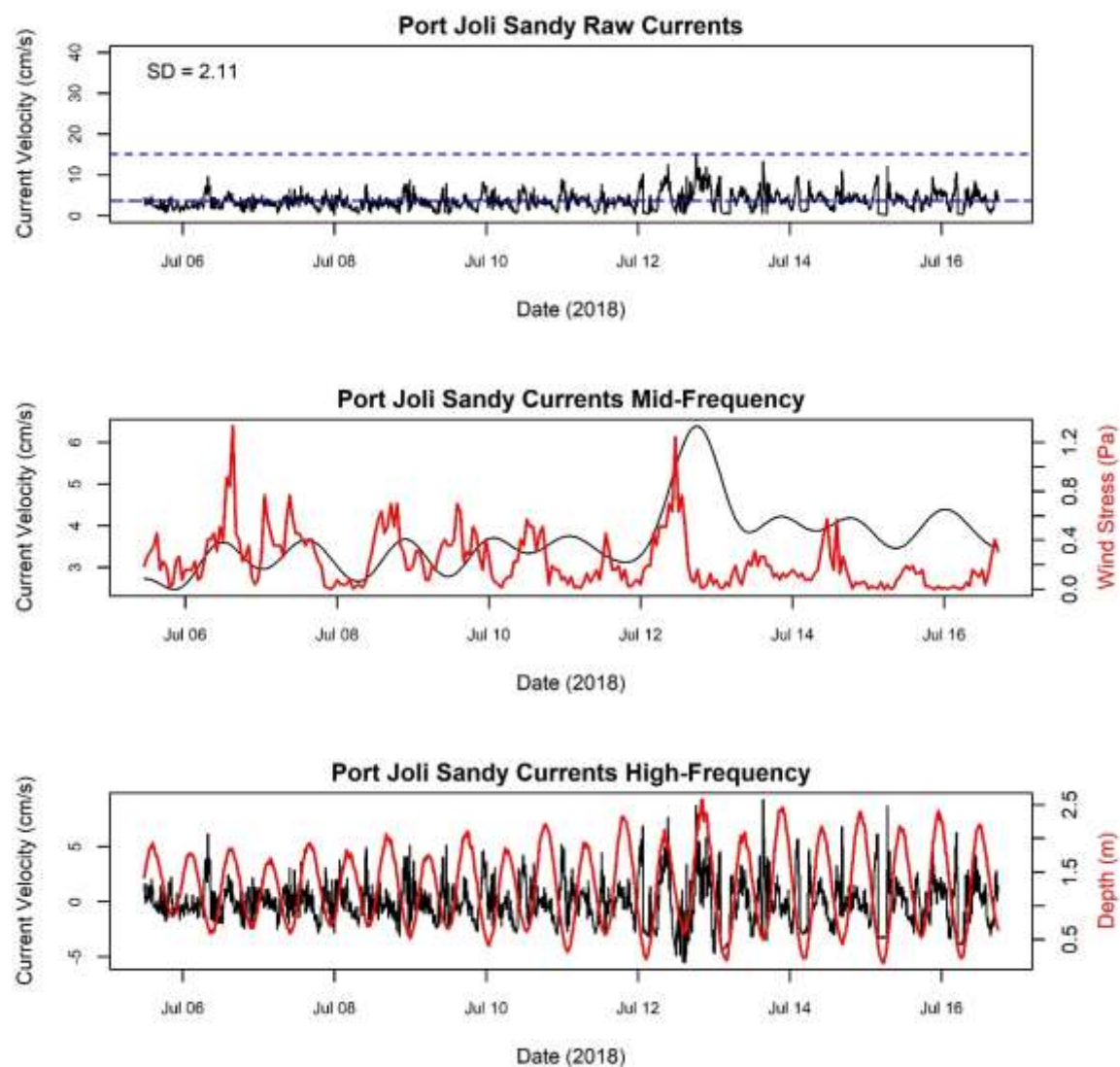
La Have

Figure S130. Raw current velocities (top panel) at La Have, and current velocities split into a mid-frequency band (middle panel, signals > 24 hours) and a high-frequency band (bottom panel, signals < 24 hours). Total wind stress is overlaid in red on mid-frequency current velocities, while depth is overlaid on high-frequency current velocities.
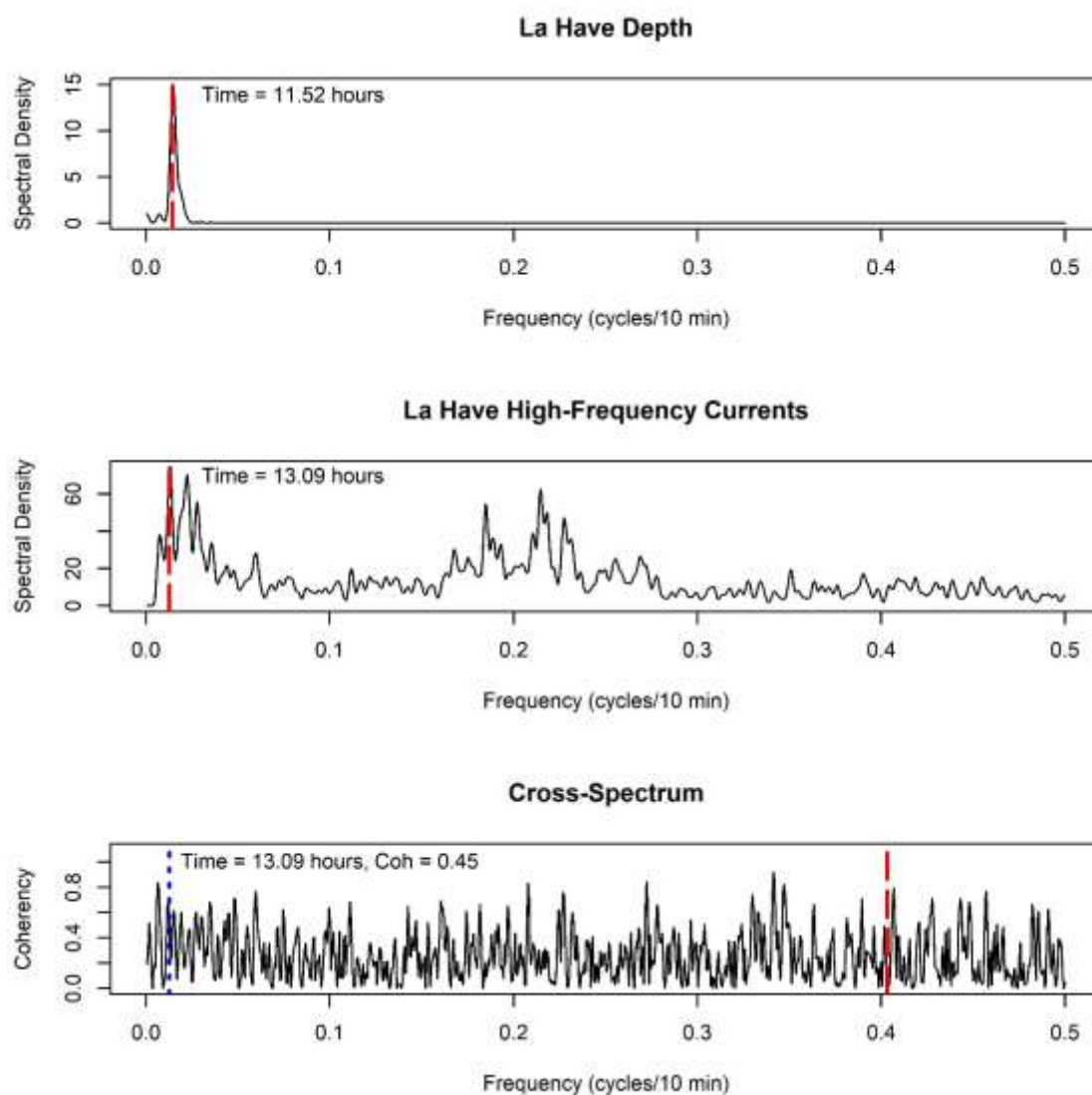
Figure S131. Spectral signatures of depth (top panel) and current (middle panel) time series at La Have. Bottom shows the coherency between time series at different frequencies. The red dotted line shows the frequency at which the highest coherency is observed, while the blue dotted line shows the frequency with the highest coherency between time series within the band of frequencies associated with the diurnal tidal constituents (0.126-0.144, 11.6-12.9 hours).

Figure S132. Cross correlation between wind stress and changes in currents in the middle-frequency band (>24 hours) at La Have. The lag with the highest correlation is shown with a red dotted line.

Mason's Island

Mason's Island Raw Currents

Mason's Island Currents Mid-Frequency

Mason's Island Currents High-Frequency

Figure S133. Raw current velocities (top panel) at Mason's Island, and current velocities split into a mid-frequency band (middle panel, signals > 24 hours) and a high-frequency band (bottom panel, signals < 24 hours). Total wind stress is overlaid in red on mid-frequency current velocities, while depth is overlaid on high-frequency current velocities.

Mason's Island Depth

Mason's Island High-Frequency Currents

Cross-Spectrum
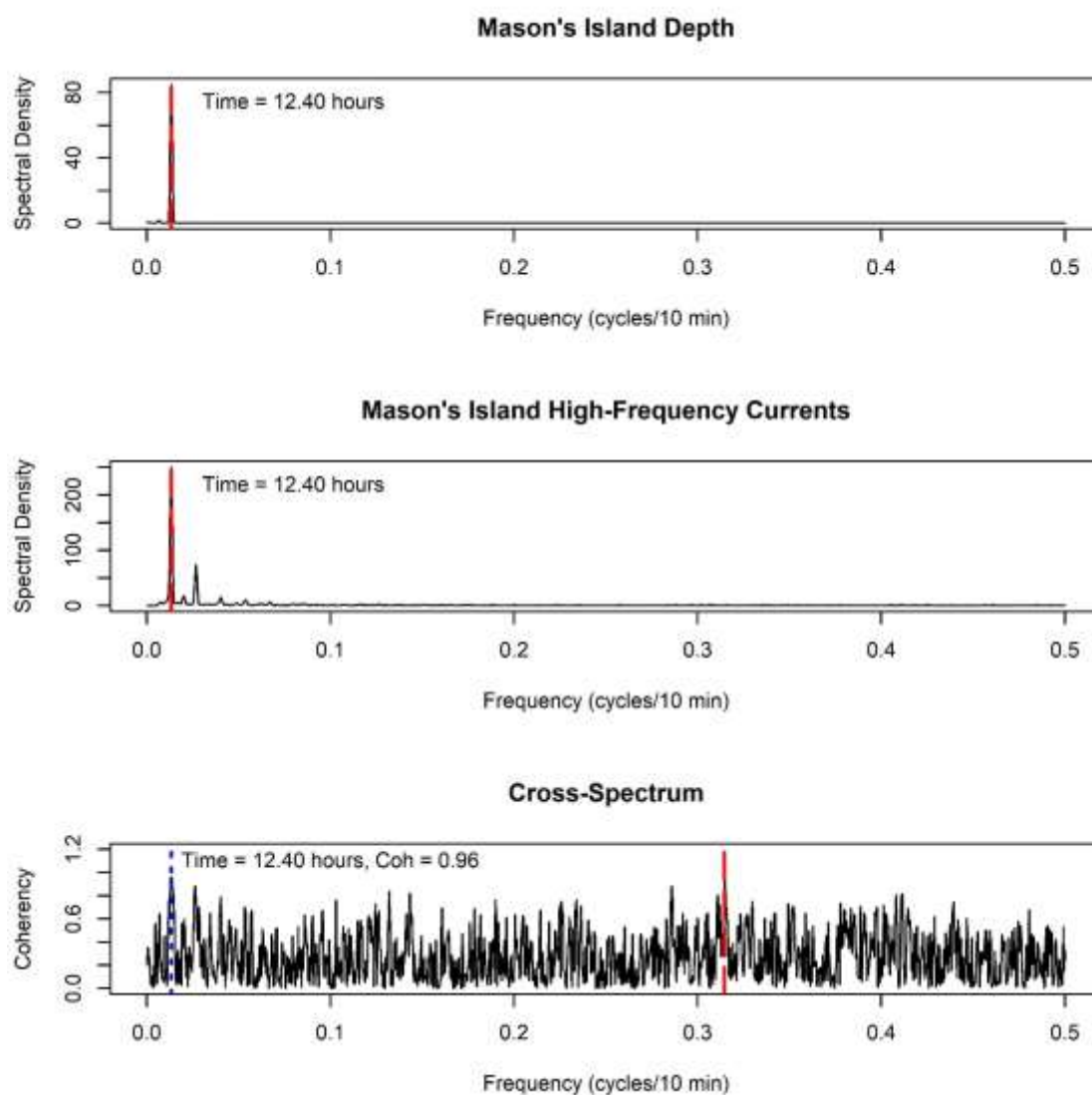
Figure S134. Spectral signatures of depth (top panel) and current (middle panel) time series at Masons's Island. Bottom shows the coherency between time series at different frequencies. The red dotted line shows the frequency at which the highest coherency is observed, while the blue dotted line shows the frequency with the highest coherency between time series within the band of frequencies associated with the diurnal tidal constituents (0.126-0.144, 11.6-12.9 hours).

Figure S135. Cross correlation between wind stress and changes in currents in the middle-frequency band (>24 hours) at Mason's Island. The lag with the highest correlation is shown with a red dotted line.
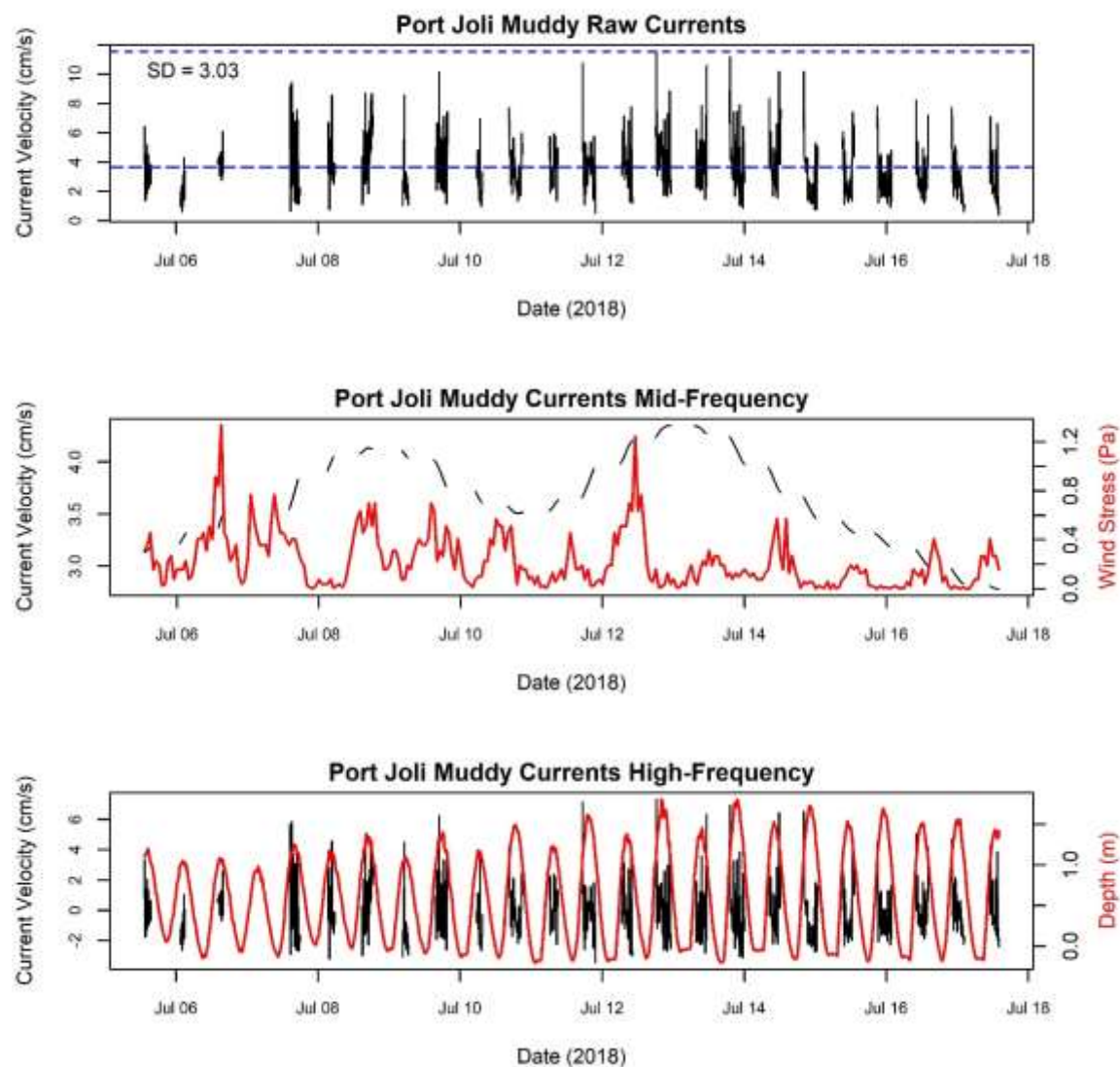
Port L'Hebert

Figure S136. Raw current velocities (top panel) at Port L'Hebert, and current velocities split into a mid-frequency band (middle panel, signals > 24 hours) and a high-frequency band (bottom panel, signals < 24 hours). Total wind stress is overlaid in red on mid-frequency current velocities, while depth is overlaid on high-frequency current velocities.
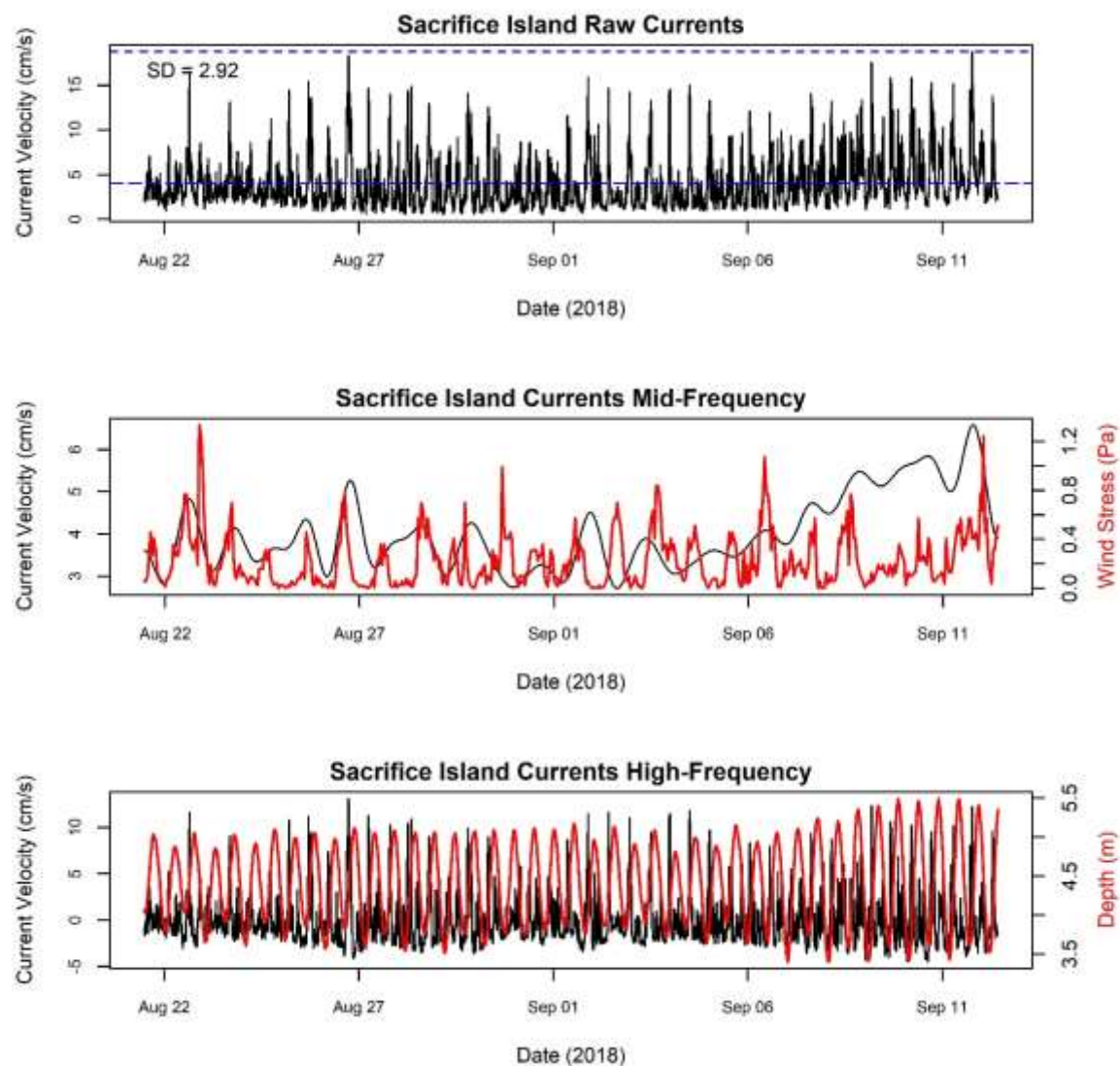
Port L'Hebert Depth

Port L'Hebert High-Frequency Currents

Cross-Spectrum
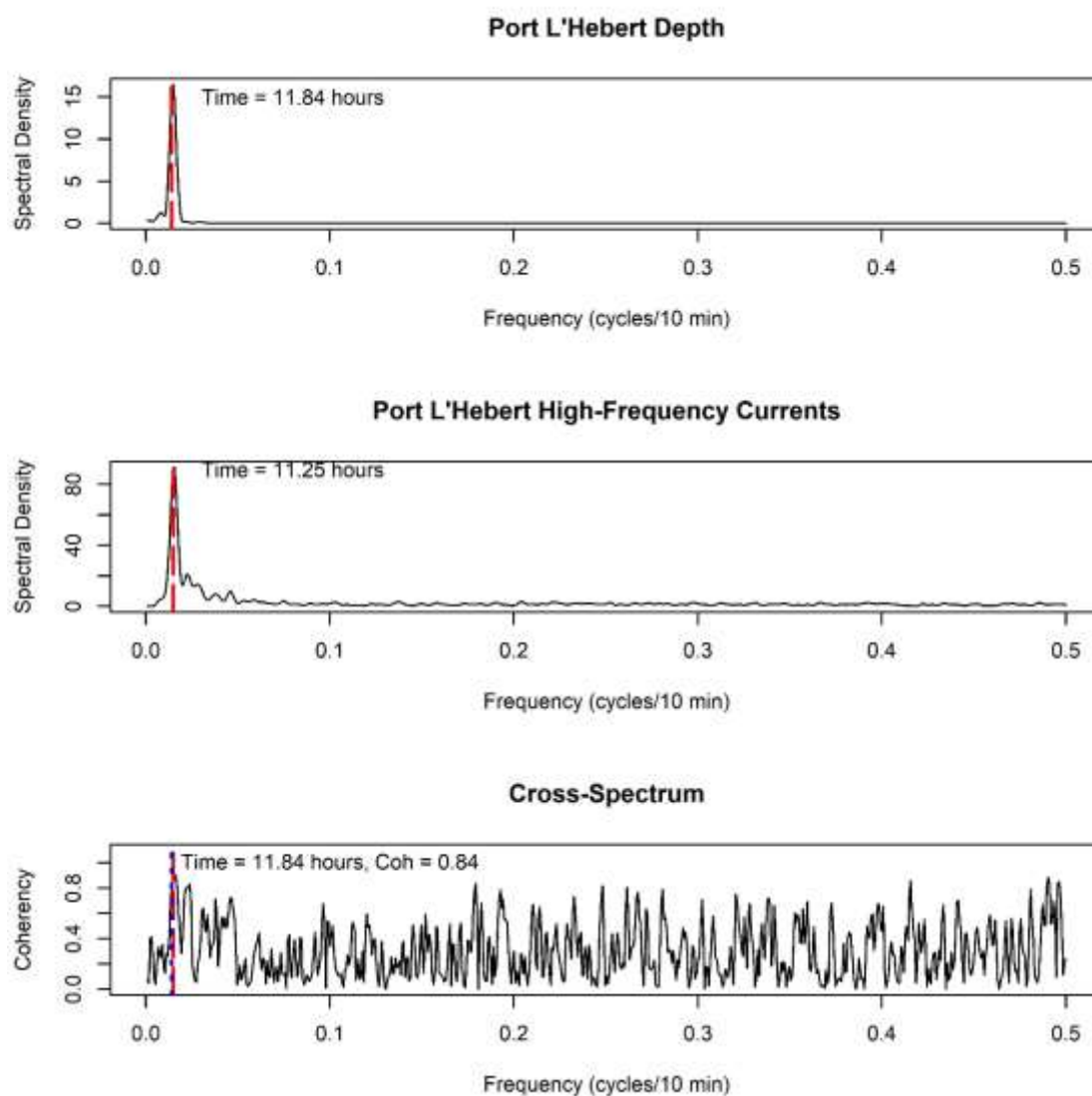
Figure S137. Spectral signatures of depth (top panel) and current (middle panel) time series at Port L'Hebert. Bottom shows the coherency between time series at different frequencies. The red dotted line shows the frequency at which the highest coherency is observed, while the blue dotted line shows the frequency with the highest coherency between time series within the band of frequencies associated with the diurnal tidal constituents (0.126-0.144, 11.6-12.9 hours).
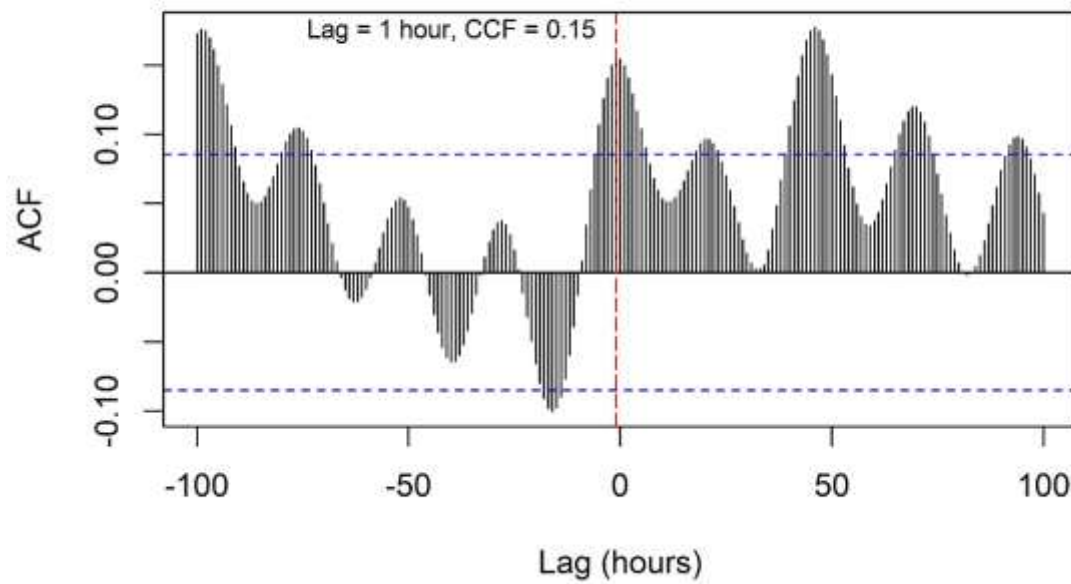
Figure S138. Cross correlation between wind stress and changes in currents in the middle-frequency band (>24 hours) at Port L'Hebert. The lag with the highest correlation is shown with a red dotted line.
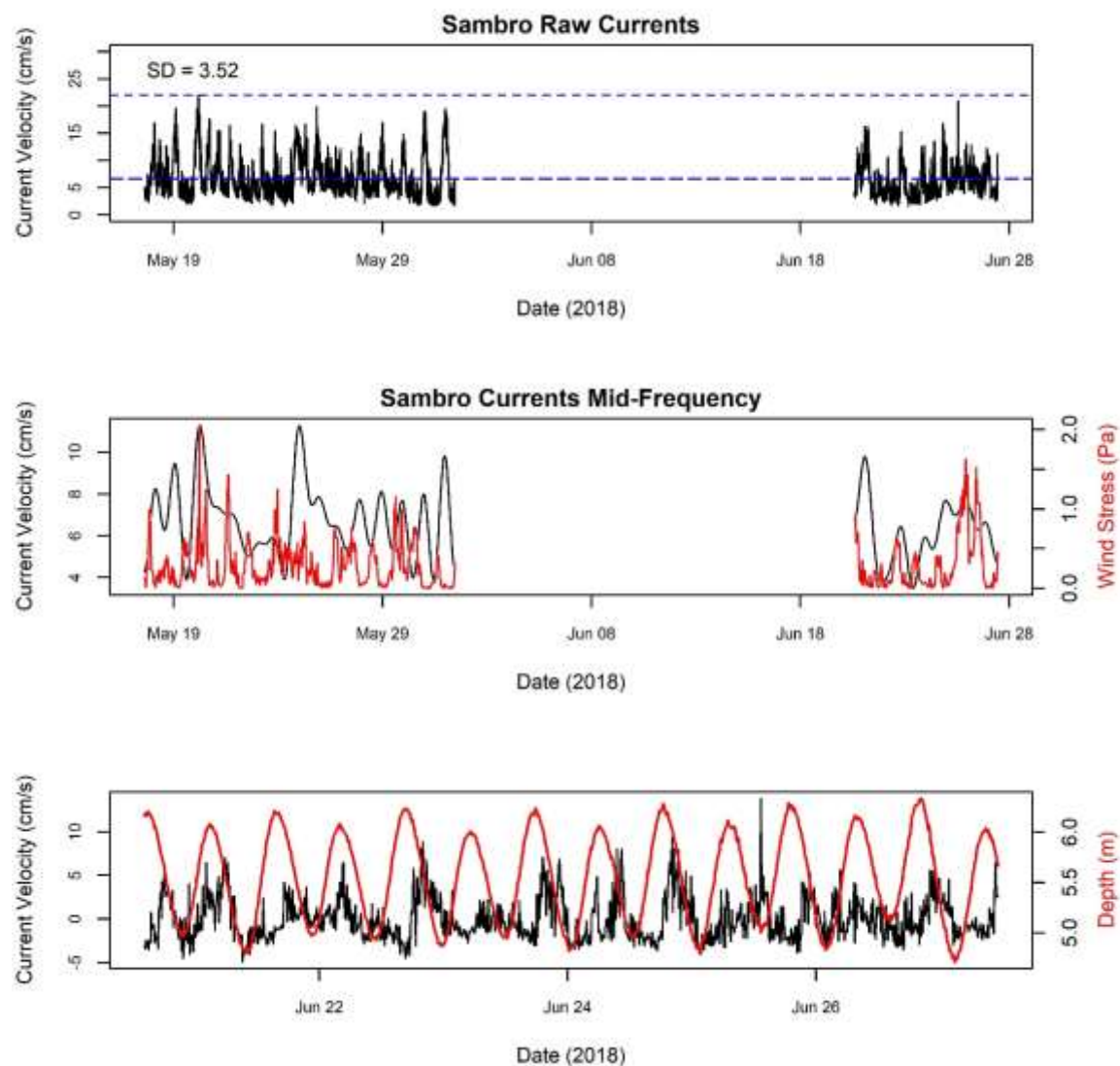
Port Joli
Sandy

Figure S139. Raw current velocities (top panel) at Port Joli sandy, and current velocities split into a mid-frequency band (middle panel, signals > 24 hours) and a high-frequency band (bottom panel, signals < 24 hours). Total wind stress is overlaid in red on mid-frequency current velocities, while depth is overlaid on high-frequency current velocities.
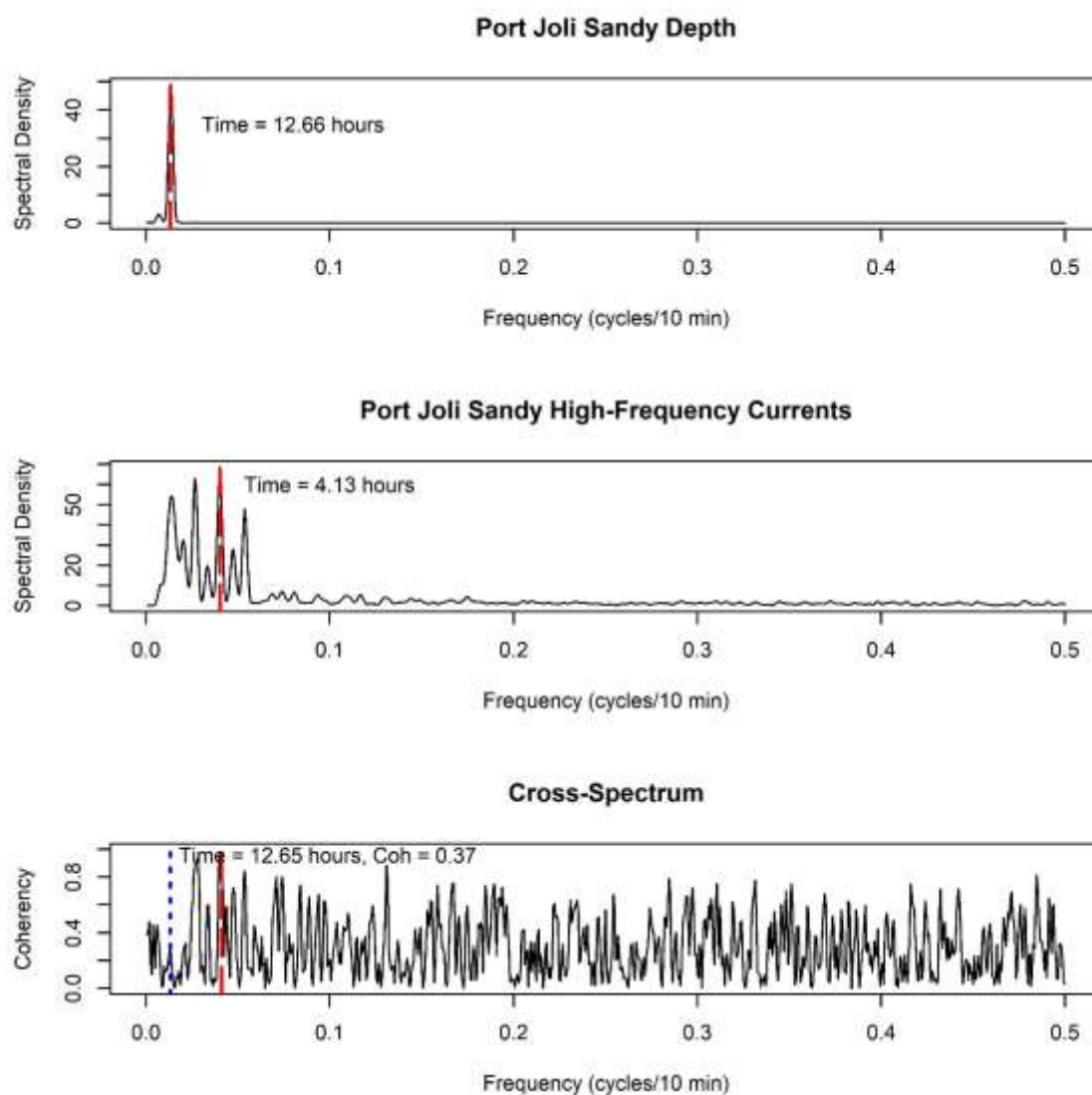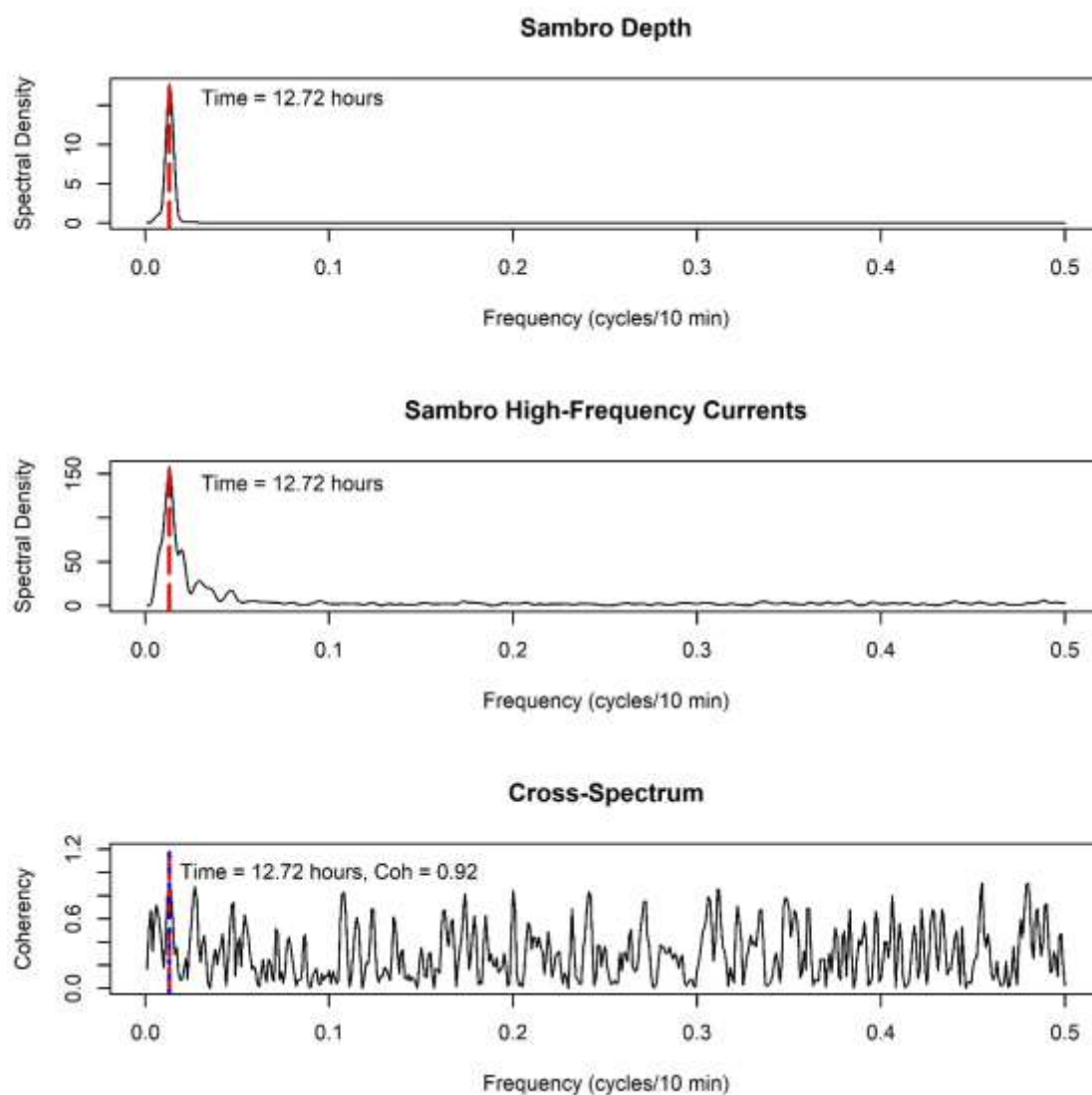
Figure S140. Spectral signatures of depth (top panel) and current (middle panel) time series at Port Joli sandy. Bottom shows the coherency between time series at different frequencies. The red dotted line shows the frequency at which the highest coherency is observed, while the blue dotted line shows the frequency with the highest coherency between time series within the band of frequencies associated with the diurnal tidal constituents (0.126-0.144, 11.6-12.9 hours).
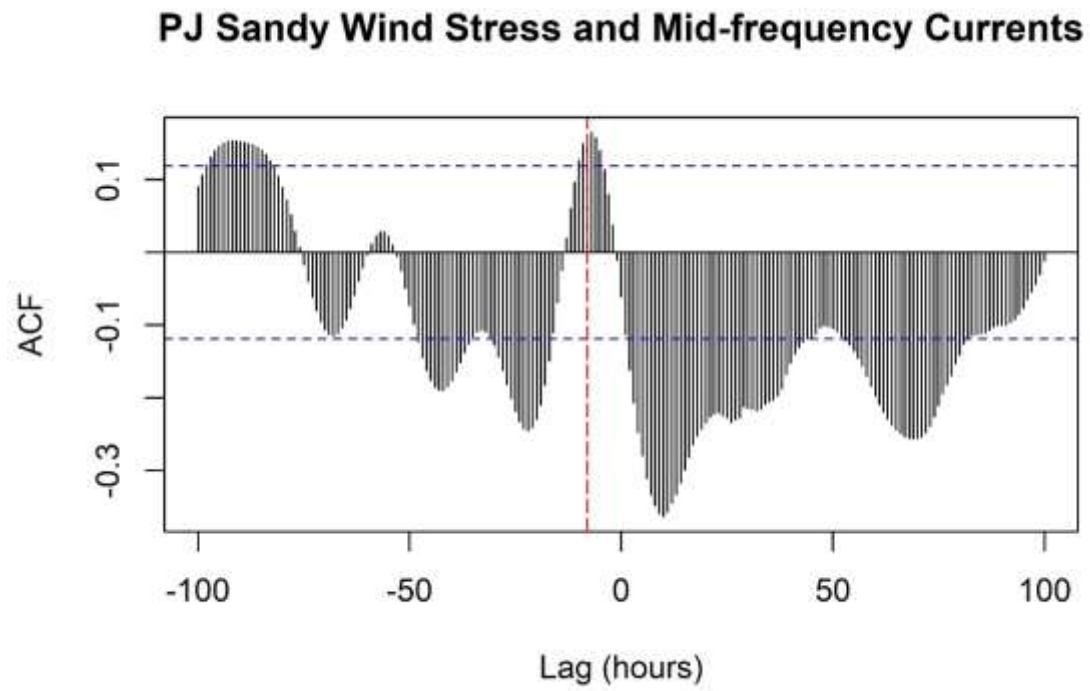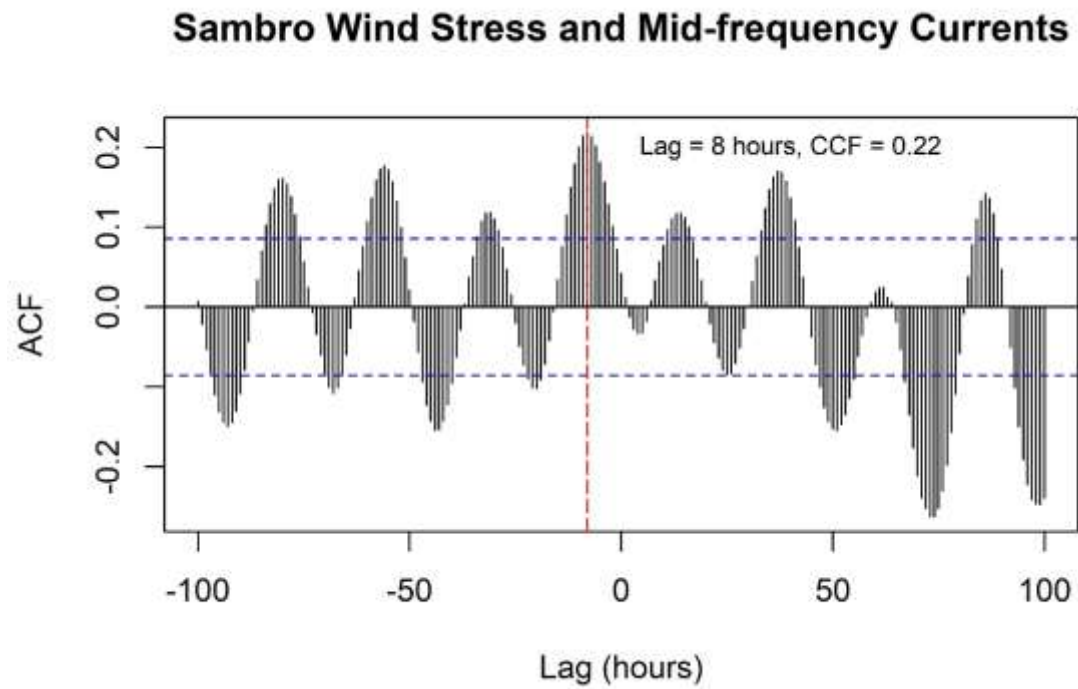
Figure S141. Cross correlation between wind stress and changes in currents in the middle-frequency band (>24 hours) at Port Joli sandy. The lag with the highest correlation is shown with a red dotted line.

Muddy

Figure S142. Raw current velocities (top panel) at Port Joli muddy, and current velocities split into a mid-frequency band (middle panel, signals > 24 hours) and a high-frequency band (bottom panel, signals < 24 hours). Total wind stress is overlaid in red on mid-frequency current velocities, while depth is overlaid on high-frequency current velocities.
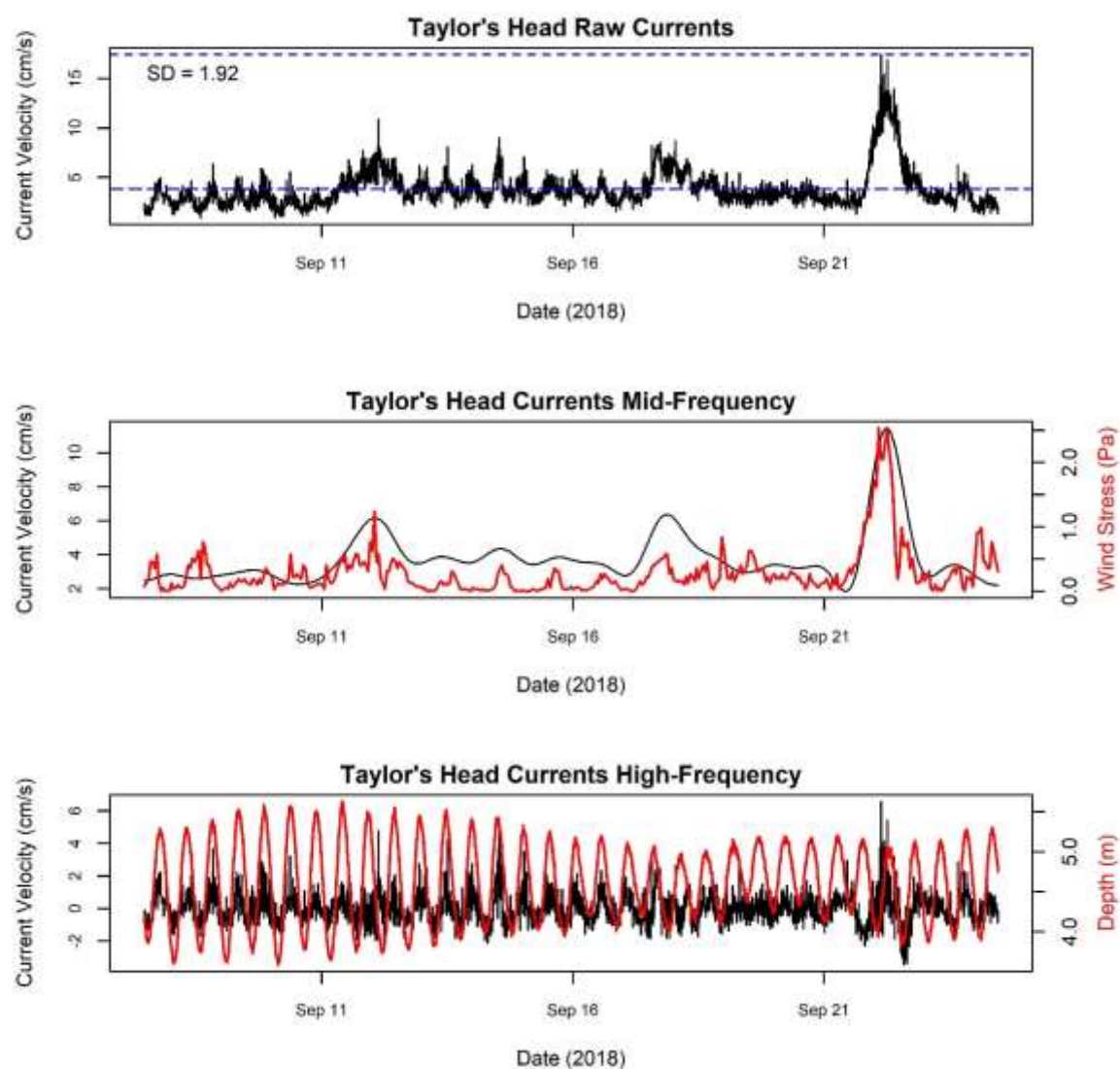
Sacrifice Island

Figure S143. Raw current velocities (top panel) at Sacrifice Island, and current velocities split into a mid-frequency band (middle panel, signals > 24 hours) and a high-frequency band (bottom panel, signals < 24 hours). Total wind stress is overlaid in red on mid-frequency current velocities, while depth is overlaid on high-frequency current velocities.

Sacrifice Island Depth

Sacrifice Island High-Frequency Currents

Cross-Spectrum
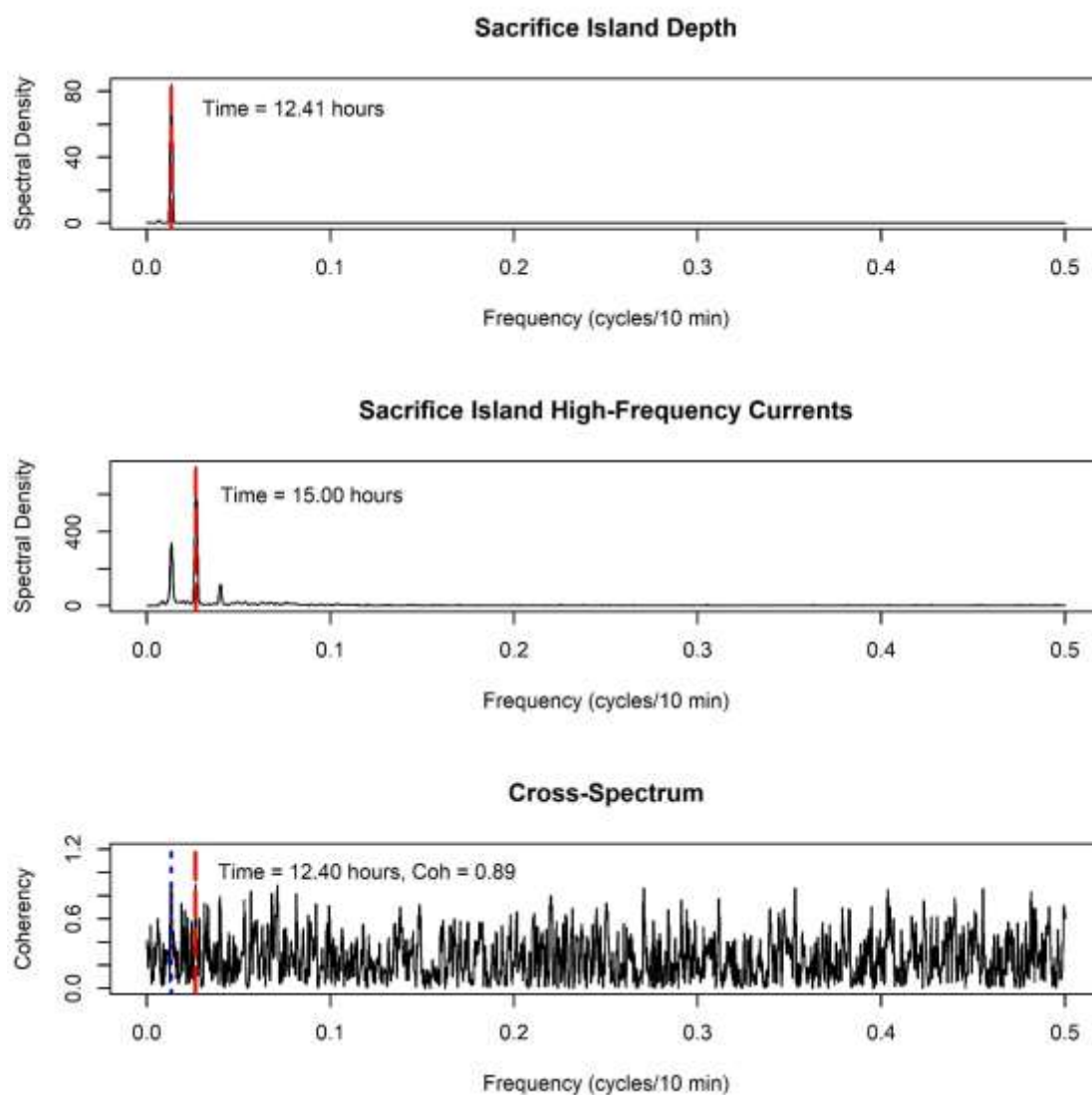
Figure S144. Spectral signatures of depth (top panel) and current (middle panel) time series at Sacrifice Island. Bottom shows the coherency between time series at different frequencies. The red dotted line shows the frequency at which the highest coherency is observed, while the blue dotted line shows the frequency with the highest coherency between time series within the band of frequencies associated with the diurnal tidal constituents (0.126-0.144, 11.6-12.9 hours).

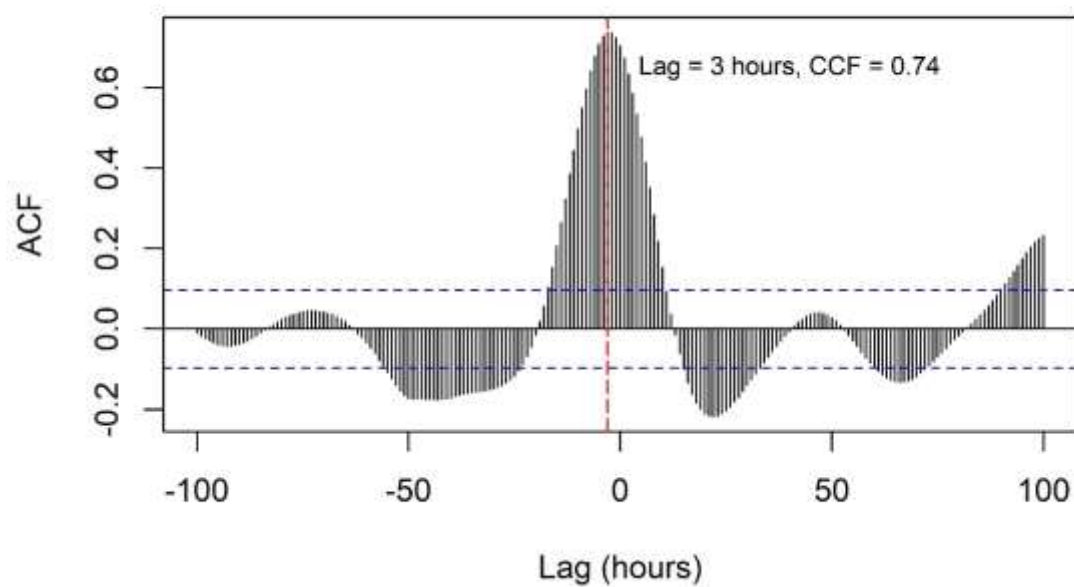## Sacrifice Island Wind Stress and Mid-frequency Currents

Figure S145. Cross correlation between wind stress and changes in currents in the middle-frequency band (>24 hours) at Sacrifice Island. The lag with the highest correlation is shown with a red dotted line.

Sambro Island

Figure S146. Raw current velocities (top panel) at Sambro Island, and current velocities split into a mid-frequency band (middle panel, signals > 24 hours) and a high-frequency band (bottom panel, signals < 24 hours). Total wind stress is overlaid in red on mid-frequency current velocities, while depth is overlaid on high-frequency current velocities.

Sambro Depth

Sambro High-Frequency Currents

Cross-Spectrum

Figure S147. Spectral signatures of depth (top panel) and current (middle panel) time series at Sambro Island. Bottom shows the coherency between time series at different frequencies. The red dotted line shows the frequency at which the highest coherency is observed, while the blue dotted line shows the frequency with the highest coherency between time series within the band of frequencies associated with the diurnal tidal constituents (0.126-0.144, 11.6-12.9 hours).

Figure S148. Cross correlation between wind stress and changes in currents in the middle-frequency band (>24 hours) at Sambro Island. The lag with the highest correlation is shown with a red dotted line.

Taylor's Head

Figure S149. Raw current velocities (top panel) at Taylor's Head, and current velocities split into a mid-frequency band (middle panel, signals > 24 hours) and a high-frequency band (bottom panel, signals < 24 hours). Total wind stress is overlaid in red on mid-frequency current velocities, while depth is overlaid on high-frequency current velocities.
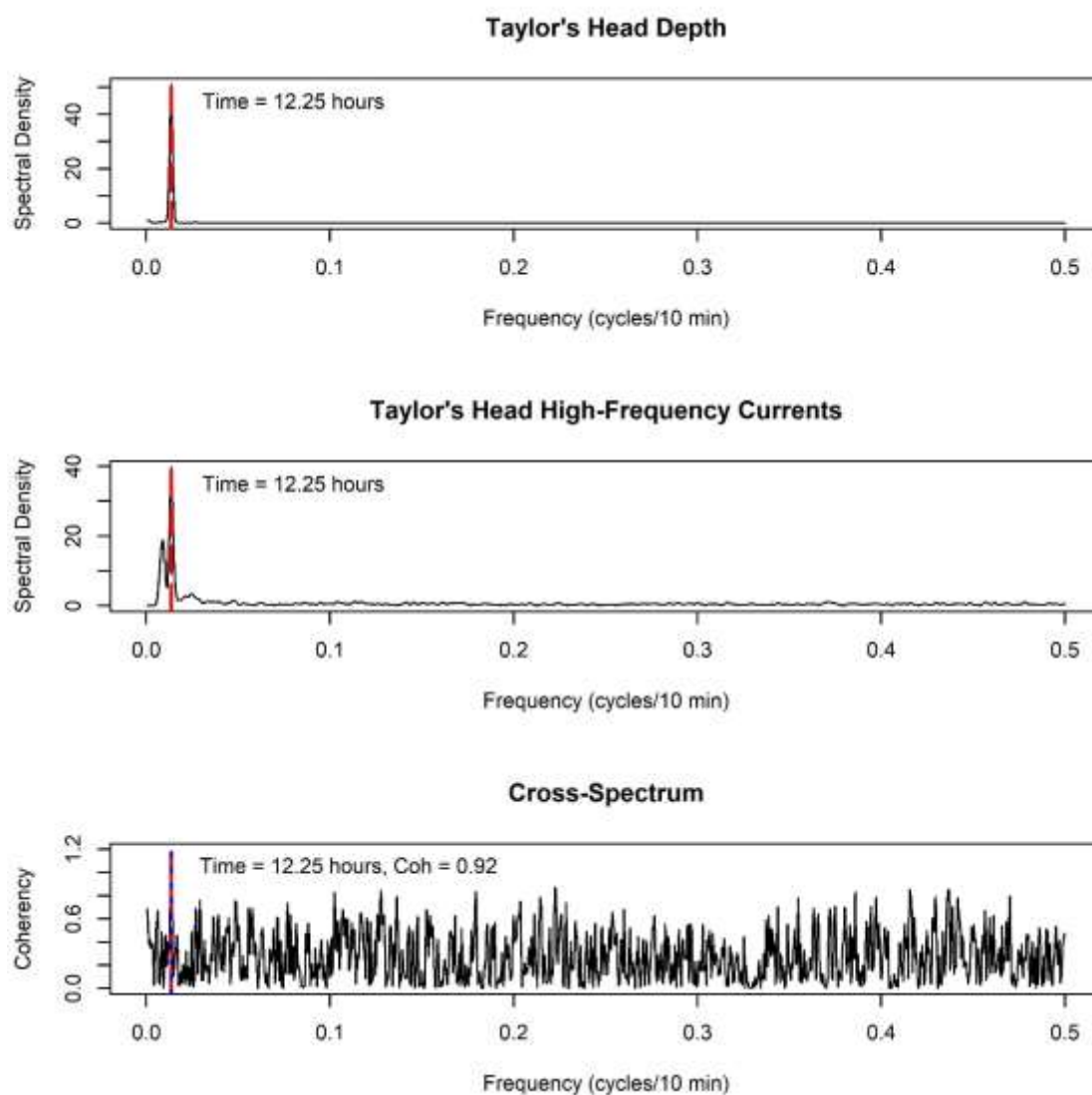
Figure S150. Spectral signatures of depth (top panel) and current (middle panel) time series at Taylor's Head. Bottom shows the coherency between time series at different frequencies. The red dotted line shows the frequency at which the highest coherency is observed, while the blue dotted line shows the frequency with the highest coherency between time series within the band of frequencies associated with the diurnal tidal constituents (0.126-0.144, 11.6-12.9 hours).

Figure S151. Cross correlation between wind stress and changes in currents in the middle-frequency band (>24 hours) at Taylor's Head. The lag with the highest correlation is shown with a red dotted line.
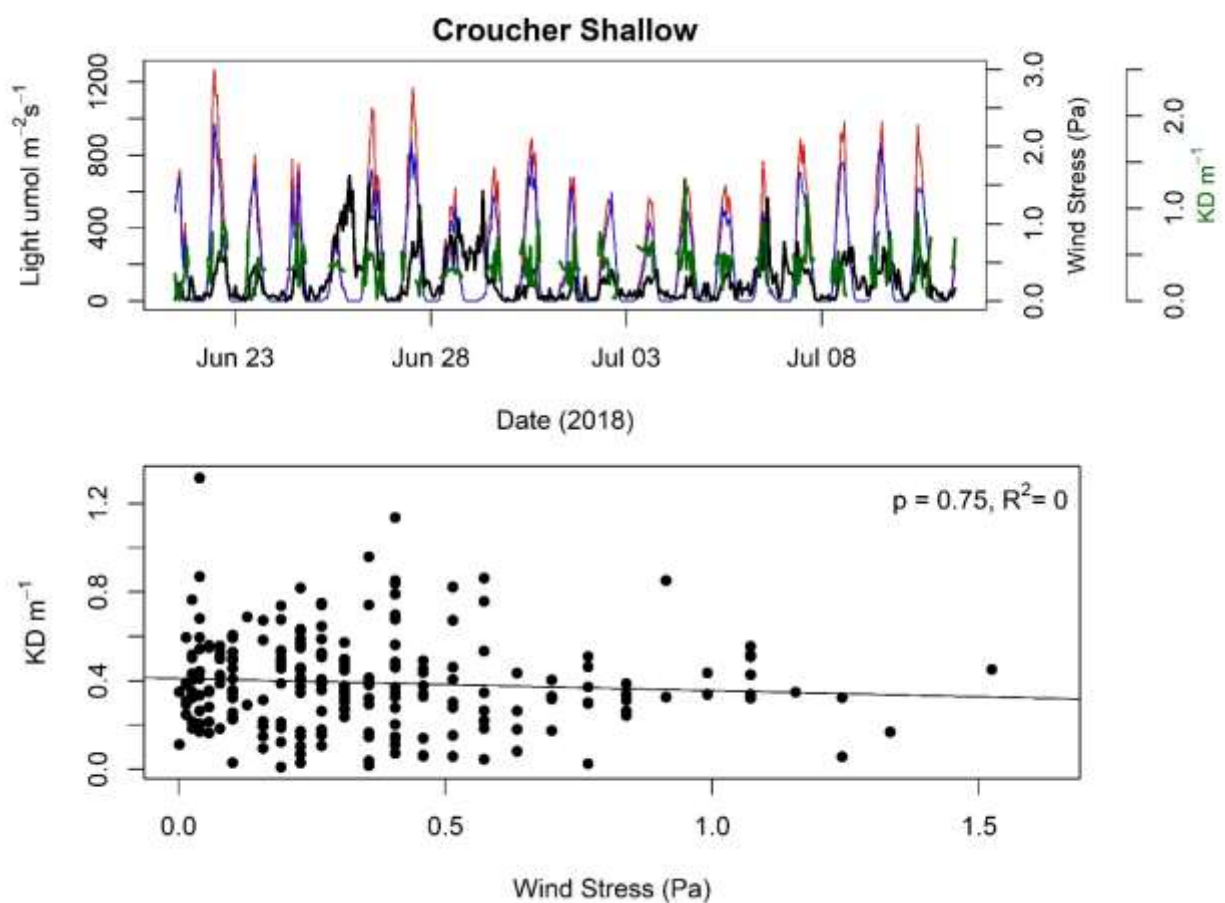
Light

Cable Island
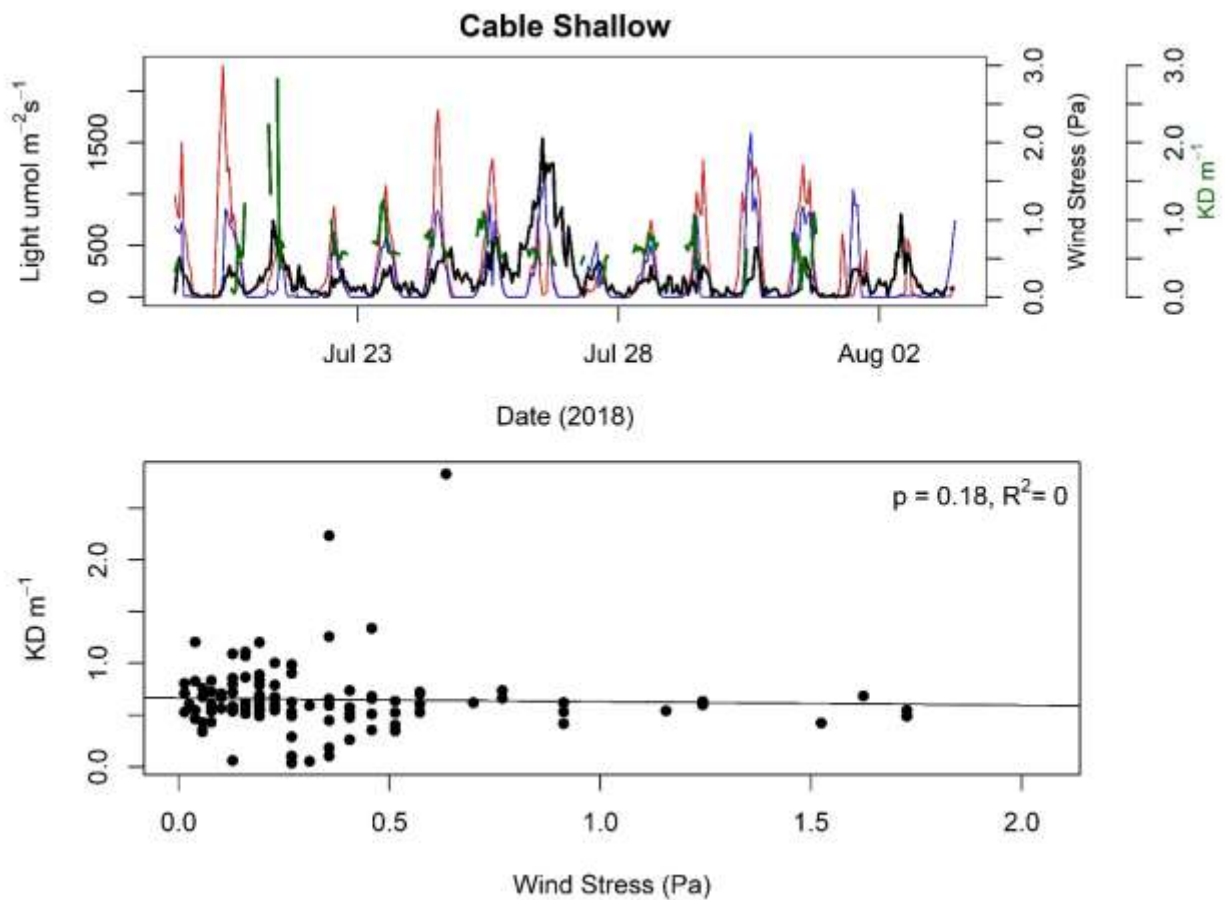
Figure S152. Light conditions in relation to wind stress at the shallow location at Cable Island. Top panel shows light readings from the top sensor (red line) and the bottom sensor (blue line). The green line on this panel shows light attenuation and the black line shows wind stress. Bottom panel shows the relationship between light attenuation and wind stress.
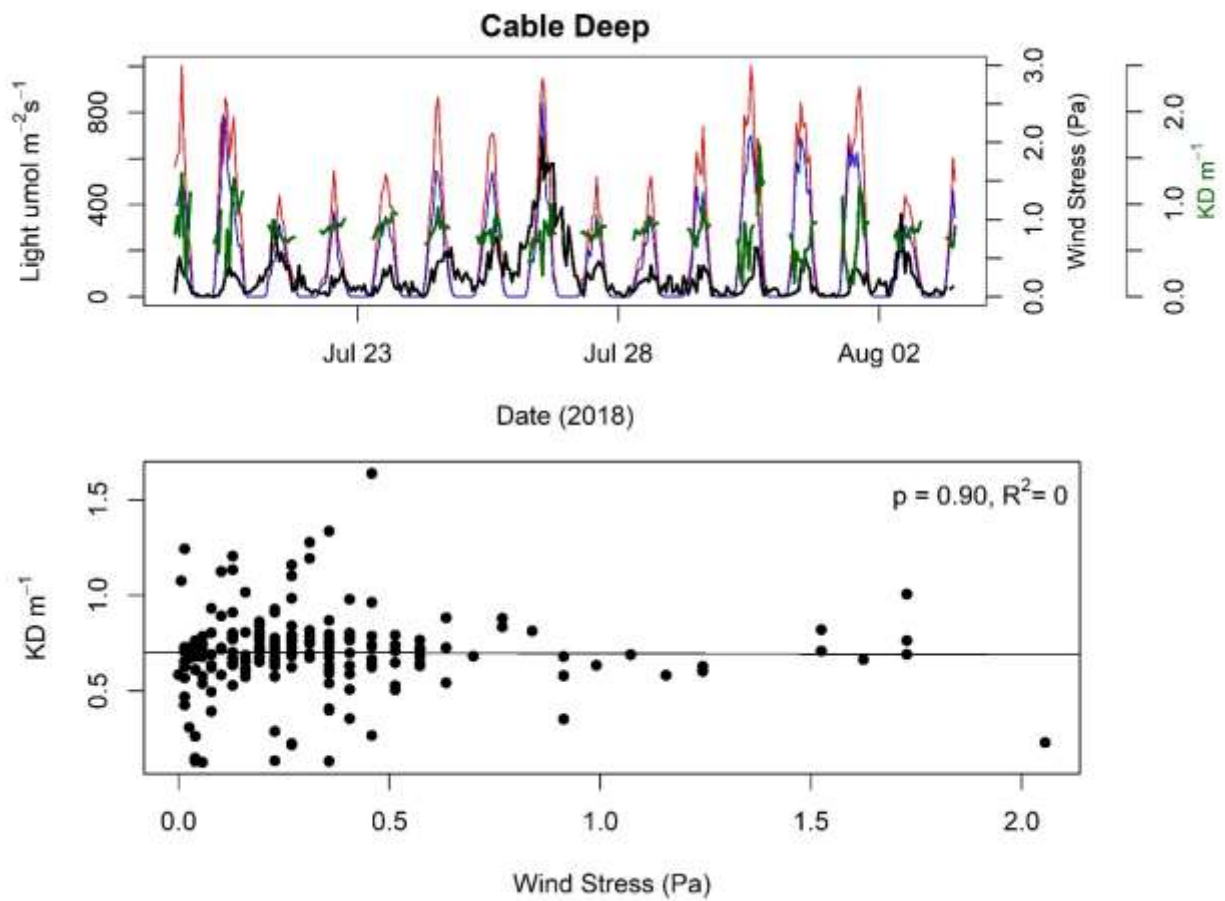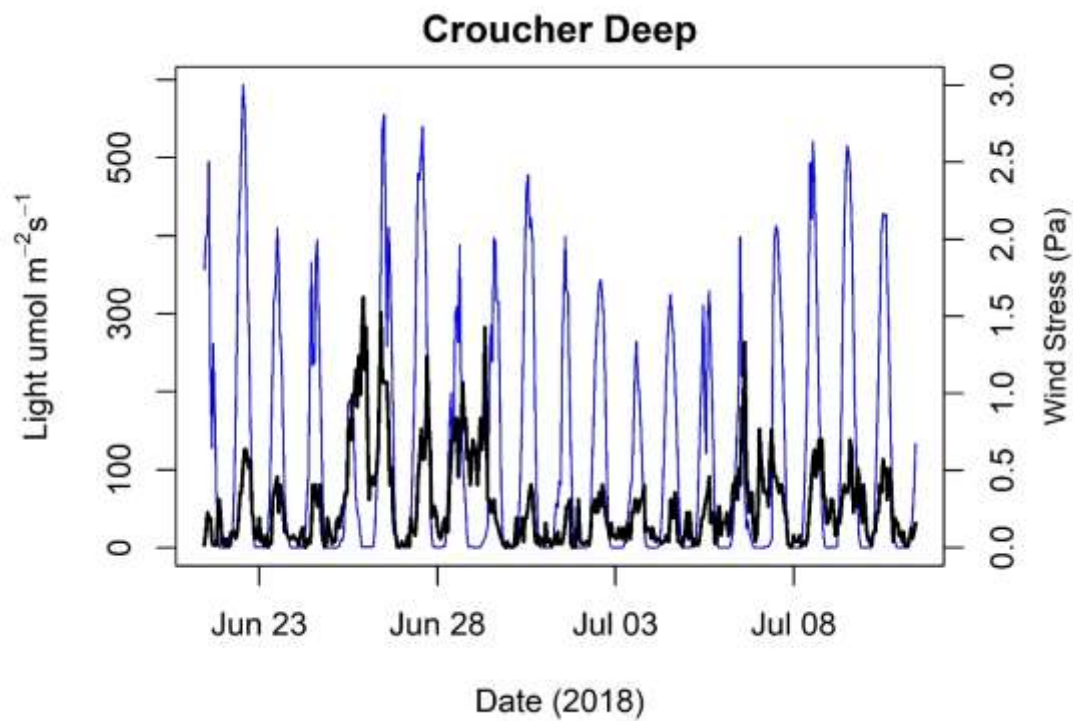
Figure S153. Light conditions in relation to wind stress at the deep location at Cable Island. Top panel shows light readings from the top sensor (red line) and the bottom sensor (blue line). The green line on this panel shows light attenuation and the black line shows wind stress. Bottom panel shows the relationship between light attenuation and wind stress.
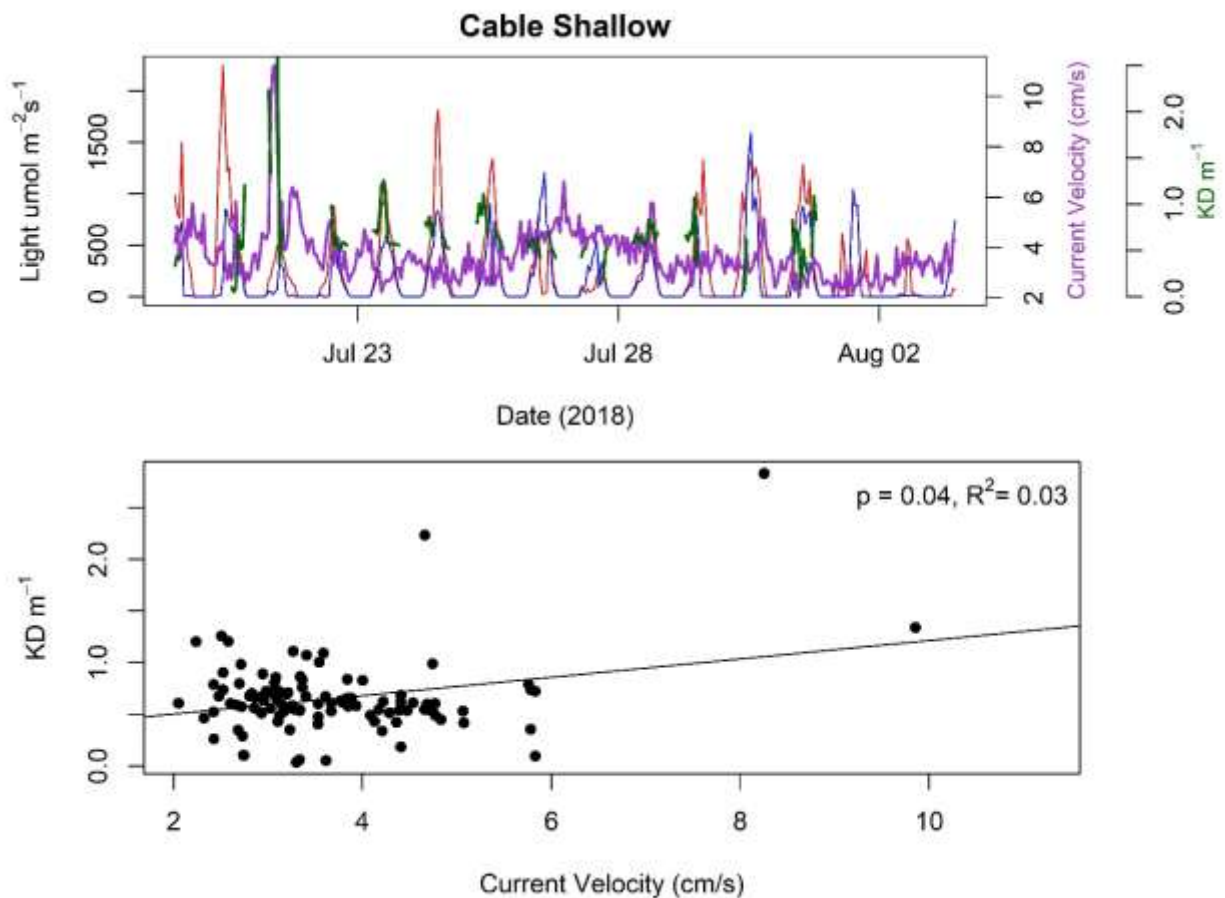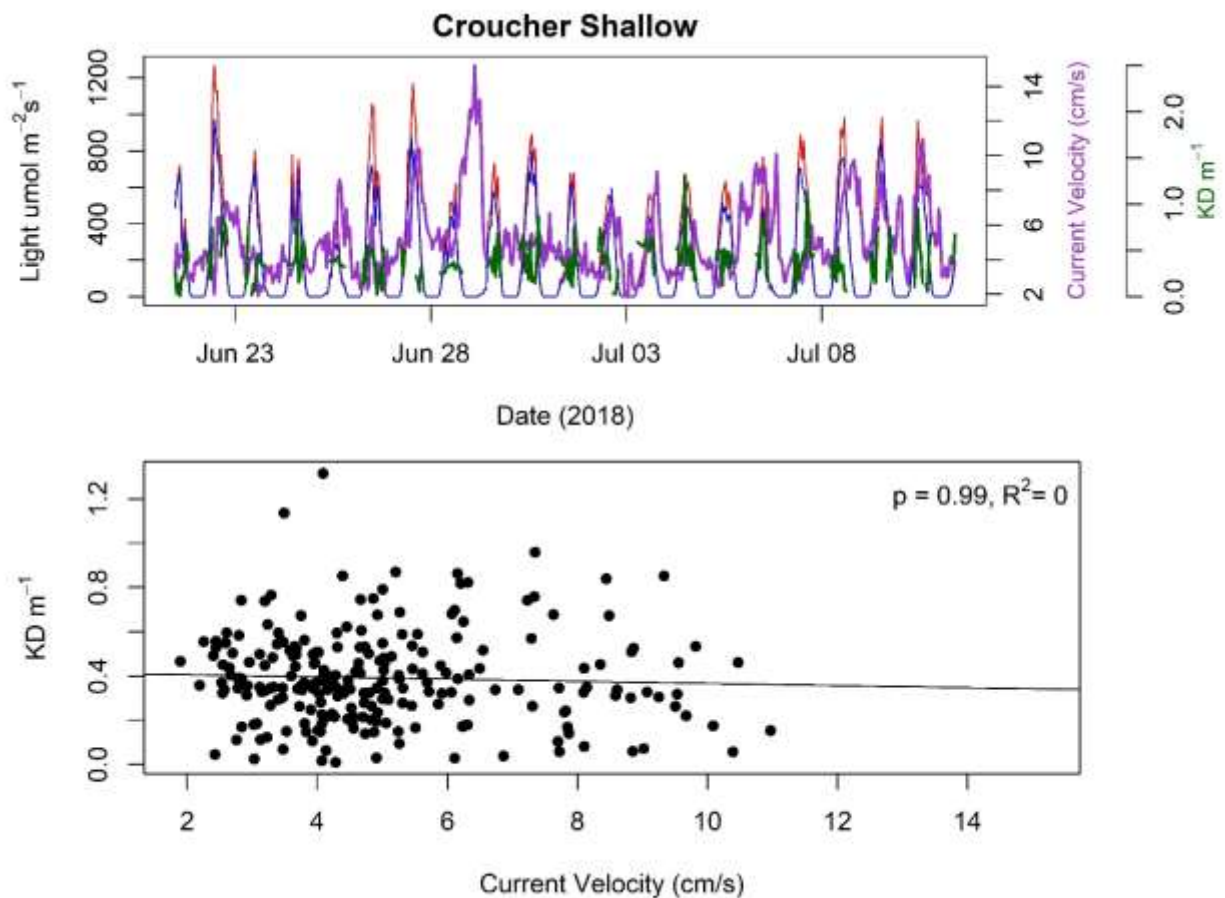
Figure S154. Light conditions in relation to current velocities at the shallow location at Cable Island. Top panel shows light readings from the top sensor (red line) and the bottom sensor (blue line). The green line on this panel shows light attenuation and the purple line shows current velocities. Bottom panel shows the relationship between light attenuation and wind stress.
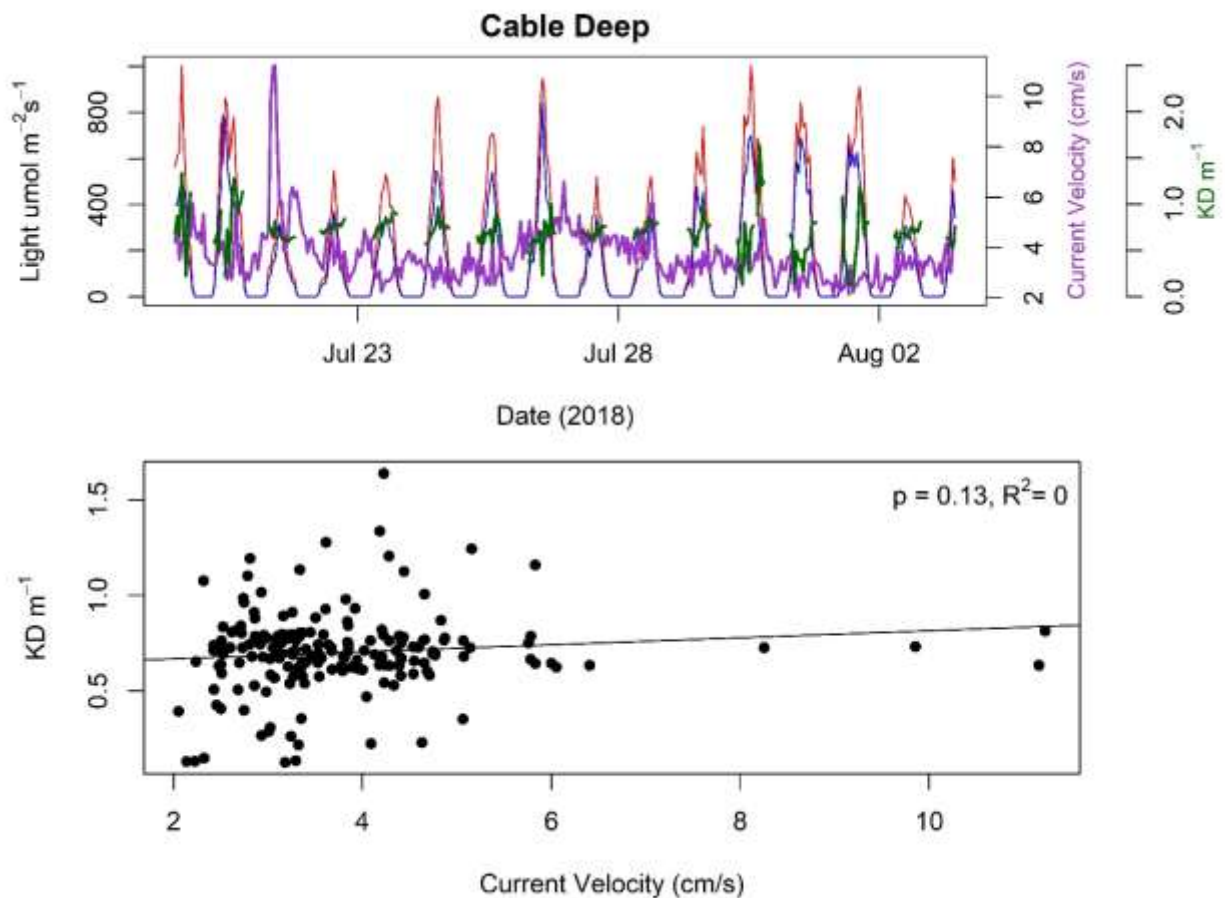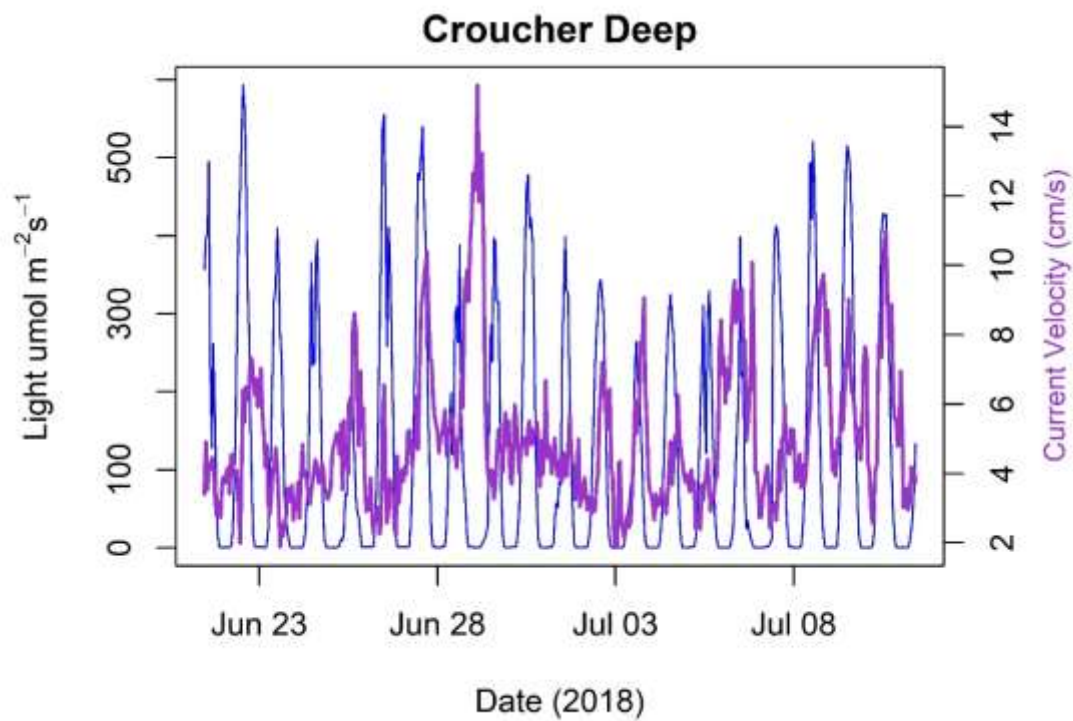
Figure S155. Light conditions in relation to current velocities at the shallow location at Cable Island. Top panel shows light readings from the top sensor (red line) and the bottom sensor (blue line). The green line on this panel shows light attenuation and the purple line shows current velocities. Bottom panel shows the relationship between light attenuation and wind stress.
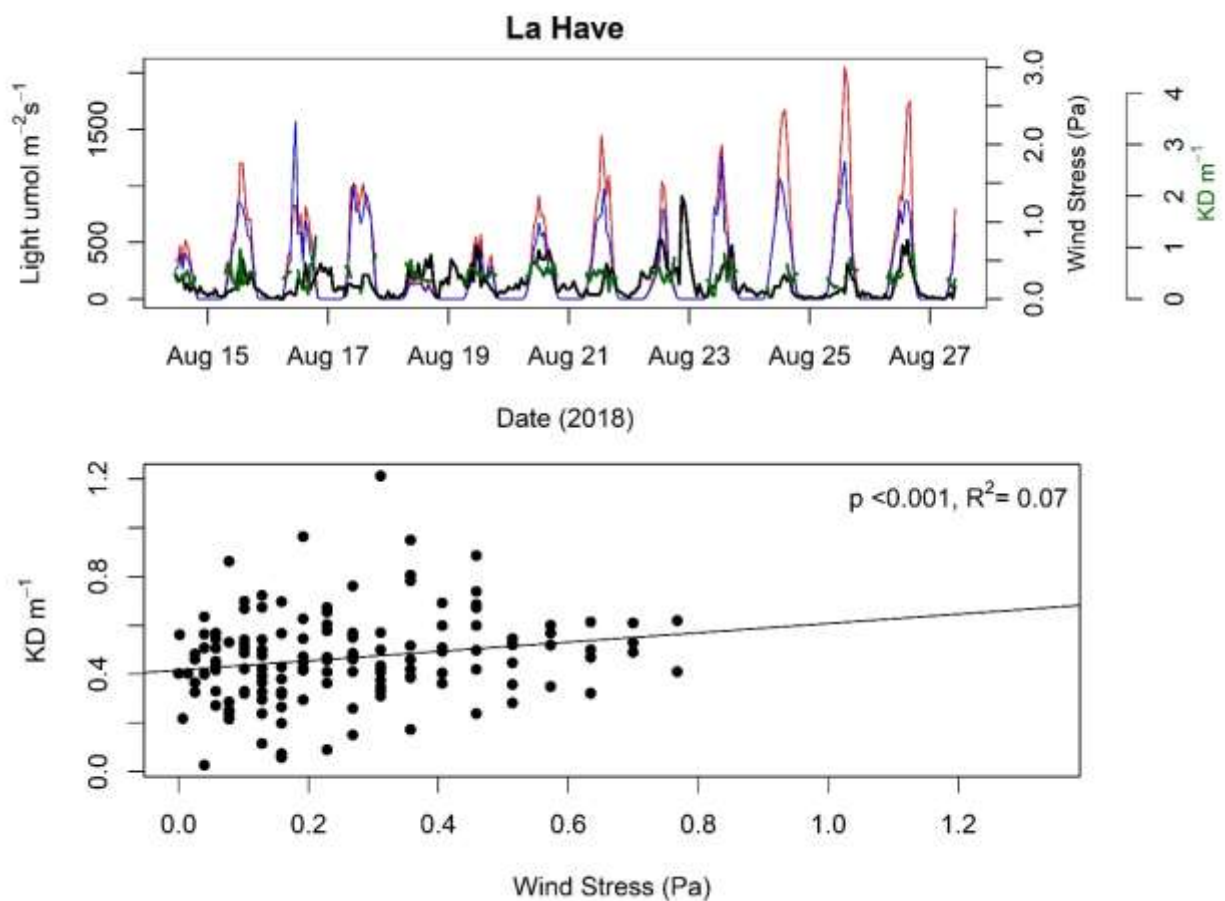
Croucher Island

Figure S156. Light conditions in relation to wind stress at the shallow location at Croucher Island. Top panel shows light readings from the top sensor (red line) and the bottom sensor (blue line). The green line on this panel shows light attenuation and the black line shows wind stress. Bottom panel shows the relationship between light attenuation and wind stress.
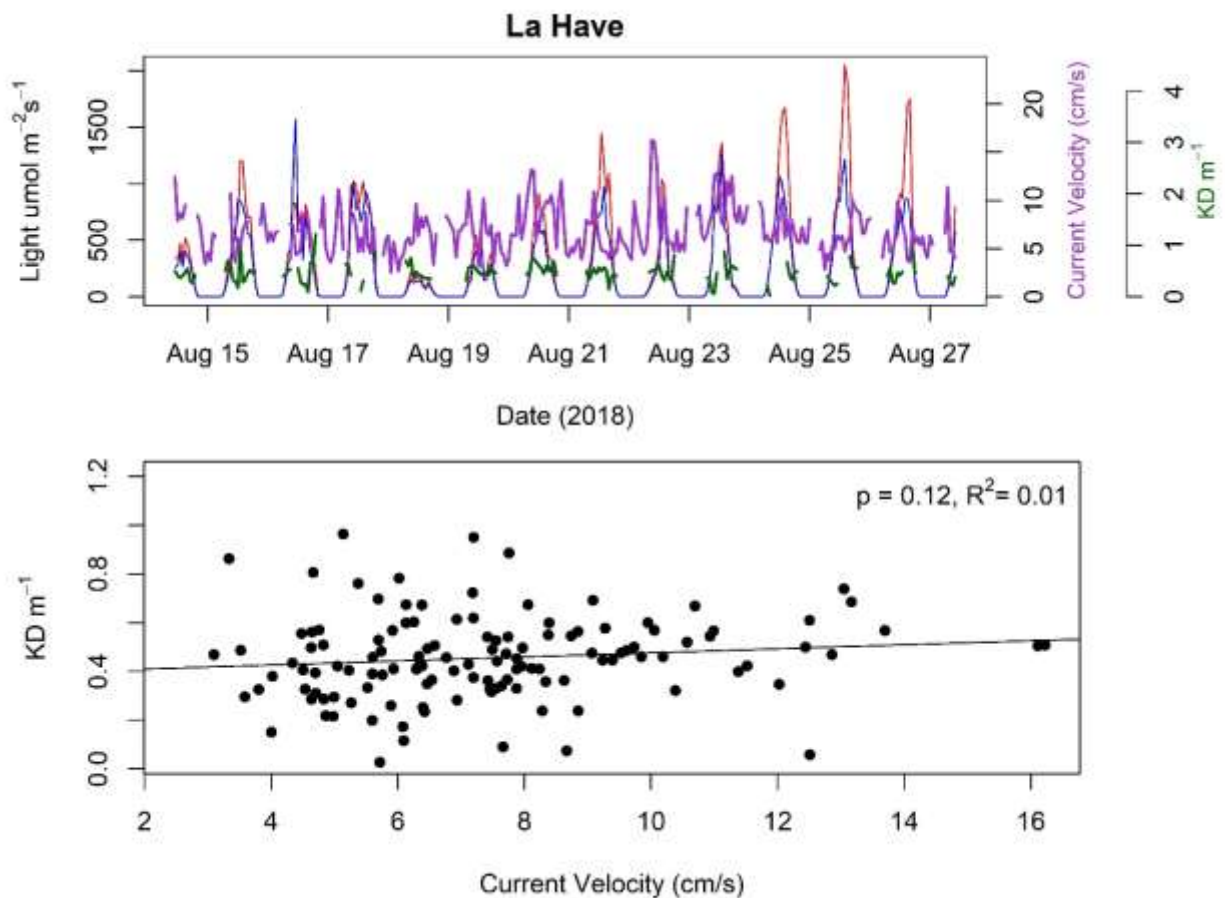
Figure S157. Light conditions in relation to wind stress at the deep location at Croucher Island. Only light readings from the bottom sensor (blue line) are available. The black line shows wind stress.

Figure S158. Light conditions in relation to current velocities at the shallow location at Croucher Island. Top panel shows light readings from the top sensor (red line) and the bottom sensor (blue line). The green line on this panel shows light attenuation and purple line shows current velocities. Bottom panel shows the relationship between light attenuation and current velocities.

Figure S159. Light conditions in relation to current velocities at the deep location at Croucher Island. Only light readings from the bottom sensor (blue line) are available. The purple line shows current velocities.

La Have

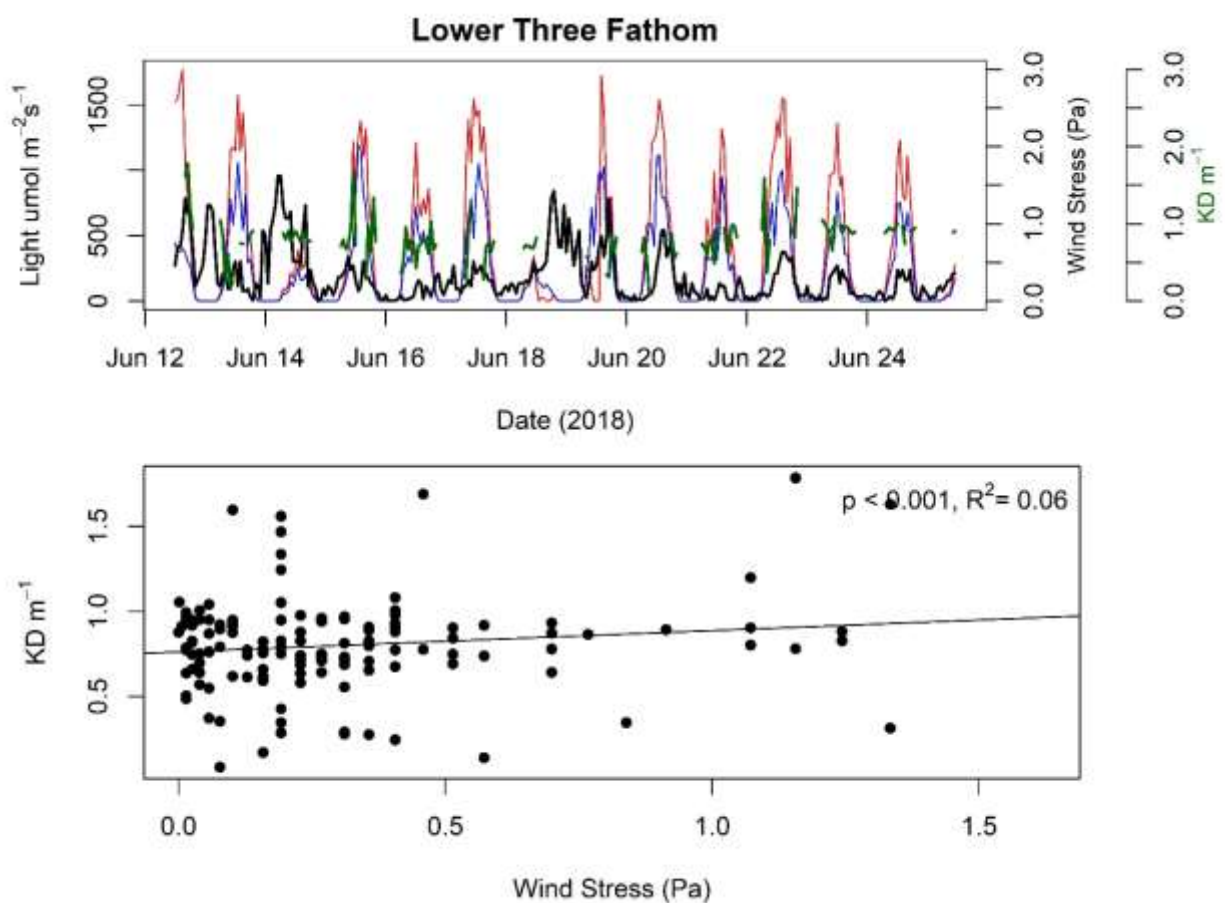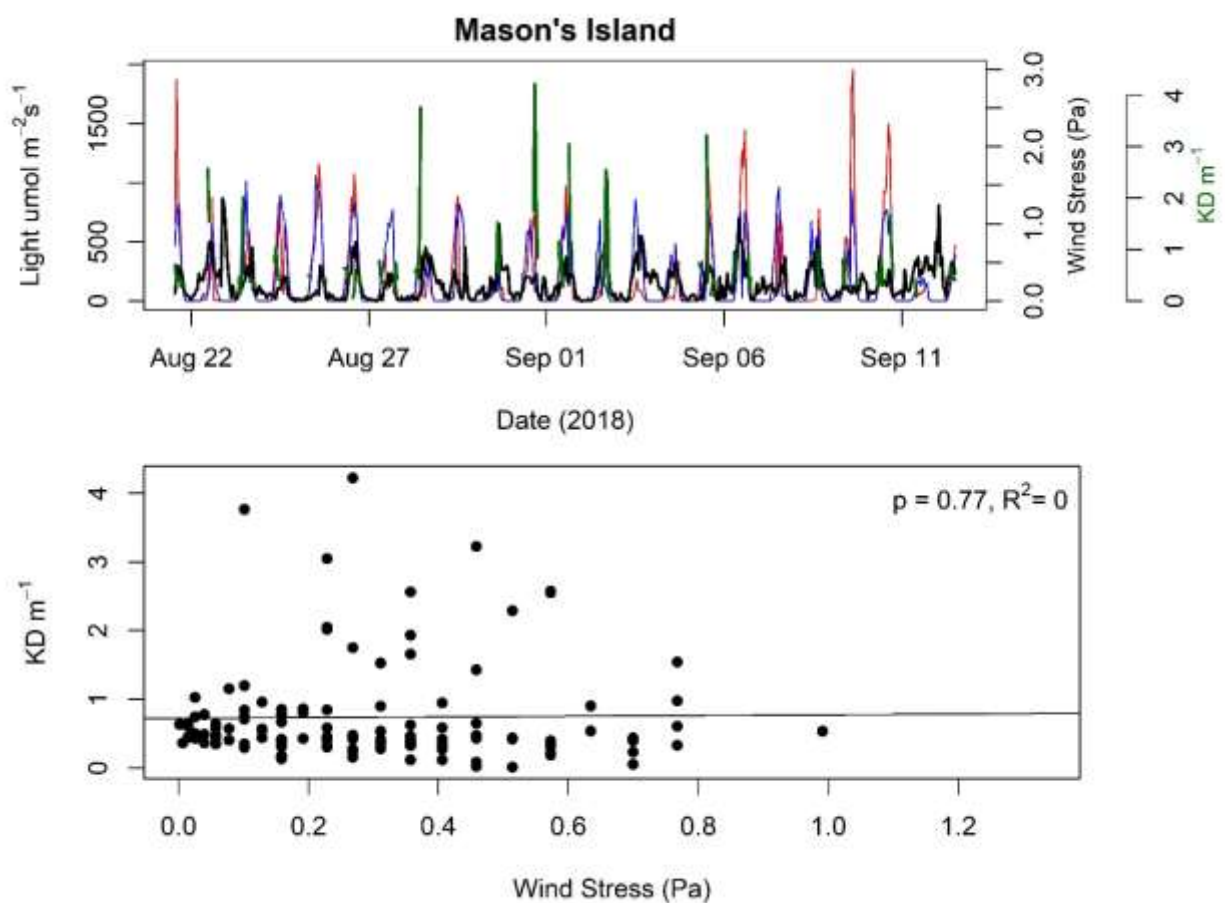Figure S160. Light conditions in relation to wind stress at the shallow location at La Have Island. Top panel shows light readings from the top sensor (red line) and the bottom sensor (blue line). The green line on this panel shows light attenuation and the black line shows wind stress. Bottom panel shows the relationship between light attenuation and wind stress.
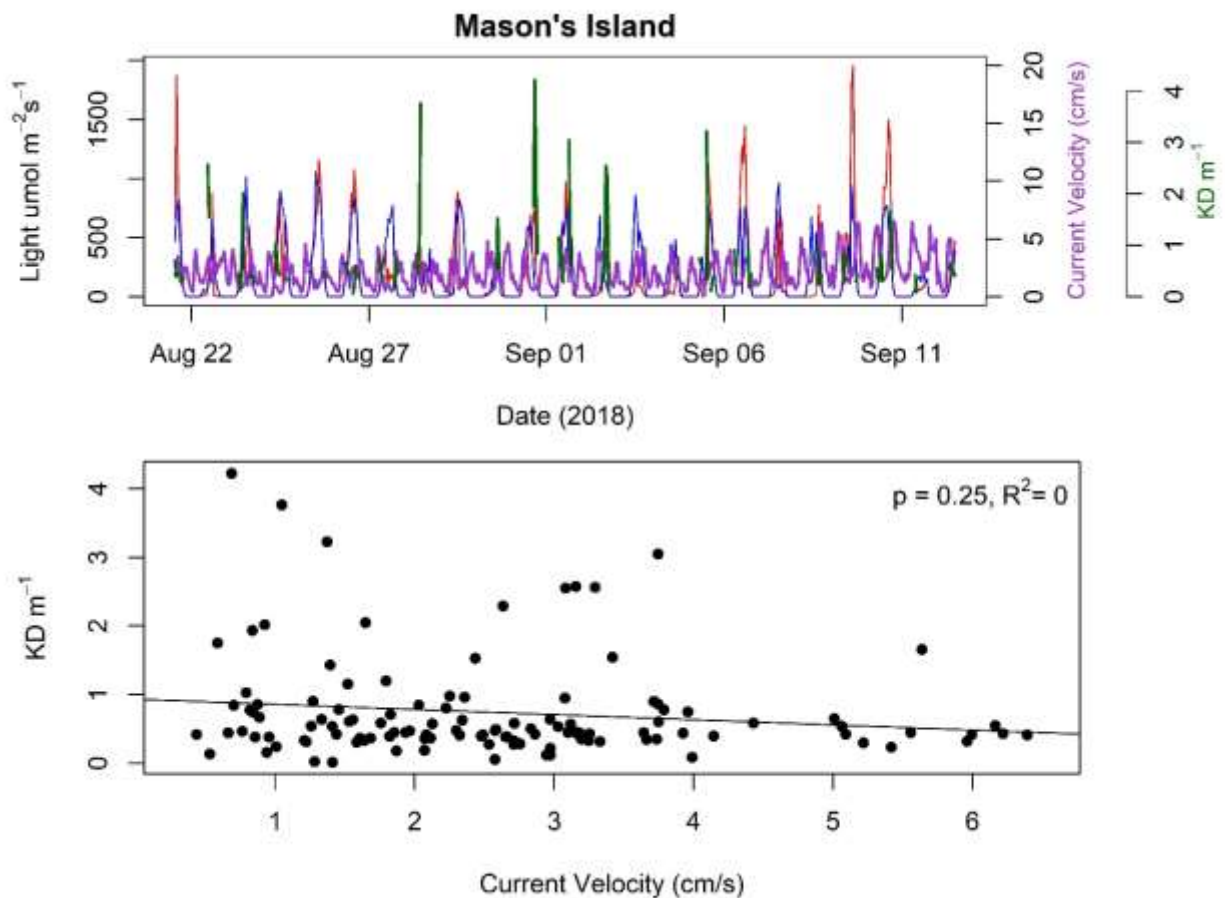
Figure S161. Light conditions in relation to current velocities at the shallow location at La Have Island. Top panel shows light readings from the top sensor (red line) and the bottom sensor (blue line). The green line on this panel shows light attenuation and the purple line shows current velocities. Bottom panel shows the relationship between light attenuation and current velocities.
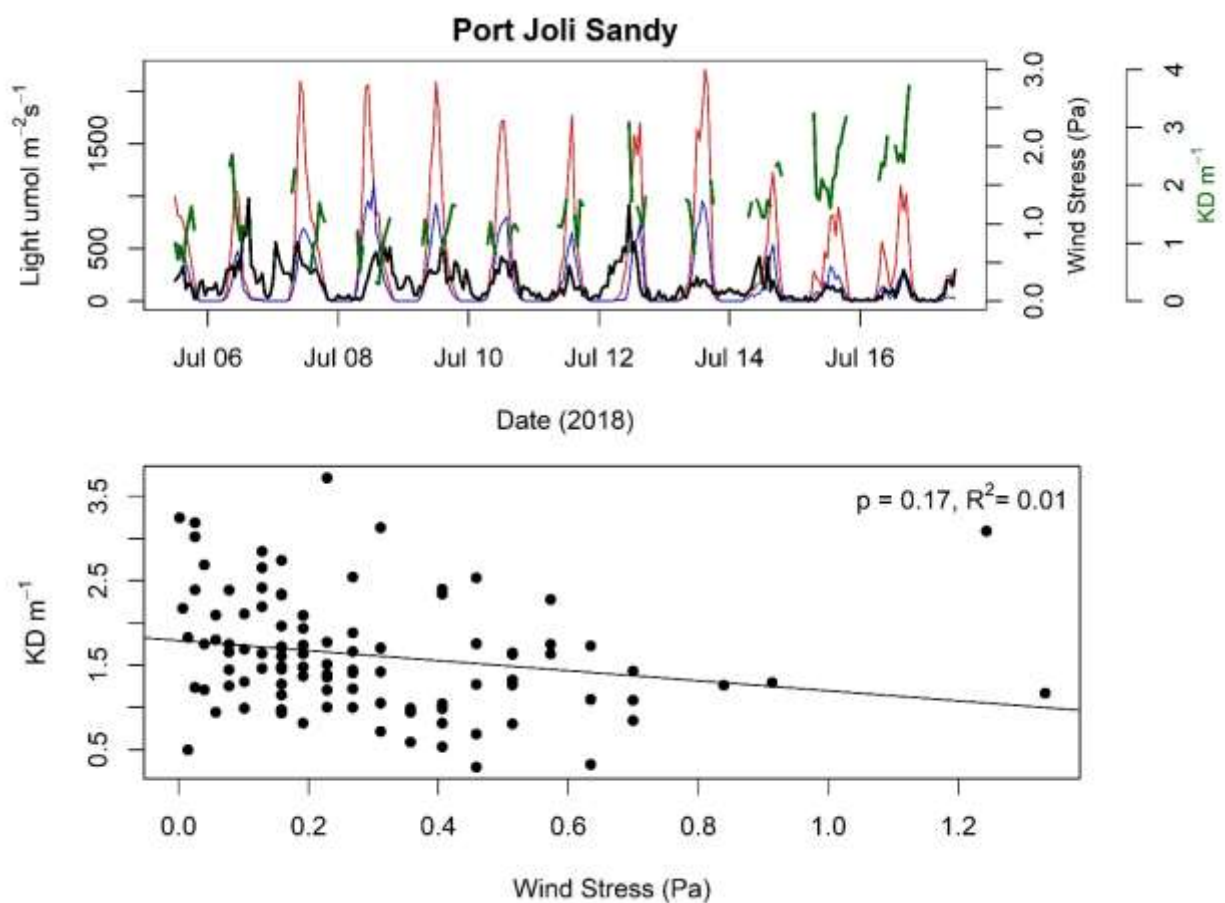
Lower Three Fathom

Figure S162. Light conditions in relation to wind stress at the shallow location at Lower Three Fathom. Top panel shows light readings from the top sensor (red line) and the bottom sensor (blue line). The green line on this panel shows light attenuation and the black line shows wind stress. Bottom panel shows the relationship between light attenuation and wind stress.

Mason's Island

Figure S163. Light conditions in relation to wind stress at the shallow location at Mason's Island. Top panel shows light readings from the top sensor (red line) and the bottom sensor (blue line). The green line on this panel shows light attenuation and the black line shows wind stress. Bottom panel shows the relationship between light attenuation and wind stress.
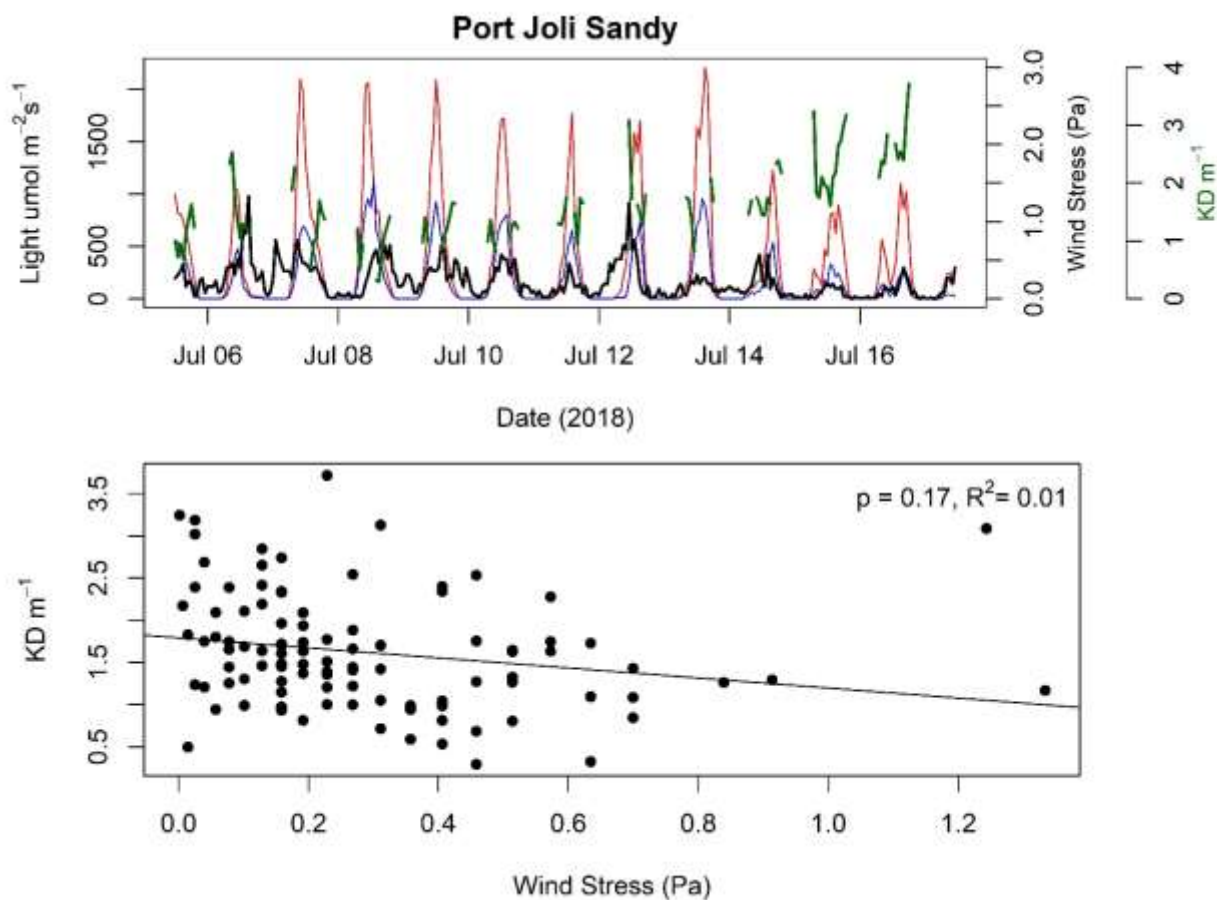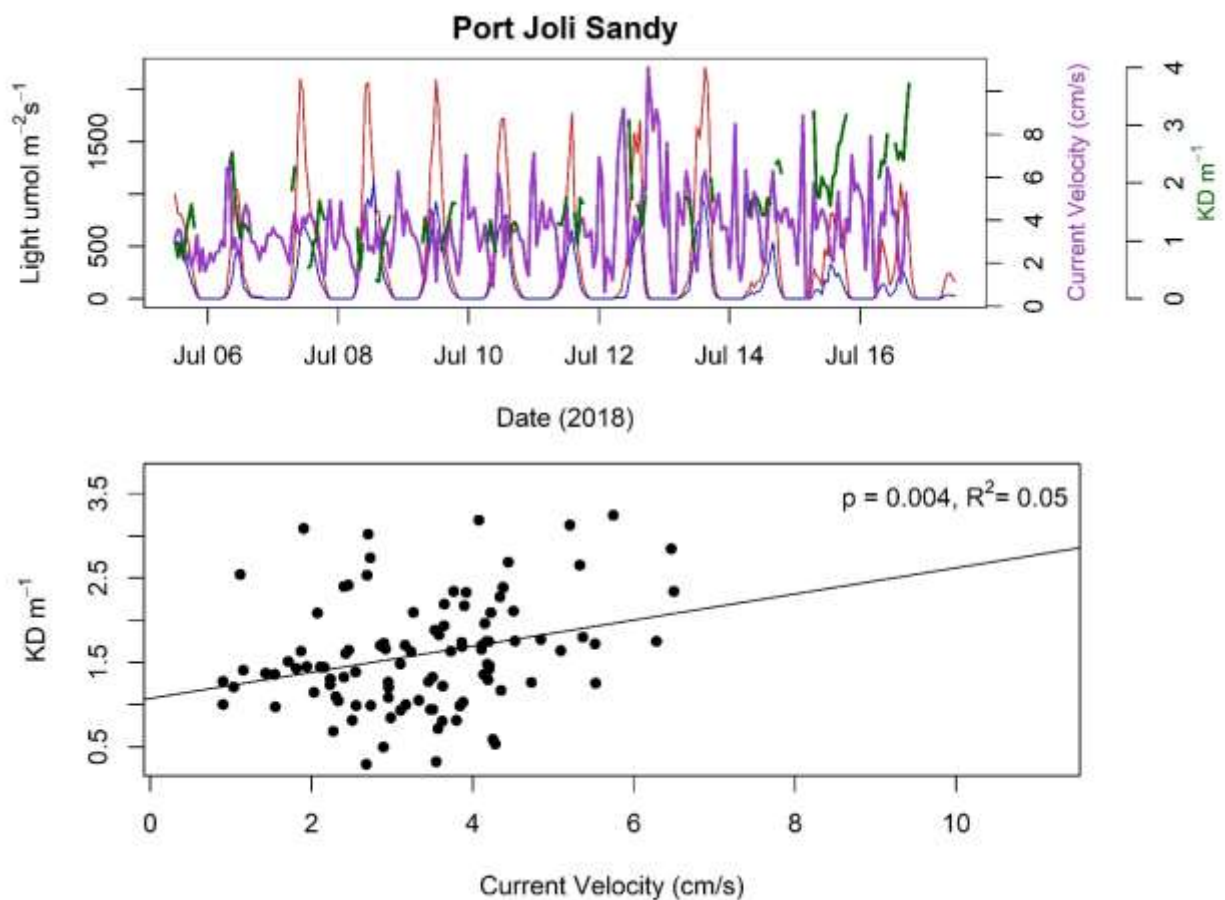
Figure S164. Light conditions in relation to current velocities at the shallow location at Mason's Island. Top panel shows light readings from the top sensor (red line) and the bottom sensor (blue line). The green line on this panel shows light attenuation and the purple line shows current velocities. Bottom panel shows the relationship between light attenuation and current velocities.
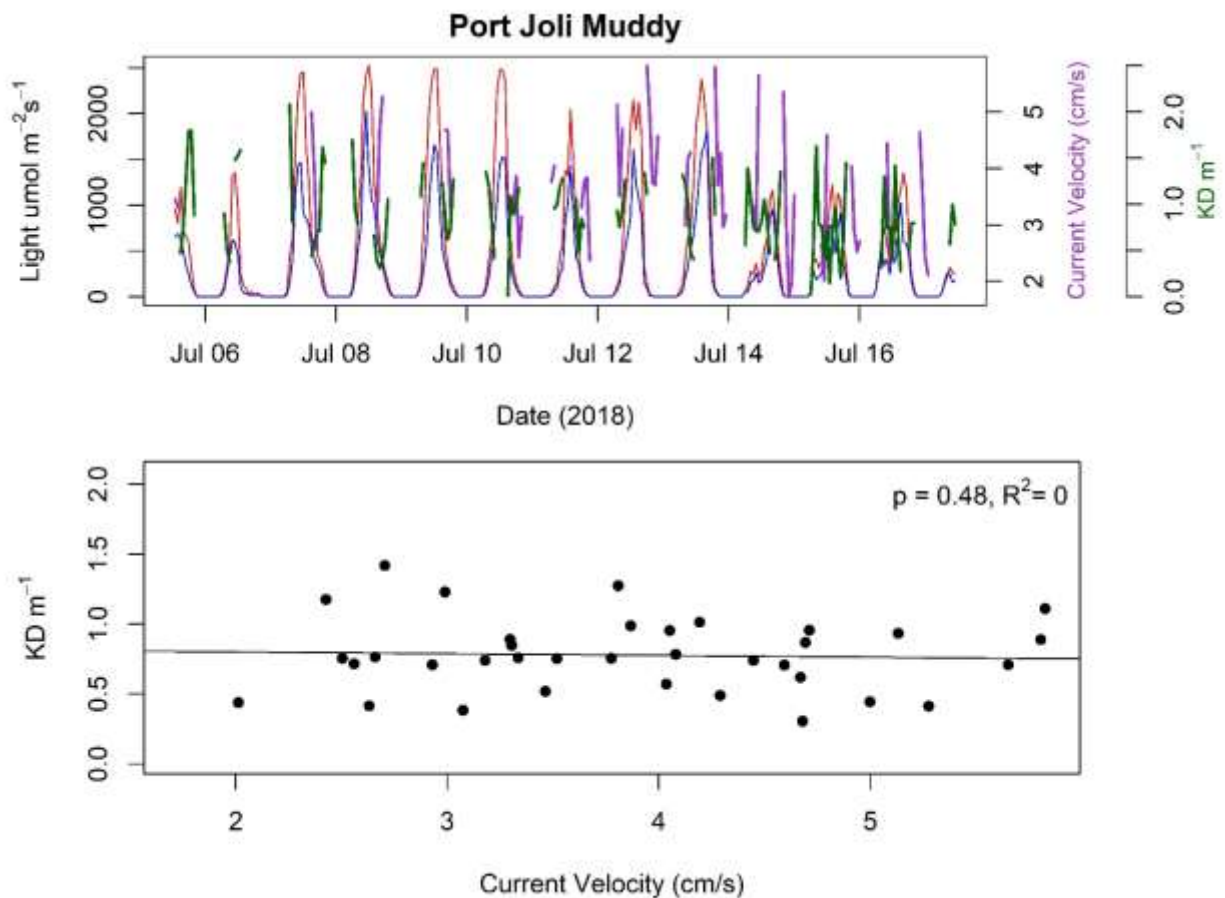
Port Joli

Figure S165. Light conditions in relation to wind stress at the sandy location at Port Joli. Top panel shows light readings from the top sensor (red line) and the bottom sensor (blue line). The green line on this panel shows light attenuation and the black line shows wind stress. Bottom panel shows the relationship between light attenuation and wind stress.

Figure S166. Light conditions in relation to wind stress at the muddy location at Port Joli. Top panel shows light readings from the top sensor (red line) and the bottom sensor (blue line). The green line on this panel shows light attenuation and the black line shows wind stress. Bottom panel shows the relationship between light attenuation and wind stress.

Figure S167. Light conditions in relation to current velocities at the sandy location at Port Joli. Top panel shows light readings from the top sensor (red line) and the bottom sensor (blue line). The green line on this panel shows light attenuation and the purple line shows current velocities. Bottom panel shows the relationship between light attenuation and current velocities.
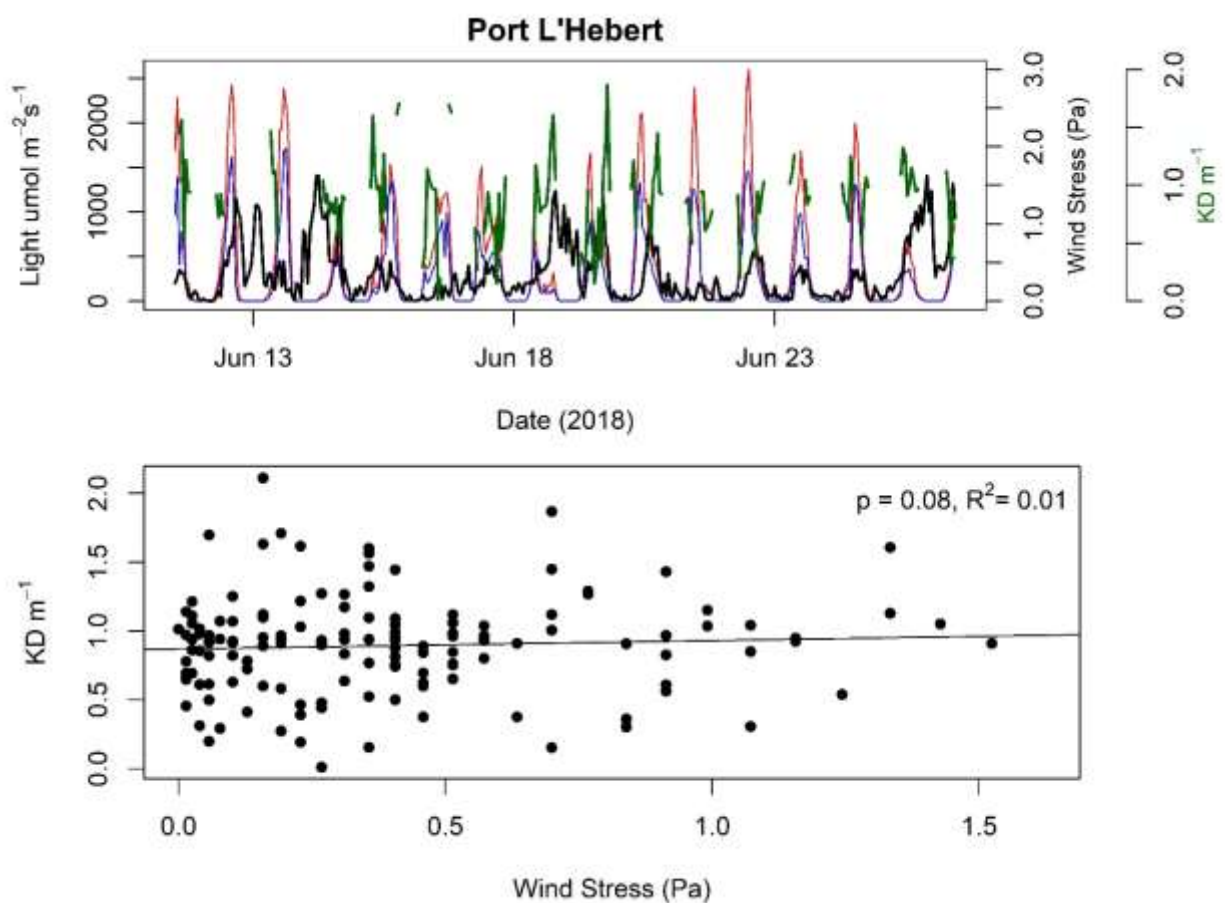
Figure S168. Light conditions in relation to current velocities at the muddy location at Port Joli. Top panel shows light readings from the top sensor (red line) and the bottom sensor (blue line). The green line on this panel shows light attenuation and the purple line shows current velocities. Bottom panel shows the relationship between light attenuation and current velocity.

Port L'Hebert

Figure S169. Light conditions in relation to current velocities at Port L'Hebert. Top panel shows light readings from the top sensor (red line) and the bottom sensor (blue line). The green line on this panel shows light attenuation and the black line shows wind stress. Bottom panel shows the relationship between light attenuation and wind stress.
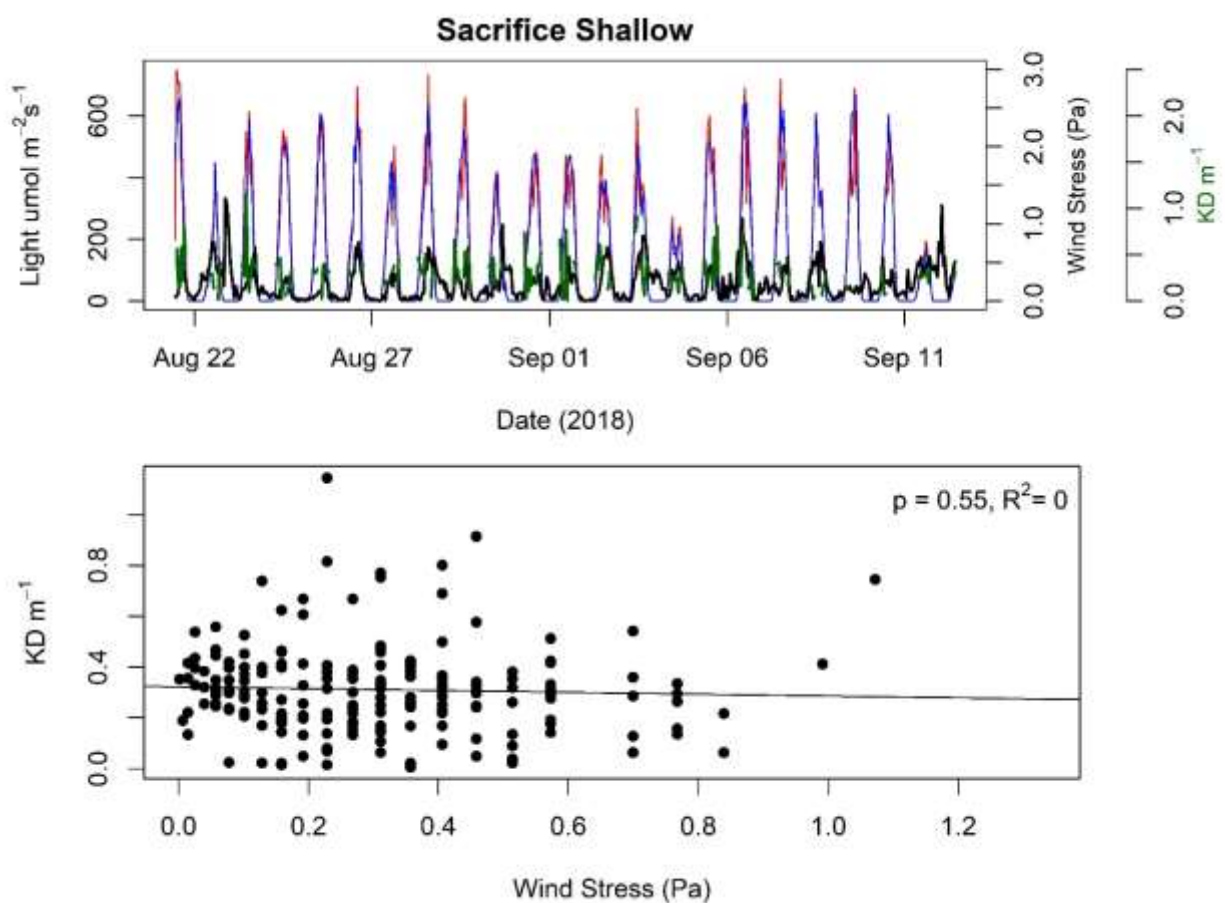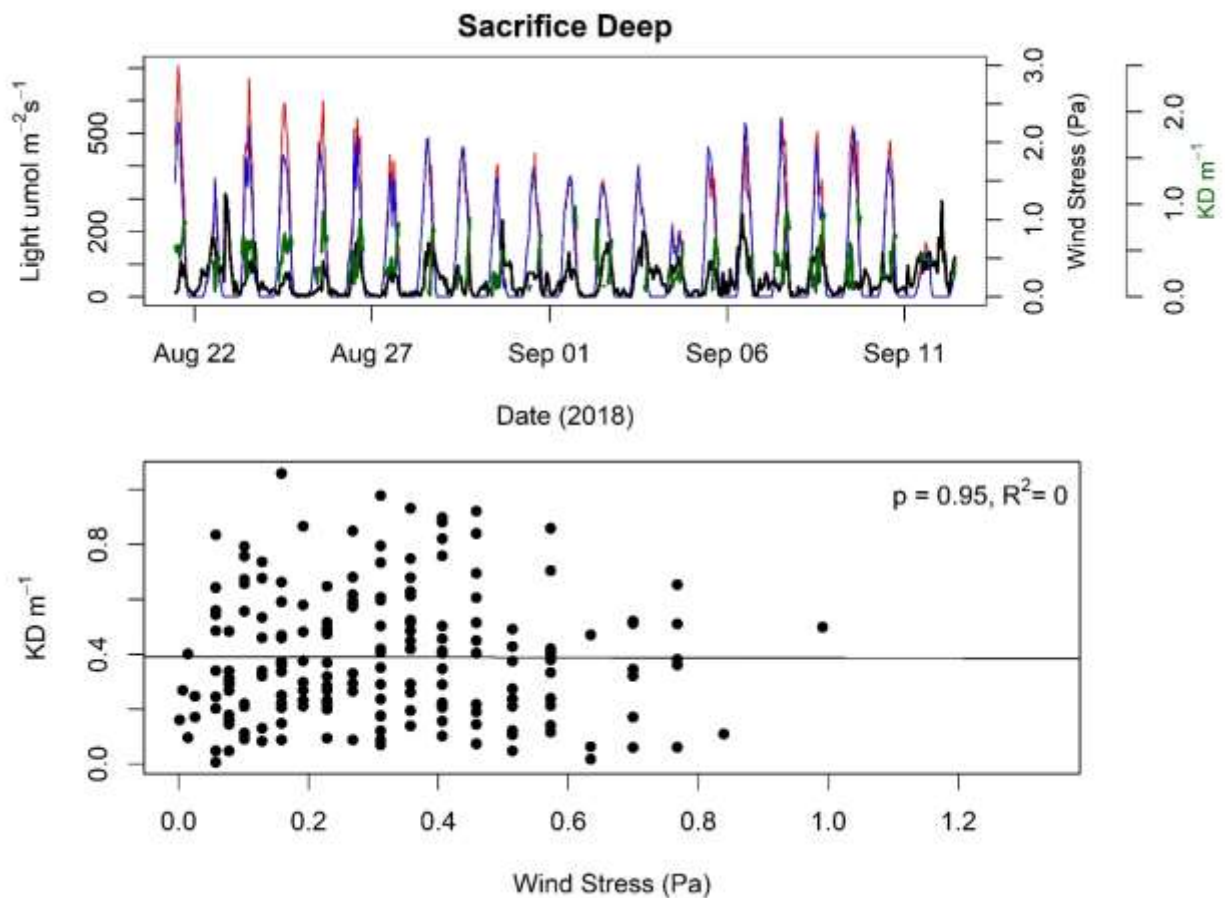
Sacrifice Island

Figure S170. Light conditions in relation to wind stress at the shallow location at Sacrifice Island. Top panel shows light readings from the top sensor (red line) and the bottom sensor (blue line). The green line on this panel shows light attenuation and the black line shows wind stress. Bottom panel shows the relationship between light attenuation and wind stress.
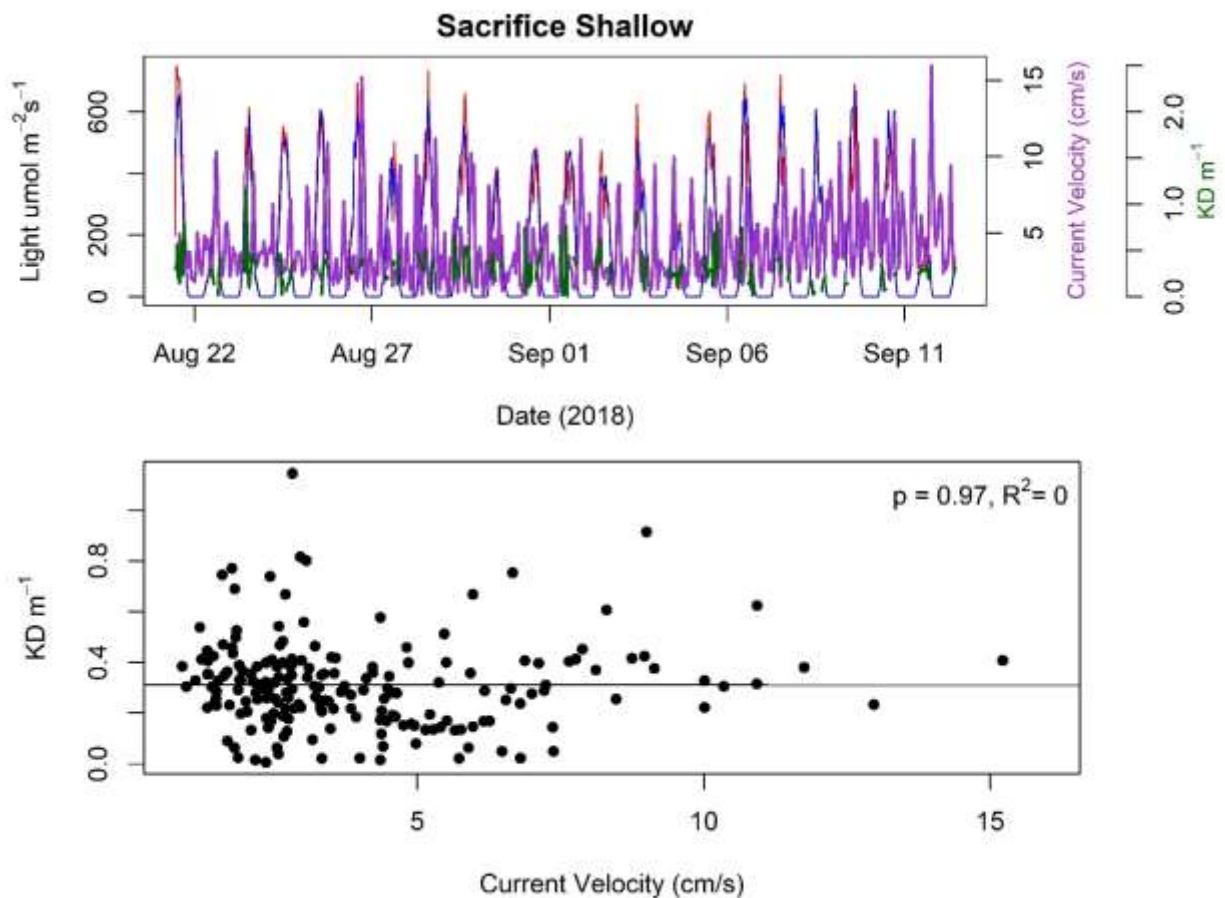
Figure S171. Light conditions in relation to wind stress at deep location at Sacrifice Island. Top panel shows light readings from the top sensor (red line) and the bottom sensor (blue line). The green line on this panel shows light attenuation and the black line shows wind stress. Bottom panel shows the relationship between light attenuation and wind stress.

Figure 172. Light conditions in relation to current velocities at the shallow location at Sacrifice Island. Top panel shows light readings from the top sensor (red line) and the bottom sensor (blue line). The green line on this panel shows light attenuation and the purple line shows current velocities. Bottom panel shows the relationship between light attenuation and current velocity.
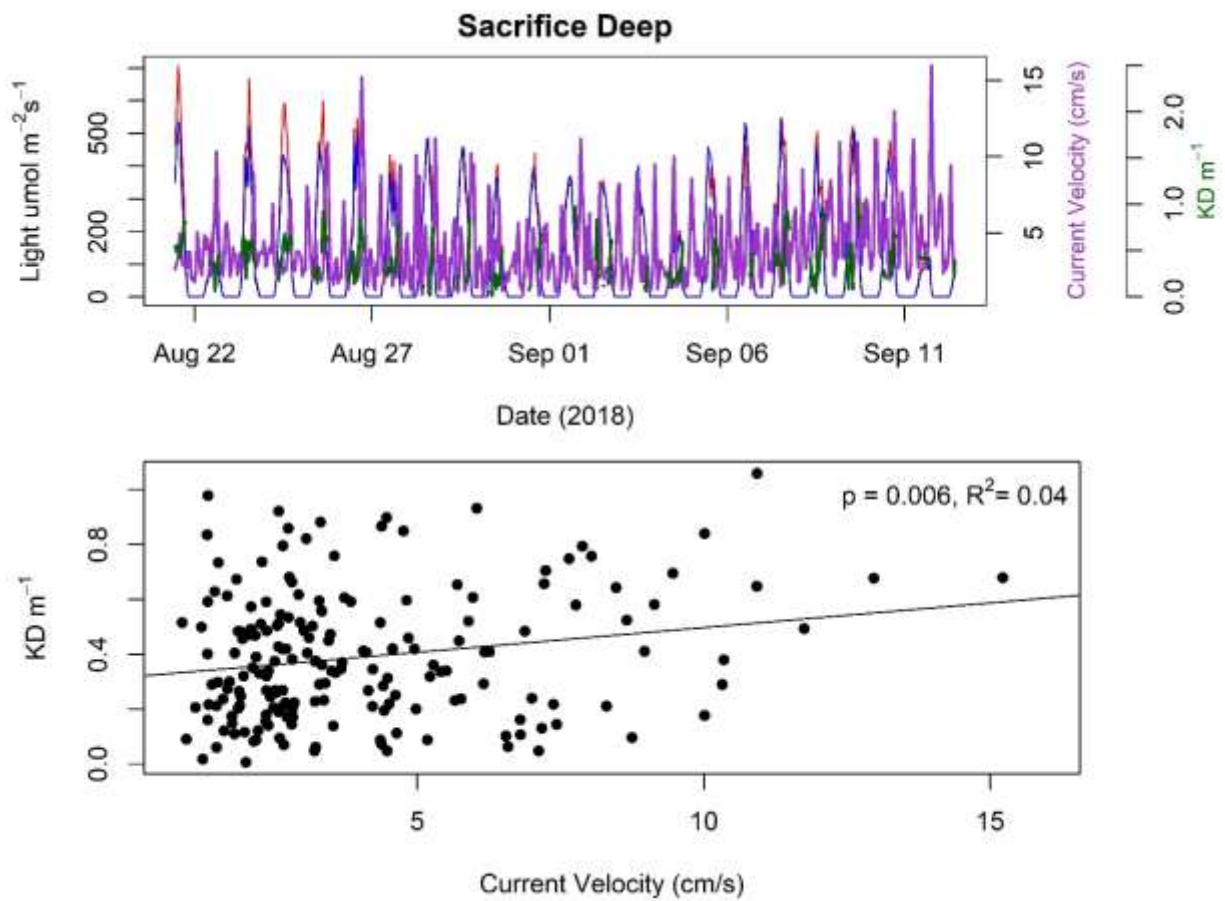
Figure S173. Light conditions in relation to current velocities at the deep location at Sacrifice Island. Top panel shows light readings from the top sensor (red line) and the bottom sensor (blue line). The green line on this panel shows light attenuation and the purple line shows current velocities. Bottom panel shows the relationship between light attenuation and current velocity.
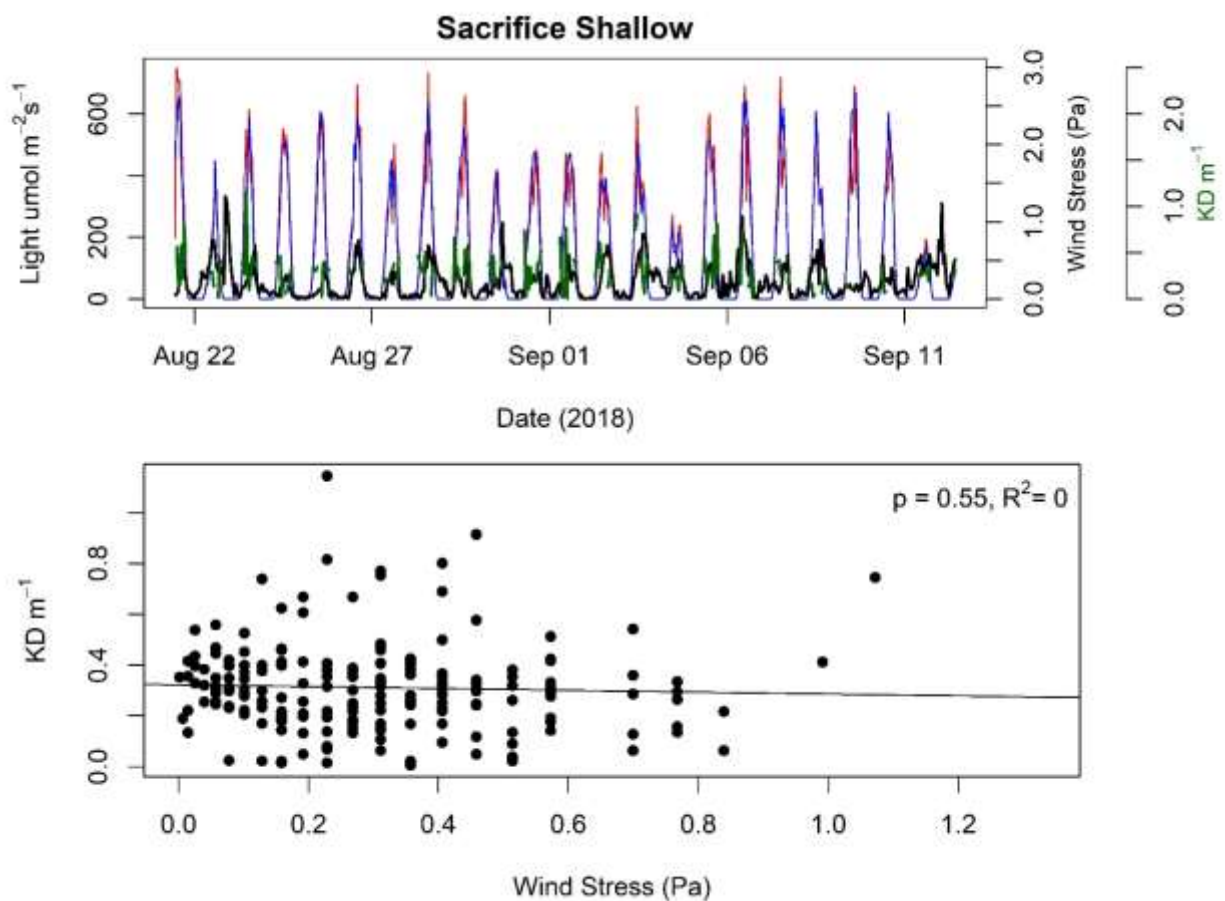
Sambro Island

Figure S174. Light conditions in relation to wind stress at the shallow location at Sambro Island. Top panel shows light readings from the top sensor (red line) and the bottom sensor (blue line). The green line on this panel shows light attenuation and the black line shows wind stress. Bottom panel shows the relationship between light attenuation and wind stress.
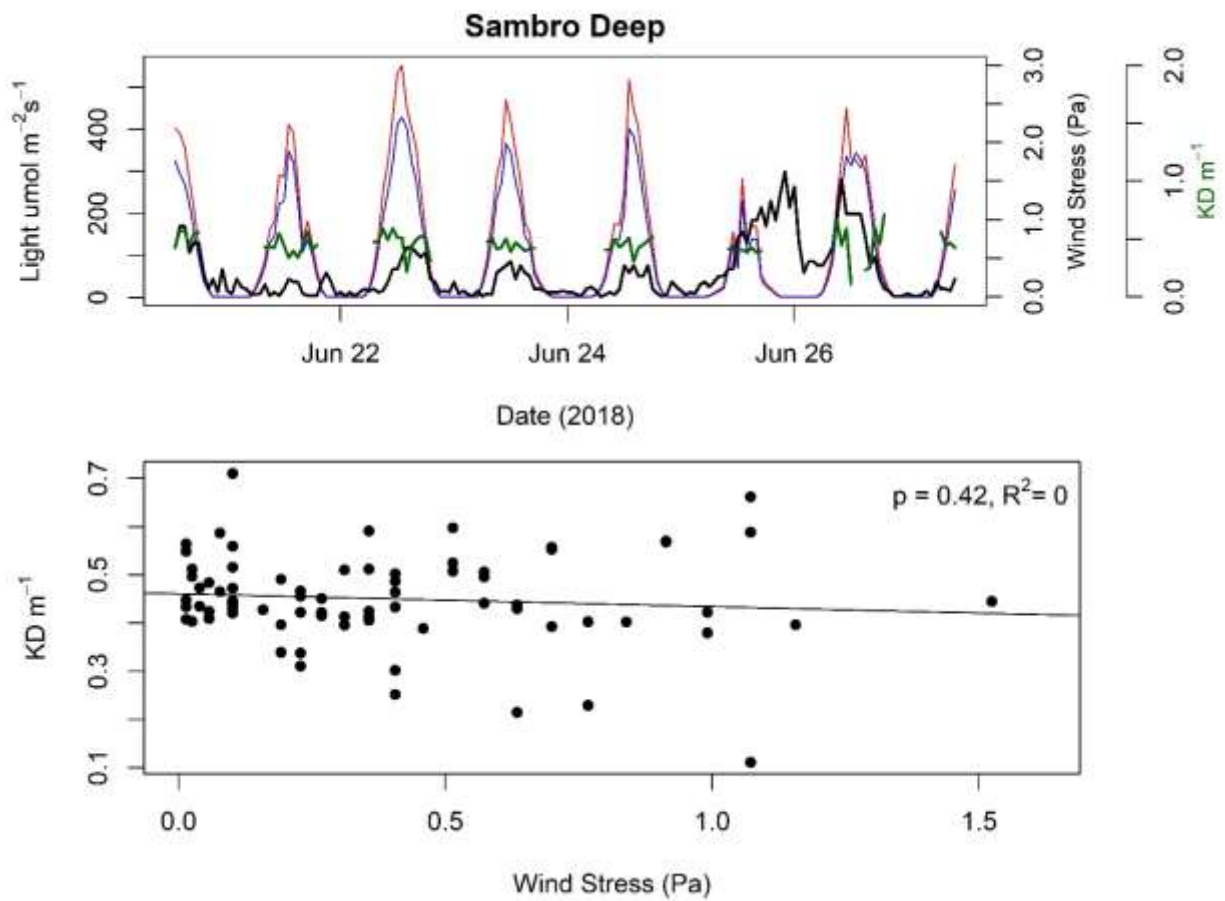
Figure S174. Light conditions in relation to wind stress at the deep location at Sambro Island. Top panel shows light readings from the top sensor (red line) and the bottom sensor (blue line). The green line on this panel shows light attenuation and the black line shows wind stress. Bottom panel shows the relationship between light attenuation and wind stress.
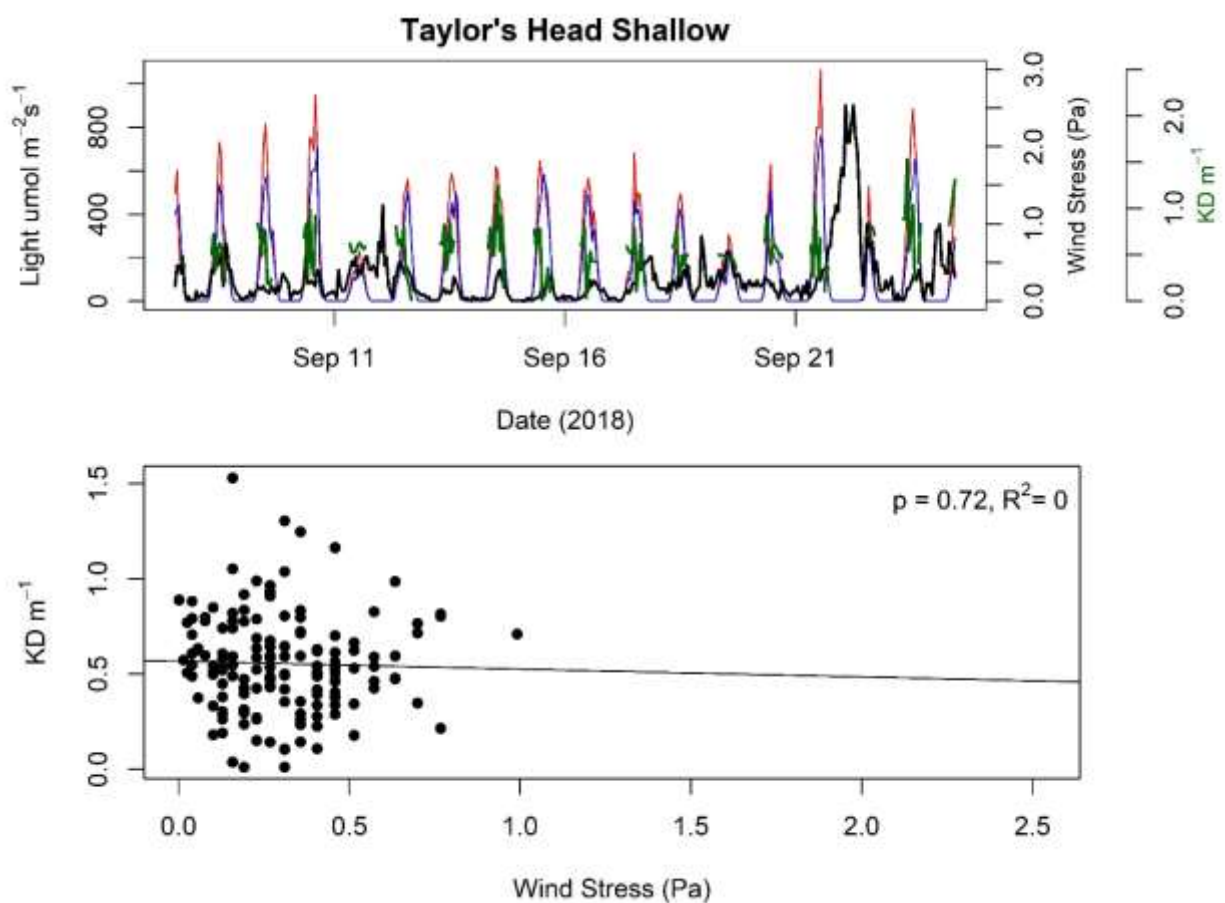
Taylor's Head

Figure S175. Light conditions in relation to wind stress at the shallow location at Taylor's Head. Top panel shows light readings from the top sensor (red line) and the bottom sensor (blue line). The green line on this panel shows light attenuation and the black line shows wind stress. Bottom panel shows the relationship between light attenuation and wind stress.
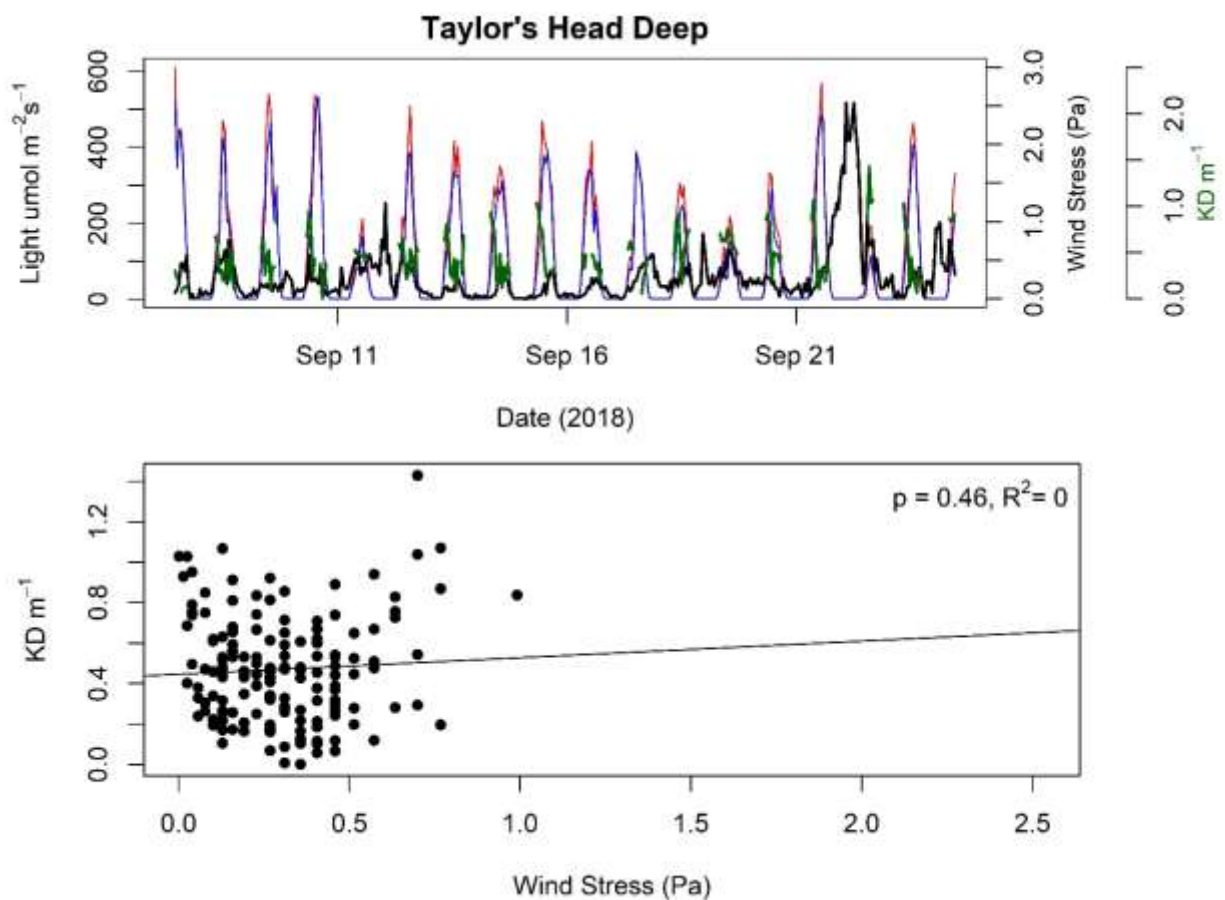
Figure S176. Light conditions in relation to current velocities at the deep location at Taylor's Head. Top panel shows light readings from the top sensor (red line) and the bottom sensor (blue line). The green line on this panel shows light attenuation and the black line shows wind stress. Bottom panel shows the relationship between light attenuation and wind stress.
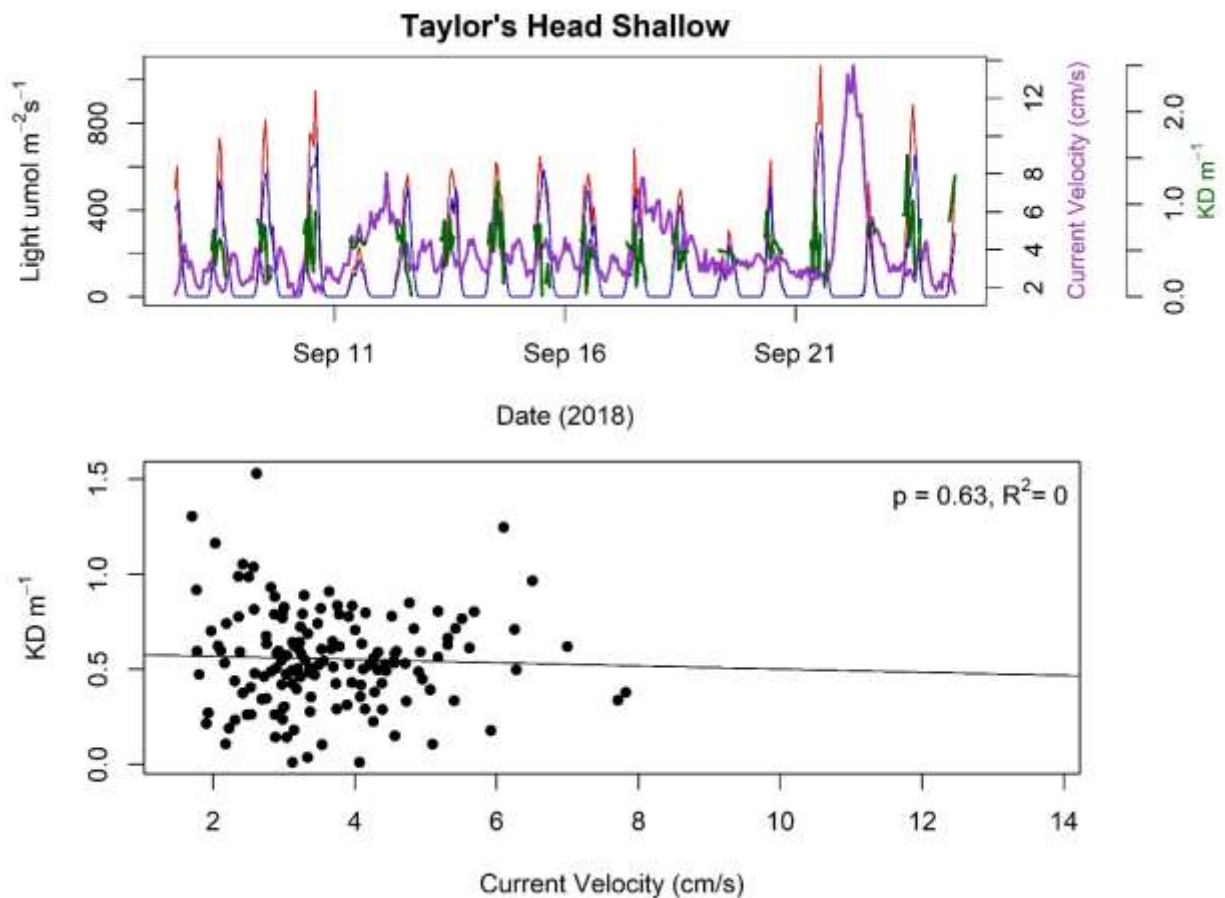
Figure S177. Light conditions in relation to current velocities at the shallow location at Taylor's Head. Top panel shows light readings from the top sensor (red line) and the bottom sensor (blue line). The green line on this panel shows light attenuation and the purple line shows current velocities. Bottom panel shows the relationship between light attenuation and current velocity.
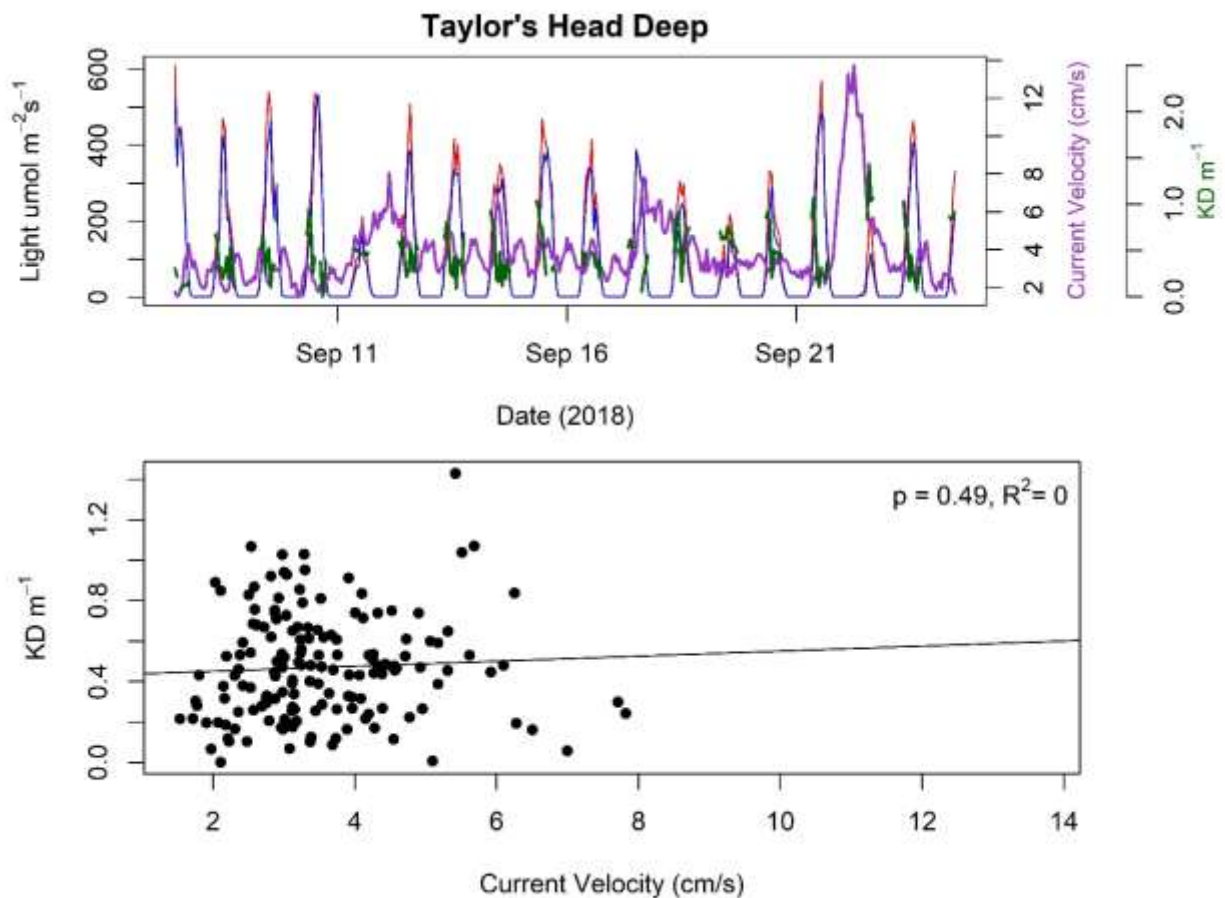
Figure S178. Light conditions in relation to current velocities at the deep location at Taylor's Head. Top panel shows light readings from the top sensor (red line) and the bottom sensor (blue line). The green line on this panel shows light attenuation and the purple line shows current velocities. Bottom panel shows the relationship between light attenuation and current velocity.